Eigenvalue-Based Spectrum Sensing for Cognitive Radio

Change Detection Problems and Fundamental Performance Limits

Von der Fakultät für Elektrotechnik und Informationstechnik
der Rheinisch-Westfälischen Technischen Hochschule Aachen
zur Erlangung des akademischen Grades eines Doktors
der Ingenieurwissenschaften genehmigte Dissertation

vorgelegt von

Diplom-Ingenieur
Martijn Franciscus Arts

aus Venray, Niederlande

Berichter: Universitätsprofessor Dr. rer. nat. Rudolf Mathar
Universitätsprofessorin Dr.-Ing. Anja Klein

Tag der mündlichen Prüfung: 15. Mai 2017

All of old. Nothing else ever.
Ever tried. Ever failed. No matter.
Try again. Fail again. Fail better.

Samuel Beckett, *Worstward Ho*

Acknowledgements

This thesis was written during my time as a research assistant at the Institute for Theoretical Information Technology of RWTH Aachen University. I would like to thank Prof. Dr. Rudolf Mathar for giving me the opportunity to work on this doctorate and for supporting me until its completion. Furthermore, I would like to thank Prof. Dr. Anja Klein for taking the time to act as the second reviewer of this thesis. Moreover, I would like to express my gratitude to Prof. Dr. Dr. Steffen Leonhardt and Prof. Dr. Dorit Merhof for agreeing to be part of the examining committee for my doctorate.

I would like to thank my former colleagues and students of the Institute for Theoretical Information Technology for good times at work over all these years.

Also, my former students Fabio König, Constantin Disch and Marius Cordts deserve credit for their work, which supported me greatly in my research projects and in writing this thesis.

Special thanks go to Georg Böcherer, Steven Corroy, Markus Rothe, Niklas Koep and Christopher Schnelling for interesting & helpful discussions, their friendship and great memories.

I am indebted to my friend and former colleague Andreas Bollig for two decades of great friendship and a very fruitful collaboration at work.

Schließlich möchte ich mich bei meinen Freunden, meiner Familie und im Speziellen bei meinen Eltern Elisabeth und Henk Arts für ihre langjährige Unterstützung und ihr Verständnis bedanken. Ganz besonderer Dank gebührt meiner Mutter für ihren unvergleichlichen Beistand und ihre unerschütterliche Zuversicht.

Düsseldorf, June 2017 Martijn Arts

Contents

1 Introduction

1.1 Motivation

The constantly growing traffic demand, caused by the shift from voice to multimedia applications, is a major challenge faced by the wireless communications industry. Unfortunately, the frequency spectrum is already a very scarce resource. Indeed, virtually all frequency bands of interest for wireless communications are already under license, see [1] for Germany and [2] for the United States. This is also reflected by the enormous prices that the German mobile operators paid to acquire new licenses: around 50 billion € for 145 MHz of bandwidth in 2001 [3, p. 51, Sec. 2.1.3] and more recently 5.1 billion € for 270 MHz of bandwidth in 2015 [4].

However, it was found that many of the current licensees do not fully utilize their reserved spectral resources. That is, over several dimensions including frequency, time and geographical location a significant portion of the spectrum is vacant, see [5, 6]. To more efficiently use these idle resources, it was suggested to break with the static spectrum management policy. Such efforts may be subsumed under the term *dynamic spectrum access* [7], which represents an application of the more general *cognitive radio* paradigm [8–10].

A particularly appealing approach to implementing dynamic spectrum access is *opportunistic spectrum access*. In this context, a transceiver is called a *primary user (PU)* or *secondary user (SU)* depending on whether he partakes in licensed or unlicensed communication, respectively. There are three distinct parts to this access paradigm: spectrum opportunity detection, spectrum opportunity exploitation and regulatory policy [7]. The latter defines the rules by which SUs may opportunistically exploit idle frequency bands after having detected them. The objective is to grant the secondary system to make more efficient use of idle spectral resources while protecting the primary system from harmful interference.

Evidently, the process of reliably detecting spectrum opportunities in low signal-to-noise ratio (SNR) environments — which is also called *spectrum sensing* — is challenging from a technical perspective. Consequently, many spectrum sensing algorithms have been discussed in the literature [11, 12]. These mainly differ with respect to their system models and their assumptions about the PU signal. As an example for a practical problem, consider the *hidden PU problem* illustrated in Figure 1.1, which is an instance of the hidden terminal problem. To ensure

detection of very weak signals and to tackle the hidden PU problem, cooperation among SUs was promptly suggested [13–16].

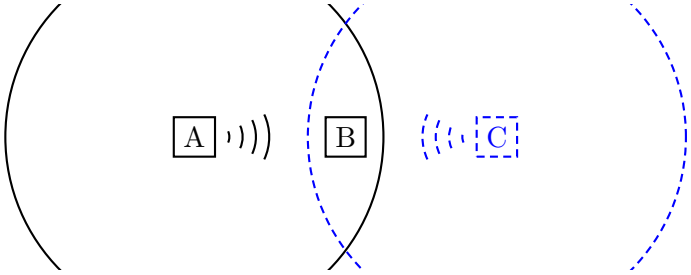

Figure 1.1: The hidden PU problem. PU A is transmitting to PU B and SU C is monitoring the channel. Since C is outside of the transmission range of A, C decides the channel is free and begins transmission. PU B now experiences harmful interference since B is in C's communication range.

A very promising class of spectrum sensing algorithms is (cooperative) *eigenvalue-based spectrum sensing* (also called *eigenvalue-based detection*) [17–24], where the detectors utilize functions of the eigenvalues of the sample covariance matrix. These algorithms rely on the assumption that the noise process of the receiver may be modeled as white and uncorrelated across receivers. Hence, the received signal should only be correlated among time or receivers if a PU signal is present. This class of algorithms makes very little assumptions about the PU signal and the system, while exhibiting good detection performance.

This thesis is dedicated to advancing (cooperative) eigenvalue-based detection in three areas. Firstly, this work aims at combining the strengths of traditional eigenvalue-based detection with the *quickest detection* paradigm, the latter of which intends to minimize detection delay. Secondly, an analysis of the robustness of eigenvalue-based detection algorithms in the presence of model uncertainties is carried out and resulting performance limits are studied. Finally, this thesis contributes to the theoretical analysis of eigenvalue-based detectors.

1.2 Outline

In the following, an overview of the contents of this thesis is given. In Chapter 2 the general notation and special functions used throughout the thesis are defined.

A brief introduction to the fundamental concepts used in this work is provided in Chapter 3. Firstly, the general spectrum sensing problem, relevant basic concepts of detection theory and the most important classes of detectors are discussed. Secondly, the concept of eigenvalue-based spectrum sensing and its main detectors are described, which are the focus of this thesis. This work makes advances in

eigenvalue-based spectrum sensing by applying results from different areas of mathematics such as random matrix theory and order statistics. Furthermore, quickest detection, a detection paradigm used to minimize detection delays, is studied in conjunction with eigenvalue-based detectors. Moreover, this work tries to establish whether the so-called SNR wall phenomenon can be observed in eigenvalue-based detection. All of these concepts are briefly presented in separate sections.

Chapter 4 establishes three important system models which are used in eigenvalue-based spectrum sensing.

Quickest detection is a paradigm which aims at minimizing the delay in detecting changes. Large detection delays are harmful to both the primary and the secondary system in opportunistic spectrum access. In Chapter 5, it is therefore studied whether concepts from quickest detection may be combined with the strengths of eigenvalue-based spectrum sensing.

In the presence of model uncertainties, detectors experience an SNR threshold below which detection is impossible irrespective of the number of samples — the so-called SNR wall. In the context of eigenvalue-based spectrum sensing, two questions arise. Firstly, can it be shown that well-known detectors suffer from an SNR wall under practical model imperfections? Secondly, can the location of the SNR threshold be characterized with respect to fundamental system parameters? Chapter 6 answers these questions by investigating the effect of two practical model uncertainties: imperfect noise power calibration, and colored and correlated noise.

Chapter 7 performs a theoretical analysis of the maximum-minus-minimum eigenvalue (MMME) detector in a dual user scenario. Considering that similar theoretical results were obtained for the well-known maximum-minimum eigenvalue (MME) detector in Chapter 5, their performances in the presence of noise power uncertainty are compared on the basis of analytical findings.

Finally, Chapter 8 concludes the thesis by summarizing the major results and discussing future research directions.

Parts of this thesis have been published in [25–30].

2 Notation

In this chapter, the general notation of this thesis is introduced. Furthermore, some special functions and probability distributions are defined, which are referenced to throughout this work.

Sets The set of natural numbers is denoted by $\mathbb{N} = \{1, 2, \dots\}$ and the set of integers is denoted by $\mathbb{Z} = \{\dots, -2, -1, 0, 1, 2, \dots\}$. Furthermore, the sets of real and complex numbers are identified by $\mathbb{R}$ and $\mathbb{C}$, respectively. The cardinality of a set $\mathcal{A}$ is written as

$$|\mathcal{A}| \ . \tag{2.1}$$

Scalars Scalars are printed in italics with normal font-weight, e.g., a and v. Note that system parameters are typically identified by uppercase symbols, e.g., N. The absolute value, the argument and the complex conjugate of the scalar v are denoted by

$$|v| \, , \arg(v) \text{ and } v^* \, , \tag{2.2}$$

respectively.

We write

$$v \gtrapprox a \tag{2.3}$$

to express that a is an approximation of a lower bound on v. That is, it is technically not a bound. However, the approximation is intended to study the behavior of a lower bound which is hard to compute exactly, see Sections 6.1.1 and 6.1.2.

Vectors Vectors are identified by lowercase symbols printed in boldface, e.g., $\mathbf{v}$. All vectors are assumed to be column vectors, unless explicitly stated otherwise. The i-th entry of the vector $\mathbf{v}$ is addressed by

$$v_i \text{ or } [\mathbf{v}]_i \ . \tag{2.4}$$

The transpose, the element-wise complex conjugate and the conjugate transpose (Hermitian transpose) of the vector $\mathbf{v}$ are denoted by

$$\mathbf{v}^{\mathrm{T}}, \mathbf{v}^{*}, \text{ and } \mathbf{v}^{\mathrm{H}}, \tag{2.5}$$

respectively. The element-wise absolute value of the vector $\mathbf{v}$ is written as

$$|\mathbf{v}| \ . \tag{2.6}$$

Relational operators like $>$, $\leq$, $=$, etc. are understood to operate element-wise on vectors. The same goes for minimum and maximum operators, e.g., $\min(\mathbf{a}, \mathbf{b})$ and $\max(\mathbf{a}, \mathbf{b})$.

Norms Let $\mathbf{v} \in \mathbb{C}^N$. The ℓ_1-norm of the vector $\mathbf{v}$ is defined as

$$\|\mathbf{v}\|_1 = \sum_{i=1}^{N} |v_i| \ . \tag{2.7}$$

The Euclidean norm or ℓ_2-norm of the vector $\mathbf{v}$ is defined as

$$\|\mathbf{v}\|_2 = \sqrt{\sum_{i=1}^{N} |v_i|^2} . \tag{2.8}$$

Matrices Matrices are written as uppercase symbols printed in boldface, e.g., $\mathbf{A}$ and $\mathbf{V}$. The entry of the matrix $\mathbf{A}$ located in the i-th row and the j-th column is identified as

$$a_{ij} \, . \tag{2.9}$$

The i-th column of the matrix $\mathbf{A}$ is addressed as

$$\mathbf{a}_i \, . \tag{2.10}$$

We write

$$\mathbf{A} = [o(i,j)]_{1 \leq i,j \leq N} \text{ or } [\mathbf{A}]_{1 \leq i,j \leq N} = o(i,j) \, , \tag{2.11}$$

to define a $N \times N$ matrix $\mathbf{A}$ entry-wise with the help of a function $o(i,j)$, where i and j identify row and column, respectively.

The transpose, the element-wise complex conjugate and the conjugate transpose (Hermitian transpose) of the matrix $\mathbf{A}$ are denoted by

$$\mathbf{A}^{\mathrm{T}}, \mathbf{A}^{*}, \text{ and } \mathbf{A}^{\mathrm{H}}, \tag{2.12}$$

respectively. Rank, trace, determinant and inverse of the matrix $\mathbf{A}$ are written as

$$\mathrm{rank}(\mathbf{A}), \mathrm{tr}(\mathbf{A}), |\mathbf{A}| \text{ and } \mathbf{A}^{-1} , \tag{2.13}$$

respectively. The vector of increasingly ordered eigenvalues of the matrix $\mathbf{A}$ is denoted by

$$\mathrm{eig}\,(\mathbf{A}) \ . \tag{2.14}$$

Special Vectors and Matrices Vectors of dimension N containing only zeros and ones are denoted by

$$\mathbf{0}_N \text{ and } \mathbf{1}_N\,, \tag{2.15}$$

respectively. Similarly, matrices of dimension $K \times N$ exclusively containing zeros and ones are written as

$$\mathbf{0}_{K\times N} \text{ and } \mathbf{1}_{K\times N}\,, \tag{2.16}$$

respectively. The identity matrix of dimension N is identified by

$$\mathbf{I}_N\,. \tag{2.17}$$

Complex Numbers The imaginary unit is defined as

$$\imath = \sqrt{-1}\,. \tag{2.18}$$

The real and imaginary part of a complex-valued scalar v are identified by

$$\mathrm{Re}(v) \text{ and } \mathrm{Im}(v)\,, \tag{2.19}$$

respectively. These operators are analogously defined for vectors and matrices, where they operate element-wise.

Special Functions The floor and ceiling functions of a scalar v are denoted by

$$\lfloor v \rfloor \text{ and } \lceil v \rceil\,, \tag{2.20}$$

respectively.

The positive part is defined as:

$$[v]^+ = \max(v, 0)\,, \tag{2.21}$$

which is analogously defined for vector or matrix argument, where it operates element-wise.

Let $\mathcal{A}, \mathcal{B}$ be arbitrary sets. Then, the indicator function for $v \in \mathcal{A}$ with $\mathcal{B} \subset \mathcal{A}$ is defined as:

$$\mathbb{I}_{\mathcal{B}}(v) = \begin{cases} 1, & \text{if } v \in \mathcal{B} \\ 0, & \text{if } v \notin \mathcal{B}\,. \end{cases} \tag{2.22}$$

The factorial of $v \in \mathbb{N}$ is defined as

$$v! = \prod_{i=1}^{v} i \tag{2.23}$$

and $0! = 1$ by convention.

The Gamma function [31, p. 255 ff., Sec. 6.1] is written as $\Gamma(v)$ for $v \in \mathbb{C}$. If $v \in \mathbb{N}$ it can be expressed with the factorial

$$\Gamma(v+1) = v! \tag{2.24}$$

and it is defined by the following improper integral otherwise (if $\mathrm{Re}(v) > 0$):

$$\Gamma(v) = \int_0^\infty u^{v-1} e^{-u} \,\mathrm{d}u\,. \tag{2.25}$$

The Pochhammer symbol (as used in the theory of special functions, also called the rising factorial) for $v, a \in \mathbb{N}$ is defined as:

$$\{v\}_a = \frac{(v+a-1)!}{(v-1)!} = \frac{\Gamma(v+a)}{\Gamma(v)}\,, \tag{2.26}$$

where $\{a\}_0 = 1$ by convention.

The a-th order modified Bessel function of the first kind for $a \in \mathbb{N}$ and $v \in \mathbb{C}$ is defined as [31, p. 376, Eq. (9.6.19)]:

$$\mathcal{I}_a(v) = \frac{1}{\pi} \int_0^\pi e^{v\cos(u)} \cos(au) \,\mathrm{d}u\,. \tag{2.27}$$

The a-th order modified Bessel function of the second kind is defined for $a, v \in \mathbb{C}$ whereRe$(a) > -\frac{1}{2}$ and $|\arg(v)| < \frac{1}{2}\pi$ as [31, p. 376, Eq. (9.6.23)]:

$$\mathcal{K}_a\,(v) = \frac{\sqrt{\pi}(\frac{1}{2}v)^a}{\Gamma(a+\frac{1}{2})} \int_1^\infty e^{-vu}(v^2-1)^{a-\frac{1}{2}} \,\mathrm{d}u\,. \tag{2.28}$$

The generalized hypergeometric function (or series) is defined as [32, p. 1010, Eq. (9.14.1.)]:

$${}_p\mathcal{F}_q(a_1,\ldots,a_p;b_1,\ldots,b_q;v) = \sum_{i=0}^{\infty} \frac{\{a_1\}_i \{a_2\}_i \cdots \{a_p\}_i}{\{b_1\}_i \{b_2\}_i \cdots \{b_q\}_i} \frac{v^i}{i!}\,. \tag{2.29}$$

Tricomi's confluent hypergeometric function (also called Kummer's function of the second kind), which is a solution to Kummer's differential equation, is defined for $\mathrm{Re}(a) > 0$ as [31, p. 505, Eq. (13.2.5)]:

$$\mathcal{U}\,(a,b,v) = \frac{1}{\Gamma(a)} \int_0^\infty e^{-vu} u^{(a-1)} (u+1)^{(b-a-1)} \,\mathrm{d}u\,. \tag{2.30}$$

Statistical Notation The probability of an event v is denoted by

$$\mathrm{P}(v)\,. \tag{2.31}$$

Conditional random variables are written as

$$v \mid u\,, \tag{2.32}$$

which means the random variable v is conditioned on the event u.

Unless explicitly noted otherwise, a probability density function (PDF) is written as f and a cumulative distribution function (CDF) is identified by F. If a subscript is present, it identifies the random variable / vector with which f or F is associated. Exceptions are the PDF and CDF of the test statistic under investigation, which are sometimes denoted by f_0 and f_1 under hypothesis $\mathcal{H}_0$ and $\mathcal{H}_1$, respectively (see also Section 3.1).

The mean (or mathematical expectation) of a random variable v is denoted by

$$\mathrm{E}[v]\,. \tag{2.33}$$

The variance of a random variable v is defined as

$$\mathrm{Var}[v] = \mathrm{E}\left[(v - \mathrm{E}[v])\,(v - \mathrm{E}[v])^*\right]\,. \tag{2.34}$$

The covariance and the correlation coefficient between two random variables v and u are defined as

$$\mathrm{Cov}[v,u] = \mathrm{E}[(v - \mathrm{E}[v])\,(u - \mathrm{E}[u])^*] \tag{2.35}$$

and

$$\mathrm{Corr}[v,u] = \frac{\mathrm{Cov}[v,u]}{\sqrt{\mathrm{Var}[v]\,\mathrm{Var}[u]}}\,, \tag{2.36}$$

respectively. The median of a random variable v is written as

$$\mathrm{median}[v]\,. \tag{2.37}$$

Let v be a random variable with corresponding PDF f_v and let o a function. In some situations, we like to emphasize according to which probability measure the mean or the median must be interpreted. For the mean we write

$$\mathrm{E}_v[o(v)] \text{ or } \mathrm{E}_{f_v}[o(v)] \tag{2.38}$$

and for the median, we write analogously

$$\underset{v}{\mathrm{median}}[o(v)] \text{ or } \underset{f_v}{\mathrm{median}}[o(v)]\,. \tag{2.39}$$

A special case is the mean of a test statistic T, where we use the shorthand notations

$$\mathrm{E}_{\mathcal{H}_0}[T] = \mathrm{E}[T \mid \mathcal{H}_0] \text{ and } \mathrm{E}_{\mathcal{H}_1}[T] = \mathrm{E}[T \mid \mathcal{H}_1] \tag{2.40}$$

to clarify under which hypothesis ($\mathcal{H}_0$ or $\mathcal{H}_1$) the mean is to be calculated, see also Section 3.1.

The i-th order statistic of a random sample $U_1, U_2, \ldots, U_K$ is denoted by

$$U_{(i)}\,, \tag{2.41}$$

for $i = 1, \ldots, K$. Please refer to Section 3.6 for a formal definition.

Estimation An estimate of the scalar a, the vector $\mathbf{a}$ and the matrix $\mathbf{A}$ are identified by

$$\hat{a}, \hat{\mathbf{a}} \text{ and } \hat{\mathbf{A}}\,, \tag{2.42}$$

respectively.

Probability Distributions The PDFs and CDFs given below can be found in [33, p. 98 ff., Sec. 3.3], [34, p. 459, Eq. (14.2)] and [35, Eq. (19)].

The univariate rectangular (or continuous uniform) distribution with support $[a, b]$ $(a < b)$ is denoted by $\mathcal{R}(a, b)$. Its PDF is

$$f(v) = \frac{1}{b-a}\, \mathbb{I}_{[a,b]}(v) \tag{2.43}$$

and its CDF follows as

$$F(v) = \begin{cases} 0, & \text{if } v < a \\ v, & \text{if } a \leq v \leq b \\ 1, & \text{if } v > b. \end{cases} \tag{2.44}$$

We call $\mathcal{R}(0, 1)$ the standard rectangular distribution.

The univariate Beta distribution with parameters $a > 0$ and $b > 0$ is denoted by $\mathrm{Beta}(a, b)$. Its PDF is given by

$$f(v) = \frac{\Gamma(a)\,\Gamma(b)}{\Gamma(a+b)}\, v^{a-1}\,(1-v)^{a-1}\,, \quad 0 < v < 1\,. \tag{2.45}$$

The mean and variance of a $\mathrm{Beta}(a, b)$ distributed random variable V are

$$\mathrm{E}[V] = \frac{a}{a+b} \tag{2.46}$$

and

$$\mathrm{Var}[V] = \frac{ab}{(a+b)^2\,(a+b+1)}\,, \tag{2.47}$$

respectively.

The univariate Gaussian (or normal) distribution with mean μ and variance σ^2 is denoted by $\mathcal{N}(\mu, \sigma^2)$. Its PDF is denoted by

$$\phi(v) = \frac{1}{\sqrt{2\pi\sigma^2}}\, e^{-\frac{(v-\mu)^2}{2\sigma^2}}\,, \quad v \in \mathbb{R} \tag{2.48}$$

and its CDF is denoted by

$$\Phi(v) = \int_{-\infty}^{v} \phi(u)\,\mathrm{d}u\,, \tag{2.49}$$

for which no closed form exists. We call $\mathcal{N}(0,1)$ the standard Gaussian distribution.

The N dimensional multivariate Gaussian (or normal) distribution with mean vector $\boldsymbol{\mu}$ and covariance matrix $\boldsymbol{\Sigma}$ is denoted by $\mathcal{N}(\boldsymbol{\mu}, \boldsymbol{\Sigma})$. Its PDF is denoted by

$$\phi(\mathbf{v}) = \frac{1}{\sqrt{(2\pi)^N\,|\boldsymbol{\Sigma}|}}\, \exp\left(-\frac{1}{2}\,(\mathbf{v}-\boldsymbol{\mu})^{\mathrm{T}}\,\boldsymbol{\Sigma}^{-1}\,(\mathbf{v}-\boldsymbol{\mu})\right)\,, \quad \mathbf{v} \in \mathbb{R}^N\,. \tag{2.50}$$

Similarly, $\mathcal{N}(\mathbf{0}_N, \mathbf{I}_N)$ is called a standard (N dimensional multivariate) Gaussian distribution.

The N dimensional multivariate complex circularly symmetric Gaussian (or normal) distribution with mean vector $\boldsymbol{\mu}$ and covariance matrix $\boldsymbol{\Sigma}$ is denoted by $\mathcal{CN}(\boldsymbol{\mu}, \boldsymbol{\Sigma})$. Note, that here $\boldsymbol{\mu} \in \mathbb{C}^N$ and $\boldsymbol{\Sigma} \in \mathbb{C}^{N\times N}$. Its PDF is given by

$$f(\mathbf{v}) = \frac{1}{\sqrt{\pi^N\,|\boldsymbol{\Sigma}|}}\, \exp\left(-(\mathbf{v}-\boldsymbol{\mu})^{\mathrm{H}}\,\boldsymbol{\Sigma}^{-1}\,(\mathbf{v}-\boldsymbol{\mu})\right)\,, \quad \mathbf{v} \in \mathbb{C}^N\,. \tag{2.51}$$

We call $\mathcal{CN}(\mathbf{0}_N, \mathbf{I}_N)$ a standard (N dimensional multivariate) circularly symmetric Gaussian distribution.

The matrix valued complex non-central correlated Wishart distribution of dimension K with N degrees of freedom, common covariance matrix $\mathbf{B}$ and non-centrality matrix $\boldsymbol{\Omega}$ is denoted by $\mathcal{CW}_K(N, \mathbf{B}, \boldsymbol{\Omega})$. See Section 3.4 for a formal definition. For the special case of complex central Wishart distributions (i.e., $\boldsymbol{\Omega} = \mathbf{0}_{K\times K}$), we omit the last parameter and write $\mathcal{CW}_K(N, \mathbf{B})$.

3 Background

This chapter contains a short introduction to the fundamental concepts, which are important to this thesis. First, a general overview of spectrum sensing is given and some important detectors are introduced in Section 3.1. Second, eigenvalue-based spectrum sensing, which is the core focus of this thesis is introduced in Section 3.2 and relevant detectors are subsequently presented.

In Chapter 5, quickest detection algorithms on the basis of eigenvalue-based spectrum sensing are introduced. Hence, the necessary background of quickest detection is given in Section 3.3.

Particularly Chapters 5 and 7 rely on results from random matrix theory. Important results that are used in the course of this thesis are revisited in Section 3.4.

Performance limits of certain detectors are analyzed in Chapter 6 and it is shown that they suffer from the so-called SNR wall phenomenon, which is outlined in Section 3.5. During said investigation concepts from order statistics are needed. Hence, Section 3.6 provides some relevant results from the theory of order statistics.

3.1 Spectrum Sensing

The term *spectrum sensing* describes the task of reliably finding spectrum opportunities (also called spectrum holes), i.e., bands that are temporarily unused by the licensed primary system. If a specific frequency band is considered, said task can be cast as a simple hypothesis testing problem:

$$\begin{aligned} \mathcal{H}_0 &: y(t) = w(t) \\ \mathcal{H}_1 &: y(t) = x(t) + w(t)\,. \end{aligned} \tag{3.1}$$

There, for a given discrete time index $t \in \mathbb{N}$, the received signal $y(t)$ contains samples of only the receiver noise $w(t)$ or an additive combination of a signal component $x(t)$ and receiver noise. Here, $x(t)$, $w(t)$ and thereby also $y(t)$ are described as random processes. Most commonly, $w(t)$ is modeled as additive white Gaussian noise (AWGN). Note, that in this formulation $x(t)$ stands for the filtered PU signal including effects of the wireless propagation channel and filtering by the receiver. It is evident that trying to infer reliable information from a single sample $y(t)$ is

inadvisable due to the randomness involved. Hence, the methods used in spectrum sensing are deeply rooted in *detection and estimation theory*, see [36, 37].

In general, detectors may be classified into two categories: *state* and *change* detectors [36,38]. While the former intend to decide between the two possible hypotheses, the latter aim at detecting a hypothesis change. For the moment, we focus on state detection and treat a particular way of change detection later in Section 3.3.

State detectors may further be divided into *block* (or fixed sample size) and *sequential* detectors according to their objective. Block detectors aim at maximizing the (correct) detection performance under a given false alarm constraint for a fixed sample size. In contrast, a sequential detector performs consecutive decision attempts, see Figure 3.1. If one of the two thresholds (h_0 or h_1) is crossed, it decides for the corresponding hypothesis. Otherwise, it takes another sample and reattempts to reach a decision since the previous one was undecidable, compare also Figure 3.2. Thereby, the detector dynamically adapts its sample size to the detection difficulty.

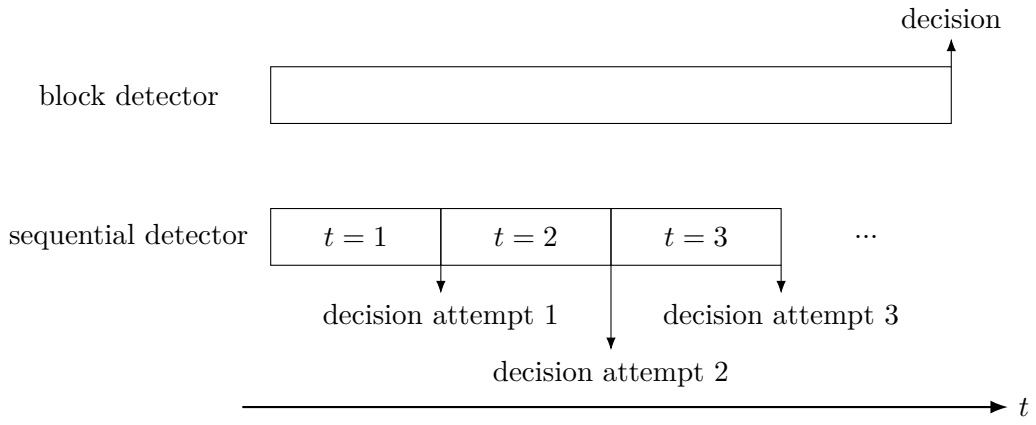

Figure 3.1: Visual comparison of block (fixed sample size) detection and sequential detection paradigms.

Although all the mentioned detection paradigms were applied to the spectrum sensing problem in the literature [11,12], block detection is the most widely deployed variant so far. Thus, we introduce relevant results from these efforts in more detail in the following.

In general, a block detector collects samples $\mathbf{y} = (y(1), y(2), \ldots, y(N))$ where the number of samples N (also called sample size) is determined beforehand. Then, it calculates a *test statistic* $T(\mathbf{y})$, which is a function of the samples, i.e., $T : \mathbb{C}^N \to \mathbb{R}$. The value of $T(\mathbf{y})$ is subsequently compared to a threshold h to form a decision:

$$T(\mathbf{y}) \underset{\mathcal{H}_0}{\overset{\mathcal{H}_1}{\gtrless}} h\,. \tag{3.2}$$

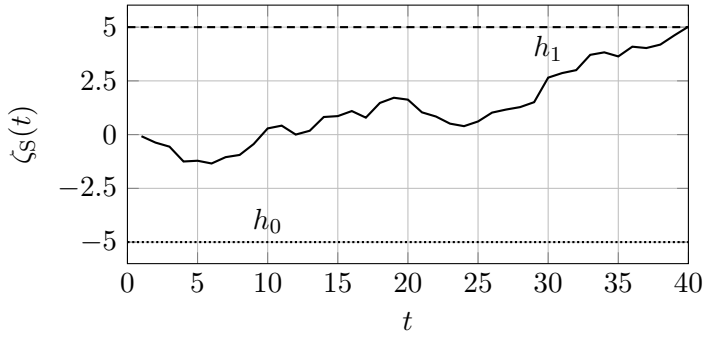

Figure 3.2: Example of the output of a sequential probability ratio test $\zeta_S(t)$, cf. [38]. The samples are taken according the $\mathcal{H}_1$ hypothesis distribution $\mathcal{N}(0.4, 1)$ and the $\mathcal{H}_0$ distribution is $\mathcal{N}(0, 1)$. The upper and lower thresholds h_1 and h_0 are also indicated. The former of which is exceeded at $t = 40$ and hence the algorithm decides for $\mathcal{H}_1$ then.

In words, if $T(\mathbf{y})$ is greater or equal to h the detector decides for hypothesis $\mathcal{H}_1$, otherwise it decides for hypothesis $\mathcal{H}_0$.

For the theoretical analysis of a detector, the input samples are modeled as random processes and consequently the test statistic T is described as a random variable. Let f_0 and f_1 denote the PDFs of the test statistic under $\mathcal{H}_0$ and $\mathcal{H}_1$, respectively. Similarly, let F_0 and F_1 be the corresponding CDFs. Note, that this treatment assumes the hypothesis does not change within the observation interval.

Evidently, a detector does not always make the correct decision. There are two kinds of errors that may occur, which are described by the two events $T \geq h \mid \mathcal{H}_0$ and $T < h \mid \mathcal{H}_1$. The first type of error occurs when the test statistic exceeds the threshold even though $\mathcal{H}_0$ is true. That is, the detector falsely decides for $\mathcal{H}_1$, which is called a *false alarm*. The second type of error occurs when the test statistic stays below the threshold although $\mathcal{H}_1$ is true. This means the detector falsely decides for $\mathcal{H}_0$, which is called *missed detection*.

The performance of a detector may be assessed by the *probability of false alarm* P_{FA} and the *probability of missed detection* P_{MD} (or equivalently the *probability of detection* P_{D}), see also Figure 3.3. Formally, they are defined as:

$$P_{\mathrm{FA}}(h) = \mathrm{P}(T \geq h \mid \mathcal{H}_0) = \int_h^\infty f_0(v)\,\mathrm{d}v = 1 - F_0(h)\,, \tag{3.3}$$

$$P_{\mathrm{MD}}(h) = \mathrm{P}(T < h \mid \mathcal{H}_1) = \int_{-\infty}^h f_1(v)\,\mathrm{d}v = F_1(h)\,, \tag{3.4}$$

$$P_{\mathrm{D}}(h) = \mathrm{P}(T \geq h \mid \mathcal{H}_1) = 1 - \mathrm{P}(T < h \mid \mathcal{H}_1) = 1 - P_{\mathrm{MD}}(h)\,. \tag{3.5}$$

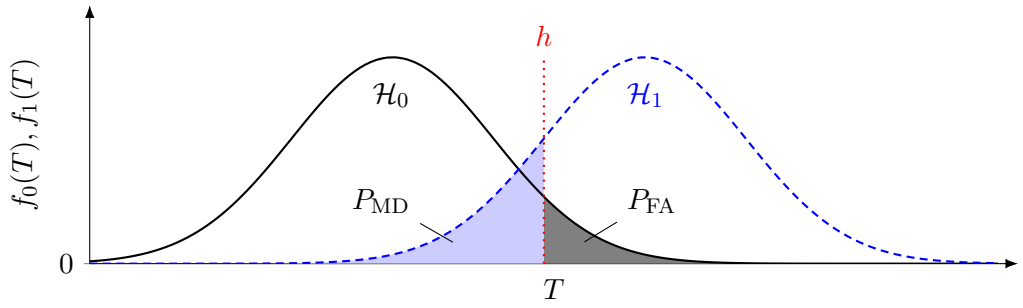

Figure 3.3: Visualization of the performance measures of a block detector, i.e., P_{FA} and P_{MD} for a given threshold h.

As can be seen from (3.3) to (3.5), the performance measures are functions of the threshold h. Fixing the system model, the sample size N and the threshold h results in constant pairs $(P_{\mathrm{FA}}(h), P_{\mathrm{MD}}(h))$ (or equivalently $(P_{\mathrm{FA}}(h), P_{\mathrm{D}}(h))$). To visualize these operating points at the detector's disposal the so-called *receiver operator characteristic (ROC)* is utilized, see Figure 3.4. It is created by plotting pairs $(P_{\mathrm{FA}}(h), P_{\mathrm{D}}(h))$ for a range of thresholds (some authors prefer $(P_{\mathrm{FA}}(h), P_{\mathrm{MD}}(h))$). The ROC is also used to compare the performance of different detectors and can be estimated from Monte Carlo simulations if theoretical expressions for (3.3) to (3.5) are not available.

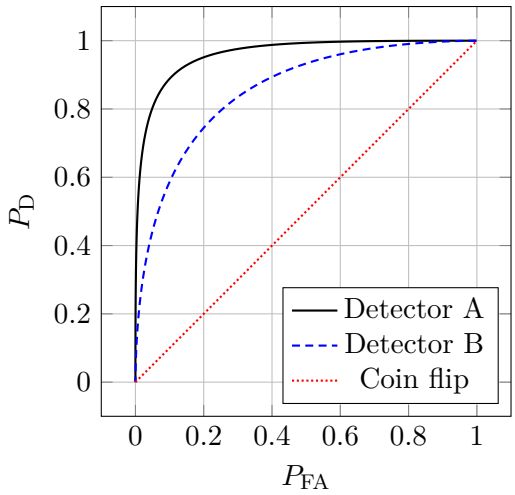

Figure 3.4: Example of a ROC of two detectors. Evidently, detector A outperforms detector B, since it offers higher P_{D} for the same P_{FA}. The ROC of a coin flip is depicted as well.

As mentioned above, typically the objective of a block detector is to minimize P_{MD}

(or equivalently maximize P_{D}) for a predetermined $P_{\mathrm{FA}} = c > 0$. If the joint PDFs of the samples under both hypotheses $f_{(\mathbf{y}|\mathcal{H}_0)}$ and $f_{(\mathbf{y}|\mathcal{H}_1)}$ are exactly known, the optimal test in that sense is given by [39]:

$$\frac{f_{(\mathbf{y}|\mathcal{H}_1)}(\mathbf{y})}{f_{(\mathbf{y}|\mathcal{H}_0)}(\mathbf{y})} \underset{\mathcal{H}_0}{\overset{\mathcal{H}_1}{\gtrless}} h(c)\,. \tag{3.6}$$

A detector derived this way is also called *Neyman-Pearson optimal*, see [36, p. 65, Th. 3.1].

Obviously, exact knowledge about the samples' PDFs under both hypotheses is a very strong assumption that is rarely encountered in practice. Particularly in spectrum sensing, the statistical model under the $\mathcal{H}_1$ hypothesis is problematic, since it strongly depends on the wireless propagation channel and the signal characteristics of the PU signal. A relevant practical case is when the PDFs under both hypotheses are known up to missing parameter vectors $\boldsymbol{\theta}_0$ and $\boldsymbol{\theta}_1$, respectively. In this case, the missing parameters may be estimated using maximum likelihood estimation (MLE) beforehand [37, p. 157 ff., Ch. 7] to obtain the so-called generalized likelihood ratio test (GLRT) [36, p. 200 ff., Sec. 6.4.2]:

$$\frac{\max\limits_{\hat{\boldsymbol{\theta}}_1} f_{(\mathbf{y}|\mathcal{H}_1,\boldsymbol{\theta}_1)}\left(\mathbf{y} \mid \hat{\boldsymbol{\theta}}_1\right)}{\max\limits_{\hat{\boldsymbol{\theta}}_0} f_{(\mathbf{y}|\mathcal{H}_0,\boldsymbol{\theta}_0)}\left(\mathbf{y} \mid \hat{\boldsymbol{\theta}}_0\right)} \underset{\mathcal{H}_0}{\overset{\mathcal{H}_1}{\gtrless}} h\,. \tag{3.7}$$

Although this test does not possess the optimality of (3.6), it works well in practice.

Detectors for spectrum sensing are faced with highly challenging demands [7,11,12, 40]. The main reasons are the volatile nature of wireless propagation channels, the multitude of modulation types deployed, the hidden PU problem (see Figure 1.1) and the high level of reliability that is desired to protect the primary system from interference. Hence, the detectors are expected to perform in the very low SNR regime. Typical values for the worst case SNR under which a detector is expected to function include SNRs of -20 dB to -22 dB or even less [17, 41, 42]. Dynamic spectrum access in the cognitive radio paradigm with spectrum sensing was first standardized in the IEEE 802.22 standard [43, 44], which aims at exploiting spectrum opportunities in TV broadcasting bands.

The detectors studied in the spectrum sensing literature may be categorized by the degree of knowledge about the PU signal required. One extreme is if no information about the PU signal is available, i.e., the detector is *blind*. An example of this class is *energy detection (ED)* and it is described in Section 3.1.1. The other extreme is that (parts of) the exact PU signal is known, which leads to detection using *matched filters* as discussed in Section 3.1.3. In the following, three well-known detectors are introduced shortly in Sections 3.1.1 to 3.1.3. Section 3.2 is dedicated to the introduction of eigenvalue-based detection, which is the focus of this thesis.

3.1.1 Energy Detection

In ED, the normalized energy of the received signal is the test statistic:

$$T_{\mathrm{ED}} = \frac{\|\mathbf{y}\|_2^2}{\sigma_w^2}\,, \tag{3.8}$$

where σ_w^2 is the variance of the receiver noise. This detector can be derived as the Neyman-Pearson optimal detector if $\mathbf{y}^{\mathrm{T}} \mid \mathcal{H}_0 \sim \mathcal{N}(\mathbf{0}_N, \sigma_w^2 \mathbf{I}_N)$ and $\mathbf{y}^{\mathrm{T}} \mid \mathcal{H}_1 \sim \mathcal{N}(\mathbf{0}_N, (\sigma_s^2 + \sigma_w^2)\mathbf{I}_N)$. The performance of this detector was studied theoretically in [45]. As mentioned above, this detector can be considered blind with respect to the PU signal as it only measures energy. Nevertheless, it requires precise knowledge of the receiver noise variance σ_w^2.

Under ideal conditions and if the PDFs are perfectly known, it is closely related to the optimal detector for zero mean digital constellations [46]. A similar result was found numerically for OFDM signals [47]. ED is also attractive due to its implementational simplicity and low computational complexity.

However, its performance rapidly deteriorates if the estimation of the receiver noise variance (or receiver noise power) is imprecise. As a result, the detector suffers from a fundamental performance limit, which prevents its operation below a certain SNR threshold that may not be overcome by increasing the number of samples. This effect is introduced in Section 3.5. Since it is difficult to reliably estimate the receiver noise power for spectrum sensing applications (see also Section 6.1), it is doubtful that ED can successfully operate in the desired very low SNR regime, cf. [48].

3.1.2 Cyclostationary (Feature) Detection

Cyclostationarity is a property of a stochastic process, which describes whether its statistical characteristics vary periodically with time [49]. Most man-made signals exhibit some kind of inherent periodicity caused by sampling, modulation, coding or pilot sequences. A prime example in modern communications is the cyclic prefix used in orthogonal frequency-division multiplexing (OFDM), which consists of a copy of the last portion of the current OFDM symbol.

A real zero-mean discrete time stochastic process $y(t)$ is said to be *second-order almost-cyclostationary in the wide sense* if its time-varying autocorrelation function

$$r_y(t, \tau) = \mathrm{E}[y(t)y(t+\tau)] \tag{3.9}$$

can be expressed as a Fourier series, where the Fourier coefficients are given by the *cyclic autocorrelation function* at *cycle frequency* $\nu \in [0, 1)$ [49, 50]:

$$R_y(\nu, \tau) = \lim_{t\to\infty} \frac{1}{N} \sum_{j=0}^{N-1} r_y(t+1, \tau)\, e^{-\imath 2\pi\nu j}\,. \tag{3.10}$$

Note, that $\imath$ stands for the imaginary unit. Thus, the process $y(t)$ is almost-cyclostationary in the wide sense, if $R_y(\nu, \tau) > 0$ for at least one $\nu \neq 0$. This concept can also be generalized to complex-valued stochastic processes, see [49, p. 649, Sec. 3.5].

In contrast, noise is typically modeled by weak (or even strong) sense stationary random processes. Such a random process $w(t)$ exhibits a time-constant autocorrelation function, i.e.,

$$r_w(t, \tau) = \mathrm{E}[w(t)w(t+\tau)] = r_w(\tau)\,. \tag{3.11}$$

Hence, $w(t)$ is not cyclostationary, since $R_w(\nu, \tau) = 0$ for $\nu \neq 0$.

Based on these assumptions, detecting the presence of communication signals may be accomplished by detecting the presence of cyclostationarity in the received signal, see [50,51] and [49, p. 665 f., Sec. 11]. In spectrum sensing, cyclostationary detection was considered early on [13, 52]. In [53] a collaborative detector exploiting multiple cyclic frequencies was introduced. Cyclostationary spectrum sensing has also been considered in conjunction with quickest detection (see Section 3.3) in [54]. Consult [11, 12] for a more complete literature overview.

Typically, cyclostationary detectors require knowledge of the PU signals' cyclic frequencies. However, for sampled linearly modulated signals with rectangular pulse shape, a detector based on compressive cyclostationary sensing was recently developed that allows blind operation with respect to the cyclic frequencies [55].

Similarly to ED, it was found that cyclostationary detection also suffers from a phenomenon called SNR wall, which prohibits detection below a certain SNR limit in the presence of model uncertainties [41], see also Section 3.5.

3.1.3 Matched Filter Detection

If the receiver possesses exact knowledge of the signal, the so-called *matched filter* is the optimal detector, cf. [36, p. 94 ff, Ch. 4]. Let $\mathbf{x} \in \mathbb{C}^N$ be the known signal and consider standard circularly symmetric Gaussian noise. That is, the received signal can be modeled as $\mathbf{y}^{\mathrm{T}} \mid \mathcal{H}_0 \sim \mathcal{CN}(\mathbf{0}_N, \sigma_w^2 \mathbf{I}_N)$ and $\mathbf{y}^{\mathrm{T}} \mid \mathcal{H}_1 \sim \mathcal{CN}(\mathbf{x}, \sigma_w^2 \mathbf{I}_N)$. Inserting the corresponding PDFs into (3.6), taking the logarithm and rearranging constant terms into the detection threshold yields the matched filter for this case:

$$T_{\mathrm{MF}} = \mathrm{Re}(\mathbf{x}^{\mathrm{H}}\mathbf{y})\,. \tag{3.12}$$

Matched filter detection is also discussed in spectrum sensing, where it is sometimes called *coherent detection* or *waveform-based sensing*, see [11, 13, 40, 56]. Not always is it assumed that the whole signal is exactly known. Instead, deterministic signal patterns like preambles and pilot patterns are considered.

Although matched filter detection seems highly desirable from a theoretical point of view, its practical applicability in spectrum sensing is very limited due to the excessive knowledge required. In addition to (parts of) the PU signal, also the channel coefficients and the noise characteristics must be known. Evidently, the test statistic is also very sensitive to synchronization problems [57]. As a result, the SU would have to perform a correct demodulation with known parameters including bandwidth, modulation type and operation frequency [11]. Since cognitive radios are envisioned to perform dynamic spectrum access in a multitude of bands, the complexity of implementation becomes prohibitive [13].

Moreover, since the channel coherence time is limited in practice, matched filter detection is prone to the SNR wall problem in the presence of model uncertainties, see Section 3.5.

3.2 Eigenvalue-Based Spectrum Sensing

Eigenvalue-based spectrum sensing, which is the focus of this thesis, utilizes functions of the eigenvalues of the sample covariance matrix as test statistics. Since in most communication models the receiver noise process is modeled to be white (typically AWGN), it is uncorrelated over time. Also, it is customary to assume the noise processes of different receivers as uncorrelated. Hence, the main idea behind eigenvalue-based spectrum sensing is to exploit correlation in the received signal if a PU is present. Correlation can be observed either among different SUs or over time. With the help of the (sample) covariance matrix, correlation can be quantified over one of these dimensions or a combination of both.

The eigenvalue-based spectrum sensing systems considered in this thesis are cooperative. Hence, if K SUs are cooperating and one potentially present PU is considered, the hypothesis test can be restated as:

$$\begin{aligned} \mathcal{H}_0 &: \mathbf{y}(t) = \mathbf{w}(t) \\ \mathcal{H}_1 &: \mathbf{y}(t) = \mathbf{x}(t) + \mathbf{w}(t)\,. \end{aligned} \tag{3.13}$$

The vectors $\mathbf{w}(t) \in \mathbb{C}^K$ and $\mathbf{x}(t) \in \mathbb{C}^K$ describe the additive receiver noise and the filtered PU signal (including wireless propagation effects and receiver filtering), respectively. Hence, each row of the vector $\mathbf{y}(t)$ contains the received samples of a particular SU at a given time $t \in \mathbb{N}$ and it is assumed that the detector has access to all of these samples.

To capture all mentioned the possibilities of exploiting correlation, we introduce the processing vector $\mathbf{z}(t) \in \mathbb{C}^{\tilde{K}}$, where $\tilde{K} = KQ$. Here, $Q \in \mathbb{N}$ is a parameter that controls if and how time correlation is considered. There are three possible modes of operation:

1. *Receiver correlation*: $K \geq 2$, $Q = 1$ and $\mathbf{z}(t) = \mathbf{y}(t)$.

2. *Time correlation*: $K = 1$, $Q \geq 2$ and $\mathbf{z}(t) = \Big(y(t), y(t-1), \ldots, y(t-Q+1)\Big)^{\mathrm{T}}$.
3. *Receiver and time correlation*: $K \geq 2$, $Q \geq 2$ and $\mathbf{z}(t) = \Big(y_1(t), \ldots, y_1(t-Q+1), \ldots, y_K(t), \ldots, y_K(t-Q+1)\Big)^{\mathrm{T}}$.

Note, that the definition of $\mathbf{z}(t)$ from the joint receiver and time correlation case contains the two other cases. This is taken advantage of in Chapter 4, where the system models used in this thesis is formally introduced.

Consider the statistical point of view, where $\mathbf{w}(t)$, $\mathbf{x}(t)$ and thereby $\mathbf{y}(t)$ are described using random processes. Then, the statistical covariance matrix with respect to the processing vector $\mathbf{z}$ is

$$\begin{aligned}\mathbf{R} &= [\mathrm{Cov}[z_i, z_j]]_{1 \leq i,j \leq \tilde{K}} = \mathrm{E}[(\mathbf{z} - \mathrm{E}[\mathbf{z}])(\mathbf{z}^{\mathrm{H}} - \mathrm{E}[\mathbf{z}^{\mathrm{H}}])] \\ &\overset{\mathrm{E}[\mathbf{z}]=\mathbf{0}_{\tilde{K}}}{=} \mathrm{E}[\mathbf{z}\mathbf{z}^{\mathrm{H}}]\,. \end{aligned} \tag{3.14}$$

The last equality holds true, since in wireless communications the statistical processes involved are virtually always assumed to be zero-mean. If we refer to the statistical covariance matrix under a specific hypothesis, we write $\mathbf{R}_0 = \mathbf{R} \mid \mathcal{H}_0$ and $\mathbf{R}_1 = \mathbf{R} \mid \mathcal{H}_1$, respectively.

Remembering that the noise process is assumed to be white, we see that $\mathbf{R}_0 = \sigma_w^2 \mathbf{I}_{\tilde{K}}$ in all three modes of operation. If both receiver and time correlation is considered, $\mathbf{R}_1$ is composed of entries from the autocorrelation functions

$$r_{y_i}(t, \tau) = \mathrm{E}[y_i(t) y_i^*(t+\tau)] \tag{3.15}$$

and the cross-correlation functions

$$r_{y_i y_j}(t, \tau) = \mathrm{E}[y_i(t) y_j^*(t+\tau)]\,, \tag{3.16}$$

for $1 \leq i, j \leq K$. Hence, if $\mathbf{y}(t) \mid \mathcal{H}_1$ is not a white random process, i.e., if the wireless propagation channel of some receivers are correlated or the signal itself is correlated over time (due to oversampling for example), $\mathbf{R}_1 \neq \sigma_w^2 \mathbf{I}_{\tilde{K}}$.

Let $\tilde{\mathbf{x}}(t)$ and $\tilde{\mathbf{w}}(t)$ be vectors that are reordered versions of $\mathbf{x}(t)$ and $\mathbf{w}(t)$, such that it holds $\mathbf{z}(t) \mid \mathcal{H}_0 = \tilde{\mathbf{w}}(t)$ and $\mathbf{z}(t) \mid \mathcal{H}_1 = \tilde{\mathbf{x}}(t) + \tilde{\mathbf{w}}(t)$. Then, it is easy to see that $\mathbf{R}_1$ is the sum of the statistical covariance matrices of $\tilde{\mathbf{x}}$ and $\tilde{\mathbf{w}}$:

$$\begin{aligned}\mathbf{R}_1 &= \mathrm{E}[\mathbf{z}\mathbf{z}^{\mathrm{H}}] = \mathrm{E}[(\tilde{\mathbf{x}} + \tilde{\mathbf{w}})(\tilde{\mathbf{x}} + \tilde{\mathbf{w}})^{\mathrm{H}}] \\ &= \mathrm{E}[\tilde{\mathbf{x}}\tilde{\mathbf{x}}^{\mathrm{H}}] + \underbrace{\mathrm{E}[\tilde{\mathbf{x}}]}_{=\mathbf{0}_{\tilde{K}}} \mathrm{E}[\tilde{\mathbf{w}}^{\mathrm{H}}] + \underbrace{\mathrm{E}[\tilde{\mathbf{w}}]}_{=\mathbf{0}_{\tilde{K}}} \mathrm{E}[\tilde{\mathbf{x}}^{\mathrm{H}}] + \mathrm{E}[\tilde{\mathbf{w}}\tilde{\mathbf{w}}^{\mathrm{H}}] \\ &= \mathbf{R}_{\tilde{\mathbf{x}}} + \mathbf{R}_{\tilde{\mathbf{w}}}\,. \end{aligned} \tag{3.17}$$

The vector of ordered eigenvalues of $\mathbf{R}$ is denoted by

$$\boldsymbol{\lambda} = \mathrm{eig}\,(\mathbf{R}) = \Big(\lambda_1, \ldots, \lambda_{\tilde{K}}\Big)^{\mathrm{T}}, \tag{3.18}$$

where $\lambda_1 \leq \lambda_2 \leq \cdots \leq \lambda_{\tilde{K}}$. Evidently, since $\boldsymbol{\lambda} = \sigma_w^2 \mathbf{1}_{\tilde{K}}$ under $\mathcal{H}_0$ and $\boldsymbol{\lambda} \neq \sigma_w^2 \mathbf{1}_{\tilde{K}}$ under $\mathcal{H}_1$, the eigenvalues may also be used to distinguish the two hypotheses. Note, however, that some detectors operate directly on the covariance matrix [58] or the autocorrelation function itself [12]. They are not considered in this work.

From a practical perspective, the covariance matrix must be estimated from the samples. Here, we treat $\mathbf{z}(t)$ as a measured realization of the underlying random process. The estimator for the covariance matrix for the zero-mean case, called *sample covariance matrix*, can be given as

$$\hat{\mathbf{R}} = \frac{1}{N - Q + 1} \sum_{i=Q}^{N} \mathbf{z}(i)\mathbf{z}(i)^{\mathrm{H}} \,. \tag{3.19}$$

The estimate $\hat{\mathbf{R}}$ converges to the statistical covariance matrix $\mathbf{R}$ for $N \to \infty$.

In analogy to the statistical matrices, we use the shorthand notation $\hat{\mathbf{R}}_0 = \hat{\mathbf{R}} \mid \mathcal{H}_0$ and $\hat{\mathbf{R}}_1 = \hat{\mathbf{R}} \mid \mathcal{H}_1$. Furthermore, we denote the vector of the ordered eigenvalues of $\hat{\mathbf{R}}$ as

$$\hat{\boldsymbol{\lambda}} = \operatorname{eig}\left(\hat{\mathbf{R}}\right) = \left(\hat{\lambda}_1, \hat{\lambda}_2, \ldots, \hat{\lambda}_{\tilde{K}}\right)^{\mathrm{T}} . \tag{3.20}$$

Both $\mathbf{R}$ and $\hat{\mathbf{R}}$ are Hermitian and positive semi-definite. Hence, their eigenvalues are real and non-negative, i.e., $\boldsymbol{\lambda} \geq 0$ and $\hat{\boldsymbol{\lambda}} \geq 0$, see [59, p. 227 f., Sec. 4.1].

Under the assumption that the noise process is white, some eigenvalue-based detectors do not require knowledge of the noise variance σ_w^2 to set a detection threshold. This can be seen by comparing the eigenvalues of $\hat{\mathbf{R}}$ with the eigenvalues of the sample covariance matrix obtained from the normalized vector $\frac{\mathbf{z}(t)}{\sigma_w}$. The latter can be viewed as a system model, where the noise process is assumed to have $\sigma_w^2 = 1$. Since it holds that

$$\operatorname{eig}\left(\hat{\mathbf{R}}\right) = \sigma_w^2 \operatorname{eig}\left(\frac{1}{\sigma_w^2}\hat{\mathbf{R}}\right) , \tag{3.21}$$

the eigenvalues of the normalized model are scaled with respect to the ones from the non-normalized model. Hence, we see from (3.22), (3.24) and (3.25) that this scaling factor cancels out in the ratio for the detectors from Sections 3.2.1 to 3.2.3 and that it is not necessary to know the value of σ_w^2 to set the corresponding thresholds. In contrast, from (3.27) and (3.28) we see that scaling affects the test statistics and hence σ_w^2 must be known to set the threshold for the detectors from Sections 3.2.4 and 3.2.5. However, it is shown in Section 6.1 that also the detectors from Sections 3.2.1 to 3.2.3 are vulnerable to model uncertainties including imperfect noise power calibration, and colored and correlated noise.

In the following, some important eigenvalue-based detectors are introduced, which are used later in this thesis.

3.2.1 MME

The first work to utilize eigenvalues of the sample covariance matrix for detection in the spectrum sensing context was the maximum-minimum eigenvalue (MME) detector introduced in [17], see also [19]. It was presented using a very general system model with multiple PUs and SUs, oversampling and multipath propagation channels (for the case of one PU, the system model is very similar to model $\mathcal{M}_{\mathrm{MP}}$ from Section 4.1). The model considers receiver and time correlation for the sample covariance matrix. As a test statistic the ratio of the largest and the smallest eigenvalue of $\hat{\mathbf{R}}$ is used:

$$T_{\mathrm{MME}} = \frac{\max(\hat{\boldsymbol{\lambda}})}{\min(\hat{\boldsymbol{\lambda}})} = \frac{\hat{\lambda}_{\tilde{K}}}{\hat{\lambda}_1} \,. \tag{3.22}$$

Note, that since $\hat{\lambda}_{\tilde{K}} \geq \hat{\lambda}_1$ it holds that $T_{\mathrm{MME}} \geq 1$. The test statistic T_{MME} is also the so-called *standard condition number (SCN)* of the sample covariance matrix.

In [17, 19] an approximate method of setting the detection threshold was suggested, which utilizes results from (asymptotic) random matrix theory (see also Section 3.4). More accurate methods of finding the threshold were derived in [60–62]. Alternative methods using standard Gaussian CDFs as approximations were suggested in [63, 64]. Under a cooperative system model without exploiting time correlation (i.e., model $\mathcal{M}_{\mathrm{FF}}$ from Section 4.2 with $Q = 1$ and $M = 1$) the probability of missed detection P_{MD} was asymptotically found in [65].

3.2.2 GLRT / BCED

The following detector was first reported in [18], where it was called *blindly combined energy detection (BCED)*. It was later also referred to as GLRT, since it can be derived as the GLRT for system model $\mathcal{M}_{\mathrm{FF}}$ from Section 4.2 when $s(t)$ is assumed to be Gaussian (with $Q = 1$ and $M = 1$, i.e., without exploiting time correlation and performing no oversampling), cf. [20–22]. It is given by the ratio of the largest eigenvalue and the trace of the sample covariance matrix:

$$T_{\mathrm{BCED}} = \frac{\max(\hat{\boldsymbol{\lambda}})}{\mathrm{tr}(\hat{\mathbf{R}})} = \frac{\hat{\lambda}_{\tilde{K}}}{\sum\limits_{i=1}^{\tilde{K}} \hat{\lambda}_i} \,. \tag{3.23}$$

In this work, we refer to the detector as GLRT in the following and use it in an alternative, equivalent form. It can be found by applying a monotonous nonlinear transformation to gain the test statistic [21]:

$$T_{\mathrm{GLRT}} = \frac{\hat{\lambda}_{\tilde{K}}}{\sum\limits_{i=1}^{\tilde{K}-1} \hat{\lambda}_i} \,. \tag{3.24}$$

The threshold can be approximately determined using results from (asymptotic) random matrix theory, see [20, 21, 66, 67]. Likewise, an approximation of P_{D} under $\mathcal{M}_{\mathrm{FF}}$ from Section 4.2 (with $Q = 1$ and $M = 1$) can be given using the standard Gaussian CDF [21, 67] or by using results from (asymptotic) random matrix theory [66].

3.2.3 QST

The *quadratic sphericity test (QST)* was derived in [23] to be optimal in the correlation-matching sense for detecting a wide sense stationary primary signal subject to a time-varying frequency selective fading channel by a single SU, which is exploiting correlation over time. It is given by the ratio of the Euclidean norm (ℓ_2-norm) and the ℓ_1-norm of the eigenvalues of the sample covariance matrix:

$$T_{\mathrm{QST}} = \frac{\sqrt{\sum_{i=1}^{\tilde{K}} \hat{\lambda}_i^2}}{\sum_{i=1}^{\tilde{K}} \hat{\lambda}_i} = \frac{\|\hat{\boldsymbol{\lambda}}\|_2}{\|\hat{\boldsymbol{\lambda}}\|_1} = \frac{\sqrt{\mathrm{tr}(\hat{\mathbf{R}}\hat{\mathbf{R}})}}{\mathrm{tr}(\hat{\mathbf{R}})}\,. \tag{3.25}$$

Note, that $\left|\hat{\lambda}_i\right| = \hat{\lambda}_i$, since $\hat{\lambda}_i \geq 0$. From Hölder's inequality [31, p. 11, Eq. 3.2.9] it can be deduced that $\left\|\hat{\boldsymbol{\lambda}}\right\|_2 \leq \left\|\hat{\boldsymbol{\lambda}}\right\|_1 \leq \sqrt{\tilde{K}} \left\|\hat{\boldsymbol{\lambda}}\right\|_2$. Hence, the support of the test statistic of the QST is bounded:

$$\frac{1}{\sqrt{\tilde{K}}} \leq T_{\mathrm{QST}} \leq 1\,. \tag{3.26}$$

To the best of our knowledge, no theoretical analysis of this detector exists so far. Thus, there is no analytical way of determining the detection threshold.

Although this detector was originally intended for a single SU system, it also shows very promising performance in cooperative settings [24].

3.2.4 MMME

The *maximum-minus-minimum eigenvalue (MMME)* detector was presented in [24]. Like the MME, it utilizes only the largest and the smallest eigenvalue in its test statistic:

$$T_{\mathrm{MMME}} = \max(\hat{\boldsymbol{\lambda}}) - \min(\hat{\boldsymbol{\lambda}}) = \hat{\lambda}_{\tilde{K}} - \hat{\lambda}_1\,. \tag{3.27}$$

By avoiding the normalization from the ratio, it shows higher detection performance compared to the MME, see [24]. However, knowledge of the noise variance σ_w^2 is required to set a threshold.

In Chapter 7 the exact PDFs of the test statistic T_{MMME} under both hypotheses are derived for a dual SU system under model $\mathcal{M}_{\mathrm{DM}}$ from Section 4.2.1 (with $Q = 1$ and $M = 1$). These results can be used to accurately set the threshold and predict the resulting detection performance (P_{D}) for a given SNR.

3.2.5 RLRT

Roy's largest root test (RLRT) simply employs the largest eigenvalue as a test statistic [68]:

$$T_{\mathrm{RLRT}} = \max(\hat{\boldsymbol{\lambda}}) = \hat{\lambda}_{\tilde{K}} \,. \tag{3.28}$$

Essentially, it was reintroduced to spectrum sensing in the derivation of the GLRT from (3.24) in [18]. Asymptotically, the RLRT can be considered to be the Neyman-Pearson optimal test for system model $\mathcal{M}_{\mathrm{FF}}$ from Section 4.2 (with $Q = 1$ and $M = 1$), if the noise variance σ_w^2 is known [67]. Hence, the GLRT from (3.24) can be viewed as a normalized version of the RLRT. There, the unknown noise variance is replaced by an estimation.

Under the system model mentioned above, the RLRT shows superior detection performance to ED, see [67]. Approximations for P_{FA} and P_{D} under said system model are also given there.

3.3 Quickest Detection

Quickest detection (QD) is a form of sequential change detection, that differs fundamentally from block detection and sequential hypothesis testing. In fact, these three detection paradigms have different detection objectives. In QD, it is assumed that the current hypothesis is known and that the detection algorithm tries to detect a change of the hypothesis with minimum delay [38,69], see Figure 3.5. This is done by sequentially taking samples and updating / reevaluating the decision function. Note, however, that QD does not aim for deciding between the hypotheses $\mathcal{H}_0$ and $\mathcal{H}_1$, in contrast to sequential hypothesis testing and block detection. In the following, we formalize the detection task, define notation and introduce the relevant performance measures. Moreover, the well-known cumulative sum (CUSUM) algorithm and a relevant generalization of the same are introduced.

Consider, without loss of generality (w.l.o.g.), the situation depicted in Figure 3.5, where the hypothesis changes from $\mathcal{H}_0$ to $\mathcal{H}_1$ at the (unknown) change time t_{c}. To describe the sampling process we introduce a sequence of random variables Z_t ($t \in \mathbb{N}$), which is independently and identically distributed (i.i.d.) with PDF f_{θ_0} with parameter θ_0 for $t < t_{\mathrm{c}}$ and according to the PDF f_{θ_1} with parameter θ_1 for $t \geq t_{\mathrm{c}}$. The detection algorithm operates sequentially on samples $z(t)$, which

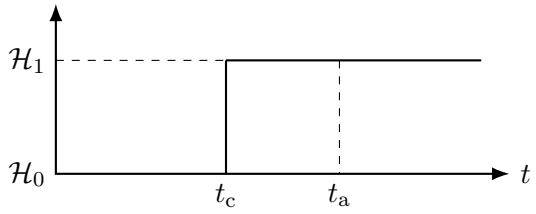

Figure 3.5: Quickest detection scenario. At t_c a change from Hypothesis $\mathcal{H}_0$ to Hypothesis $\mathcal{H}_1$ occurs. The detection algorithm raises an alarm at t_a. The detection delay is defined as $\tau_\mathrm{d} = t_\mathrm{a} - t_\mathrm{c} + 1$, compare also (3.30) and (3.32).

are realizations of the corresponding random variables Z_t, in order to detect the hypothesis change.

The performance measures of QD procedures are the *mean time to false alarm* $\bar{\tau}_\mathrm{fa}$ and the *mean time to detection* $\bar{\tau}_\mathrm{d}$ (also called conditional mean delay), which are defined as

$$\bar{\tau}_\mathrm{fa} = \mathrm{E}_{f_{\theta_0}}[t_\mathrm{a}] \tag{3.29}$$

and

$$\bar{\tau}_\mathrm{d} = \mathrm{E}_{f_{\theta_1}}\left[t_\mathrm{a} - t_\mathrm{c} + 1 \mid t_\mathrm{a} \geq t_\mathrm{c},\, \mathcal{Z}_1^{(t_\mathrm{c}-1)}\right], \tag{3.30}$$

respectively [38, p. 151 f., Eqs. (4.4.1), (4.4.2)]. There, the trajectory of the observations before t_c, that is for $1 \leq t \leq (t_\mathrm{c} - 1)$, is denoted by

$$\mathcal{Z}_1^{(t_\mathrm{c}-1)} = \left[Z_1, Z_2, \ldots, Z_{(t_\mathrm{c}-1)}\right]. \tag{3.31}$$

Note, that t_c and t_a are random variables. For the theoretical analysis, also the *worst mean delay* $\bar{\tau}_\mathrm{d}^\star$ is important, which is defined as [38, p. 152, Eq. (4.4.3)], [70]:

$$\bar{\tau}_\mathrm{d}^\star = \sup_{t_\mathrm{c} \geq 1} \operatorname{ess\,sup} \mathrm{E}_{f_{\theta_1}}\left[t_\mathrm{a} - t_\mathrm{c} + 1 \mid t_\mathrm{a} \geq t_\mathrm{c}, \mathcal{Z}_1^{(t_\mathrm{c}-1)}\right]. \tag{3.32}$$

Observe, that the random variable t_a depends on the detection algorithm $\mathcal{G}$, which operates on the samples $z(t)$ and performs detection attempts for every time index t. Hence, the performance measures defined in (3.29), (3.30) and (3.32) evidently depend on $\mathcal{G}$ as well and we denote these by $\bar{\tau}_\mathrm{fa}(\mathcal{G})$, $\bar{\tau}_\mathrm{d}(\mathcal{G})$ and $\bar{\tau}_\mathrm{d}^\star(\mathcal{G})$ to emphasize this dependence. Now, we can state the detection objective of an optimal QD algorithm for $c > 1$, cf. [38, p. 165 f., Sec. 5.2.1], [69, p. 130 ff., Sec. 6.2], [70]:

$$\begin{aligned} \underset{\mathcal{G}}{\text{minimize}} \quad & \bar{\tau}_\mathrm{d}^\star(\mathcal{G}) \\ \text{subject to} \quad & \bar{\tau}_\mathrm{fa}(\mathcal{G}) \geq c\,. \end{aligned} \tag{3.33}$$

That is, an optimal QD algorithm minimizes the worst mean delay under a predetermined lower bound on the mean time to false alarm.

If both parameters θ_0 and θ_1 are known, i.e., if both PDFs f_{θ_0} and f_{θ_1} are known exactly, the optimal QD algorithm is the CUSUM. It was proposed in [71] and calculates a cumulative sum of the samples' log-likelihood ratio (LLR). Let the LLR of a single sample v be denoted by

$$l(v) = \log\left(\frac{f_{\theta_1}(v)}{f_{\theta_0}(v)}\right) . \tag{3.34}$$

The CUSUM algorithm can be defined in different, equivalent forms. The following one lends itself to a recursive formulation, cf. [38, 70–72]:

$$\begin{aligned}
\zeta_{\mathrm{C}}(t) &= \sum_{j=1}^{t} \log\left(\frac{f_{\theta_1}(z(j))}{f_{\theta_0}(z(j))}\right) - \min_{0\le m\le t} \sum_{i=1}^{m} \log\left(\frac{f_{\theta_1}(z(i))}{f_{\theta_0}(z(i))}\right) \\
&= \max_{0\le m\le t} \sum_{i=m+1}^{t} l(z(i)) = \max\left\{0, \max_{0\le m\le (t-1)} \sum_{i=m+1}^{t} l(z(i))\right\} \\
&= \max\left\{0, \max_{0\le m\le (t-1)} \sum_{i=m+1}^{t-1} l(z(i)) + l(z(t))\right\} \\
&= \left[\zeta_{\mathrm{C}}(t-1) + l(z(t))\right]^{+} .
\end{aligned} \tag{3.35}$$

For this, we define $\zeta_{\mathrm{C}}(0) = 0$ and use the convention that a sum evaluates to zero if its lower boundary is greater than the upper one.

Intuitively, after the change time, i.e., for $t \ge t_{\mathrm{c}}$, the probability that $l(z(t)) > 0$ is larger than the probability that $l(z(t)) < 0$. Hence, we expect $\zeta_{\mathrm{C}}(t)$ to grow over time. In other words, the CUSUM algorithm from (3.35) tries to collect evidence for a consistent positive drift of the LLR, compare also Figure 3.6. Once the value $\zeta_{\mathrm{C}}(t)$ exceeds a predefined threshold, an alarm is raised.

Conversely, before the change time ($t < t_{\mathrm{c}}$) we expect the LLR to be negative most of the time. As a result, $\zeta_{\mathrm{C}}(t)$ should be (close to) zero in this case. Evidently, the detection threshold is a trade off between the mean time to false alarm $\bar{\tau}_{\mathrm{fa}}$ and the mean time to detection $\bar{\tau}_{\mathrm{d}}$. It is common practice to periodically restart the CUSUM some time before $\bar{\tau}_{\mathrm{fa}}$, since it is expected that the algorithm raises a false alarm eventually, if left running indefinitely. Note also, that accumulating negative values in $\zeta_{\mathrm{C}}(t)$ would lead to greater detection delays.

Optimality of the CUSUM in the sense of (3.33) was first established in [70] for the asymptotic case that the mean time to false alarm goes to infinity ($c \to \infty$ in (3.33)). Non-asymptotic optimality was later proven in [73]. An alternative proof was given in [74]. Theoretical analysis of the CUSUM (e.g., [70, 75, 76]) and related algorithms rely heavily on results from *sequential analysis* [77]. This is due to the

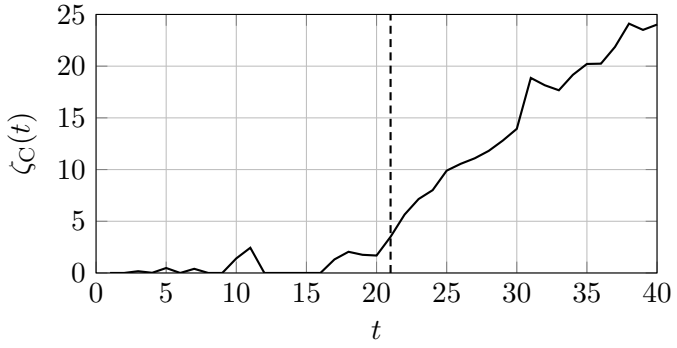

Figure 3.6: Example of the output of the CUSUM $\zeta_{\mathrm{C}}(t)$. The samples were $\mathcal{N}(0,1)$ and $\mathcal{N}(1.5,1)$ distributed before and after the change time $t_{\mathrm{c}} = 21$ (dashed line), respectively. Note, that by chance $\zeta_{\mathrm{C}}(20) > 0$, which would reduce the detection delay in this run.

fact that the CUSUM can be interpreted as a sequential probability ratio test [78] (with lower threshold zero and upper threshold set to the desired value discussed above), which is simply restarted if the test falls below the lower threshold [71], compare also Figure 3.2.

As mentioned above, the CUSUM may only be applied if the PDFs of the samples are known under both hypotheses. Especially in spectrum sensing, this is impossible in general, since the PDF under $\mathcal{H}_1$ depends on unknown parameters like the SNR and the channels' characteristics. Consider the case where the PDF of the samples is known exactly under $\mathcal{H}_0$ and known up to the parameter θ_1 under $\mathcal{H}_1$. We emphasize the dependency of the latter PDF on the parameter θ_1 by designating it as $f_{\theta_1}(z(t);\theta_1)$ in the following. Similarly, we write $l(z(t);\theta_1)$ for the LLR there. Under these circumstances, a MLE [37, p. 157 ff., Ch. 7] of the parameter θ_1 may be incorporated into the CUSUM algorithm to obtain the so-called *generalized likelihood ratio (GLR)* algorithm as suggested in [70], see also [38, p. 52 ff., Sec. 2.4.3]:

$$\begin{aligned}\zeta_{\mathrm{G}}(t) &= \max_{0\le m\le t} \sup_{\hat{\theta}_1} \log\left(\prod_{i=m+1}^{t} \frac{f_{\theta_1}(z(i);\hat{\theta}_1)}{f_{\theta_0}(z(i))}\right) = \max_{0\le m\le t} \sup_{\hat{\theta}_1} \sum_{i=m+1}^{t} \log\left(\frac{f_{\theta_1}(z(i);\hat{\theta}_1)}{f_{\theta_0}(z(i))}\right) \\ &= \max_{0\le m\le t} \sup_{\hat{\theta}_1} \sum_{i=m+1}^{t} l(t;\hat{\theta}_1)\,. \end{aligned} \tag{3.36}$$

Note, that the internal variable m essentially estimates the change time. The GLR from (3.36) can be considered a sequential variant of the well-known GLRT, which is widely used in classical hypothesis testing, cf. [36, p. 200 ff., Sec. 6.4.2]. Note, however, that it cannot formulated recursively. Hence, its computational complexity is significantly higher compared to the CUSUM.

3.4 Random Matrix Theory

Random matrix theory (RMT) studies the distributions of matrix valued random variables and their properties. The development of theoretical results was driven by a variety of practical problems arising in statistics [79], physics [80] and (communications) engineering [81]. In this work, we utilize so-called *Wishart* matrices, which arise when studying the matrix product $\mathbf{U}\mathbf{U}^{\mathrm{H}}$, where the entries of $\mathbf{U}$ are i.i.d. and Gaussian. They were first studied in the paper [82] in 1928 — that can also be considered as the beginning of the field of RMT — and they are named in honor after the author of said paper.

We first introduce the Wishart distribution in its most general form and discuss important special cases later. Let $\mathbf{V} = \mathbf{U}\mathbf{U}^{\mathrm{H}}$, where each column of $\mathbf{U}$ is i.i.d. according to a complex circularly symmetric Gaussian distribution, i.e., $\mathbf{u}_i \sim \mathcal{CN}(\mathbf{a}_i, \mathbf{B})$ with mean vectors $\mathbf{a}_i \in \mathbb{C}^K$ for $i = 1, \ldots, N$ and common covariance matrix $\mathbf{B}$. We collect the mean vectors as columns of the mean matrix $\mathbf{A}$. Then, $\mathbf{V}$ is complex non-central Wishart distributed with dimension K and N degrees of freedom with non-centrality matrix $\mathbf{\Omega} = \mathrm{E}[\mathbf{U}]\mathrm{E}[\mathbf{U}]^{\mathrm{H}} = \mathbf{A}\mathbf{A}^{\mathrm{H}}$, which we denote by $\mathbf{V} \sim \mathcal{CW}_K(N, \mathbf{B}, \mathbf{\Omega})$. Its PDF was derived in [83] as

$$f_{\mathbf{V}}(\mathbf{V}) = e^{-\mathrm{tr}\left(\mathbf{B}^{-1}\mathbf{A}\mathbf{A}^{\mathrm{H}}\right)}\, {}_0\tilde{\mathcal{F}}_1(N; \mathbf{B}^{-1}\mathbf{A}\mathbf{A}^{\mathrm{H}}\mathbf{B}^{-1}\mathbf{V}) \frac{e^{-\mathrm{tr}(\mathbf{B}^{-1}\mathbf{V})}}{\tilde{\Gamma}_K(N)\,|\mathbf{B}|^N} \left|\mathbf{V}^{N-K}\right|, \quad (3.37)$$

where

$$\tilde{\Gamma}_a(b) = \pi^{\frac{1}{2}a(a-1)} \prod_{i=1}^{a} \Gamma(b - i + 1)\,, \quad (3.38)$$

and ${}_p\tilde{\mathcal{F}}_q(a_1, \ldots, a_p; b_1, \ldots, b_q; \mathbf{C})$ is a generalized multivariate hypergeometric series for a hermitian matrix argument $\mathbf{C}$, see [83, Eqs. (83)-(85) and (87)].

There are three properties that we use to describe the type of Wishart distribution at hand. First, a Wishart distribution can be *real* or *complex*, depending on whether the columns $\mathbf{u}_i$ are real or complex Gaussian distributed. Second, we distinguish *central* and *non-central* Wishart distributions, which correspond to the cases when the mean matrix is $\mathbf{A} = \mathbf{0}_{K\times N}$ and $\mathbf{A} \neq \mathbf{0}_{K\times N}$, respectively. Finally, we call a Wishart distribution *uncorrelated* if $\mathbf{B} = \mathbf{I}_K$ and *correlated* otherwise.

In [82] the PDF of real correlated central Wishart matrices was developed. The extension to the corresponding non-central case was discussed in [84] and the PDF was given for the cases that $\mathbf{\Omega}$ is of rank two in [85] and of rank three in [86]. The components with which the PDF for the general rank case can be formulated was developed in [87–90]. The PDF of the complex correlated Wishart distributions was derived in [91] for the central case and in [83] for the non-central case as given in (3.37) above. The Wishart distribution can be shown to be a natural exponential

family [92], which is a class of probability distributions with certaint properties that is of high importance in statistics and estimation / detection theory [93].

Of main interest in this work, however, are the joint distributions of the ordered eigenvalues of Wishart matrices. The PDF of the joint ordered eigenvalues of real central uncorrelated Wishart matrices was independently found by [94–97], while the generalization to the corresponding correlated case was derived in [98]. In [83, Eq. (102)], where also (3.37) was developed, the joint PDF of the ordered eigenvalues of complex correlated non-central Wishart matrices was deduced. There, a generalized hypergeometric series was utilized, which has the product of two hermitian matrices as argument. Said function depends on the so-called zonal polynomials of its matrix arguments, see [83, eqs. (83)-(85) and (88)] and [99, p. 85 ff., ch. 5]. Later, it was shown that when the eigenvalues of both matrices in the argument of the hypergeometric series are distinct, a more convenient equivalent formulation utilizing a determinant of a matrix built from scalar hypergeometric series of products of their eigenvalues can be derived [100, Lemma 3]. Here, we use a representation of the PDF in a special form involving the product of the determinants of two special matrices, which was initially given in [101]. This formulation allows description of the joint ordered eigenvalue PDFs of several types of Wishart matrices in a similar form [102]. For the special cases of complex uncorrelated central, complex correlated central and complex uncorrelated non-central Wishart matrices the joint PDF of the ordered eigenvalues $\boldsymbol{\lambda} = \operatorname{eig}(\mathbf{V})$ can be given with $\boldsymbol{\beta} = \operatorname{eig}(\mathbf{B})$ and $\boldsymbol{\omega} = \operatorname{eig}(\boldsymbol{\Omega})$ as [102, Eq. (1) and Tab. I]:

$$f_{\boldsymbol{\lambda}}(\boldsymbol{\lambda}) = c_{\mathcal{CW}} \, |\boldsymbol{\Xi}(\boldsymbol{\lambda})| \, |\boldsymbol{\Theta}(\boldsymbol{\lambda}, \boldsymbol{\beta}, \boldsymbol{\omega})| \prod_{i=1}^{K} \xi(\lambda_i) \,, \tag{3.39}$$

when $\boldsymbol{\beta}$ and $\boldsymbol{\omega}$ are all distinct and non-zero. The special matrices $\boldsymbol{\Xi}(\boldsymbol{\lambda}), \boldsymbol{\Theta}(\boldsymbol{\lambda}, \boldsymbol{\beta}, \boldsymbol{\omega})$, the function $\xi(\lambda_i)$ and the normalizing constant $c_{\mathcal{CW}}$ are defined in Table 3.1 and (3.40) to (3.46). Note, that also very important contributions concerning the marginal PDFs were made in [102] and some important theorems for dealing with these functions were given there.

type	$c_{\mathcal{CW}}$	$\boldsymbol{\Xi}(\boldsymbol{\lambda})$	$\boldsymbol{\Theta}(\boldsymbol{\lambda}, \boldsymbol{\beta}, \boldsymbol{\omega})$	$\xi(\lambda_i)$
uncorrelated central	c_{UC}	$\boldsymbol{\mathcal{V}}_{\mathbf{1}}(\boldsymbol{\lambda})$	$\boldsymbol{\mathcal{V}}_{\mathbf{1}}(\boldsymbol{\lambda})$	$\lambda_i^{N-K} \, e^{-\lambda_i}$
uncorrelated non-central	c_{UN}	$\boldsymbol{\mathcal{V}}_{\mathbf{1}}(\boldsymbol{\lambda})$	$\mathbf{F}(\boldsymbol{\lambda}; \boldsymbol{\omega})$	$\lambda_i^{N-K} \, e^{-\lambda_i}$
correlated central	c_{CC}	$\boldsymbol{\mathcal{V}}_{\mathbf{1}}(\boldsymbol{\lambda})$	$\mathbf{E}(\boldsymbol{\lambda}, \boldsymbol{\beta})$	λ_i^{N-K}

Table 3.1: Table with different forms for the joint eigenvalue PDF.

The normalizing constants of the PDFs follow as

$$c_{\mathrm{UC}} = \left[\prod_{i=1}^{K} (N-i)! \prod_{j=1}^{K} (K-j)! \right]^{-1}, \tag{3.40}$$

$$c_{\mathrm{UN}} = \frac{\prod_{i=1}^{K} e^{-\omega_i}}{[(N-K)!]^K \, |\boldsymbol{\mathcal{V}}_{\mathbf{1}}(\boldsymbol{\lambda})|}, \tag{3.41}$$

$$c_{\mathrm{CC}} = c_{\mathrm{UC}} \prod_{i=1}^{K} (i-1)! \, \frac{|\mathbf{B}|^{-N}}{|\boldsymbol{\mathcal{V}}_{\mathbf{2}}(\boldsymbol{\beta})|}. \tag{3.42}$$

Above, we have used further special matrices that are defined in the following: the Vandermonde matrix

$$[\boldsymbol{\mathcal{V}}_{\mathbf{1}}(\boldsymbol{\lambda})]_{1 \le i,j \le K} = \lambda_{K-j+1}^{i-1}, \tag{3.43}$$

another closely related matrix

$$[\boldsymbol{\mathcal{V}}_{\mathbf{2}}(\boldsymbol{\beta})]_{1 \le i,j \le K} = -\beta_{K-j+1}^{1-i}, \tag{3.44}$$

a matrix containing scalar hypergeometric functions [32, Eq. (9.14.1)] as entries

$$[\mathbf{F}(\boldsymbol{\lambda}; \boldsymbol{\omega})]_{1 \le i,j \le K} = {}_0\mathcal{F}_1(N-K+1; \lambda_{K-i+1} \, \omega_{K-j+1}) \tag{3.45}$$

and a matrix containing exponential functions as entries

$$[\mathbf{E}(\boldsymbol{\lambda}, \boldsymbol{\beta})]_{1 \le i,j \le K} = e^{-\frac{\lambda_{K-j+1}}{\beta_{K-i+1}}}. \tag{3.46}$$

In addition to the non-asymptotic case discussed above, many asymptotic results exist in RMT. This is also due to the fact that many problems in RMT are very involved or even intractable to solve exactly. A good overview of asymptotic and non-asymptotic results relevant to spectrum sensing can be found in [103].

3.5 SNR Walls in Signal Detection

Signal detectors are typically designed and analyzed under simplified and idealized system models. In the practical application, however, the detector is deployed in a real world setting and is expected to perform robustly. In any theoretical model, some modeling uncertainties remain and model parameters, which must be estimated in practical scenarios, are only known up to a finite precision. It turns out, that such model uncertainties lead to a threshold of the SNR, below which the detector fails to robustly detect signals, even if the number of samples (i.e., the observation time) goes to infinity. The largest SNR for which this phenomenon

can be encountered under the model uncertainties in question is called the *SNR wall* [48].

For a formal definition of the SNR wall we follow [48]. The system model must explicitly account for model uncertainties. Each model component (say signal, channel and noise) is considered to take on probability distributions / statistical processes belonging to a set instead of having a fixed statistical description. This set is chosen to reflect the relevant model uncertainties of that component. Hence, the noise process may follow any process $W \in \mathbb{W}$ in the noise uncertainty set $\mathbb{W}$. Analogously, the same description is defined for the PU signal $S \in \mathbb{S}$ and the wireless channel $H \in \mathbb{H}$.

As an example, assumptions about the power, spectral coloring or stationarity of the receivers' noise may be imperfect. For the communication channel the type of fading and the coherence time may be unknown and for the PU signal the waveform or modulation type might be uncertain. Also, practical receivers are never perfect, such that effects like non-ideal filtering, I/Q imbalance or quantization may be worth investigating, cf. [41, 48].

Let T denote the test statistic of the detector under investigation, which is calculated from a block of N samples and let h be the detection threshold. The probabilities of missed detection and false alarm given the tuple (W, S, H) are defined as

$$P_{\mathrm{FA}}(W) = \mathrm{P}(T \geq h \mid \mathcal{H}_0, W)\,, \tag{3.47}$$

$$P_{\mathrm{MD}}(W, S, H) = \mathrm{P}(T < h \mid \mathcal{H}_1, W, S, H)\,. \tag{3.48}$$

That is, $P_{\mathrm{FA}}(W)$ and $P_{\mathrm{MD}}(W, S, H)$ depend on the instances W, S, H in contrast to the definitions from (3.3) to (3.5).

A detector is said to achieve an operating point $(P^\star_{\mathrm{FA}}, P^\star_{\mathrm{MD}})$ *robustly*, if this point is an upper bound of the performance measures for all possible instances of the tuple (W, S, H):

$$\sup_{W \in \mathbb{W}} P_{\mathrm{FA}}(W) \leq P^\star_{\mathrm{FA}}\,, \tag{3.49}$$

$$\sup_{\substack{W \in \mathbb{W}, S \in \mathbb{S} \\ H \in \mathbb{H}}} P_{\mathrm{MD}}(W, S, H) \leq P^\star_{\mathrm{MD}}\,. \tag{3.50}$$

We call a detector *non-robust*, if $(P^\star_{\mathrm{FA}}, P^\star_{\mathrm{MD}})$ with $P^\star_{\mathrm{FA}}, P^\star_{\mathrm{MD}} \in (0, 0.5)$ cannot be robustly achieved, even if N becomes arbitrarily large. Based on this, the SNR wall α_{wall} is defined as the largest SNR value, for which the detector is non-robust:

$$\alpha_{\mathrm{wall}} = \sup\{\alpha_c \mid \text{detector is non-robust } \forall\, \alpha < \alpha_c\}\,. \tag{3.51}$$

An equivalent definition for non-robustness can be given as follows. A detector is non-robust if and only if the set of medians of the test statistic T overlaps for all

$N > 0$, i.e.,

$$\left\{ \underset{W}{\text{median}}[T \mid \mathcal{H}_0] \;\middle|\; W \in \mathbb{W} \right\} \cap \left\{ \underset{W,S,H}{\text{median}}[T \mid \mathcal{H}_1] \;\middle|\; W \in \mathbb{W}, S \in \mathbb{S}, H \in \mathbb{H} \right\} \neq \emptyset \,. \tag{3.52}$$

In [48], the equivalent definition for non-robustness from (3.52) was given using the mean instead of the median. However, in this case the equivalence only holds if the probability distributions of the test statistic are symmetric under both hypotheses.

To the best of our knowledge, the first use of the term SNR wall appeared in [46], where fundamental requirements of spectrum sensing systems for weak signals were explored. However, the existence of the phenomenon was shown much earlier for ED in [104]. Since ED relies on the energy of the received signal (see Section 3.1.1), the receiver noise power must be known in order to determine the detection threshold, cf. [45]. Consider, that the receiver noise power is not exactly known and its uncertainty can be summarized by a single value $\rho > 1$ (called noise uncertainty factor). If the noise power is known to lie in the interval $[\rho^{-1}\sigma_w^2, \rho\sigma_w^2]$ about the nominal value σ_w^2, the threshold must be set with respect to the worst case to guarantee a false alarm rate less or equal to the desired value, see [48, Eq. (4)]. As a result, the detector becomes non-robust if the signal power does not exceed the noise uncertainty range $(\rho - \rho^{-1})\sigma_w^2$. Consequently, the SNR wall of ED is [41, 48, 104]

$$\alpha_{\text{wall}}^{\text{ED}} = \frac{\rho^2 - 1}{\rho} \,. \tag{3.53}$$

Note, that in [104] originally two factors were used to describe the uncertainty interval. The presence of the SNR wall of ED was experimentally verified in a wireless cognitive radio testbed [57, 105].

The noise uncertainty factor is typically supplied in decibels (dB) in the literature, i.e.,

$$\rho_{\text{dB}} = 10 \log_{10}(\rho) \,. \tag{3.54}$$

In the literature values in the range 0.5 dB $\leq \rho_{\text{dB}} \leq$ 2 dB are typically discussed, cf. [17, 18, 41, 48].

In [46] it was shown, that if the noise uncertainty is high enough and the receiver uses quantization, detection can become impossible irrespective of the detector. The existence of SNR walls for detectors relying on higher moments of the received signals was investigated in [106]. There, also the effect of a limited dynamic range of the receiver was studied. Aspects of coordination between competing opportunistic spectrum access users / systems and resulting SNR walls from the lack thereof were explored in [40].

Cyclostationary feature detection (see Section 3.1.2) under noise uncertainty was investigated in [41]. There it was found that the same SNR wall as ED is present.

Depending on the system model, the cyclostationary feature detector may exploit the channel coherence to improve detection performance. However, the SNR wall is merely improved by a factor of the limited channel coherence time. Another strategy, which combines coherent detection of a deterministic component of the primary signal with a matched filter and subsequent ED, was also studied there. Said detector also improves the SNR wall of ED only by a factor of the channel coherence time. Some more advanced noise calibration techniques that also take uncertainty about the spectral coloring of the noise into account were investigated in [48]. Also, the tradeoff between communication capacity and robustness was explored there.

The results discussed above lead to the conjecture that all implementable wireless detection schemes suffer from SNR walls caused by model uncertainties [41].

The potential benefits of known noise power for cooperative eigenvalue-based spectrum sensing were investigated in [67] and an analytical expression of the performance gap between RLRT (see (3.28)) and the GLRT (see (3.24)) was derived. A comparison of the effects of noise uncertainty between ED and RLRT indicated that the latter detector seems to suffer less from noise uncertainty [107]. Furthermore, it was shown in [65, Eq. (30)] that a minimum SNR for detection is required for detectors, which rely on the largest eigenvalue for detection:

$$\alpha > \frac{1}{\sqrt{KN}}\,. \tag{3.55}$$

Below this threshold, the asymptotic distribution of the largest eigenvalue becomes the same under both hypotheses. Note, that this threshold can be further refined by using the results from [108, Eq. (25)] as suggested by [67]. Evidently, the SNR limit from (3.55) is not an SNR wall since it depends on the number of samples.

Apart from our results discussed in Chapter 6, we are not aware of other work proving the existence of SNR walls in (cooperative) eigenvalue-based spectrum sensing.

3.6 Order Statistics

The field of *order statistics* deals with the mathematical description of ordered random variables and their statistical properties, see [33, 109, 110] for example. It can be applied when a random sample of a certain size is taken, which is subsequently sorted and where the statistics of the sorted sample are of interest. It is typically assumed that each unordered observation may be modeled as an i.i.d. random variable with known probability distribution. Said case is relevant in this work and is formally introduced in this section.

Let $U_1, U_2, \ldots, U_K$ be an unordered random sample of size K, where the random variables U_i are i.i.d. with PDF f_U and CDF F_U for $i = 1, \ldots, K$. Then, we denote

the ordered random sample as $U_{(1)} \leq U_{(2)} \leq \cdots \leq U_{(K)}$ and $U_{(i)}$ is called the i-th *order statistic* of the sample.

In general, the CDF $F_{U_{(i)}}$ and the PDF $f_{U_{(i)}}$ of the i-th order statistic $U_{(i)}$ are [33, p. 229, Th. 5.4.4]:

$$F_{U_{(i)}}(u) = \sum_{j=i}^{K} \binom{K}{j} \left[F_U(u)\right]^j \left[1 - F_U(u)\right]^{K-j} \tag{3.56}$$

and

$$f_{U_{(i)}}(u) = \frac{K!}{(i-1)!\,(K-i)!}\, f_U(u) \left[F_U(u)\right]^{i-1} \left[1 - F_U(u)\right]^{K-i}, \tag{3.57}$$

respectively.

For this work, the joint PDF $f_{(U_{(i)},U_{(j)})}$ of two order statistics $U_{(i)}$ and $U_{(j)}$, where $1 \leq i < j \leq K$, is of interest. It can be found as [33, p. 230, Th. 5.4.6]:

$$f_{(U_{(i)},U_{(j)})}(u,v) = \frac{K!\, f_U(u)\, f_U(v) \left[F_U(u)\right]^{i-1} \left[F_U(v) - F_U(u)\right]^{j-i-1} \left[1 - F_U(v)\right]^{K-j}}{(i-1)!\,(j-i-1)!\,(K-j)!}, \tag{3.58}$$

for $-\infty < u < v < \infty$. Similarly, the joint PDF of a subset of order statistics [109, p. 12, Eq. (2.2.2)] and of all order statistics [33, p. 230, Th. 5.4.6] can be given.

A closer look on (3.56) to (3.58) reveals that for a lot of underlying population distributions (f_U / F_U) it becomes intractable to derive the exact distributions or moments of the order statistics. Hence, approximations play a major role in order statistics, e.g., [109, p. 56 ff., Ch. 4].

3.6.1 Order Statistics of a Rectangular Sample

Closed form results for the order statistics may be obtained for samples from elementary distributions like the standard rectangular distribution. In Section 6.1.1, order statistics of a standard rectangular distributed sample are utilized. Hence, we shortly review some important results here. For this, let $U_{(i)}$ be the i-th order statistic from an i.i.d. standard rectangular sample of size K. Thus, each unordered sample $U_i \sim \mathcal{R}(0,1)$ for $i = 1, \ldots, K$ and its PDF and CDF are given in (2.43) and (2.44), respectively.

Inserting these into the general form (3.57) and using (2.24) yields (see [109, p. 14, Ex. 2.3.] or [33, p. 230, Ex. 5.4.5]):

$$f_{(U_{(i)})}(u) = \frac{\Gamma(K+1)}{\Gamma(i)\,\Gamma(K-i+1)} u^{i-1} \left(1+u\right)^{(K-i+1)-1} \mathbb{I}_{[0,1]}(u). \tag{3.59}$$

By comparing (3.59) with (2.45) we find that the i-th order statistic of an i.i.d. standard rectangular sample of size K is $\mathrm{Beta}(i, K - i + 1)$ distributed.

Likewise, the corresponding joint PDF of the smallest and the largest order statistic can be derived by inserting f_U and F_U into the general form (3.58) to obtain:

$$f_{(U_{(1)},U_{(K)})}(u, v) = K(K-1)\,(v-u)^{(K-2)}\,, \tag{3.60}$$

which is valid for $0 \leq u < v \leq 1$ and zero otherwise.

3.6.2 Order Statistics of a Gaussian Sample

An important case are the order statistics from an i.i.d. Gaussian sample. Unfortunately, the CDF of a Gaussian random variable cannot be given in a closed form. Hence, also the distributions of Gaussian order statistics are problematic and must be approximated in general. However, due to the symmetry of the Gaussian PDF around its mean, some helpful relations for the moments can be derived [110, p. 95 ff., Ch. 9]. We review two relations here, which is later used in Section 6.1.2. For this, let $U_{(i)}$ denote the i-th order statistic of an i.i.d. Gaussian sample of size K for $i = 1, \ldots, K$, where the unordered sample U_i is $\mathcal{N}(\mu, \sigma^2)$ distributed.

Then, the following relation holds [110, p. 96, Eq. (9.2)]:

$$\mathrm{E}[U_{(i)}] = 2\mu - \mathrm{E}[U_{(K-i+1)}]\,. \tag{3.61}$$

Also, if the size of the sample K is odd, i.e., if $K = 2j + 1$ for $j \in \mathbb{N}$, it holds that [110, p. 96, Eq. (9.5)]:

$$\mathrm{E}[U_{(i+1)}] = \mu\,. \tag{3.62}$$

4 System Models for Cooperative Eigenvalue-Based Spectrum Sensing

This chapter introduces the system models, which are used in this work. The three models vary in complexity with respect to the considered wireless propagation channel and are referred to as model $\mathcal{M}_{\mathrm{MP}}$, $\mathcal{M}_{\mathrm{FF}}$ and $\mathcal{M}_{\mathrm{DM}}$ respectively. First, we introduce common aspects of both models in a general model description. Second, the more sophisticated model $\mathcal{M}_{\mathrm{MP}}$ that assumes a multipath propagation channel is presented in Section 4.1. Thereafter, model $\mathcal{M}_{\mathrm{FF}}$, which is a special case of $\mathcal{M}_{\mathrm{MP}}$, is presented in Section 4.2. Model $\mathcal{M}_{\mathrm{DM}}$, which is again a special case of model $\mathcal{M}_{\mathrm{FF}}$ is shortly discussed in Section 4.2.1. The latter two models exhibit convenient mathematical properties that are helpful for the theoretical analysis of (cooperative) detectors.

In this work, we consider collaborative spectrum sensing systems, which consist of K cooperating SUs. All SUs tune to a specific frequency band and collect complex baseband samples. The received samples are shared with a fusion center that aims at deciding whether a PU is present. We make a simplifying assumption that only one PU is potentially present. Note, however, that this assumption is similarly present in related literature, e.g., [21, 65, 107, 111, 112].

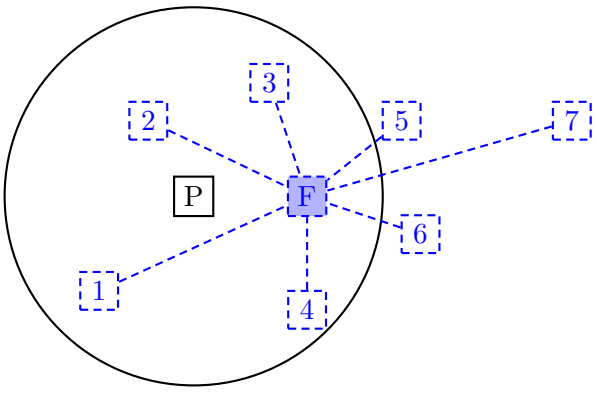

Figure 4.1: Example of a cooperative spectrum sensing system with fusion center F, seven cooperating SUs and one PU P. Note, that the SUs 1 to 4 are in transmission range of P, while the SUs 5 to 7 are not.

By stacking the received complex baseband samples of the SUs into a time dependent column vector $\mathbf{y}(t)$ (of dimension K) in discrete time $t \in \mathbb{Z}$, we can formalize the basic hypothesis testing problem as:

$$\begin{aligned} \mathcal{H}_0 &: \mathbf{y}(t) = \mathbf{w}(t) \\ \mathcal{H}_1 &: \mathbf{y}(t) = \mathbf{x}(t) + \mathbf{w}(t)\,. \end{aligned} \tag{4.1}$$

Here, $\mathbf{w}(t)$ describes the additive receiver noise and $\mathbf{x}(t)$ stands for the signal sent by the PU including channel effects as well as filtering at the receiver. In other words, if hypothesis $\mathcal{H}_0$ is true only noise is received, whereas if $\mathcal{H}_1$ is true the distorted PU signal with additive noise is received.

Note, that we assume the receivers to start sampling at time index $t = 1$. Defining $t \in \mathbb{Z}$ is a technicality to ensure a well defined model, when considering multipath propagation channels.

Unless explicitly stated otherwise, $\mathbf{w}(t)$ is modeled as white Gaussian noise, which is i.i.d. for each time-index t, following a K-dimensional zero mean complex circularly symmetric Gaussian distribution with covariance matrix $\sigma_w^2 \mathbf{I}_K$. That is $\mathbf{w}(t) \sim \mathcal{CN}(\mathbf{0}_K, \sigma_w^2 \mathbf{I}_K)$.

The sequence of symbols sent by the PU (excluding any channel / filtering effects) is denoted by $s(t)$. Unless stated otherwise, we assume that $s(t)$ is a zero-mean random variable of unknown distribution with variance σ_s^2 that is i.i.d. for each discrete time-index t.

Note, we assume the PU symbol sequence $s(t_1)$ and the receiver noise $\mathbf{w}(t_2)$ to be independent for every given time indices t_1 and t_2.

In eigenvalue-based spectrum sensing, PU signals are detected on the basis of the sample covariance matrix, which exposes correlation. Here, typically correlation among multiple receivers or correlation over time is exploited. Note, that these two types of correlations may also be combined. Hence, our system model incorporates both time and receiver correlation, where the exact mode of operation can be specified by the model parameter $Q \in \mathbb{N}$.

To account for correlation over time, let $\mathbf{z}(t)$ be the *processing vector* used in calculating the sample covariance matrix, defined as

$$\mathbf{z}(t) = \Big(y_1(t), y_1(t-1), \ldots, y_1(t-Q+1), \ldots, y_K(t), \ldots, y_K(t-Q+1)\Big)^{\mathrm{T}}. \tag{4.2}$$

The parameter Q controls how many consecutive time points are included in estimating the sample covariance matrix and was referred to as *smoothing factor* in [19]. Choosing $Q \geq 2$ enables estimating the covariance among time differences, while $Q = 1$ must be chosen to estimate the covariance between multiple SUs only.

We combine $(N-Q+1)$ sample vectors into the $(KQ)\times(N-Q+1)$ processing matrix $\mathbf{Z}$:

$$\begin{aligned}\mathbf{Z} &= \Big(\mathbf{z}(Q), \mathbf{z}(Q+1), \ldots, \mathbf{z}(N)\Big) \\ &= \begin{pmatrix} y_1(Q) & y_1(Q+1) & \ldots & y_1(N) \\ y_1(Q-1) & y_1(Q) & \ldots & y_1(N-1) \\ \vdots & \vdots & \ddots & \vdots \\ y_1(1) & y_1(2) & \ldots & y_1(N-Q+1) \\ \vdots & \vdots & \ddots & \vdots \\ y_K(Q) & y_K(Q+1) & \ldots & y_K(N) \\ \vdots & \vdots & \ddots & \vdots \\ y_K(1) & y_K(2) & \ldots & y_K(N-Q+1) \end{pmatrix}. \end{aligned} \tag{4.3}$$

Arranging the sample vectors in this way, results in ensuring that N unique samples from each SU are collected in the matrix $\mathbf{Z}$, irrespective of the choice of Q. To ease readability, we define $\tilde{K} = KQ$.

Based on these definitions the $\tilde{K}\times\tilde{K}$ sample covariance matrix can be calculated as

$$\hat{\mathbf{R}} = \frac{1}{N-Q+1}\sum_{i=Q}^{N}\mathbf{z}(i)\mathbf{z}(i)^{\mathrm{H}} = \frac{1}{N-Q+1}\,\mathbf{Z}\mathbf{Z}^{\mathrm{H}}\,. \tag{4.4}$$

For the theoretical analysis, it is convenient to formulate the system model in matrix form. Let

$$\tilde{\mathbf{W}} = \Big(\tilde{\mathbf{w}}(Q), \tilde{\mathbf{w}}(Q+1), \ldots, \tilde{\mathbf{w}}(N)\Big)\,, \tag{4.5}$$

with

$$\tilde{\mathbf{w}}(t) = \Big(w_1(t), \ldots, w_1(t-Q+1), \ldots, w_K(t), \ldots, w_K(t-Q+1)\Big)^{\mathrm{T}} \tag{4.6}$$

and let $\tilde{\mathbf{X}}$, $\tilde{\mathbf{x}}(t)$ be defined analogously. Then, the system model can still be formulated additively for all choices of Q, i.e., under $\mathcal{H}_0$ it holds that $\mathbf{Z} = \tilde{\mathbf{W}}$ and under $\mathcal{H}_1$ it holds that $\mathbf{Z} = \tilde{\mathbf{X}} + \tilde{\mathbf{W}}$. If no time correlation is considered, i.e., if $Q = 1$, the model simplifies to $\mathbf{Z} = \mathbf{Y} = \mathbf{W}$ under $\mathcal{H}_0$ and $\mathbf{Z} = \mathbf{Y} = \mathbf{X} + \mathbf{W}$ under $\mathcal{H}_1$. Here, $\mathbf{W} = \Big(\mathbf{w}(1), \ldots, \mathbf{w}(N)\Big)$, and $\mathbf{X}$ as well as $\mathbf{Y}$ are defined analogously.

In eigenvalue-based spectrum sensing, the test statistic is a function of the eigenvalues of the sample covariance matrix. Hence, we denote the vector containing the ordered eigenvalues of $\hat{\mathbf{R}}$ by

$$\hat{\boldsymbol{\lambda}} = \Big(\hat{\lambda}_1, \hat{\lambda}_2, \ldots, \hat{\lambda}_{\tilde{K}}\Big)^{\mathrm{T}}\,, \tag{4.7}$$

where the eigenvalues are sorted ascending, that is $\hat{\lambda}_1 \leq \cdots \leq \hat{\lambda}_{\tilde{K}}$.

4.1 Multipath Propagation Channel Model ($\mathcal{M}_{\mathrm{MP}}$)

The following model, referred to as model $\mathcal{M}_{\mathrm{MP}}$, considers a multipath propagation environment. Let $h_i(t)$ denote the channel impulse response from the PU to the i-th SU (where $i = 1, \ldots, K$), which is assumed to describe both the effects of the wireless channel and the receiver filter.

Then, the received noiseless signal $x_i(t)$ at SU i is given by:

$$x_i(t) = \sum_{j=1}^{t_h} h_i(j)\, s\left(\left\lceil \frac{t-j+1}{M} \right\rceil\right), \tag{4.8}$$

which is the convolution of the oversampled PU symbol sequence $s(t)$ and the channel impulse response. For simplicity we assume that the sample rate is a multiple of the symbol rate, which is expressed by the oversampling factor $M \in \mathbb{N}$. There, t_h is the length of the channel impulse response, i.e., $h_i(t) = 0$ for $t \leq 0$ and $t > t_h$. For this model it is assumed that the channel impulse response stays constant during the observation time.

This system model is similar to the one used in [17–19] . Here, however, only one PU is considered and oversampling is treated implicitly by our model.

4.2 Flat Fading and Memoryless Channel Model ($\mathcal{M}_{\mathrm{FF}}$)

The model $\mathcal{M}_{\mathrm{FF}}$, which is introduced in this section, is a special case of the more general model $\mathcal{M}_{\mathrm{MP}}$. It does not account for multipath propagation effects and can be described as a flat fading and memoryless channel model. Instead, the effects of the wireless channel and the receiver filter are described by a complex channel coefficient vector $\mathbf{h}$. Here, $\mathbf{h}$ is assumed to be fixed but unknown and constant during the observation time.

The received noiseless signal of the SUs is given by:

$$\mathbf{x}(t) = \mathbf{h}\, s\left(\left\lceil \frac{t}{M} \right\rceil\right). \tag{4.9}$$

Hence, we see that model $\mathcal{M}_{\mathrm{FF}}$ is a special case of model $\mathcal{M}_{\mathrm{MP}}$ with channel length $t_h = 1$.

To abstract from the concrete realization of the channel coefficient vector $\mathbf{h}$, we define the average receiver SNR, which is constant for the observation time due to the stationarity of the involved random processes:

$$\alpha = \frac{\mathrm{E}\left[\left\|\mathbf{h}\, s(t)\right\|_2^2\right]}{\mathrm{E}\left[\left\|\mathbf{w}(t)\right\|_2^2\right]} = \frac{\sigma_s^2 \left\|\mathbf{h}\right\|_2^2}{K\sigma_w^2}. \tag{4.10}$$

This system model is widely used for the analysis of cooperative eigenvalue-based spectrum sensing systems, e.g., [21, 65, 67, 107], with slight variations of the PU signal assumptions.

Under $\mathcal{H}_0$ the statistical covariance matrix can be readily found as $\mathbf{R}_0 = \mathbf{R}_{\tilde{\mathbf{w}}} = \sigma_w^2 \mathbf{I}_{\tilde{K}}$. However, under $\mathcal{H}_1$ the form of $\mathbf{R}_1$ depends heavily on the chosen parameters. In later sections, the special case when no time correlation is respected and no oversampling is performed is of interest, i.e., when $Q = 1$ and $M = 1$. In this case, it is easy to show that $\mathbf{R}_{\mathbf{x}} = \sigma_s^2 \mathbf{h}\mathbf{h}^{\mathrm{H}}$ and consequently $\mathbf{R}_1 = \sigma_s^2 \mathbf{h}\mathbf{h}^{\mathrm{H}} + \sigma_w^2 \mathbf{I}_K$. Since $\mathbf{R}_{\mathbf{x}}$ is of rank one and $\mathbf{R}_{\mathbf{w}}$ is a scaled identity matrix, their eigenvalues can be readily found as

$$\mathrm{eig}\left(\mathbf{R}_{\mathbf{x}}\right) = \left(0, \ldots, 0, \sigma_s^2 \left\|\mathbf{h}\right\|_2^2\right)^{\mathrm{T}} \tag{4.11}$$

and

$$\mathrm{eig}\left(\mathbf{R}_{\mathbf{w}}\right) = \sigma_w^2 \mathbf{1}_K \,, \tag{4.12}$$

respectively. Moreover, since $\mathbf{R}_{\mathbf{w}}$ is a scaled identity matrix it holds (see also (3.17)):

$$\mathrm{eig}\left(\mathbf{R}_1\right) = \mathrm{eig}\left(\mathbf{R}_{\mathbf{x}}\right) + \mathrm{eig}\left(\mathbf{R}_{\mathbf{w}}\right) \,. \tag{4.13}$$

Hence, under this model and when $Q = M = 1$ the vector of eigenvalues $\boldsymbol{\lambda}$ of $\mathbf{R}$ follows as:

$$\boldsymbol{\lambda} = \begin{cases} \left(\sigma_w^2, \ldots, \sigma_w^2\right)^{\mathrm{T}} = \sigma_w^2 \mathbf{1}_K, & \text{under } \mathcal{H}_0 \\ \left(\sigma_w^2, \ldots, \sigma_w^2, \sigma_s^2 \left\|\mathbf{h}\right\|_2^2 + \sigma_w^2\right)^{\mathrm{T}}, & \text{under } \mathcal{H}_1 \,. \end{cases} \tag{4.14}$$

4.2.1 Flat Fading and Memoryless Channel Model for Digitally Modulated Signals ($\mathcal{M}_{\mathsf{DM}}$)

So far, it was assumed that $s(t)$ is a zero-mean random variable of unknown distribution with variance σ_s^2 that is i.i.d. for each discrete time-index t. For model $\mathcal{M}_{\mathrm{DM}}$, however, we assume $s(t)$ to be a *discrete* zero-mean random variable with variance σ_s^2 and unknown probability mass function (PMF), which is also i.i.d. for each discrete time-index t. Hence, this model is a special case with which digitally modulated signals in the baseband can be described (i.e., linearly modulated passband signals). This includes widely used modulation techniques such as phase-shift keying (PSK) and quadrature amplitude modulation (QAM) for example, cf. [113, 114].

5 Quickest Eigenvalue-Based Spectrum Sensing

Quickest detection (see Section 3.3) has been applied to the spectrum sensing problem and was termed *quickest spectrum sensing* in the literature. It was first investigated for Gaussian signal and noise in [72] and for sinusoidal signals with Gaussian noise in [115]. Investigating quickest detection procedures on the basis of cyclostationary features was done in [54]. Collaboration between multiple SUs for quickest spectrum sensing was considered in [111, 116]. Also, an extension of quickest spectrum sensing for multi-antenna receivers was proposed in [117].

To the best of our knowledge, quickest spectrum sensing using eigenvalues of the sample covariance matrix has not been investigated under a centralized and collaborative system model like the ones from Chapter 4. Recently, a decentralized quickest detection approach using eigenvalues of the sample covariance matrix was proposed [118], where no fusion center is present. Instead, the SUs share the computational load and exchange messages to estimate the sample covariance matrix. However, the system model of said work is entirely different to the centralized collaborative spectrum sensing paradigm considered here.

In this chapter, we first discuss the characteristics and requirements of the two types of possible change detection problems in spectrum sensing in Section 5.1. Furthermore, we introduce the concept of centralized collaborative quickest eigenvalue-based spectrum sensing and the necessary changes to the system model in Section 5.2. Then, we develop two exact algorithms in a simplified dual SU scenario for both known and unknown SNR in Section 5.3. There, we obtain some valuable results for the general K SU case and compare the detection performance to regular eigenvalue-based block detection for the dual SU case.

Parts of this chapter have been published in [25, 27].

5.1 Change Detection Problems in Spectrum Sensing

In this section, we discuss the two types of possible hypothesis changes in a spectrum sensing setting and assess the consequences of the detection delay for both cases.

In order to focus the analysis on the spectrum sensing algorithms and their associated delays, we assume the SUs to have a dual radio architecture [11, Sec. III.A.].

That is, they have two separate radio transceiver modules: one for sensing and one for communicating data. This way, we may ignore spectrum access strategies and networking issues for this analysis.

There are two possible types of hypothesis changes. Either a previously occupied frequency band becomes free again ($\mathcal{H}_1$ to $\mathcal{H}_0$) or a PU appears that starts transmitting on the band, which was free before ($\mathcal{H}_0$ to $\mathcal{H}_1$). In the former situation a spectrum opportunity emerges, while in the latter it vanishes. In Figure 5.1 both situations are visualized and relevant time points including associated delays are described, which are important in the analysis of change detection algorithms. The

Figure 5.1: Change detection problems in spectrum sensing. At t_c a change from Hypothesis $\mathcal{H}_0$ (unoccupied channel) to Hypothesis $\mathcal{H}_1$ (occupied channel) occurs. The detection algorithm raises an alarm at t_a and the detection delay is defined as $\tau_\mathrm{d} = t_\mathrm{a} - t_\mathrm{c} + 1$. The reverse situation that an occupied channel becomes free happens at $\tilde{t}_\mathrm{c}$ with analogously defined alarm time $\tilde{t}_\mathrm{a}$ and detection delay $\tilde{\tau}_\mathrm{d}$. The duration shaded in gray indicates interference for the primary system, while the duration in white symbolizes wasted transmission potential for the secondary system.

delay introduced by the detection algorithm has different practical implications for both the primary and the secondary system depending on the type of hypothesis change.

Let us consider the $\mathcal{H}_1$ to $\mathcal{H}_0$ change, i.e., an occupied band becoming free again. Here, the detection delay leads to an access delay of the secondary system, thereby shortening the available transmission window for the SUs. While being an inefficiency in the secondary system, the delay has no direct negative effect on the primary system. If a false alarm is raised, meaning that the channel is falsely declared to be free, however, interference for the primary system is inevitable since the SUs start communicating on the band. Ongoing transmissions of the licensed primary system may be corrupted in this case. Thus, this change is critical with respect to detection accuracy.

If we examine the change from $\mathcal{H}_0$ to $\mathcal{H}_1$, a PU starts transmitting on the band, changing its occupancy status from free to occupied. In this case, the detection

delay will cause interference for the primary system, since the SUs do not immediately terminate their communication on that band. Thus, the detection delay causes a direct negative effect on the (licensed) primary system.

Hence, we argue quickest detection techniques offer the most potential for improvement in the $\mathcal{H}_0$ to $\mathcal{H}_1$ case. Especially PUs that are in the immediate vicinity of several SUs will benefit directly from decreased delays. There, a strong PU signal is received, such that the detection task is comparatively easy and the quickest detection algorithm has the chance to detect the change significantly faster than a block detector.

5.2 System Model for Quickest Eigenvalue-Based Spectrum Sensing

This section introduces a system model to enable centralized, collaborative QD based on the eigenvalues of the sample covariance matrix for spectrum sensing. In contrast to block detection — where the goal is to reliably detect the current hypothesis — in QD it is assumed the current hypothesis is known and that a change to the other hypothesis shall be detected with minimal delay. Hence, in QD detection attempts are performed for every sample. An alarm is declared if the threshold is exceeded and the sampling / detection process is continued otherwise, see Section 3.3.

To use a function of the eigenvalues of the sample covariance matrix as a test statistic in QD, a time-dependent version of the model must be conceived. We introduce a block index $k \in \mathbb{N}$ and define $\hat{\boldsymbol{\lambda}}(k)$ as the vector of ordered eigenvalues of the sample covariance matrix calculated from the k-th consecutive block of N non-overlapping samples:

$$\hat{\mathbf{R}}(k) = \mathbf{Z}(k)\,\mathbf{Z}(k)^{\mathrm{H}}, \tag{5.1}$$

where

$$\mathbf{Z}(k) = (\mathbf{z}(Q + (k-1)N), \mathbf{z}(Q + 1 + (k-1)N), \cdots, \mathbf{z}(kN)) \; . \tag{5.2}$$

Here, $\mathbf{z}(t)$ is the processing vector as defined in (4.2).

Hence, also the test statistic becomes time-dependent: $T(k)$. Consider the MME (cf. (3.22)) for example, which is used in the remainder of this chapter:

$$T_{\mathrm{MME}}(k) = \frac{\hat{\lambda}_{\tilde{K}}(k)}{\hat{\lambda}_1(k)} \, . \tag{5.3}$$

Thus, the idea is to split up the big block of samples used in eigenvalue-based block detection into smaller ones, in order to perform sequential detection attempts in

the spirit of QD, see also Figure 5.2. Note, that the block size of each smaller block, denoted by N, is a trade off between the estimation accuracy of the sample covariance matrix on the one hand and the detection delay on the other hand.

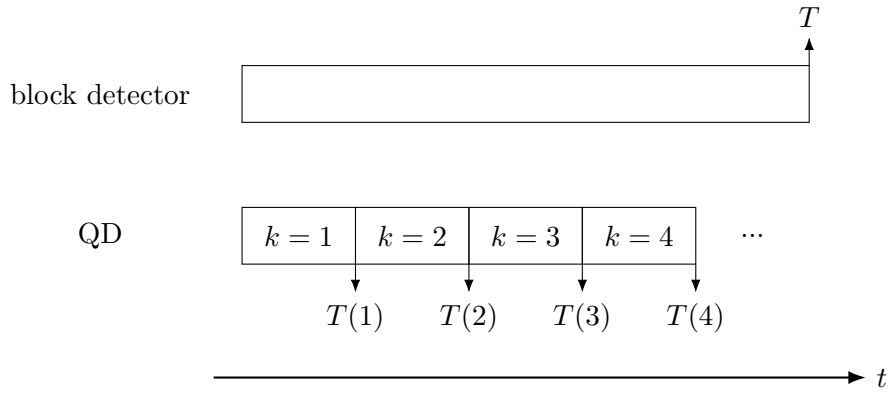

Figure 5.2: In the top part, a classical block detector with a fixed sample size is shown. In contrast, in the bottom part the block structure of our quickest eigenvalue-based spectrum sensing methodology is depicted, which uses only a fraction of the block detectors' samples for each detection attempt.

Since in QD it is typically assumed that the input samples of the algorithm, i.e., $T_{\mathrm{MME}}(k)$ in our case, are i.i.d. according to the distribution corresponding to the hypothesis at that particular time instance k, we need to make an additional assumption. That is, no hypothesis change may happen within a block. This can be mathematically expressed as $t_{\mathrm{c}} \in \{(k-1)N + 1 \mid k \in \mathbb{N}\}$. Note, however, that an analogous assumption is present in the analysis of block detection algorithms.

5.3 Exact Algorithms for a Dual User Scenario

Commonly used algorithms in QD utilize the LLR for detection, see Section 3.3. Consequently, to determine the LLR, knowledge of the PDFs of the test statistics under both hypotheses are required. In this section, the MME is considered as a test statistic and using a very simple system model, i.e., model $\mathcal{M}_{\mathrm{DM}}$ with two cooperating SUs and $Q = M = 1$ (cf. Section 4.2.1), the exact PDFs of the test statistic can be found under both hypotheses. This enables us to give exact QD algorithms for this scenario.

First, the distributions of the sample covariance matrix are identified in Section 5.3.1 for a general number of cooperating SUs K. Then, for $K = 2$, the PDF of the test statistic are given under $\mathcal{H}_0$ from the literature in Section 5.3.2 and under $\mathcal{H}_1$ it

is derived by generalizing a result from the literature in Section 5.3.3. Since evaluation of the PDFs can be demanding for large numbers of samples N, we derive alternative expressions that can be conveniently evaluated using double precision floating point arithmetic in Section 5.3.4. Based on these results exact quickest eigenvalue-based spectrum sensing algorithms are given for detecting changes from $\mathcal{H}_0$ to $\mathcal{H}_1$ and from $\mathcal{H}_1$ to $\mathcal{H}_0$ in Sections 5.3.5 and 5.3.6, respectively. The results obtained in this section are then evaluated numerically in Section 5.3.7.

5.3.1 Distributions of the Sample Covariance Matrix and its Eigenvalues

This section identifies the distributions of the sample covariance matrix under both hypotheses for a general number of cooperating SUs K and a general finite number of samples N for model $\mathcal{M}_{\mathrm{DM}}$ without exploiting time correlation and without oversampling, i.e., $Q = 1$ and $M = 1$ (see Section 4.2.1).

Since scaling of the sample covariance matrix results in the same scaling of all its eigenvalues, the ratio of T_{MME} is unaffected, cf. Section 3.2. Thus, we omit the normalization factor N^{-1} and use the non-normalized sample covariance matrix $\hat{\mathbf{R}} = \mathbf{Y}\mathbf{Y}^{\mathrm{H}}$ in the following. Similarly, the test statistic T_{MME} is only dependent on the average SNR α, but independent of the actual noise power under both hypotheses. Hence, our system model uses the SNR as a parameter directly and we assume w.l.o.g. $\sigma_w^2 = 1$.

Distribution under Hypothesis $\mathcal{H}_0$

Under hypothesis $\mathcal{H}_0$, the non-normalized sample covariance matrix is simply $\hat{\mathbf{R}}_0 = \mathbf{W}\mathbf{W}^{\mathrm{H}}$. Since every entry of $\mathbf{W}$ is i.i.d., following a standard complex circularly symmetric Gaussian distribution, the statistic covariance matrix of a column is the identity matrix ($\mathbf{I}_K$). This random matrix is called a complex uncorrelated central Wishart matrix of dimension K with N degrees of freedom [83], which we denote by $\hat{\mathbf{R}}_0 \sim \mathcal{CW}_K(N, \mathbf{I}_K)$ (see also Section 3.4). The PDF of $\hat{\mathbf{R}}_0$ and the joint PDF of its ordered eigenvalues can be found with the help of Table 3.1 and (3.39).

Distribution under Hypothesis $\mathcal{H}_1$

Under hypothesis $\mathcal{H}_1$ the non-normalized sample covariance matrix $\hat{\mathbf{R}}_1 = (\mathbf{X} + \mathbf{W})(\mathbf{X} + \mathbf{W})^{\mathrm{H}}$. To derive a distribution, we would have to assume knowledge of the distribution of the PU signal $s(t)$. Instead, we first assume that $s(t)$ is constant and known. Later, we discuss the situation when $s(t)$ is random.

Let $\mathbf{s} = (s(1), \ldots, s(N))$, i.e., the *row* vector of N PU symbols. For the following, we assume that both $\mathbf{s}$ and $\mathbf{h}$ are fixed and known in order to derive conditional

probability distributions. Since we consider no oversampling ($M = 1$) here, the signal matrix is

$$\mathbf{X} = \mathbf{h}\mathbf{s}\,. \tag{5.4}$$

Hence, for known $\mathbf{s}$ and $\mathbf{h}$ the sample covariance matrix under $\mathcal{H}_1$ can be written as

$$\left(\hat{\mathbf{R}}_1 \mid \mathbf{s}, \mathbf{h}\right) = (\mathbf{X} + \mathbf{W})(\mathbf{X} + \mathbf{W})^{\mathrm{H}} = \check{\mathbf{W}}\check{\mathbf{W}}^{\mathrm{H}}\,, \tag{5.5}$$

where each column is i.i.d. according to a complex circularly symmetric Gaussian, i.e., $\check{\mathbf{w}}_i \sim \mathcal{CN}(\mathbf{x}_i, \mathbf{I}_K)$ for $i = 1, \ldots, N$. Thus, $\left(\hat{\mathbf{R}}_1 \mid \mathbf{s}, \mathbf{h}\right)$ follows a complex uncorrelated non-central Wishart distribution of dimension K with N degrees of freedom and non-centrality matrix $\boldsymbol{\Omega} = \mathrm{E}\left[\check{\mathbf{W}}\right]\mathrm{E}\left[\check{\mathbf{W}}^{\mathrm{H}}\right]$, which we denote by $\left(\hat{\mathbf{R}}_1 \mid \mathbf{s}, \mathbf{h}\right) \sim \mathcal{CW}_K(N, \mathbf{I}_K, \boldsymbol{\Omega})$, see [83] and Section 3.4. Here, the non-centrality matrix can be simplified as follows

$$\begin{aligned}\boldsymbol{\Omega} &= \mathrm{E}\left[\check{\mathbf{W}}\right]\mathrm{E}\left[\check{\mathbf{W}}^{\mathrm{H}}\right] = \mathbf{X}\mathbf{X}^{\mathrm{H}} = \sum_{i=1}^{N}\mathbf{x}_i(\mathbf{x}_i)^{\mathrm{H}} = \sum_{i=1}^{N}|s(i)|^2\,\mathbf{h}\mathbf{h}^{\mathrm{H}} \\ &= \|\mathbf{s}\|_2^2\,\mathbf{h}\mathbf{h}^{\mathrm{H}}\,. \end{aligned} \tag{5.6}$$

This model for constant $\mathbf{s}$ and $\mathbf{h}$ is very similar to the one presented in [119], which was used to propose a detector based on the largest eigenvalue of the sample covariance matrix.

Since $\boldsymbol{\Omega}$ from (5.6) is evidently a rank one matrix, its ordered eigenvalue vector can be readily given as

$$\boldsymbol{\omega} = \mathrm{eig}\,(\boldsymbol{\Omega}) = \left(0, \ldots, 0, \|\mathbf{s}\|_2^2\,\|\mathbf{h}\|_2^2\right)^{\mathrm{T}}\,. \tag{5.7}$$

The PDF of a general non-central Wishart distribution was given in [83], see (3.37). Here, however, the non-centrality matrix is rank one and the common covariance matrix of the noise vectors is an identity matrix. Hence, this is a special case of an uncorrelated Wishart distribution and the PDF may be simplified considerably. First, we note that the argument of the generalized multivariate hypergeometric series in (3.37) is a matrix of rank one, since it holds with (5.6) that

$$\boldsymbol{\Omega}\mathbf{A} = \|\mathbf{s}\|_2^2\;\mathbf{h}\mathbf{h}^{\mathrm{H}}\mathbf{A} \tag{5.8}$$

Note, that it holds for the product of two matrices $\mathbf{V}$ and $\mathbf{U}$ that [120, p. 97]

$$\mathrm{rank}(\mathbf{V}\mathbf{U}) \leq \min(\mathrm{rank}(\mathbf{V}), \mathrm{rank}(\mathbf{U}))\,. \tag{5.9}$$

Hence, the eigenvalues of $\boldsymbol{\Omega}\mathbf{A}$ are easily determined as

$$\mathrm{eig}\,(\boldsymbol{\Omega}\mathbf{A}) = \mathrm{eig}\left(\|\mathbf{s}\|_2^2\,\mathbf{h}\mathbf{h}^{\mathrm{H}}\mathbf{A}\right) = (0, \ldots, 0, \mathbf{h}^{\mathrm{H}}\mathbf{A}\mathbf{h})^{\mathrm{T}}\,. \tag{5.10}$$

The hypergeometric series ${}_0\tilde{\mathcal{F}}_1(N;\cdot)$ of hermitian matrix argument in (3.37) is defined using so-called (complex) zonal polynomials, which are functions of the eigenvalues of the matrix argument, see [83, Eqs. (85),(35) and (19)] and [99, p. 83 ff., Ch. 5]. If only one eigenvalue is non-zero, however, all contributions to the multivariate series, except terms exclusively involving powers of the non-zero eigenvalue, become zero. One can see this by utilizing the equivalence between zonal polynomials and the so-called Schur polynomials and invoking [99, p. 93, Eq. (4)]. Hence, here, the multivariate hypergeometric series is equivalent to the hypergeometric series of scalar argument, i.e.,

$$ {}_0\tilde{\mathcal{F}}_1(N;\|\mathbf{s}\|_2^2\,\mathbf{h}\mathbf{h}^{\mathrm{H}}\mathbf{A}) = {}_0\mathcal{F}_1(N;\mathbf{h}^{\mathrm{H}}\mathbf{A}\mathbf{h})\,. \tag{5.11} $$

Noting that

$$ \mathrm{tr}(\boldsymbol{\Omega}) = \mathrm{tr}\left(\|\mathbf{s}\|_2^2\,\mathbf{h}\mathbf{h}^{\mathrm{H}}\right) = \|\mathbf{s}\|_2^2\,\|\mathbf{h}\|_2^2 \tag{5.12} $$

and utilizing (5.11) we can simplify (3.37) to obtain the PDF of the sample covariance matrix under $\mathcal{H}_1$ given $\mathbf{s}$ and $\mathbf{h}$ as

$$ f_{(\hat{\mathbf{R}}_1|\mathbf{s},\mathbf{h})}(\hat{\mathbf{R}}\mid\mathbf{s},\mathbf{h}) = e^{-\|\mathbf{s}\|_2^2\|\mathbf{h}\|_2^2}\,{}_0\mathcal{F}_1(N;\|\mathbf{s}\|_2^2\,\mathbf{h}^{\mathrm{H}}\hat{\mathbf{R}}\mathbf{h})\,\frac{e^{-\mathrm{tr}(\hat{\mathbf{R}})}}{\tilde{\Gamma}_K(N)}\,\left|\hat{\mathbf{R}}\right|^{N-K}\,. \tag{5.13} $$

There, $\tilde{\Gamma}_K(N)$ is defined by (3.38).

Next, we turn to the distribution of the joint ordered eigenvalues of $(\hat{\mathbf{R}}_1\mid\mathbf{s},\mathbf{h})$. In general, it can be found by consulting Table 3.1 and (3.39). However, if the noncentrality matrix of the Wishart distribution does not exhibit full rank (or if some eigenvalues coincide), the formulation (3.39) becomes undefined. Instead one has to evaluate the appropriate limit of the PDF, see [121, Lemma 2] and [122, Lemma 3]. A version of PDF of the joint ordered eigenvalues for the case that the noncentrality matrix is of arbitrary rank can be found in [102, eqs. (5) and (6)], which was derived in a slightly different form in [123, Lemma 1, eqs. (46)-(48)] with the technique mentioned above.

We prefer the version from [102, Eqs. (5) and (6)], since it is in form of the product of two determinants like (3.39). However, the normalizing constant of the PDF is not given there. It can be derived by rearranging the version from [123, Eqs. (46)-(48)] and noting their normalizing constant must be multiplied by the factor

$$ \frac{[(N-K)!]^K}{\prod\limits_{i=\mathrm{rank}(\boldsymbol{\Omega})+1}^{K}(N-i)!} \tag{5.14} $$

to yield the normalizing constant of [102, Eq. (5)].

Inserting $\operatorname{rank}(\mathbf{\Omega}) = 1$ as well as the results from (5.7) and (5.12) into [102, Eq. (5)] and simplifying yields the PDF of the joint ordered eigenvalues of the sample covariance matrix under $\mathcal{H}_1$ given $\mathbf{s}$ and $\mathbf{h}$:

$$f_{(\hat{\boldsymbol{\lambda}}|\mathbf{s},\mathbf{h})}(\hat{\boldsymbol{\lambda}} \mid \mathbf{s},\mathbf{h}) = \check{c}_{\mathrm{UN}} \left|\check{\boldsymbol{\mathcal{V}}}_{\mathbf{1}}(\hat{\boldsymbol{\lambda}})\right| \left|\check{\mathbf{F}}(\hat{\boldsymbol{\lambda}}; \|\mathbf{s}\|_2^2 \, \|\mathbf{h}\|_2^2)\right| \prod_{i=1}^{K} \hat{\lambda}_i^{N-K} e^{-\hat{\lambda}_i}\,, \tag{5.15}$$

where $\check{\boldsymbol{\mathcal{V}}}_{\mathbf{1}}(\hat{\boldsymbol{\lambda}}) = \left[\hat{\lambda}_{K-i+1}^{K-j}\right]_{1\le i,j\le K}$,

$$\check{c}_{\mathrm{UN}} = \frac{e^{-\|\mathbf{s}\|_2^2 \|\mathbf{h}\|_2^2}}{\left[\|\mathbf{s}\|_2^2 \, \|\mathbf{h}\|_2^2\right]^{(K-1)} \prod\limits_{i=1}^{K}(K-1-i)! \prod\limits_{i=1}^{K}(N-i)!}\,, \tag{5.16}$$

and

$$\left[\check{\mathbf{F}}(\hat{\boldsymbol{\lambda}}; a)\right]_{1\le i,j\le K} = \begin{cases} \frac{{}_0\mathcal{F}_1(N-K+1; a\,\hat{\lambda}_{K-i+1})}{(N-K)!}, & \text{for } i = 1,\dots,K \text{ and } j = 1 \\ \hat{\lambda}_{K-i+1}^{K-j}, & \text{for } i = 1,\dots,K \text{ and } j = 2,\dots,K\,. \end{cases} \tag{5.17}$$

We observe in (5.13) that the density $f_{(\hat{\mathbf{R}}_1|\mathbf{h},\mathbf{s})}$ is a function of $\|\mathbf{s}\|_2^2$ and $\mathbf{h}$, while $f_{(\hat{\boldsymbol{\lambda}}|\mathbf{h},\mathbf{s})}$ from (5.15) is a function of the term $\|\mathbf{s}\|_2^2 \, \|\mathbf{h}\|_2^2$. Hence, in the following we denote them by $f_{(\hat{\mathbf{R}}_1|\|\mathbf{s}\|_2^2,\mathbf{h})}$ and $f_{(\hat{\boldsymbol{\lambda}}|\|\mathbf{s}\|_2^2,\|\mathbf{h}\|_2^2)}$, respectively.

Evidently, it is not realistic that the spectrum sensing system has knowledge of the exact PU signal sequence. Typically, we would instead model the PU signal stochastically. However, it is similarly unrealistic to assume any knowledge about these distributions is available. Nevertheless, we examine this case and gain valuable insights, which lead to a suitable approximation. For this, let us again assume that the PU signal sequence $\mathbf{s}$ is random, as is the case in model $\mathcal{M}_{\mathrm{DM}}$ from Section 4.2.1. There, we assume a digital modulation, such that $s(t)$ takes on complex symbols from a symbol alphabet $\mathbb{M}$. Since $s(t)$ is i.i.d. for every time instance t, the PMF may be described as $\mathrm{P}(s(t) = v_i)$ for $v_i \in \mathbb{M}$ and $i = 1,\dots,|\mathbb{M}|$. As the conditional probability densities $f_{(\hat{\mathbf{R}}_1|\|\mathbf{s}\|_2^2,\mathbf{h})}$ and $f_{(\hat{\boldsymbol{\lambda}}|\|\mathbf{s}\|_2^2,\|\mathbf{h}\|_2^2)}$ are functions of $\|\mathbf{s}\|_2^2$, we require the PMF of $\|\mathbf{s}\|_2^2$. It depends on the PMF of $|s(t)|^2$, which can be given as

$$\mathrm{P}\left(|s(t)|^2 = u_j\right) = \sum_{i:|v_i|^2=u_j} \mathrm{P}(s(t) = v_i)\,. \tag{5.18}$$

The order of the individual symbols in the sequence $\mathbf{s}$ is obviously irrelevant for $\mathrm{P}(\|\mathbf{s}\|_2^2 = v_i)$, where $i = 1,\dots,|\mathcal{P}|$ and $\mathcal{P}$ is the countable set of possible norms of the sequence. To find the PMF $\mathrm{P}(\|\mathbf{s}\|_2^2 = v_i)$ one has to find all possible ways to partition v_i into a sum of the number of occurrences of possible $|s(t)|^2$. Then,

$\mathrm{P}(\|\mathbf{s}\|_2^2 = v_i)$ follows as the sum over the probability of encountering these partitions. Each partition follows a multinomial distribution with event probabilities $\mathrm{P}(|s(t)|^2 = u_j)$, compare [124, p. 137, Ch. 2, Def. 7].

Then, the PDF of the sample covariance matrix under $\mathcal{H}_1$ given $\mathbf{h}$ can be found as

$$\begin{aligned} f_{(\hat{\mathbf{R}}_1|\mathbf{h})}(\hat{\mathbf{R}}) &= \sum_{v\in\mathcal{P}} \mathrm{P}\left(\|\mathbf{s}\|_2^2 = v\right) f_{\left(\hat{\mathbf{R}}_1|\|\mathbf{s}\|_2^2,\mathbf{h}\right)}\left(\hat{\mathbf{R}} \mid \|\mathbf{s}\|_2^2 = v, \mathbf{h}\right) \\ &= \mathrm{E}_{\|\mathbf{s}\|_2^2}\left[f_{\left(\hat{\mathbf{R}}_1|\|\mathbf{s}\|_2^2,\mathbf{h}\right)}\left(\hat{\mathbf{R}} \mid \|\mathbf{s}\|_2^2, \mathbf{h}\right)\right]. \end{aligned} \tag{5.19}$$

Analogously, the PDF of the ordered eigenvalues of the sample covariance matrix under $\mathcal{H}_1$ is

$$\begin{aligned} f_{\left(\hat{\boldsymbol{\lambda}}|\|\mathbf{h}\|_2^2\right)}(\hat{\boldsymbol{\lambda}}) &= \sum_{v\in\mathcal{P}} \mathrm{P}\left(\|\mathbf{s}\|_2^2 = v\right) f_{\left(\hat{\boldsymbol{\lambda}}|\|\mathbf{s}\|_2^2,\|\mathbf{h}\|_2^2\right)}\left(\hat{\boldsymbol{\lambda}}, \|\mathbf{s}\|_2^2 = v, \|\mathbf{h}\|_2^2\right) \\ &= \mathrm{E}_{\|\mathbf{s}\|_2^2}\left[f_{\left(\hat{\boldsymbol{\lambda}}|\|\mathbf{s}\|_2^2,\|\mathbf{h}\|_2^2\right)}\left(\hat{\boldsymbol{\lambda}} \mid \|\mathbf{s}\|_2^2, \|\mathbf{h}\|_2^2\right)\right]. \end{aligned} \tag{5.20}$$

Obviously, for large numbers of samples N the number of elements $|\mathcal{P}|$ in the set possible norms of the sequence $\mathbf{s}$ becomes huge. Hence, even if the PMF of $\|\mathbf{s}\|_2^2$ was known, explicit calculation of $f_{\hat{\mathbf{R}}_1}$ and $f_{\hat{\boldsymbol{\lambda}}}$ becomes intractable. However, we may use the (strong) law of large numbers [33, p. 235, Th. 5.5.9] to obtain a reasonable approximation. Since $s(t)$ is i.i.d. over for each t, the same holds also for $|s(t)|^2$. It is also directly evident that $\mathrm{E}\left[|s(t)|^2\right] < \infty$, since the PU sends with a limited transmission power. Thus, for large N the probability to observe a sequence, where $\|\mathbf{s}\|_2^2$ deviates a large amount from $\mathrm{E}\left[\|\mathbf{s}\|_2^2\right]$ is very small and we may approximate the two PDFs from (5.19) and (5.20) as

$$f_{(\hat{\mathbf{R}}_1|\mathbf{h})}(\hat{\mathbf{R}}) \approx f_{\left(\hat{\mathbf{R}}_1|\|\mathbf{s}\|_2^2,\mathbf{h}\right)}\left(\hat{\mathbf{R}} \mid \mathrm{E}\left[\|\mathbf{s}\|_2^2\right], \mathbf{h}\right) \tag{5.21}$$

and

$$f_{\left(\hat{\boldsymbol{\lambda}}|\|\mathbf{h}\|_2^2\right)}(\hat{\boldsymbol{\lambda}}) \approx f_{\left(\hat{\boldsymbol{\lambda}}|\|\mathbf{s}\|_2^2,\|\mathbf{h}\|_2^2\right)}\left(\hat{\boldsymbol{\lambda}} \mid \mathrm{E}\left[\|\mathbf{s}\|_2^2\right], \|\mathbf{h}\|_2^2\right), \tag{5.22}$$

respectively.

The latter PDF may be further simplified by noting that

$$\mathrm{E}\left[\|\mathbf{s}\|_2^2\right] = \mathrm{E}\left[\sum_{i=1}^{N} |s(i)|^2\right] = N\,\mathrm{E}[|s(t)|^2] = N\sigma_s^2. \tag{5.23}$$

Using the definition of the average SNR from (4.10) and (5.23), we may substitute the term

$$\mathrm{E}\left[\|\mathbf{s}\|_2^2\right] \|\mathbf{h}\|_2^2 = \alpha K N \tag{5.24}$$

in (5.22) to obtain a formulation that is solely dependent on system parameters and the average SNR. Thus, to analyze test statistics that are not functions of the sample covariance matrix itself but only of its eigenvalues, we may approximate the distribution of $\left(\hat{\mathbf{R}}_1 \mid \mathbf{h}\right)$ using a $\mathcal{CW}_K(N, \mathbf{I}_K, \alpha \mathbf{1}_{K\times K})$ distribution, cf. (5.6), (5.7) and (5.12). Note, that the approximation is exact for PSK modulations, since $|\mathcal{P}| = 1$ and $\mathrm{P}(\|\mathbf{s}\|_2^2 = N\sigma_s^2) = 1$.

As a result, knowledge of the channel realization becomes superfluous for the approximated joint ordered eigenvalue PDF from (5.22) and instead it becomes a function of the average SNR instead. This result is useful for the theoretical analysis of eigenvalue-based spectrum sensing algorithms.

5.3.2 Test Statistic PDF under Hypothesis $\mathcal{H}_0$

The CDF of the SCN of several types of Wishart matrices was studied in [125] and a convenient representation was given, where only a single integration is left to perform. For the overwhelming majority of cases this integral cannot be solved and must be evaluated numerically. However, especially for the uncorrelated noncentral Wishart case, the functions involved are increasingly difficult to evaluate numerically for large numbers of samples N.

For a precise first comparison of quickest eigenvalue-based spectrum sensing and classical eigenvalue-based spectrum sensing, exact PDFs of the test statistics are desired to rule out numerical uncertainties of the results. By confining the number of SUs to $K = 2$, the sample covariance matrices are distributed according to $\hat{\mathbf{R}}_0 \sim \mathcal{CW}_2(N, \mathbf{I}_2)$ and $\hat{\mathbf{R}}_1 \sim \mathcal{CW}_2(N, \mathbf{I}_2, \alpha\, N\, \mathbf{1}_{2\times 2})$, respectively. It turns out, that for this simplification the PDFs of the test statistic can be found exactly under both hypotheses. Hence, we have investigated this scenario in more detail, so that for the following $K = 2$ is assumed. Note also, that since we are only considering the MME as test statistic in this chapter, we denote it by T instead of T_{MME} to increase readability.

The PDF of the test statistic for $K = 2$ under $\mathcal{H}_0$ was also given in [125], however, a more concise formulation without finite sums can be found in [62]:

$$\begin{aligned} f_0(T) &= \frac{\Gamma(2N)}{\Gamma(N)\Gamma(N-1)} \left(1 - \frac{1}{T}\right)^2 \left(\frac{1}{T}\right)^N \left(1 + \frac{1}{T}\right)^{-2N} \\ &= \frac{(N-1)\Gamma(2N)}{[\Gamma(N)]^2} \frac{(T-1)^2\, T^{(N-2)}}{(T+1)^{2N}}, \end{aligned} \tag{5.25}$$

which is valid for $T \geq 1$ and zero otherwise.

5.3.3 Derivation of the Test Statistic PDF under Hypothesis $\mathcal{H}_1$

To develop the PDF of the test statistic for $K = 2$ under hypothesis $\mathcal{H}_1$, we generalize a result given in [126]. For $K = N = 2$ a version of the PDF was given there, which was studied in a multiple-input and multiple-output (MIMO) beamforming context. We generalize this result to the case of $K = 2$ and arbitrary N.

Let $\boldsymbol{\omega} = (\omega_1, \omega_2)^{\mathrm{T}}$ denote the vector of ordered eigenvalues of the non-centrality matrix $\boldsymbol{\Omega}$. Then, we can find the joint PDF of the ordered eigenvalues of $\hat{\mathbf{R}}_1$ with Table 3.1 and (3.39):

$$\begin{aligned} f_{\hat{\boldsymbol{\lambda}}}(\hat{\boldsymbol{\lambda}}) &= c_{\mathrm{UN}} \left|\boldsymbol{\mathcal{V}}_{\mathbf{1}}(\hat{\boldsymbol{\lambda}})\right| \left|\mathbf{F}(\hat{\boldsymbol{\lambda}}; \boldsymbol{\omega})\right| \prod_{i=1}^{2} \xi(\hat{\lambda}_i) \\ &= \frac{e^{-(\omega_1+\omega_2)}}{[(N-2)!]^2\,(\omega_2-\omega_1)} e^{-(\hat{\lambda}_1+\hat{\lambda}_2)}\,(\hat{\lambda}_2-\hat{\lambda}_1)\,(\hat{\lambda}_1\hat{\lambda}_2)^{(N-2)} \left|\mathbf{F}(\hat{\boldsymbol{\lambda}}; \boldsymbol{\omega})\right| , \end{aligned} \tag{5.26}$$

where $\left|\boldsymbol{\mathcal{V}}_{\mathbf{1}}(\hat{\boldsymbol{\lambda}})\right|$ is the determinant of a Vandermonde matrix built from $\hat{\boldsymbol{\lambda}}$, $\left|\mathbf{F}(\hat{\boldsymbol{\lambda}}; \boldsymbol{\omega})\right|$ is the determinant of a 2×2 matrix, where the entry of the i-th row and j-th column can be expressed with standard generalized hypergeometric functions ${}_0\mathcal{F}_1(N-1; \hat{\lambda}_{(3-j)}\omega_{(3-i)})$ (see (2.29)), $\xi(\hat{\lambda}_i) = \hat{\lambda}_i^{(N-2)}\, e^{-\hat{\lambda}_i}$ and

$$c_{\mathrm{UN}} = \frac{e^{-(\omega_1+\omega_2)}}{[(N-2)!]^2\,(\omega_2-\omega_1)} . \tag{5.27}$$

The test statistic of the MME is the ratio of the largest and the smallest eigenvalue. Obviously, for $K = 2$ is holds that $\hat{\lambda}_2 = T\hat{\lambda}_1$, cf. (3.22). Hence, we derive the desired PDF of the test statistic by applying the following transformation:

$$\begin{aligned} f_1(T) &= \int_0^\infty \hat{\lambda}_1\, f_{\hat{\boldsymbol{\lambda}}}(T\hat{\lambda}_1, \hat{\lambda}_1)\, \mathrm{d}\hat{\lambda}_1 \\ &= c_{\mathrm{UN}} \int_0^\infty e^{-\hat{\lambda}_1(T+1)} \hat{\lambda}_1^2 (T-1)(T\hat{\lambda}_1^2)^{(N-2)} \left|\mathbf{F}((T\hat{\lambda}_1, \hat{\lambda}_1)^{\mathrm{T}}; \boldsymbol{\omega})\right| \mathrm{d}\hat{\lambda}_1 . \end{aligned} \tag{5.28}$$

Here, the determinant in (5.28) can be explicitly calculated to obtain

$$\begin{aligned} \left|\mathbf{F}((T\hat{\lambda}_1, \hat{\lambda}_1)^{\mathrm{T}}; \boldsymbol{\omega})\right| &= {}_0\mathcal{F}_1(N-1; T\hat{\lambda}_1\omega_2)\, {}_0\mathcal{F}_1(N-1; \hat{\lambda}_1\omega_1) \\ &\quad - {}_0\mathcal{F}_1(N-1; T\hat{\lambda}_1\omega_1)\, {}_0\mathcal{F}_1(N-1; \hat{\lambda}_1\omega_2) . \end{aligned} \tag{5.29}$$

Inserting the result from (5.29) into (5.28) yields:

$$f_1(T) = c_{\mathrm{UN}}(T-1)T^{(K-2)} \int_0^\infty e^{-\hat{\lambda}_1(T+1)} \hat{\lambda}_1^{(2K-2)} \\ {}_0\mathcal{F}_1(N-1; T\hat{\lambda}_1\omega_2)\, {}_0\mathcal{F}_1(N-1; \hat{\lambda}_1\omega_1) \\ - {}_0\mathcal{F}_1(N-1; T\hat{\lambda}_1\omega_1)\, {}_0\mathcal{F}_1(N-1; \hat{\lambda}_1\omega_2)\, \mathrm{d}\hat{\lambda}_1 \,. \quad (5.30)$$

Since the integral in (5.30) does not seem to posses a closed-form antiderivative, we aim at deriving a series expansion which can be well approximated. This was similarly done in [126] to obtain the version of the PDF for $K = N = 2$. The hypergeometric function ${}_0\mathcal{F}_1(a+1; v)$ can also be written in terms of the a-th order modified Bessel function of the first kind $\mathcal{I}_a(v)$ [31, p. 377, Eq. (9.6.47)]:

$${}_0\mathcal{F}_1(a+1; v) = a!\, v^{-\left(\frac{a}{2}\right)}\, \mathcal{I}_a(2\sqrt{v}) \,. \quad (5.31)$$

Inserting (5.29) into (5.28), using (5.31) and simplifying gives:

$$f_1(T) = c_{\mathrm{UN}}\,[(N-2)!]^2(T-1)T^{(N-2)}(T\omega_1\omega_2)^{-\left(\frac{N-2}{2}\right)} \\ \int_0^\infty \hat{\lambda}_1^N e^{-\hat{\lambda}_1(T+1)} \Big[\mathcal{I}_{(N-2)}(2\sqrt{T\hat{\lambda}_1\omega_2})\, \mathcal{I}_{(N-2)}(2\sqrt{T\hat{\lambda}_1\omega_1}) \quad (5.32) \\ - \mathcal{I}_{(N-2)}(2\sqrt{T\hat{\lambda}_1\omega_1})\, \mathcal{I}_{(N-2)}(2\sqrt{T\hat{\lambda}_2\omega_1})\Big]\, \mathrm{d}\hat{\lambda}_1 \,.$$

Lacking an analytical solution of the integral in (5.32), we use the series expansion of the a-th order modified Bessel function of the first kind $\mathcal{I}_a(\cdot)$ [31, p. 375, Eq. (9.6.10)]:

$$\mathcal{I}_a(v) = \sum_{i=0}^{\infty} \frac{1}{i!\,\Gamma(i+a+1)} \left(\frac{v}{2}\right)^{(2i+a)} \,. \quad (5.33)$$

Substituting the Bessel functions by their series expansion from (5.33) in (5.32), using that

$$\left(\sum_{i=0}^{\infty} a_i\right)\left(\sum_{j=0}^{\infty} b_j\right) = \sum_{i=0}^{\infty}\sum_{j=0}^{\infty} a_i b_j \quad (5.34)$$

and simplifying we arrive at:

$$f_1(T) = c_{\mathrm{UN}}\,[(N-2)!]^2(T-1)T^{(N-2)} \sum_{i=0}^{\infty}\sum_{j=0}^{\infty} \frac{\left(\omega_1^j\,(T\omega_2)^i - (T\omega_1)^i\,\omega_2^j\right)}{i!\,j!\,\Gamma(i+N-1)\,\Gamma(j+N-1)} \\ \int_0^\infty \hat{\lambda}_1^{(i+j+2N-2)} e^{-\hat{\lambda}_1(T+1)}\, \mathrm{d}\hat{\lambda}_1 \,. \quad (5.35)$$

The remaining definite integral can be found explicitly [32, p. 340, Eq. (3.351.3)], where we have additionally used the relation from (2.24), as:

$$\int_0^\infty v^b \, e^{-av} \, \mathrm{d}v = \frac{b!}{a^{(b+1)}} = \frac{\Gamma(b+1)}{a^{(b+1)}} \, . \tag{5.36}$$

Utilizing this result and relation (2.24) again, we obtain $f_1(T)$ for $\omega_1 \neq \omega_2$:

$$f_1(T) = \frac{e^{-(\omega_1+\omega_2)} \, (T-1) T^{(N-2)}}{(\omega_2 - \omega_1)} \sum_{i=0}^{\infty} \sum_{j=0}^{\infty} \frac{\Gamma(i+j+2N-1) \, T^i \left(\omega_1^j \omega_2^i - \omega_1^i \omega_2^j \right)}{\Gamma(i+1) \, \Gamma(j+1) \, \Gamma(i+N-1) \, \Gamma(j+N-1) (T+1)^{(i+j+2N-1)}} \, , \tag{5.37}$$

which is valid for $T \geq 1$ and zero otherwise. Note, that this formulation is more general than needed, since the eigenvalue vector $\boldsymbol{\omega}$ is known under the system model here.

The non-centrality matrix $\boldsymbol{\Omega}$ for our system model has rank one. Hence, its eigenvalues were found explicitly in (5.7) as $\omega_2 = 2\alpha N$ and $\omega_1 = 0$. Inserting these values into (5.37) and using the convention $0^0 = 1$, we see that $(2\alpha N)^i 0^j = 0 \;\; \forall \, j \neq 0$ and analogously $(2\alpha N)^j 0^i = 0 \;\; \forall \, i \neq 0$. Writing both the minuend and the subtrahend as individual sums and incorporating the symmetry with respect to the summation variable, we can merge both terms into a single sum. This results in the desired PDF of the test statistic T under hypothesis $\mathcal{H}_1$:

$$f_1(T) = \frac{(T-1) T^{(N-2)}}{e^{(2\alpha N)}} \sum_{i=0}^{\infty} \frac{(T^i - 1) \, \Gamma(i+2N-1) \, (2\alpha N)^{(i-1)}}{\Gamma(i+1) \, \Gamma(i+N-1) \, \Gamma(N-1) \, (T+1)^{(i+2N-1)}} \, , \tag{5.38}$$

which is valid for $T \geq 1$ and zero otherwise. Note, that this formulation depends on the SNR α directly.

For vanishing SNR, the PDF $f_0(T)$ must be a special case of $f_1(T)$. Examining (5.38) in the limit for $\alpha \to 0$, the only non-zero term of the sum is for $i = 1$ and thus:

$$\lim_{\alpha \to 0} f_1(T) = \frac{(N-1)\Gamma(2N)}{[\Gamma(N)]^2} \, \frac{(T-1)^2 \, T^{(N-2)}}{(T+1)^{2N}} = f_0(T) \, . \tag{5.39}$$

In Figure 5.3 the PDFs $f_0(T)$ and $f_1(T)$ are depicted for two choices of N, the latter PDF is shown for different values of the SNR α. Note, that for large values of N, such as the choices in Figure 5.3, evaluation of the PDFs is difficult. Section 5.3.4 discusses techniques to circumvent numerical problems and derives representations of both $f_0(T)$ and $f_1(T)$, which were used for numerical evaluation of these functions in this chapter. Further below, Figure 5.4 shows the left part of Figure 5.3 in more detail and also depicts empirical PDFs obtained by Monte Carlo simulation as a verification of the theoretical results.

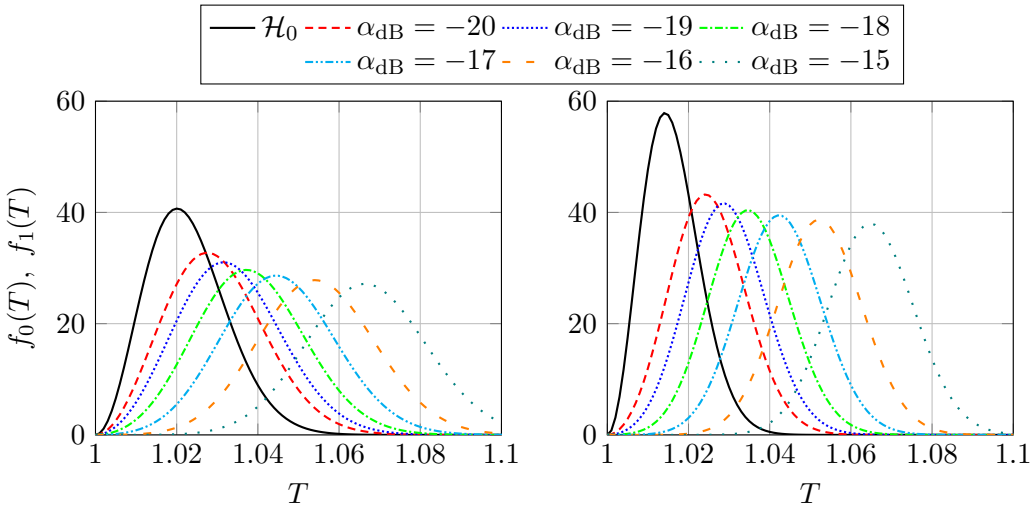

Figure 5.3: Plot of $f_0(T)$ and $f_1(T)$ for different values of the SNR α_{dB} in [dB]. *Left:* $N = 10000$. *Right:* $N = 20000$.

5.3.4 Techniques for Numerical Evaluation of the PDFs for Large N

Particularly for large numbers of samples N, which are necessary in very low SNR spectrum sensing, numerical evaluation of $f_0(T)$ and $f_1(T)$ is challenging. The values encountered during calculation quickly exceed the range of the (64 bit) IEEE 754 double precision floating point format (also called binary64) [127], that is most typically used in numerical computing software like `MATLAB` [128]. Moreover, since $f_1(T)$ involves an infinite sum it must be approximated. Using arbitrary-precision arithmetic as a remedy for these hardships is not an option due to unacceptably long computation time. We present versions of both PDFs in this section, that we have evaluated successfully for large K during our investigations.

Evaluation of the $\mathcal{H}_0$ PDF for Large N

The goal is to increase the numerical range by performing the numerically critical calculations in the logarithmic space. There, we make use of the log-gamma function $\log(\Gamma(v))$. In `MATLAB` [128], which we used for numerical evaluation, an implementation of the log-gamma function is built-in under the function name `gammaln`.

By reformulating $f_0(T)$ from (5.25), such that the problematic parts of the computation are executed in the logarithmic space with the help of the log-gamma

function, the following formulation is gained:

$$f_0(T) = (N-1)\,(T-1)^2 \exp\Big((N-2)\,\log(T) - 2N\log(T+1) + \log(\Gamma(2N)) - 2\log(\Gamma(N))\Big)\,. \tag{5.40}$$

With this representation, we were able to evaluate $f_0(T)$ for $N > 100000$, which is not possible with a direct implementation of (5.25).

Evaluation of the $\mathcal{H}_1$ PDF for Large N

In addition to gamma functions and powers with large exponent, $f_1(T)$ contains an infinite sum. Hence, it can only be evaluated approximately, which we do by stopping the computation after a finite number of summands (I_s). Similarly to the approach for $f_0(T)$, we reformulate $f_1(T)$ from (5.38) such that log-gamma functions can be utilized:

$$f_1(T) \approx (T-1)\sum_{i=0}^{I_s} \exp(\varsigma_i + i\log(T)) - \exp(\varsigma_i), \tag{5.41}$$

where

$$\varsigma_i = \log(\Gamma(i+2N-1)) - \log(\Gamma(i+1)) - (2\alpha N) - \log(\Gamma(N-1)) + (N-2)\log(T) - (i+2N-1)\log(T+1) + (i-1)\log(2\alpha N)\,. \tag{5.42}$$

A special case of $f_1(T)$ for $N = 2$ was derived in [126], which also contains an infinite sum. There, a stopping criterion for choosing an appropriate number of summands (I_s) was suggested, which states that the summation may be stopped when further summands only add a negligible amount (say ≤ 0.5 %) to the summation. For the general version with arbitrary N, however, this criterion fails since the main contribution to the summation is not located in the first summands anymore.

To achieve a reasonable approximation, we used a criterion that checks whether the integral of the PDF $f_1(T)$ is sufficiently close to one. More precisely, we numerically integrate $f_1(T)$ with a trapezoidal quadrature rule with a bin width of 0.001 over the interval $[1, 10]$. If this numerically evaluated integral deviates less than 10^{-5} from one, we consider the approximation as reasonable. In Table 5.1, values for I_s are summarized that result in a reasonable approximation, when evaluating $f_1(T)$ according to (5.41). Note, that Table 5.1 was created by successively checking multiples of the current order of magnitude for I_s, i.e., 10, 20, ..., 90, 100, 200, ..., 900, 1000, 2000, ..., and picking the first value for which the criterion described above is fulfilled.

In order to verify the theoretical derivations of $f_0(T)$ and $f_1(T)$ as well as their representations for adequate numerical evaluation from (5.40) and (5.41), we performed a Monte Carlo simulation with 10^7 instances to obtain empirical estimates

	I_s for SNR α_{dB} in [dB]				
N	$\alpha_{\mathrm{dB}} = -20$	$\alpha_{\mathrm{dB}} = -15$	$\alpha_{\mathrm{dB}} = -10$	$\alpha_{\mathrm{dB}} = -5$	$\alpha_{\mathrm{dB}} = 0$
50	10	20	30	60	200
100	20	30	50	200	300
500	30	60	200	400	2000
1000	50	200	300	800	3000
5000	200	400	2000	4000	20000
10000	300	800	3000	7000	30000
50000	2000	4000	20000	40000	200000
100000	3000	7000	30000	70000	300000

Table 5.1: Upper bound of summation (I_s) to achieve a reasonable approximation of f_1 using (5.41) for different values of the number of samples N and the SNR α_{dB} in [dB].

for the PDFs using `MATLAB` [128]. There, in each instance a sample covariance matrix with $N = 10000$ samples was calculated and subsequently the MME detector was executed. The samples were generated according to the specifications of model $\mathcal{M}_{\mathrm{DM}}$ with $K = 2$ SUs, where the PU used PSK modulation with eight signaling points. From the resulting values of the test statistic, histograms were created.

Figure 5.4 depicts $f_0(T)$ and $f_1(T)$, where the latter is shown for different values of the SNR α_{dB}. Additionally, the results from the aforementioned Monte Carlo simulation are drawn as crosses. Evidently, the theoretical findings are in perfect agreement with the empirical results.

5.3.5 Exact Algorithms for the Detection of Vanishing Spectrum Opportunities

In this section, based on the results from Sections 5.3.1 to 5.3.4, we give an exact eigenvalue-based QD algorithm, which is designed to detect the hypothesis change from $\mathcal{H}_0$ to $\mathcal{H}_1$. It can be argued, that this is the more interesting of the two possible types of changes, since the detection delay directly disrupts the operation of the primary system, see Section 5.1. Here, both the ideal case when the SNR is known and the practically relevant case when the SNR is unknown are considered.

Known SNR

First, we investigate the ideal case when the SNR is known at the receiver. Obviously, this scenario is unrealistic, since knowledge of the SNR automatically implies

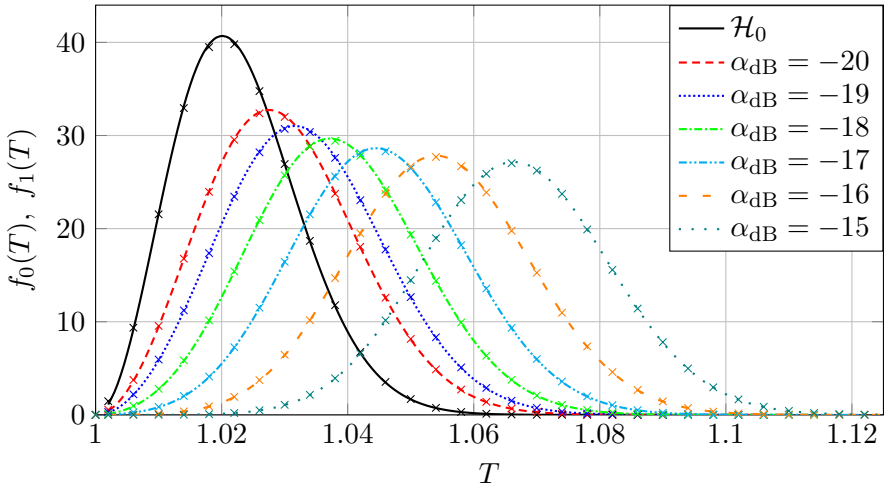

Figure 5.4: Plot of $f_0(T)$ and $f_1(T)$ for different values of the SNR α_{dB} in [dB]. The number of samples is $N = 10000$. Crosses indicate empirical values obtained from a Monte Carlo simulation.

that it is known whether a PU is present. Still, this case serves as a performance upper bound for the case of unknown SNR.

To apply the CUSUM algorithm (see (3.35)) to the detection problem at hand, the LLR must be determined. For our system model, it can be derived by inserting (5.25) and (5.37) into its definition from (3.34) and simplifying:

$$l(k) = \log\left(\frac{e^{-2\alpha N}}{(T(k)-1)}\sum_{i=0}^{\infty}\frac{(T(k)^i-1)\,(2\alpha N)^{(i-1)}\ \{2N\}_{(i-1)}}{\Gamma(i+1)\,(T(k)+1)^{(i-1)}\ \{N\}_{(i-1)}}\right). \tag{5.43}$$

There, we make use of the Pochhammer symbol, see (2.26). Note, that (5.43) can be evaluated numerically using the same techniques like the one used for the PDFs in Section 5.3.4.

Using the LLR from (5.43), the CUSUM algorithm follows as:

$$\zeta_{\mathrm{C}}(k) = [\zeta_{\mathrm{C}}(k-1) + l(k)]^{+}. \tag{5.44}$$

The application of QD using a block-wise scheme seems straightforward. However, it must be stressed that the PDFs involved in the LLR ($f_0(T)$ and $f_1(T)$) must be exactly known, which is difficult in practice. Nevertheless, we may assume that for more realistic scenarios with $K > 2$ and large numbers of samples, the PDFs may be approximated using asymptotic results from RMT. Moreover, it might seem tempting to use more complicated methods to update the covariance matrix in each block as well, e.g., by a sliding window approach. However, this is problematic since for the LLR the samples of the test statistic $T(k)$ are assumed to be i.i.d. before

and after the change. Otherwise, finding the joint distribution exploited in (5.44) might be very challenging. Also, if a change happens within a block neither $f_0(T)$ nor $f_1(T)$ are an exact model. Nonetheless, the test statistic will reflect this change, even if the model is — strictly speaking — undefined for this particular block. We limit ourselves to study the simplified case here to clarify whether it is justified to investigate more realistic models in the future.

When applying the CUSUM detector, a detection threshold h_C must be determined beforehand. For this purpose and to assess the detection performance in advance, theoretical results on the mean time to detection $\bar{\tau}_\mathrm{d}$ and mean time to false alarm $\bar{\tau}_\mathrm{fa}$ are desired, which are the main performance measures in QD (cf. Section 3.3). In general, exact calculation of $\bar{\tau}_\mathrm{d}$ and $\bar{\tau}_\mathrm{fa}$ is intractable and as an alternative bounds were studied in the literature. Particularly upper bounds on $\bar{\tau}_\mathrm{d}$ and lower bounds on $\bar{\tau}_\mathrm{fa}$ are of interest.

In [38, p. 175, Eq. (5.2.69)] an upper bound on the worst mean delay $\bar{\tau}_\mathrm{d}^\star$ can be found:

$$\bar{\tau}_\mathrm{d} \leq \bar{\tau}_\mathrm{d}^\star \leq \frac{(h_\mathrm{C} + \gamma_{f_1})}{\mathrm{E}_{f_1}\left[l(k)\right]}\,, \tag{5.45}$$

where

$$\gamma_f = \sup_{\delta>0} \mathrm{E}_f\left[l(k) - \delta \mid l(k) \geq \delta > 0\right] \tag{5.46}$$

is an upper bound on the so-called excess over the boundary. The worst mean delay $\bar{\tau}_\mathrm{d}^\star$ itself is defined in (3.32).

We consider two lower bounds on $\bar{\tau}_\mathrm{fa}$, the second of which is very elementary. First, we find from [38, p. 176, Eq. (5.2.77)]:

$$\bar{\tau}_\mathrm{fa} \geq \frac{1}{\mathrm{E}_{f_0}\left[l(k)\right]} \left(\frac{e^{-(\varphi_{f_0} h_\mathrm{C})} - 1}{\varphi_{f_0}} + h_\mathrm{C} + \gamma_{f_0} \right)\,, \tag{5.47}$$

where φ_f is the single non-zero root of

$$\mathrm{E}_f[e^{-\varphi_f\, l(k)}] = 1\,. \tag{5.48}$$

Hence, for φ_{f_0}, we must consider:

$$\mathrm{E}_{f_0}[e^{-\varphi_{f_0}\, l(k)}] = \int_1^\infty \left(\frac{f_1(T;\alpha)}{f_0(T)}\right)^{-\varphi_{f_0}} f_0(T)\,\mathrm{d}T \stackrel{!}{=} 1\,. \tag{5.49}$$

Evidently, $\varphi_{f_0} = -1$ solves (5.49), since only the integral over $f_1(T;\alpha)$ remains. We can readily simplify (5.47) to gain:

$$\bar{\tau}_\mathrm{fa} \geq \frac{1}{\mathrm{E}_{f_0}\left[l(k)\right]} \left(1 - e^{h_\mathrm{C}} + h_\mathrm{C} + \gamma_{f_0}\right)\,. \tag{5.50}$$

The second, much simpler bound is [38, p. 177, Eq. (5.2.78)]:

$$\bar{\tau}_{\mathrm{fa}} \geq e^{h_{\mathrm{C}}} \,. \tag{5.51}$$

Under the system model discussed here, neither $\mathrm{E}_{f_0}[l(k)]$ nor $\mathrm{E}_{f_1}[l(k)]$, γ_{f_0} or γ_{f_1} are tractable analytically. However, numerical evaluation is possible, see Section 5.3.7.

When evaluating the bounds stated above, it must be remembered that our QD algorithms work on the timescale of the block index k, compare Section 5.2. Thus, to translate the bounds to a sample based timescale, they must be multiplied by the number of samples N used in each block.

A performance evaluation of the CUSUM is done in Section 5.3.7.

Unknown SNR

In spectrum sensing, the SNR is unknown to the SUs since they are aspiring towards finding out whether a PU is present or not. When the SNR is unknown, the CUSUM algorithm cannot be used anymore. Instead, a generalization of the CUSUM, the so-called GLR algorithm, may be applied in this case, see Section 3.3.

Here, the single unknown parameter in the test statistic PDF under $\mathcal{H}_1$ is the SNR α. So far, we have not explicitly incorporated this dependency in our notation. However, in the following we emphasize this dependency by writing $f_1(T;\alpha)$ instead of $f_1(T)$ and similarly $l(k;\alpha)$ instead of $l(k)$ for the LLR.

Utilizing the GLR algorithm from (3.36) in this scenario results in the following formulation, where $\hat{\alpha}$ is the estimated SNR:

$$\zeta_{\mathrm{G}}(k) = \max_{0\leq m\leq k} \sup_{\hat{\alpha}} \sum_{i=m+1}^{k} \log\left(\frac{f_1(T(i);\hat{\alpha})}{f_0(T(i))}\right) = \max_{0\leq m\leq k} \sup_{\hat{\alpha}} \sum_{i=m+1}^{k} l(k;\hat{\alpha})\,. \tag{5.52}$$

There, the variable m is an estimate of the change time t_{c}, i.e., the block index after which the LLR showed a consistent positive trend, see also (3.36). To the best of our knowledge, the MLE for the SNR cannot given in a closed-form for $f_1(T;\alpha)$, such that we numerically evaluate the supremum in (5.52).

The GLR algorithm cannot be formulated recursively, since the SNR estimate $\hat{\alpha}$ must be recalculated for each new sample. Hence, all input samples of the algorithm must be stored. Therefore the GLR has a higher computational complexity and high memory requirements, compared to the CUSUM. Generally speaking, one tries to avoid using the GLR algorithm because of that. In our case, however, an input sample of the GLR is $T(k)$. It is based on the eigenvalues of the sample covariance matrix, which was calculated from a block of N samples. If we aim at replacing an MME block detector by our QD variant, the latter would use a fraction of the

number of samples of the former, say $\frac{1}{5}$ to $\frac{1}{100}$. Compared to the complexity of the eigenvalue calculation and the covariance matrix estimation, the added complexity of the GLR appears in a different light. Here, the GLR only needs to store $T(k)$ and not the samples $\mathbf{y}(t)$ of the receivers. Also, it estimates the SNR and the variable m using a number of values, that is much smaller than N.

A detailed performance evaluation of the GLR algorithm, including a comparison with standard MME block detection is conducted in Section 5.3.7.

5.3.6 Exact Algorithms for the Detection of Emerging Spectrum Opportunities

This section studies an exact algorithm for the second kind of hypothesis change, i.e., $\mathcal{H}_1$ to $\mathcal{H}_0$. In this case, the detection delay manifests as secondary system inefficiency due to wasting transmission time, but the detection accuracy is crucial to prevent disruption of ongoing primary system communication, see also Section 5.1.

Known SNR

Let us first investigate the ideal case again, where the SNR is known to the SUs. Here, detecting a change from $\mathcal{H}_1$ to $\mathcal{H}_0$ corresponds to the inverse situation of Section 5.3.5. Consequently, the LLR $\tilde{l}(k)$ for this scenario follows as:

$$\tilde{l}(k) = \log\left(\frac{f_0(T(k))}{f_1(T(k))}\right) = -l(k)\,. \tag{5.53}$$

Note, that it is directly related to the LLR for the $\mathcal{H}_0$ to $\mathcal{H}_1$ change from (5.43).

Utilizing the result from (5.43), the recursively formulated CUSUM algorithm for this case directly follows as:

$$\tilde{\zeta}_{\mathrm{C}}(k) = \left[\tilde{\zeta}_{\mathrm{C}}(k-1) - l(k)\right]^{+}\,. \tag{5.54}$$

Note, that the bounds on $\bar{\tau}_{\mathrm{d}}$ and $\bar{\tau}_{\mathrm{fa}}$ from Section 5.3.5 can be readily converted to the $\mathcal{H}_1$ to $\mathcal{H}_0$ scenario by substituting $\tilde{l}(k)$ for $l(k)$ and by exchanging f_0 with f_1 and vice versa in (5.45) and (5.50), respectively. Hence, the upper bound on $\bar{\tau}_{\mathrm{d}}^{\star}$ follows as:

$$\bar{\tau}_{\mathrm{d}} \leq \bar{\tau}_{\mathrm{d}}^{\star} \leq \frac{(h_{\mathrm{C}} + \gamma_{f_0})}{-\mathrm{E}_{f_0}\left[l(k)\right]}\,, \tag{5.55}$$

where

$$\gamma_f = \sup_{\delta>0}\ \mathrm{E}_f\left[\tilde{l}(k) - \delta \mid \tilde{l}(k) \geq \delta > 0\right] \tag{5.56}$$

and

$$\bar{\tau}_{\mathrm{d}}^{\star} = \sup_{t_{\mathrm{c}} \geq 1} \operatorname{ess\,sup} \mathrm{E}_{f_0} \left[t_{\mathrm{a}} - t_{\mathrm{c}} + 1 \mid t_{\mathrm{a}} \geq t_{\mathrm{c}}, \mathcal{T}_1^{(t_{\mathrm{c}}-1)} \right] . \tag{5.57}$$

The lower bound on $\bar{\tau}_{\mathrm{fa}}$ is:

$$\bar{\tau}_{\mathrm{fa}} \geq \frac{-1}{\mathrm{E}_{f_1}\left[l(k)\right]} \left(1 - e^{h_{\mathrm{C}}} + h_{\mathrm{C}} + \gamma_{f_1} \right) . \tag{5.58}$$

The performance of this CUSUM is evaluated in Section 5.3.7.

Unknown SNR

A similar reasoning can be applied to the practical case, when the SNR is unknown. In the LLR (5.53), numerator and denominator are swapped, when compared to the LLR for the $\mathcal{H}_0$ to $\mathcal{H}_1$ scenario. Hence, the MLE for the SNR applies to the denominator and the GLR must be adapted. As a consequence, the supremum present in (5.52) must be changed to an infimum. Also, a negative sign can be factored out, such that the LLR derived in (5.43) can be reused directly. Hence, the GLR algorithm for the $\mathcal{H}_1$ to $\mathcal{H}_0$ case follows as:

$$\tilde{\zeta}_{\mathrm{G}}(k) = \max_{0 \leq m \leq k} \inf_{\hat{\alpha}} - \sum_{i=m+1}^{k} \log \left(\frac{f_1(T(i);\hat{\alpha})}{f_0(T(i))} \right) = \max_{0 \leq m \leq k} \inf_{\hat{\alpha}} - \sum_{i=m+1}^{k} l(k;\hat{\alpha}) . \quad \textbf{(5.59)}$$

A numerical evaluation of the performance of this GLR algorithm, including a comparison with classical MME block detection is carried out in Section 5.3.7.

5.3.7 Numerical Evaluation

In this section, we evaluate the algorithms from Sections 5.3.5 and 5.3.6 numerically. First, we investigate the mean time to detection $\bar{\tau}_{\mathrm{d}}$ and the mean time to false alarm $\bar{\tau}_{\mathrm{fa}}$ of the CUSUM and the GLR obtained from Monte Carlo simulations for the $\mathcal{H}_0$ to $\mathcal{H}_1$ hypothesis change. Second, we compare the performance of the GLR algorithm with a standard MME block detector. Then, the algorithms for the second type of hypothesis change ($\mathcal{H}_1$ to $\mathcal{H}_0$) are examined similarly.

To estimate the $\bar{\tau}_{\mathrm{d}}$ and the $\bar{\tau}_{\mathrm{fa}}$, a Monte Carlo simulation with 1000 instances was performed in `MATLAB` [128] for both types of hypothesis changes. In each instance the CUSUM and the GLR are executed for a total run-time of 10000 blocks. There, for every block a sample covariance matrix is calculated from N samples created according to model $\mathcal{M}_{\mathrm{DM}}$ with $K = 2$ SUs. The PU utilizes PSK modulation with eight signaling points. Moreover, both algorithms are executed twice, where the first run operates on samples created under $\mathcal{H}_0$ and the second run on samples

created under $\mathcal{H}_1$. For the detection performance this is a worst case scenario with $t_c = 1$. If the hypothesis would switch during the simulation, the algorithm might detect a longer consecutive positive drift, resulting in potentially faster detection. The supremum in (5.52) and the infimum in (5.59) were numerically determined in the range $[-20.5, -5]$ dB in 0.1 dB steps for the GLR.

Evaluation of the $\mathcal{H}_0$ to $\mathcal{H}_1$ Algorithms

The estimated $\bar{\tau}_d$ and $\bar{\tau}_{fa}$ for both the CUSUM and the GLR, which were obtained from the Monte Carlo simulation are plotted over the threshold in Figures 5.5 and 5.6, respectively. There, we denote the threshold of the CUSUM as h_C and the one of the GLR as h_G. Moreover, the corresponding theoretical bounds for the CUSUM from (5.45), (5.50) and (5.51), which were evaluated numerically, are plotted there. Note, that Figure 5.6 uses logarithmic scaling for the ordinate.

In Figure 5.5 one can see that the GLR has a lower mean time to detection $\bar{\tau}_d$ than the CUSUM when their thresholds are chosen the same. However, in Figure 5.6 we notice that for the same threshold, the GLR generates false alarms earlier than the CUSUM on average. Hence, we have visualized an exemplary choice of thresholds for both algorithms, which results in the same $\bar{\tau}_{fa}$ by the gray lines. With the help of these, it is evident that the GLR exhibits a higher $\bar{\tau}_d$ than the CUSUM on average. This is in agreement with our expectation, since the CUSUM has precise knowledge of the SNR while the GLR has to perform an estimation of it.

The GLR shows a more aggressive behavior compared to the CUSUM, see above. This is caused by the interplay of two effects, which predominantly occur for smaller run-times k. Firstly, the SNR estimation is heavily dependent on the concrete realizations of the first samples of the test statistic. Secondly, the GLR tries to determine the onset of a positive trend of the LLR when choosing m. Hence, the GLR will likely find a continuous sequence of the input samples, which fit better to the $\mathcal{H}_1$ model given by the PDF for some choice of m and $\hat{\alpha}$, than the CUSUM $\mathcal{H}_1$ model with known SNR α. Both of these effects and their interaction can be seen in Figure 5.7, where the output of the CUSUM and the GLR is shown for a particular run on the same input samples. There, also the internal variables m and $\hat{\alpha}$ of the GLR are depicted. If the SNR estimation of the GLR returns the actual SNR, i.e., $\hat{\alpha} = \alpha$, it behaves identically to the CUSUM, as can be seen by comparing (5.44) and (5.52). This can also be observed in Figure 5.7, where for larger k the estimated SNR is close to the actual value.

Comparison of the $\mathcal{H}_0$ to $\mathcal{H}_1$ Algorithms with Block Detection

Evidently, QD and block detection pursue different objectives. Hence, it is delicate to create a fair comparison between the GLR algorithm and the MME block

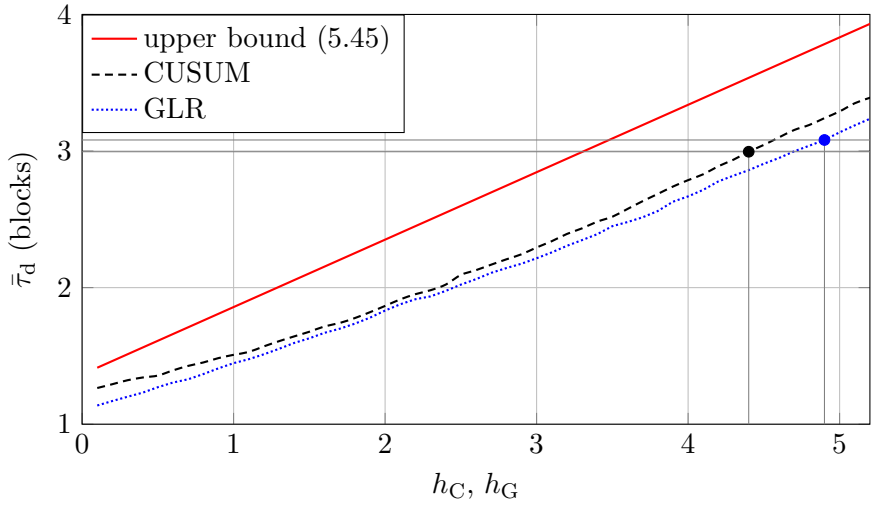

Figure 5.5: $\bar{\tau}_\mathrm{d}$ of the CUSUM and the GLR for $\mathcal{H}_0$ to $\mathcal{H}_1$ obtained from Monte Carlo simulations for $N = 10000$ and SNR $\alpha_\mathrm{dB} = -17$ dB, including the upper bound for the CUSUM from (5.45). The gray vertical lines and gray horizontal lines visualize a choice of thresholds for which both algorithms exhibit the same $\bar{\tau}_\mathrm{fa}$, cf. Figure 5.6.

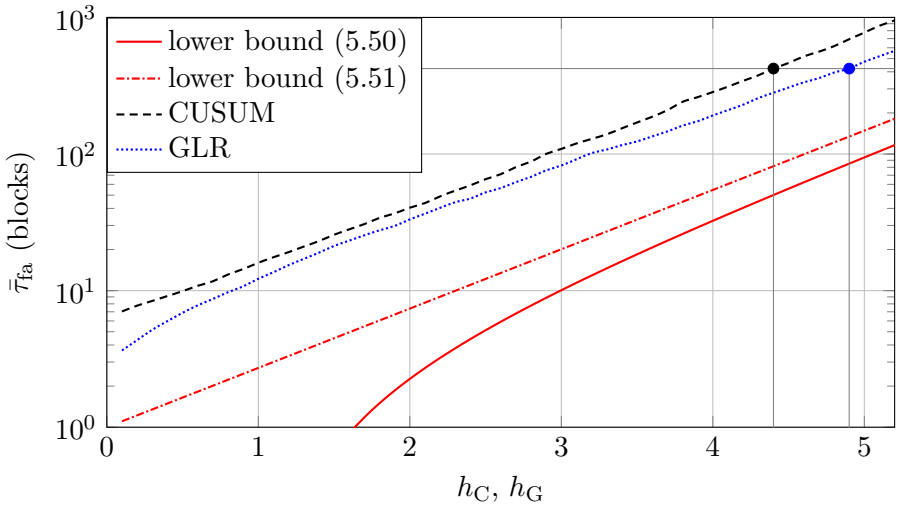

Figure 5.6: $\bar{\tau}_\mathrm{fa}$ of the CUSUM and the GLR for $\mathcal{H}_0$ to $\mathcal{H}_1$ obtained from Monte Carlo simulations for $N = 10000$ and SNR $\alpha_\mathrm{dB} = -17$ dB, including the lower bounds for the CUSUM from (5.50) and (5.51). The gray vertical lines and gray horizontal lines visualize a choice of thresholds for which both algorithms exhibit the same $\bar{\tau}_\mathrm{fa}$.

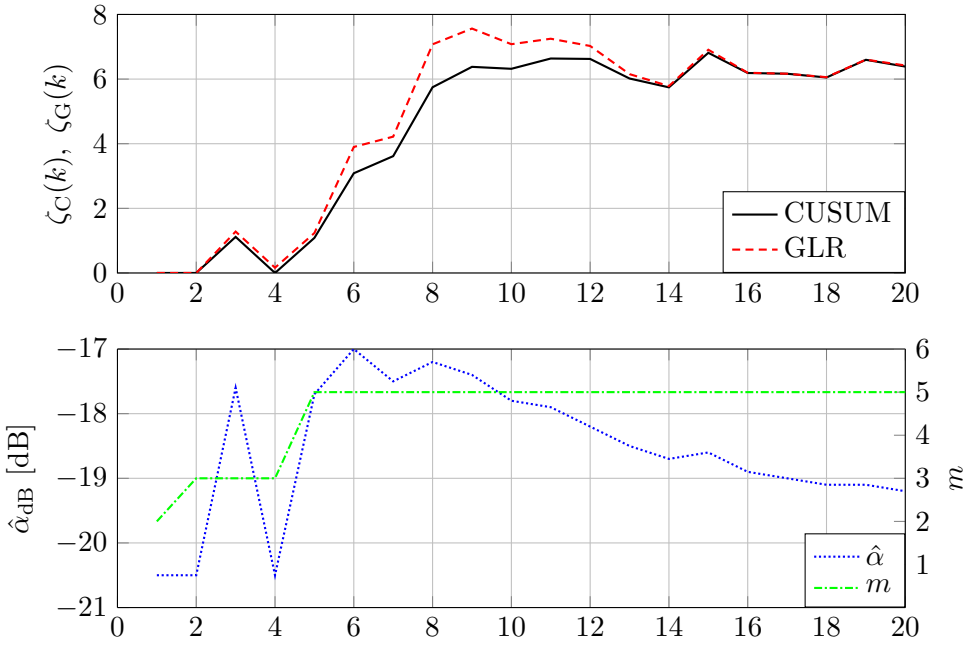

Figure 5.7: Comparison of one particular run of the CUSUM and the GLR algorithm for $\mathcal{H}_0$ to $\mathcal{H}_1$ with $N = 10000$ and SNR $\alpha_{\mathrm{dB}} = -19$ dB. The internal variables m and $\hat{\alpha}_{\mathrm{dB}}$ in [dB] of the GLR algorithm are shown in the bottom plot on separate ordinates.

detector. Here, we are mainly interested in finding out, whether the QD approach presented in Section 5.2 is feasible at all. We presume that it can reduce the detection delay in certain situations due to its ability to adapt dynamically to the difficulty of the detection task.

In the following evaluation, we compare the GLR algorithm against a MME block detector, which was designed for an exemplary operating point. Note, that using the results for the test statistic PDFs of the MME from (5.25) and (5.37), we can choose a threshold and obtain the resulting detection performance for a given SNR by numerically integrating the PDFs, cf. (3.3) and (3.5). Designing the MME detector for a block size of 10^5 samples and choosing the threshold $h = 1.0146$, results in $P_{\mathrm{FA}} = 0.015$ and $P_{\mathrm{D}} = 0.928$ for an SNR of $\alpha_{\mathrm{dB}} = -20$ dB. This serves as the reference point in the following evaluation.

A visualization of the P_{FA} and P_{D} of the GLR algorithm operating with $N = 10000$, i.e., a tenth of the block size of the block detector, at different run-times k is presented in Figure 5.8. There, the threshold $h_{\mathrm{G}} = 4.47$ of the GLR was empirically chosen to exhibit $P_{\mathrm{FA}} = 0.015$ at $k = 10$ — the false alarm rate of the block detector at its run-time. Estimating P_{D} and P_{FA} for the GLR was done by determining the fraction of the 1000 Monte Carlo instances, which at the given block index k have

correctly detected the signal under $\mathcal{H}_1$ and have raised false alarms under $\mathcal{H}_0$, respectively.

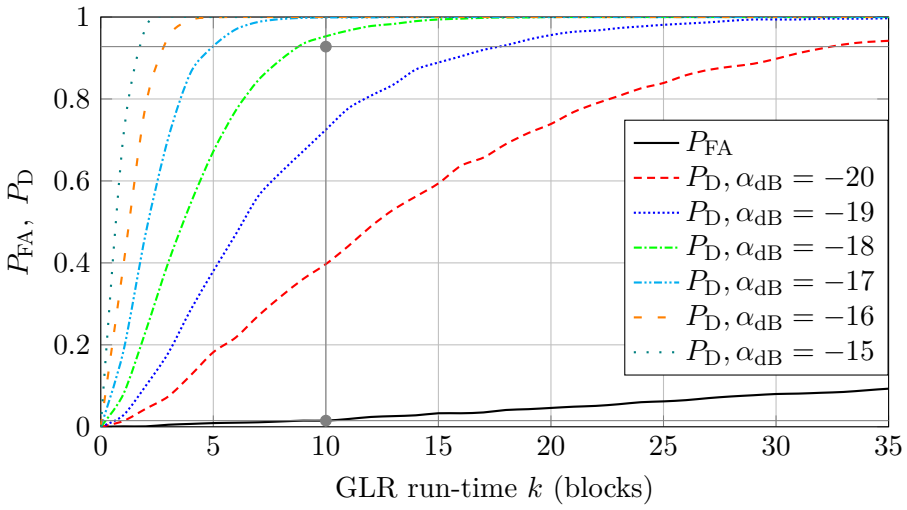

Figure 5.8: Performance of the GLR algorithm for $\mathcal{H}_0$ to $\mathcal{H}_1$ from (5.52), evaluated as P_{D} and P_{FA} over the algorithm run-time for the threshold $h_{\mathrm{G}} = 4.47$. Different SNRs in [dB] are considered for P_{D}. The gray circular markers and the thin gray lines indicate the performance of the MME block detector designed for a block length of 10^5 samples and $P_{\mathrm{FA}} = 0.015$, which results in $P_{\mathrm{D}} = 0.928$ at SNR $\alpha_{\mathrm{dB}} = -20$ dB.

One can see, that the GLR is indeed capable of detecting signals faster than the MME block detector at a lower or comparable false alarm rate, if the SNR is higher than -18 dB. For very low SNRs, however, the MME block detector seems to be faster and more reliable. This is due to the design paradigm of the block detector, which aims at robustly achieving a desired detection performance for the lowest considered SNR. Evidently, if one evaluates the detectors in practical scenarios over an interval of SNRs, say for example $[0, -20]$ dB, we see the advantages of the QD approach. For a wide range of SNRs, the GLR reliably detects with shorter delays with better or comparable false alarm performance. Hence, it may diminish the reaction time to free the channel significantly in case a PU desires to initiate a transmission. The drawback is that the GLR has to sacrifice detection performance in the very low SNR regime, where the MME block detector performs more favorably for a range of approximately 2 dB.

Naturally, this is due to the fact that the GLR algorithm does not use the entirety of samples, but rather smaller blocks to calculate the sample covariance matrices than the block detector. Thus, the choice of N is a trade-off between detection delay in the average case versus the low SNR detection performance. In Figure 5.9, this trade-off is visualized, where the P_{D} and P_{FA} of the GLR are shown for SNR

$\alpha_{\mathrm{dB}} = -20$ dB and different N. The thresholds h_{G} were chosen empirically, such that after 10^5 samples $P_{\mathrm{FA}} = 0.015$. For $N = 5000, 10000, 15000$ this results in the thresholds $h_{\mathrm{G}} = 6.15, 4.47, 4.02$, respectively.

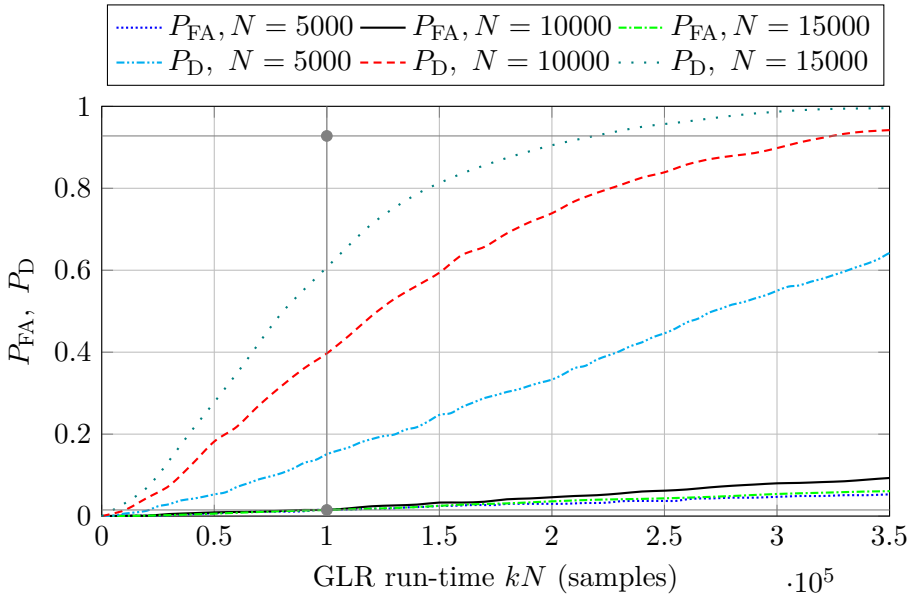

Figure 5.9: Performance of the GLR algorithm for $\mathcal{H}_0$ to $\mathcal{H}_1$ from (5.52), evaluated as P_{D} and P_{FA} over the algorithm run-time for different N and SNR $\alpha_{\mathrm{dB}} = -20$ dB for P_{D}. The gray circular markers and the thin gray lines indicate the performance of the MME block detector designed for a block length of 10^5 samples and $P_{\mathrm{FA}} = 0.015$, which results in $P_{\mathrm{D}} = 0.928$ at SNR $\alpha_{\mathrm{dB}} = -20$ dB.

The above characteristics lead to the idea of hybrid detection schemes, in which the GLR is terminated after a certain run-time — for example after 10 blocks in the above situation and a subsequent execution of a MME block detector with a block size of $10N$ to account for signals with less than -18 dB. Note, that the sample covariance matrix with $10N$ samples can be easily calculated on the basis of the sample covariance matrices $\hat{\mathbf{R}}(k)$ with $k = 1, \ldots, 10$ that are generated for the GLR. This might be an interesting approach to investigate in future work.

Evaluation of the $\mathcal{H}_1$ to $\mathcal{H}_0$ Algorithms

In Figures 5.10 and 5.11 estimations for the $\bar{\tau}_{\mathrm{d}}$ and the $\bar{\tau}_{\mathrm{fa}}$ obtained from Monte Carlo simulation for the CUSUM and the GLR for the $\mathcal{H}_1$ to $\mathcal{H}_0$ change are shown. There, also the corresponding upper and lower bounds for the CUSUM from (5.51), (5.55) and (5.58) are depicted.

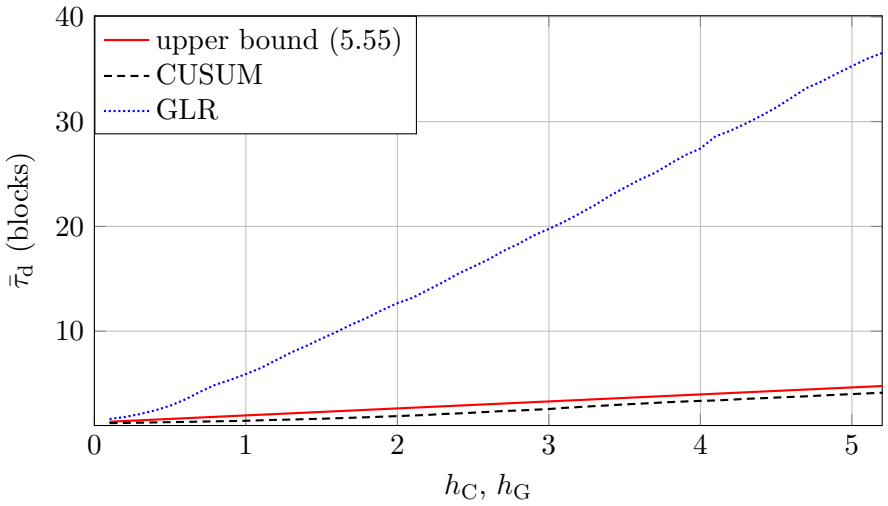

Figure 5.10: $\bar{\tau}_{\mathrm{d}}$ of the CUSUM and the GLR for $\mathcal{H}_1$ to $\mathcal{H}_0$ obtained from Monte Carlo simulations for $N = 10000$ and SNR $\alpha_{\mathrm{dB}} = -17$ dB, including the upper bound for the CUSUM from (5.55).

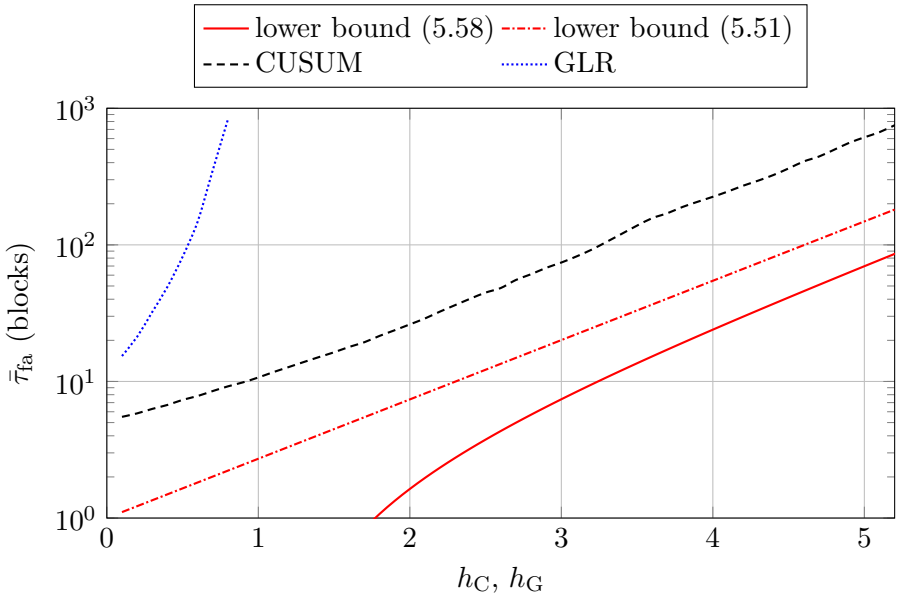

Figure 5.11: $\bar{\tau}_{\mathrm{fa}}$ of the CUSUM and the GLR for $\mathcal{H}_1$ to $\mathcal{H}_0$ obtained from Monte Carlo simulations for $N = 10000$ and SNR $\alpha_{\mathrm{dB}} = -17$ dB, including the lower bounds for the CUSUM from (5.51) and (5.58).

While the CUSUM performance looks fine, the GLR has significantly larger $\bar{\tau}_{\mathrm{d}}$ and $\bar{\tau}_{\mathrm{fa}}$ than the CUSUM. At first glance, for $\bar{\tau}_{\mathrm{fa}}$ this seems positive, but for $\bar{\tau}_{\mathrm{d}}$ this is worrying. Indeed, the performance of the GLR is unsatisfactory and we see in the following why the detection problem faced by the GLR in the $\mathcal{H}_1$ to $\mathcal{H}_0$ scenario is ill-posed.

To see this, we have plotted the LLR $\tilde{l}$ for the $\mathcal{H}_1$ to $\mathcal{H}_0$ change over the value of the test statistic T in Figure 5.12 for different values of the SNR. Note, that this figure can also be referred to for the $\mathcal{H}_0$ to $\mathcal{H}_1$ change by remembering that $l(k) = -\tilde{l}(k)$.

Consider the situation under $\mathcal{H}_0$, where only noise is received. There, the SNR estimation will most likely return the smallest possible value in the allowed interval, i.e., -20.5 dB for the parameters used in the simulation. Thus, the LLR curve with the smallest positive values is evaluated in the GLR. Hence, in contrast to the $\mathcal{H}_0$ to $\mathcal{H}_1$ case, here the $\bar{\tau}_{\mathrm{d}}$ is constant and the $\bar{\tau}_{\mathrm{fa}}$ is dependent on the SNR! As a consequence, here the false alarm performance adapts dynamically to the SNR, while the detection performance is constant.

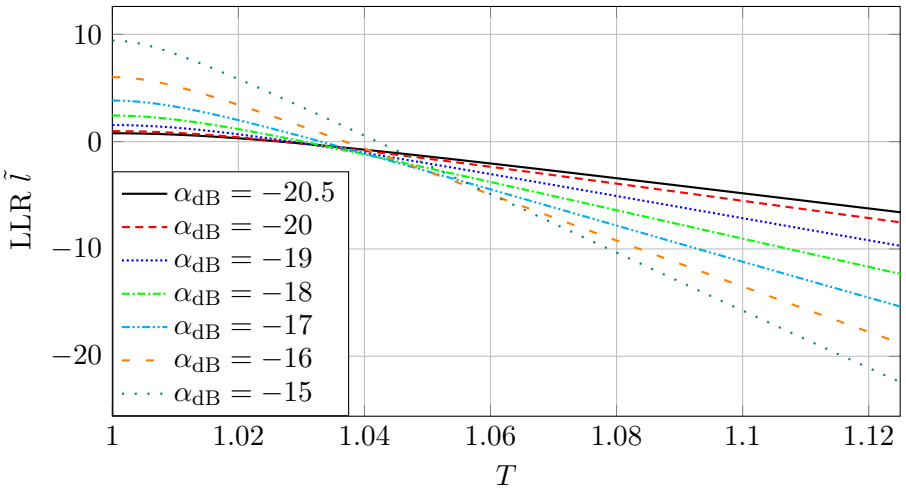

Figure 5.12: Plot of the LLR $\tilde{l}$ for $\mathcal{H}_1$ to $\mathcal{H}_0$ over T for $N = 10000$ and different values of the SNR in [dB].

Comparison of the $\mathcal{H}_1$ to $\mathcal{H}_0$ Algorithms with Block Detection

The effects described above can also be observed in Figure 5.13, where the GLR is compared to classical MME block detection. Clearly, the QD approach misses the advantages displayed in the $\mathcal{H}_0$ to $\mathcal{H}_1$ case, here. We conclude that a direct inversion of the $\mathcal{H}_0$ to $\mathcal{H}_1$ detection process does not lead to a reduction of detection delay in the $\mathcal{H}_1$ to $\mathcal{H}_0$ case. For this type of hypothesis change, the block detection paradigm seems better suited and more reliable, as was already conjectured in Section 5.1.

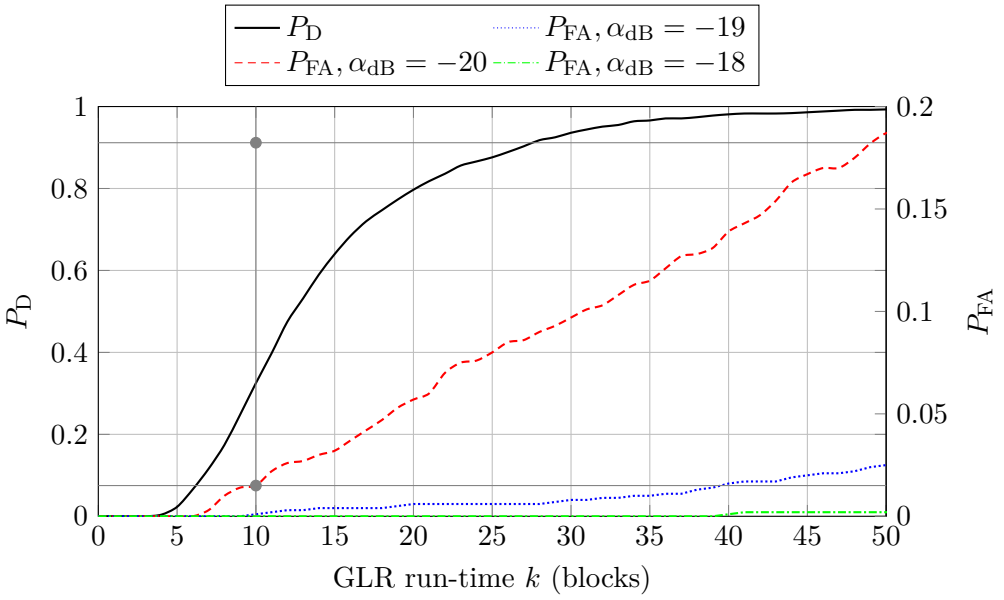

Figure 5.13: Performance of the GLR algorithm for $\mathcal{H}_1$ to $\mathcal{H}_0$ from (5.59), evaluated as P_D and P_FA over the algorithm run-time for the threshold $h_\mathrm{G} = 2.39$. Note, that P_D is plotted on the left ordinate and P_FA is plotted on the right ordinate for different SNRs α_dB in [dB]. The gray circular markers and the thin gray lines indicate the performance of the MME block detector also designed to detect the change from $\mathcal{H}_1$ to $\mathcal{H}_0$ for a block length of 10^5 samples and $P_\mathrm{FA} = 0.015$ at SNR $\alpha_\mathrm{dB} = -20$ dB, which results in $P_\mathrm{D} = 0.9117$.

5.4 Summary

In this chapter, we introduced centralized and collaborative quickest eigenvalue-based spectrum sensing. The characteristics and requirements of change detection problems in spectrum sensing were discussed. It was found, that the $\mathcal{H}_0$ to $\mathcal{H}_1$ hypothesis transition is more likely to benefit from the quickest change detection framework compared to the $\mathcal{H}_1$ to $\mathcal{H}_0$ change. Moreover, a modified time-dependent system model was introduced, which was used to develop algorithms and for comparison to eigenvalue-based block detection.

Two pairs of exact algorithms for both types of possible hypothesis changes were developed in Section 5.3 on the basis of the MME detector. For model $\mathcal{M}_\mathrm{DM}$, which considers digitally modulated signals and a flat fading wireless channel, the PDFs of the sample covariance matrices and its eigenvalues were given under both hypotheses for known signal and channel. Then, a very practical approximation for the PDFs under $\mathcal{H}_1$ for general digitally modulated signals was derived, which does not need explicit knowledge of the signal's realization. Moreover, it was shown that

the approximated joint ordered eigenvalue PDF does not require knowledge of the channel realization and is a function of the average SNR.

For the special case of $K = 2$ cooperating SUs, analytical results for the test statistic PDFs of the MME may be obtained. The PDF of the test statistic was taken from the literature under $\mathcal{H}_0$. Under $\mathcal{H}_1$, a result from literature, which is valid for $K = N = 2$, was generalized to arbitrary N to obtain the desired PDF of the test statistic. Thereby, a more general result was found, that could potentially be applied to other system models. Numerical evaluation of the test statistic PDFs is difficult for large N. In Section 5.3.4 formulations of the test statistic PDFs were derived, which can be conveniently evaluated using double precision floating point arithmetic for large N.

Based on these results, exact quickest eigenvalue-based spectrum sensing algorithms were given in Sections 5.3.5 and 5.3.6, which consider the $\mathcal{H}_0$ to $\mathcal{H}_1$ and the $\mathcal{H}_1$ to $\mathcal{H}_0$ change, respectively. There, algorithms for both the ideal case of known SNR and the practical case of unknown SNR were introduced. A numerical evaluation, including a comparison with classical MME block detection, was performed in Section 5.3.7.

For the $\mathcal{H}_0$ to $\mathcal{H}_1$ change it was found that for a wide range of SNRs the QD approach allows reducing the detection delay at similar or better false alarm rate. In the very low SNR regime, however, the block detector exhibits lower detection delay with better detection rate. Thus, the parameter N, which describes the number of samples used in each detection attempt in the GLR, constitutes a trade-off between average detection delay and the worst case performance.

In contrast to the $\mathcal{H}_0$ to $\mathcal{H}_1$ change, the QD approach was found to be inferior to block detection under the $\mathcal{H}_1$ to $\mathcal{H}_0$ change. However, in Section 5.1, where the two types of change detection problems were discussed more generally, it was already conjectured that the $\mathcal{H}_0$ to $\mathcal{H}_1$ change is the more promising candidate to benefit from QD.

For practical application of the algorithms, a generalization to allow cooperation of K SUs under more realistic wireless channels is desired. Moreover, it was argued that a hybrid detection strategy combining the strengths of QD and block detection may be worth investigating in future research.

6 Robust Eigenvalue-Based Detection and Performance Limits

This chapter studies the robustness and the performance limits of cooperative eigenvalue-based spectrum sensing systems in the presence of model uncertainties. So far, little is known in this regard. There exists an SNR threshold for detection (see (3.55)), which depends on both the number of SUs K and the number of samples N. However, it is still unclear whether an SNR wall phenomenon exists, cf. Section 3.5, which is an SNR threshold that may not be overcome by increasing the number of samples.

We consider two model uncertainties a cooperative eigenvalue-based spectrum sensing system faces in practical scenarios. Firstly, we thoroughly investigate the performance degradations caused by an imperfect calibration of the SUs noise powers in Section 6.1. Secondly, we briefly study the performance limits in the presence of colored and correlated noise in Section 6.2.

Parts of this chapter have been published in [28–30].

6.1 Imperfect Noise Power Calibration

In this section, we analyze the effect of uncertainties in the noise power calibration on a cooperative spectrum sensing system and quantify the performance limits of three well-known detectors: MME, GLRT and QST, which were introduced in Section 3.2. Parts of this section have been published in [28].

Eigenvalue-based detectors are commonly thought to be immune to the noise uncertainty problem in the literature, see [17, 18] for example. Indeed, if a single SU (exploiting time correlation) is concerned, the noise power may be factored out in both numerator and denominator and thus it cancels out in the ratio for the detectors (3.22), (3.24) and (3.25), see Section 3.2.

For a cooperative system, knowledge of the noise powers is not needed if and only if the noise powers of the receivers are *exactly* the same. Otherwise, a calibration step must be performed to scale the noise powers of the receivers to a common level to be able to set the detection threshold. Assuming this calibration step to be perfect is unrealistic and can be refuted by the same reasoning that states a noise power uncertainty must be considered in the first place, see Section 3.5.

Particularly problematic is the fact that the SUs may reside in different geographical locations with diverse environmental characteristics like temperature, humidity and electromagnetic interference that influence the noise powers of the receivers.

Measuring the receiver noise power — or the noise distribution / process for that matter — is a challenging problem in spectrum sensing. Most critical is the fact that a receiver can never be sure whether the target band is truly free at a given point in time. This, however, is a necessary prerequisite for accurate measurement of the receiver noise characteristics. A practical approach is therefore to disconnect the antenna from the rest of the receiver circuitry to obtain the desired measurements. Obviously, since the receiver circuit is altered by this routine also the noise power may change slightly. Moreover, it is still not guaranteed that the receiver only records noise, since parts of the PU signal might still be picked up through electromagnetic interference in a non-perfectly shielded receiver. Additionally, the calibration time cannot be chosen arbitrarily long, which constrains the estimation accuracy. Furthermore, calibration must be repeated periodically to adapt to changes caused by the environment, e.g., through temperature fluctuations.

A simplified version of a suitable calibration process can be described as follows. Let us assume an estimated version of the statistical covariance matrix of the receiver noise is available, denoted by $\hat{\mathbf{\Sigma}}$. If the noise process is mutually independent from other users (which is a reasonable simplification here), this matrix is diagonal and can be estimated by performing a noise power measurement at each receiver. Then the fusion center may scale the noise power of each receiver to the nominal value $\sigma_w^2 = 1$ by calculating

$$\mathbf{Y}_{\text{calib}} = \hat{\mathbf{\Sigma}}^{-\frac{1}{2}} \mathbf{Y} \,. \tag{6.1}$$

It is evident that estimation errors cause the calibrated noise power to deviate from the desired nominal value.

To investigate the influence of a mismatch in the noise power calibration of a cooperative eigenvalue-based spectrum sensing system we assume that model $\mathcal{M}_{\text{FF}}$ without exploiting time correlation and without oversampling ($Q = M = 1$) from Section 4.2 is exact for the channel and the PU signal. The noise is modeled having uncertainty with respect to the noise power after calibration of the receivers. For this, the noise distribution is not fixed but is assumed to belong to a set, i.e., $W \in \mathbb{W}$, where $\mathbb{W}$ contains all (K-dimensional) zero mean complex circularly symmetric Gaussian distributions with diagonal covariance matrix $\mathbf{\Sigma} = \text{diag}(\sigma_{w_1}^2, \ldots, \sigma_{w_K}^2)$. There, the noise power $\sigma_{w_i}^2$ of a SU $i = 1, \ldots, K$ is not known exactly or rather deviates from the nominal value. This models the remaining uncertainty about the noise powers after imperfect calibration and its influence on the detectors is quantified in the remainder of this section. Said calibration mismatch has an influence on the detectors, as can be readily seen by the statistical covariance matrix under $\mathcal{H}_0$, which is now $\mathbf{R}_0 = \mathbf{\Sigma}$ compared to a scaled identity matrix in the ideal case.

As discussed in Section 3.5, non-robustness of a detector can be investigated using (3.52). In this chapter, we perform an isolated analysis of uncertainties affecting the noise. Hence, we define the following shorthand notations relevant for our case:

$$\mathbb{T}_{\mathcal{H}_0} := \left\{ \underset{W}{\text{median}}[T \mid \mathcal{H}_0] \;\middle|\; W \in \mathbb{W} \right\}, \tag{6.2}$$

$$\mathbb{T}_{\mathcal{H}_1}(\alpha) := \left\{ \underset{W,\alpha}{\text{median}}[T \mid \mathcal{H}_1] \;\middle|\; W \in \mathbb{W}, \alpha \right\}. \tag{6.3}$$

Finding the SNR wall can be achieved by finding the largest SNR value α for which the two sets $\mathbb{T}_{\mathcal{H}_0}$ and $\mathbb{T}_{\mathcal{H}_1}(\alpha)$ overlap for all $N > 0$. Deriving a closed-form expression for $\mathbb{T}_{\mathcal{H}_0}$ and $\mathbb{T}_{\mathcal{H}_1}(\alpha)$ is very difficult in general. Hence, we only consider the asymptotic case ($N \to \infty$) in the following. As a result, the analysis simplifies considerably.

For the model considered in this chapter, $\mathbb{T}_{\mathcal{H}_0}$ and $\mathbb{T}_{\mathcal{H}_1}(\alpha)$ can be described as intervals of real numbers. Lets assume the median sets $\mathbb{T}_{\mathcal{H}_0}$ and $\mathbb{T}_{\mathcal{H}_1}(\alpha)$ overlap for some $\alpha > 0$. Also, keep in mind the definition of the hypothesis test from (3.2). Our goal is to find the value of the SNR α where the upper boundary of $\mathbb{T}_{\mathcal{H}_0}$ coincides with the lower boundary of $\mathbb{T}_{\mathcal{H}_1}(\alpha)$. Said SNR value defines the largest SNR for which the detector becomes non-robust in the asymptotic regime, cf. case b) in Figure 6.1. Consequently, we refer to this value as the SNR wall in the asymptotic regime. Note, that the interval boundaries of $\mathbb{T}_{\mathcal{H}_0}$ and $\mathbb{T}_{\mathcal{H}_1}(\alpha)$ used to find the intersection may be described also define the worst case behavior under both Hypotheses $\mathcal{H}_0$ and $\mathcal{H}_1$ for $N \to \infty$, respectively.

It must be stressed, that the SNR wall in the asymptotic regime is not necessarily the true SNR wall according to the definition from (3.51). To establish equivalence, it has to be shown that there is no larger SNR value α for which the detector is non-robust for all $0 < N < \infty$. However, most typically the separation between the test statistic PDFs f_0 and f_1 increases as N increases. Consequently, also the separation between their respective medians grows when increasing N. Thus, it is a common technique to investigate detectors in the asymptotic regime, see, e.g., [41, 48, 104].

Deriving a closed-form expression of the lower boundary of the interval $\mathbb{T}_{\mathcal{H}_1}(\alpha)$ can also be very difficult in general. However, obtaining lower and upper bounds on the lower boundary of the interval $\mathbb{T}_{\mathcal{H}_1}(\alpha)$ is often viable. Based on such results, lower and upper bounds on the SNR wall in the asymptotic regime can be constructed. This technique is depicted in Figure 6.1 by cases a) and c).

In the following sections, we investigate the performance limit of the MME, GLRT and QST detectors from (3.22), (3.24) and (3.25) under imperfect noise calibration. Lower and upper bounds on the SNR wall are derived in the asymptotic regime ($N \to \infty$) as discussed above. Three scenarios are analyzed.

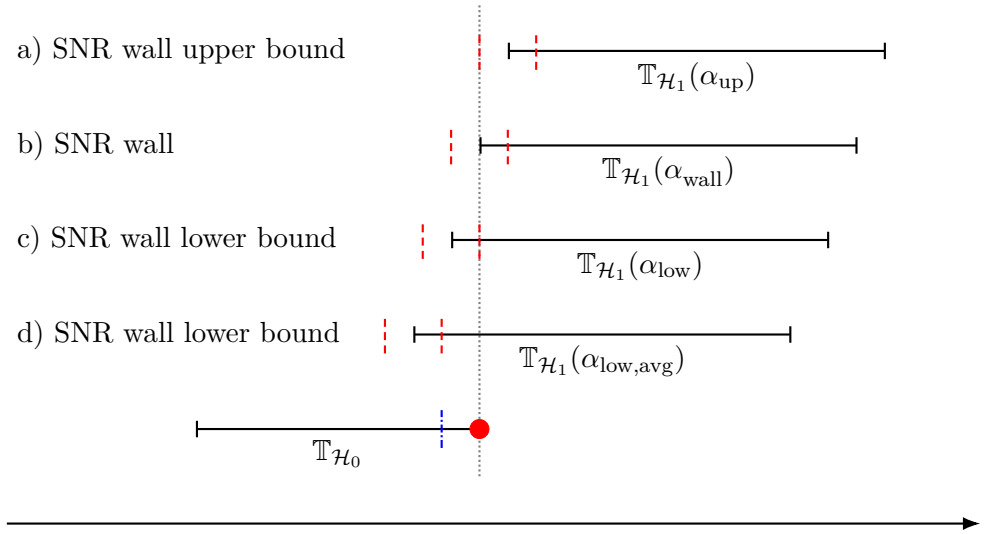

Figure 6.1: Visualization of the intersection point between the upper boundary of the interval $\mathbb{T}_{\mathcal{H}_0}$ (large dot) and the lower boundary of the interval $\mathbb{T}_{\mathcal{H}_1}(\alpha)$. Said intersection point defines the SNR wall in the asymptotic regime as seen in case b). Also depicted are lower and upper bounds (dashed lines) of the lower interval boundary of $\mathbb{T}_{\mathcal{H}_1}(\alpha)$. If these bounds are utilized to find intersections with the upper boundary of the interval $\mathbb{T}_{\mathcal{H}_0}$, upper and lower bounds on the SNR wall in the asymptotic regime are obtained. This is shown in cases a) and c), respectively. Note, that as α decreases the interval $\mathbb{T}_{\mathcal{H}_1}(\alpha)$ moves to the left, i.e., it holds $\alpha_{\text{low}} \leq \alpha_{\text{wall}} \leq \alpha_{\text{up}}$. If the upper bound of the lower interval boundary of $\mathbb{T}_{\mathcal{H}_1}(\alpha)$ is intersected with an arbitrary point in the interval $\mathbb{T}_{\mathcal{H}_0}$ (dash-dotted line), another lower bound of the SNR wall in the asymptotic regime can be found, see case d). This case is used to study the difference of the performance limits between average and worst case scenarios.

First, an average case is examined, where a rectangular distribution is assigned to the noise powers after calibration in Section 6.1.1, such that they are confined to a fixed interval. Second, another average case is investigated, where a Gaussian distribution is assumed to describe the noise powers after calibration in Section 6.1.2, which more closely matches typical assumptions about the distribution of measurement errors. For both Sections 6.1.1 and 6.1.2 lower bounds on the SNR wall in the asymptotic regime for all three detectors are obtained, corresponding to case d) in Figure 6.1. A tighter lower bound for the MME and the GLRT by investigating the worst case scenario of the test statistic under $\mathcal{H}_0$ is found in Section 6.1.3, which matches case c) in Figure 6.1. Finding the worst case for imperfectly calibrated receivers under $\mathcal{H}_1$ seems to be a very involved problem. This is due to the fact that the noise covariance matrix is not a scaled identity anymore and the additiv-

ity of the eigenvalues of $\mathbf{R_x}$ and $\mathbf{R_w}$ from (4.13) is lost. However, by deriving a lower bound on the test statistic under $\mathcal{H}_1$, an upper bound on the SNR wall in the asymptotic regime is obtained for the MME and the GLRT detector in Section 6.1.4, which is visualized by case a) in Figure 6.1. The worst case analysis for the QST under $\mathcal{H}_0$ already leads to the study of complicated non-convex optimization problems. Hence, we omitted further investigations of the QST, since they would not significantly extend the findings already obtained. The results of this section are numerically evaluated in Section 6.1.5.

6.1.1 Performance Limits for Rectangular Distributed Noise Powers

As introduced in Section 3.5, when studying the performance limits of detectors under noise uncertainty, the actual noise power is often modeled to be confined to a fixed interval in the literature [41,48,104]. This aspect is reflected here, where we assume that the noise power of a SU after calibration may lie in an interval with noise uncertainty factor $\rho > 1$ under $\mathcal{H}_0$, i.e., $\sigma_{w_i}^2 \in [\rho^{-1}\sigma_w^2, \rho\sigma_w^2]$. However, we additionally assume a rectangular distribution to study an average case scenario. In contrast, the SUs are thought to be perfectly calibrated under $\mathcal{H}_1$. Such a scenario may be suitable if it is hard to estimate the true distribution, but the interval boundaries can be specified. In this case it is reasonable to model this uncertainty with the help of a rectangular distribution.

Under $\mathcal{H}_0$, consider the noise distribution $W \in \mathbb{W}$ as introduced above in Section 6.1. Additionally, the noise powers of the SUs $\sigma_{w_i}^2$, $i = 1, \ldots, K$ are assumed to be i.i.d. and to follow a rectangular distribution with support $[\rho^{-1}\sigma_w^2, \rho\sigma_w^2]$, i.e., $\sigma_{w_i}^2 \sim \mathcal{R}(\rho^{-1}\sigma_w^2, \rho\sigma_w^2)$. Note, that for all detectors under consideration here the common factor σ_w^2 cancels out in the ratio, see also Section 3.2. Hence, we assume $\sigma_w^2 = 1$ for the nominal noise power w.l.o.g. in the following to increase readability of the derivations. Thus, the support of the rectangular distributions is simply $[\rho^{-1}, \rho]$ in the remainder of this section.

By showing that the sets of means for the test statistic under both hypotheses overlap in the asymptotic regime ($N \to \infty$), we prove that there is an SNR wall and obtain a lower bound since the case under investigation does not correspond to the worst case, see Section 6.1 and case d) in Figure 6.1.

MME Detector

The test statistic of the MME detector from (3.22) is the ratio of the extreme eigenvalues. In the asymptotic regime ($N \to \infty$) these correspond to the largest and the smallest noise powers in the $K \times K$ diagonal covariance matrix $\mathbf{\Sigma}$ under the model considered here. Due to the assumptions this is equivalent to studying

the order statistic of an affinely transformed standard rectangular distribution with K samples, compare also Section 3.6.

Let $U_{(1)} \leq \cdots \leq U_{(i)} \leq \cdots \leq U_{(K)}$ denote the order statistic of an i.i.d. random sample with K samples from a standard rectangular distribution, see Sections 3.6 and 3.6.1.

Using the affine transformation $(\rho-\rho^{-1})\,U_{(i)}+\rho^{-1}$ for $i = 1, \ldots, K$, the asymptotic mean of the MME test statistic under $\mathcal{H}_0$ can be found as

$$\mathrm{E}_{\mathcal{H}_0}[T_{\mathrm{MME}}] = \mathrm{E}\left[\frac{(\rho-\rho^{-1})U_{(K)}+\rho^{-1}}{(\rho-\rho^{-1})U_{(1)}+\rho^{-1}}\right] = \mathrm{E}\left[\frac{U_{(K)}+(\rho^2-1)^{-1}}{U_{(1)}+(\rho^2-1)^{-1}}\right]. \tag{6.4}$$

To increase readability of the derivation, consider the substitution $a := (\rho^2-1)^{-1}$. It is easy to see that linearly transforming the joint PDF of the smallest and the largest order statistic, i.e., $U_{(1)}$ and $U_{(K)}$, from (3.60) by a in each argument solely changes its domain to $a \leq u < v \leq 1+a$. Thus, we can calculate the mean of T_{MME} under $\mathcal{H}_0$ by solving the following integral, where the order of integration cannot be interchanged without also changing the integration limits:

$$\begin{aligned}
\mathrm{E}\left[\frac{U_{(K)}+a}{U_{(1)}+a}\right] &= \int_{u=a}^{1+a}\int_{v=u}^{1+a} \frac{v}{u}\, f_{(U_{(1)},U_{(K)})}(u,v)\,\mathrm{d}v\,\mathrm{d}u \\
&= K(K-1)\int_{u=a}^{1+a} u^{-1}\int_{v=u}^{1+a} v\,(v-u)^{(K-2)}\,\mathrm{d}v\,\mathrm{d}u \\
&= (K-1)(1+a)\int_{a}^{1+a}\frac{(1+a-u)^{(K-1)}}{u}\,\mathrm{d}u + \int_{a}^{1+a}(1+a-u)^{(K-1)}\,\mathrm{d}u \\
&= (K-1)(1+a)\int_{a}^{1+a}\frac{(1+a-u)^{(K-1)}}{u}\,\mathrm{d}u + \frac{1}{K}\,.
\end{aligned} \tag{6.5}$$

The remaining integral in (6.5) can be found by using the binomial theorem, solving

the resulting integrals and rearranging:

$$\begin{aligned}
&\int_a^{1+a} \frac{(1+a-u)^{(K-1)}}{u}\,\mathrm{d}u \\
&= \int_a^{1+a} \frac{1}{u} \sum_{i=0}^{N-1} \binom{K-1}{i} (1+a)^{(K-i-1)} (-u)^i \,\mathrm{d}u \\
&= \sum_{i=1}^{K-1} \binom{K-1}{i} (1+a)^{(K-i-1)} \int_a^{1+a} (-u)^{(i-1)}\,\mathrm{d}u + (1+a)^{(K-1)} \int_a^{1+a} \frac{1}{u}\,\mathrm{d}u \\
&= \sum_{i=1}^{K-1} \binom{K-1}{i} (1+a)^{(K-i-1)} (-1)^i \left(\frac{(1+a)^i}{i} - \frac{a^i}{i} \right) \\
&\quad + (1+a)^{(K-1)} \log\left(\frac{1+a}{a}\right). \qquad (6.6)
\end{aligned}$$

Inserting the result into (6.5), resubstituting a and simplifying we finally gain the desired result:

$$\mathrm{E}_{\mathcal{H}_0}[T_{\mathrm{MME}}] = \frac{(K-1)\,\rho^{2K}}{(\rho^2-1)^K} \left(\log(\rho^2) + \sum_{i=1}^{(K-1)} \binom{K-1}{i} \frac{(-1)^i}{i} (1-\rho^{-2i}) \right) + \frac{1}{K}. \qquad (\mathbf{6.7})$$

Unfortunately, (6.7) is a rather complicated expression which does not seem to possess a significantly easier formulation. As an alternative, we derive an approximation of $\mathrm{E}_{\mathcal{H}_0}[T_{\mathrm{MME}}]$ by utilizing a first order bivariate Taylor expansion.

Consider the more general multivariate function $o : \mathbb{R}^K \to \mathbb{R}$. Then the first order Taylor approximation of o about the point $\boldsymbol{\theta} = (\theta_1, \ldots, \theta_K)^{\mathrm{T}}$ is [129]:

$$o(\mathbf{v}) \approx o(\boldsymbol{\theta}) + \sum_{i=1}^{K} (v_i - \theta_i) \left. \frac{\partial\, o(\mathbf{v})}{\partial v_i} \right|_{(\mathbf{v}=\boldsymbol{\theta})}. \qquad (6.8)$$

Hence, approximating $\mathrm{E}_{\mathcal{H}_0}[T_{\mathrm{MME}}]$ about the point $(\mathrm{E}_{\mathcal{H}_0}[\lambda_K], \mathrm{E}_{\mathcal{H}_0}[\lambda_1])$ in this way yields:

$$\begin{aligned}
\mathrm{E}_{\mathcal{H}_0}[T_{\mathrm{MME}}] &= \mathrm{E}_{\mathcal{H}_0}\left[\frac{\lambda_K}{\lambda_1}\right] \\
&\approx \mathrm{E}_{\mathcal{H}_0}\left[\frac{\mathrm{E}_{\mathcal{H}_0}[\lambda_K]}{\mathrm{E}_{\mathcal{H}_0}[\lambda_1]} + \frac{\lambda_K - \mathrm{E}_{\mathcal{H}_0}[\lambda_K]}{\mathrm{E}_{\mathcal{H}_0}[\lambda_1]} - \frac{\mathrm{E}_{\mathcal{H}_0}[\lambda_K](\lambda_1 - \mathrm{E}_{\mathcal{H}_0}[\lambda_1])}{\mathrm{E}_{\mathcal{H}_0}[\lambda_1]^2}\right] \\
&= \frac{\mathrm{E}_{\mathcal{H}_0}[\lambda_K]}{\mathrm{E}_{\mathcal{H}_0}[\lambda_1]} + \frac{\overbrace{\mathrm{E}_{\mathcal{H}_0}\left[\lambda_K - \mathrm{E}_{\mathcal{H}_0}[\lambda_K]\right]}^{=0}}{\mathrm{E}_{\mathcal{H}_0}[\lambda_1]} - \frac{\mathrm{E}_{\mathcal{H}_0}[\lambda_K]\overbrace{\mathrm{E}_{\mathcal{H}_0}[\lambda_1 - \mathrm{E}_{\mathcal{H}_0}[\lambda_1]]}^{=0}}{\mathrm{E}_{\mathcal{H}_0}[\lambda_1]^2} \\
&= \frac{\mathrm{E}_{\mathcal{H}_0}[\lambda_K]}{\mathrm{E}_{\mathcal{H}_0}[\lambda_1]}. \qquad (6.9)
\end{aligned}$$

Approximating the ratio of two random variables using this approach can be problematic when the random variable in the denominator has a support including zero. Here, however, the eigenvalues have support $[\rho^{-1}, \rho]$ with $\rho > 1$.

Note, that the correlation between numerator and denominator is ignored in the approximation (6.9), since it only depends on the marginal distributions of λ_K and λ_1. Under the assumptions taken, they can be expressed again by affine transformations of the marginal distributions of the i-th order statistic $U_{(i)}$, which are beta distributed, see (3.59). That is, it holds $U_{(i)} \sim \mathrm{Beta}(i, K - i + 1)$ with mean

$$\mathrm{E}[U_{(i)}] = \frac{i}{K+1} \tag{6.10}$$

and variance

$$\mathrm{Var}[U_{(i)}] = \frac{i(K-i+1)}{(K+1)^2(K+2)}\,, \tag{6.11}$$

see also Section 3.6.

With the help of (6.9) and (6.10) as well as the affine transformation $(\rho - \rho^{-1})\,U_{(i)} + \rho^{-1}$ for $i = 1, \ldots, K$ it follows that

$$\mathrm{E}_{\mathcal{H}_0}[\lambda_i] = \mathrm{E}\left[(\rho - \rho^{-1})\,U_{(i)} + \rho^{-1}\right] = (\rho - \rho^{-1})\frac{i}{K+1} + \rho^{-1}\,. \tag{6.12}$$

Thus, the approximation of $\mathrm{E}_{\mathcal{H}_0}[T_{\mathrm{MME}}]$ follows as:

$$\begin{aligned}\mathrm{E}_{\mathcal{H}_0}[T_{\mathrm{MME}}] &\approx \frac{\mathrm{E}_{\mathcal{H}_0}[\lambda_K]}{\mathrm{E}_{\mathcal{H}_0}[\lambda_1]} = \frac{(\rho - \rho^{-1})\frac{K}{K+1} + \rho^{-1}}{(\rho - \rho^{-1})\frac{1}{K+1} + \rho^{-1}} \\ &= \frac{K\rho^2 + 1}{K + \rho}\,. \end{aligned} \tag{6.13}$$

Since the correlation between λ_1 and λ_K is ignored, it is of interest to calculate the correlation between them. With (6.10) and (6.11) as well as the joint distribution of $(U_{(1)}, U_{(K)})$ it is readily shown that the correlation coefficient between λ_1 and λ_K is

$$\begin{aligned}\mathrm{Corr}[\lambda_1, \lambda_K] &= \mathrm{Corr}[U_{(1)}, U_{(K)}] \\ &= \frac{\mathrm{E}[U_{(1)}U_{(K)}] - \mathrm{E}[U_{(1)}]\mathrm{E}[U_{(K)}]}{\sqrt{\mathrm{Var}[U_{(1)}]\mathrm{Var}[U_{(K)}]}} = \frac{1}{K}\,. \end{aligned} \tag{6.14}$$

There, we have used that

$$\begin{aligned}\mathrm{E}[U_{(1)}U_{(K)}] &= K(K-1)\int_{u=0}^{1}\int_{v=u}^{1} u\,v\,(v-u)^{(K-2)}\,\mathrm{d}v\,\mathrm{d}u \\ &= K\int_{0}^{1} u\,(1-u)^{K-1}\,\mathrm{d}u - \int_{0}^{1} u\,(1-u)^{K}\,\mathrm{d}u \\ &= \frac{1}{K+1} - \frac{1}{K+1} + \frac{1}{K+2} = \frac{1}{K+2}\,. \end{aligned} \tag{6.15}$$

Thus, we expect the approximation from (6.13) to get tighter for a larger number of cooperating users, since the correlation between λ_1 and λ_K gets smaller when K increases.

As already mentioned, under $\mathcal{H}_1$ we assume the SUs to be perfectly calibrated, that is $\sigma_{w_i}^2 = \sigma_w^2 = 1$ for $i = 1, \ldots, K$. With the asymptotic eigenvalues from (4.14) and using (4.10) we obtain

$$\mathrm{E}_{\mathcal{H}_1}[T_{\mathrm{MME}}] = \sigma_s^2\,\|\mathbf{h}\|_2^2 + 1 = K\alpha + 1\,. \tag{**6.16**}$$

In order to find the SNR wall, we seek the value of the SNR at which the means under both hypotheses start to overlap, see also Section 3.5. More precisely, we need to find the SNR for which it holds that

$$\mathrm{E}_{\mathcal{H}_0}[T_{\mathrm{MME}}] \stackrel{!}{=} \mathrm{E}_{\mathcal{H}_1}[T_{\mathrm{MME}}] \tag{6.17}$$

Since we have not considered the worst case under both hypotheses here, this value is a lower bound on the actual SNR wall. Inserting (6.16) into (6.17) and solving for α we obtain a lower bound on the SNR wall:

$$\alpha_{\mathrm{wall}}^{\mathrm{MME}} \geq \frac{\mathrm{E}_{\mathcal{H}_0}[T_{\mathrm{MME}}] - 1}{K}\,. \tag{**6.18**}$$

By numerically evaluating (6.7) and inserting the value into (6.18), a lower bound for the SNR wall can be calculated. A simple closed-form approximation for this lower bound can be found by inserting the approximation from (6.13) into (6.18) and simplifying:

$$\alpha_{\mathrm{wall}}^{\mathrm{MME}} \gtrapprox \frac{\rho^2 - 1}{K}\left(\frac{K-1}{K+\rho^2}\right)\,. \tag{**6.19**}$$

We perform a detailed numerical evaluation of these results in Section 6.1.5 and show, among other things, that the approximation (6.19) is very tight for relevant values of the parameters in spectrum sensing.

GLRT Detector

The GLRT detector relies on the ratio of the largest eigenvalue and the sum of the remaining smaller eigenvalues, see (3.24). As we have seen in the preceding analysis of the MME detector, respecting the correlation between the eigenvalues resulted in a cumbersome expression. Here, we would need to solve K ordered integrals to find the exact mean value. Hence, we expect an even less tractable derivation than the one for (6.7), so we directly turn to approximations for the GLRT. In Section 6.1.5 we later see that this approach is justified by the tightness of the approximations.

Note, that for $K = 2$ the GLRT degenerates to the MME. Hence, for the following derivations we assume $K \geq 3$.

Analogous to the approximation derived for the MME detector, we use the first order multivariate Taylor approximation from (6.8) and develop $\mathrm{E}_{\mathcal{H}_0}[T_{\mathrm{GLRT}}]$ about the point $\boldsymbol{\theta} = (\mathrm{E}_{\mathcal{H}_0}[\lambda_1], \ldots, \mathrm{E}_{\mathcal{H}_0}[\lambda_K])^{\mathrm{T}}$:

$$\begin{aligned}
\mathrm{E}_{\mathcal{H}_0}[T_{\mathrm{GLRT}}] &= \mathrm{E}_{\mathcal{H}_0}\left[\frac{\lambda_K}{\sum_{i=1}^{K-1}\lambda_i}\right] \\
&\approx \frac{\mathrm{E}_{\mathcal{H}_0}[\lambda_K]}{\sum_{i=1}^{K-1}\mathrm{E}_{\mathcal{H}_0}[\lambda_i]} + \sum_{i=1}^{K}\underbrace{\mathrm{E}_{\mathcal{H}_0}[\lambda_i - \mathrm{E}_{\mathcal{H}_0}[\lambda_i]]}_{=0}\frac{\partial\, T_{\mathrm{GLRT}}(\boldsymbol{\lambda})}{\partial\lambda_i} \\
&= \frac{\mathrm{E}_{\mathcal{H}_0}[\lambda_K]}{\sum_{i=1}^{K-1}\mathrm{E}_{\mathcal{H}_0}[\lambda_i]}\,. \qquad (6.20)
\end{aligned}$$

Again, we make use of the mean of the eigenvalues $\mathrm{E}_{\mathcal{H}_0}[\lambda_i]$ for $i = 1, \ldots, K$, which were already given in (6.12). The denominator of (6.20) can be simplified as follows:

$$\begin{aligned}
\sum_{i=1}^{K-1}\mathrm{E}_{\mathcal{H}_0}[\lambda_i] &= \sum_{i=1}^{K-1}(\rho - \rho^{-1})\frac{i}{K+1} + \rho^{-1} \\
&= \frac{\rho - \rho^{-1}}{K+1}\sum_{i=1}^{K-1} i + (K-1)\,\rho^{-1} \\
&= \frac{\rho - \rho^{-1}}{K+1}\frac{(K-1)K}{2} + (K-1)\,\rho^{-1} \\
&= (K-1)\left(\frac{1}{2}(\rho - \rho^{-1})\frac{K}{K+1} + \rho^{-1}\right)\,. \qquad (6.21)
\end{aligned}$$

Inserting this result into (6.20) we obtain the desired approximation of $\mathrm{E}_{\mathcal{H}_0}[T_{\mathrm{GLRT}}]$:

$$\mathrm{E}_{\mathcal{H}_0}[T_{\mathrm{GLRT}}] \approx \frac{\mathrm{E}_{\mathcal{H}_0}[\lambda_K]}{\sum_{i=1}^{K-1}\mathrm{E}_{\mathcal{H}_0}[\lambda_i]} = \frac{1}{K-1}\,\frac{(\rho - \rho^{-1})\frac{K}{K+1} + \rho^{-1}}{\frac{1}{2}(\rho - \rho^{-1})\frac{K}{K+1} + \rho^{-1}}\,. \qquad (\mathbf{6.22})$$

Under $\mathcal{H}_1$, where the receivers are assumed to be perfectly calibrated, the mean of the test statistic can easily be found as

$$\mathrm{E}_{\mathcal{H}_1}[T_{\mathrm{GLRT}}] = \frac{K\alpha + 1}{(K-1)}\,, \tag{**6.23**}$$

by utilizing (4.10) and (4.14).

Analogous to the derivation for the MME detector, finding the SNR for which $\mathrm{E}_{\mathcal{H}_0}[T_{\mathrm{GLRT}}]$ and $\mathrm{E}_{\mathcal{H}_1}[T_{\mathrm{GLRT}}]$ overlap results in a lower bound on the SNR wall of the GLRT:

$$\alpha_{\mathrm{wall}}^{\mathrm{GLRT}} \geq \frac{(K-1)\,\mathrm{E}_{\mathcal{H}_0}[T_{\mathrm{GLRT}}] - 1}{K}\,. \tag{**6.24**}$$

Inserting (6.22) into (6.24) yields an approximation for the lower bound in this rectangular scenario:

$$\alpha_{\mathrm{wall}}^{\mathrm{GLRT}} \gtrapprox \frac{(\rho - \rho^{-1})\frac{K}{K+1} + \rho^{-1}}{K(\frac{1}{2}(\rho - \rho^{-1})\frac{K}{K+1} + \rho^{-1})} - \frac{1}{K}\,. \tag{**6.25**}$$

Although the above result manifests itself in closed-form, it is still rather complicated and cumbersome to interpret. However, we can find an approximation that is much simpler, while still being accurate enough for the range of parameters encountered in this spectrum sensing context. The approximation can be derived in two different ways, that lead to the same result.

First, consider the sum of the means of all eigenvalues under $\mathcal{H}_0$, for which it holds:

$$\begin{aligned}\sum_{i=1}^{K} \mathrm{E}_{\mathcal{H}_0}[\lambda_i] &= \mathrm{E}_{\mathcal{H}_0}\left[\sum_{i=1}^{K} \lambda_i\right] = \mathrm{E}_{\mathcal{H}_0}[\mathrm{tr}(\mathbf{\Sigma})] \\ &= \mathrm{tr}(\mathrm{E}_{\mathcal{H}_0}[\mathbf{\Sigma}]) = \sum_{i=1}^{K} \mathrm{E}_{\mathcal{H}_0}[\sigma_{w_i}^2] = K\,\frac{\rho + \rho^{-1}}{2}\,. \end{aligned} \tag{6.26}$$

For large K, the summation over the mean of all eigenvalues except the largest one is approximately equal to the sum of the mean of the noise powers of $K-1$ SUs:

$$\sum_{i=1}^{K-1} \mathrm{E}_{\mathcal{H}_0}[\lambda_i] \approx \sum_{i=1}^{K-1} \mathrm{E}_{\mathcal{H}_0}[\sigma_{w_i}^2] \tag{6.27}$$

$$= (K-1)\,\frac{\rho + \rho^{-1}}{2}\,. \tag{6.28}$$

There, we essentially ignore the ordering of the eigenvalues, which is introduced by sorting them from smallest to largest. Thus, we have obtained an approximation of the denominator of (6.20).

Second, one can directly study the right part of (6.21) for large K, that is for $K \to \infty$:

$$\lim_{K\to\infty} \left(\frac{1}{2}(\rho - \rho^{-1}) \frac{K}{K+1} + \rho^{-1} \right) = \frac{\rho}{2} - \frac{1}{2}\rho^{-1} + \rho^{-1} = \frac{\rho + \rho^{-1}}{2} \,. \tag{6.29}$$

Hence, replacing the right part of (6.21) with the asymptotic value for $K \to \infty$, we arrive at the same approximation for the denominator of (6.20).

Applying this approximation to the result of (6.20), one finds:

$$\mathrm{E}_{\mathcal{H}_0}[T_{\mathrm{GLRT}}] \approx \frac{\mathrm{E}_{\mathcal{H}_0}[\lambda_K]}{\sum_{i=1}^{K-1} \mathrm{E}_{\mathcal{H}_0}[\lambda_i]} \approx \frac{(\rho - \rho^{-1}) \frac{K}{K+1} + \rho^{-1}}{(K-1)\,\frac{\rho+\rho^{-1}}{2}} \,. \tag{6.30}$$

While significantly simpler, we can take a further approximation step by noticing that

$$\mathrm{E}_{\mathcal{H}_0}[\sigma_{w_i}^2] = \frac{\rho + \rho^{-1}}{2} \approx 1 \,, \tag{6.31}$$

for the range of values for the noise uncertainty factor ρ that are commonly discussed in literature. On a logarithmic scale (see (3.54)), we predominantly find values in the range 0.5 dB $\leq \rho_{\mathrm{dB}} \leq$ 2 dB, cf. [17, 18, 41, 48]. In Table 6.1 typical values for ρ in both logarithmic and normal scale are shown including the resulting values for $\mathrm{E}_{\mathcal{H}_0}[\sigma_{w_i}^2] = \frac{\rho+\rho^{-1}}{2}$. Also, in Figure 6.2 the term $\frac{1}{2}(\rho - \rho^{-1})\frac{K}{K+1} + \rho^{-1}$, which was approximated by the constant one in the derivation above is depicted for different values of SUs and different noise uncertainty factors. One can see that especially for larger numbers of SUs, say $K \geq 8$, and for moderate noise uncertainty factors, say $\rho_{\mathrm{dB}} \leq 1$ dB, the approximations taken in (6.28) are reasonable.

ρ_{dB} in [dB]	ρ	$\frac{\rho+\rho^{-1}}{2}$
0.5	1.1220	1.0066
1.0	1.2589	1.0266
1.5	1.4125	1.0602
2.0	1.5849	1.1079

Table 6.1: Typical values for the noise uncertainty factor ρ_{dB} in [dB] and normal scale with resulting values for $\frac{\rho+\rho^{-1}}{2}$.

By inserting (6.31) into the approximation from (6.30), we finally obtain a much simpler approximation:

$$\begin{aligned} \mathrm{E}_{\mathcal{H}_0}[T_{\mathrm{GLRT}}] &\approx \frac{\mathrm{E}_{\mathcal{H}_0}[\lambda_K]}{\sum_{i=1}^{K-1} \mathrm{E}_{\mathcal{H}_0}[\lambda_i]} \approx \frac{(\rho - \rho^{-1}) \frac{K}{K+1} + \rho^{-1}}{(K-1)} \\ &= \frac{\rho^2 K + 1}{\rho\,(K+1)(K-1)} \,. \end{aligned} \tag{6.32}$$

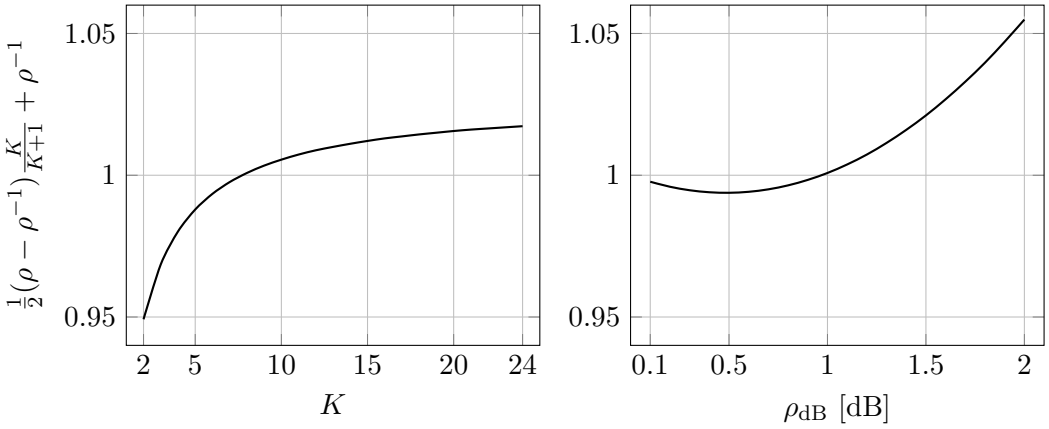

Figure 6.2: Value of the term $\frac{1}{2}(\rho-\rho^{-1})\frac{K}{K+1}+\rho^{-1}$ for different numbers of SUs and different noise uncertainty factors. *Left:* $\rho_{\mathrm{dB}} = 1$ dB. *Right:* $K = 8$.

Now, we can also use this result to find a more favorable formulation for the approximation of the lower bound on the SNR wall of the GLRT detector under this rectangular model by inserting (6.32) into (6.24) and simplifying:

$$\alpha_{\mathrm{wall}}^{\mathrm{GLRT}} \gtrapprox \frac{1}{K}\left(\frac{\rho^2 K+1}{\rho\,(K+1)}-1\right) = \frac{\rho^2 K+1}{\rho\,(K+1)K}-\frac{1}{K}\,. \tag{6.33}$$

We perform a detailed numerical comparison of the results obtained in Section 6.1.5, which includes the different approximations of $\mathrm{E}_{\mathcal{H}_0}[T_{\mathrm{GLRT}}]$ from (6.22), (6.30) and (6.32) and the approximations of the lower bound on the SNR wall of the GLRT detector from (6.25) and (6.33).

QST Detector

The QST detector can be expressed as the ratio of the ℓ_2-norm and the ℓ_1-norm of the eigenvalues, see (3.25). Although this detector was originally derived to exploit correlation over time for a single SU and was not specifically developed for the collaborative system model employed here, we nevertheless include it in this study since it shows very promising performance also in collaborative scenarios [24].

Since both numerator and denominator are functions, which operate on all eigenvalues in the same manner, no ordering of the eigenvalues must be respected. Thus, the joint PDF of the eigenvalues under $\mathcal{H}_0$ in the asymptotic regime for this scenario

is

$$f_{\boldsymbol{\lambda}}(\boldsymbol{\lambda}) = \prod_{i=1}^{K} \frac{1}{\rho - \rho^{-1}} \, \mathbb{I}_{[\rho^{-1},\rho]}(\lambda_i) = \frac{1}{(\rho - \rho^{-1})^K} \, \mathbb{I}_{[\rho^{-1},\rho]^K}(\boldsymbol{\lambda}) \, . \tag{6.34}$$

Consequently, we can find $\mathrm{E}_{\mathcal{H}_0}[T_{\mathrm{QST}}]$ by solving the following integral:

$$\mathrm{E}_{\mathcal{H}_0}[T_{\mathrm{QST}}] = \int_{-\infty}^{\infty} \cdots \int_{-\infty}^{\infty} \frac{\|\boldsymbol{\lambda}\|_2}{\|\boldsymbol{\lambda}\|_1} \, f_{\boldsymbol{\lambda}}(\boldsymbol{\lambda}) \, \mathrm{d}\lambda_1 \ldots \mathrm{d}\lambda_K = \frac{1}{(\rho - \rho^{-1})^K} \int_{\rho^{-1}}^{\rho} \cdots \int_{\rho^{-1}}^{\rho} \frac{\|\boldsymbol{\lambda}\|_2}{\|\boldsymbol{\lambda}\|_1} \, \mathrm{d}\lambda_1 \ldots \mathrm{d}\lambda_K \, . \tag{**6.35**}$$

Unfortunately, we are not aware of a closed-form solution of this integral. Instead, we have numerically evaluated (6.35) using the "cubature" multidimensional integral evaluation library from [130].

Under $\mathcal{H}_1$, where the SUs are assumed to be perfectly calibrated, utilizing the results from (4.10) and (4.14) readily gives the mean of the test statistic as

$$\mathrm{E}_{\mathcal{H}_1}[T_{\mathrm{QST}}] = \frac{\sqrt{(K\alpha + 1)^2 + K - 1}}{K(\alpha + 1)} \, . \tag{**6.36**}$$

Here, finding the SNR value for which $\mathrm{E}_{\mathcal{H}_0}[T_{\mathrm{QST}}]$ and $\mathrm{E}_{\mathcal{H}_1}[T_{\mathrm{QST}}]$ coincide — i.e., $\mathrm{E}_{\mathcal{H}_0}[T_{\mathrm{QST}}] \stackrel{!}{=} \mathrm{E}_{\mathcal{H}_1}[T_{\mathrm{QST}}]$ — leads to the following quadratic equation:

$$\alpha^2 + \alpha \, \frac{2(K \, \mathrm{E}_{\mathcal{H}_0}[T_{\mathrm{QST}}]^2 - 1)}{K \, (\mathrm{E}_{\mathcal{H}_0}[T_{\mathrm{QST}}]^2 - 1)} + \frac{K \, \mathrm{E}_{\mathcal{H}_0}[T_{\mathrm{QST}}]^2 - 1}{K \, (\mathrm{E}_{\mathcal{H}_0}[T_{\mathrm{QST}}]^2 - 1)} \stackrel{!}{=} 0 \, . \tag{6.37}$$

Solving (6.37) gives two solution candidates for the value of α, which is denoted by α_1 and α_2 in the following.

The first solution candidate α_1 can be shown to be non-negative:

$$\alpha_1 = \frac{-(\overbrace{K\mathrm{E}_{\mathcal{H}_0}[T_{\mathrm{QST}}]^2}^{\geq 1} - 1) - \sqrt{(K\mathrm{E}_{\mathcal{H}_0}[T_{\mathrm{QST}}]^2 - 1)(K-1)}}{K(\underbrace{\mathrm{E}_{\mathcal{H}_0}[T_{\mathrm{QST}}]^2}_{\leq 1} - 1)} \geq 0 \, . \tag{6.38}$$

This can be seen by recalling it holds $\frac{1}{\sqrt{K}} \leq T_{\mathrm{QST}} \leq 1$ for the test statistic of the QST, which was shown in Section 3.2.3. With the monotonicity of the mean, it follows for the mean that $\frac{1}{\sqrt{K}} \leq \mathrm{E}[T_{\mathrm{QST}}] \leq 1$. Hence, $\frac{1}{K} \leq \mathrm{E}_{\mathcal{H}_0}[T_{\mathrm{QST}}]^2 \leq 1$ and we can see that the denominator must always be non-positive. Note also, that $K \geq 2$.

Similarly, we notice that $K\mathrm{E}_{\mathcal{H}_0}[T_{\mathrm{QST}}]^2 - 1 \geq 0$. Thus, the numerator is non-positive and in total $\alpha_1 \geq 0$.

Using analogous reasoning, the second solution candidate α_2 can be shown to be non-positive:

$$\alpha_2 = \frac{-(\overbrace{K\mathrm{E}_{\mathcal{H}_0}[T_{\mathrm{QST}}]^2}^{\geq 1} - 1) + \sqrt{(K\mathrm{E}_{\mathcal{H}_0}[T_{\mathrm{QST}}]^2 - 1)(K-1)}}{K(\underbrace{\mathrm{E}_{\mathcal{H}_0}[T_{\mathrm{QST}}]^2}_{\leq 1} - 1)} \leq 0\,. \tag{6.39}$$

Notice that $K\mathrm{E}_{\mathcal{H}_0}[T_{\mathrm{QST}}]^2 - 1 \leq K - 1$ and hence it follows

$$\sqrt{(K\mathrm{E}_{\mathcal{H}_0}[T_{\mathrm{QST}}]^2 - 1)(K-1)} \geq K\mathrm{E}_{\mathcal{H}_0}[T_{\mathrm{QST}}]^2 - 1\,. \tag{6.40}$$

As a result, the numerator is non-negative. However, since we know from the definition that the SNR must be non-negative, the solution candidate α_2 is invalid.

Using α_1 as the valid solution to (6.37), we obtain the lower bound on the SNR wall

$$\alpha_{\mathrm{wall}}^{\mathrm{QST}} \geq \alpha_1 = \frac{-(K\mathrm{E}_{\mathcal{H}_0}[T_{\mathrm{QST}}]^2 - 1)}{K(\mathrm{E}_{\mathcal{H}_0}[T_{\mathrm{QST}}]^2 - 1)} + \sqrt{\frac{(K\mathrm{E}_{\mathcal{H}_0}[T_{\mathrm{QST}}]^2 - 1)(K-1)}{K^2(\mathrm{E}_{\mathcal{H}_0}[T_{\mathrm{QST}}]^2 - 1)^2}}\,. \tag{6.41}$$

Concrete values for this lower bound may be calculated by numerically evaluating (6.35), which is done in Section 6.1.5.

6.1.2 Performance Limits for Gaussian Distributed Noise Powers

The scenario from Section 6.1.1 investigates the performance limits of the detectors when the noise powers of the SUs lie within a fixed interval and follow a rectangular distribution. However, measurement errors are commonly modeled with Gaussian distributions. This section analyzes an average case scenario with a (truncated) Gaussian distribution, that more closely resembles the situation we would expect after an imperfect calibration step.

Two problems occur if we assume the noise powers after calibration to follow a Gaussian under $\mathcal{H}_0$, which manifest due to the infinitely long tails of the distribution. Firstly, there is a non-zero probability that negative eigenvalues occur. This is not possible since both the statistical and the sample covariance matrix are positive semi-definite, see also Section 3.2. Secondly, eigenvalues may theoretically become arbitrarily large, even though no signal is present. In other words, the fact that the support of the Gaussian density is the set of real numbers, contradicts characteristic properties of eigenvalue-based spectrum sensing. Nevertheless, if the

chosen Gaussian distribution fulfills some simple conditions, it still is an attractive model for the imperfect calibration process.

Consider the following model under $\mathcal{H}_0$, where the noise powers of the SUs $\sigma_{w_i}^2$, $i = 1, \ldots, K$ after calibration are i.i.d., each following a Gaussian $\mathcal{N}(\sigma_w^2, \vartheta^2)$ distribution. If the area under the Gaussian density within a certain range of standard deviations around the mean is very close to one and the left border of said interval is positive, we may neglect the fact that there is a non-zero probability that non-positive noise powers occur. Let p denote the area under the density in the interval $[\sigma_w^2 - \beta\vartheta, \sigma_w^2 + \beta\vartheta]$ with $\beta \geq 0$, compare also Figure 6.3. The factor β controls the extent of the interval around the mean and thereby the area p.

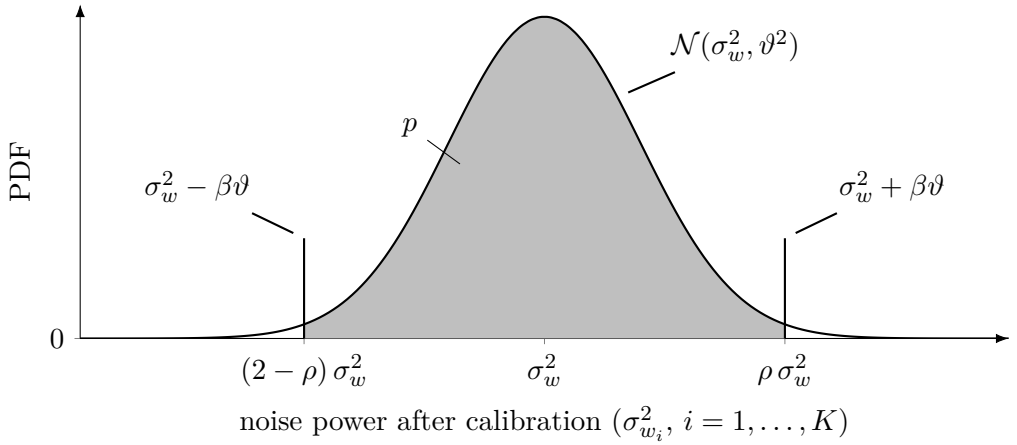

Figure 6.3: Gaussian distribution of the SU noise power after calibration with relevant parameters.

As can be seen in Figure 6.3, the left and right borders of the interval are labeled in two different ways. We describe the right border using a noise uncertainty factor ρ, which was also used in Section 6.1.1 and related work in the literature, e.g., [41,48,104]. However, the left border of the interval is $(2-\rho)\,\sigma_w^2$ in contrast to $\rho^{-1}\sigma_w^2$. This results from the fact that the Gaussian PDF is symmetric about its mean, which is why we also chose the noise uncertainty interval to be symmetric.

By using this parametrization, one can specify the model in two ways. Firstly, one could estimate the standard deviation ϑ of the Gaussian distribution by analyzing the calibration process, choosing a factor β and calculating the resulting noise uncertainty factor:

$$\rho = 1 + \frac{\vartheta\beta}{\sigma_w^2}\,. \tag{6.42}$$

Secondly, one can specify a noise uncertainty factor (e.g., to compare two models), choose a factor β and obtain the resulting standard deviation of the Gaussian

distribution:

$$\vartheta = \frac{(\rho - 1)\,\sigma_w^2}{\beta}\,. \tag{6.43}$$

When determining β, one chooses the probability p that the noise power of a SU after calibration lies within β standard deviations around the nominal value. The probability p can easily be obtained by

$$\begin{aligned} p &= \Phi\left(\frac{\sigma_w^2 + \beta\vartheta - \sigma_w^2}{\vartheta}\right) - \Phi\left(\frac{\sigma_w^2 - \beta\vartheta - \sigma_w^2}{\vartheta}\right) \\ &= \Phi(\beta) - \Phi(-\beta) \\ &= 2\,\Phi(\beta) - 1\,. \end{aligned} \tag{6.44}$$

Some typical choices for β and the resulting values for p and $1 - p$ are summarized in Table 6.2.

β	p	$1 - p$
1	0.6826894	0.3173105
2	0.9544997	0.0455002
3	0.9973002	0.0026997
4	0.9999366	0.0000633
5	0.9999994	0.0000005

Table 6.2: Typical values for the parameter β and resulting probability p (rounded to seven decimal places) that the noise power of a SU after calibration falls within β standard deviations around the nominal value σ_w^2.

Summarizing, if it holds that $\sigma_w^2 - \beta\vartheta > 0$ (or equivalently $\rho < 2$) and the parameter β is chosen such that p is close to one, this model fulfills the following properties:

1. The SU noise power after calibration is modeled with a Gaussian distribution, i.e., small deviations from the nominal value occur more often than large ones.

2. If β is sufficiently large, the effects due to the remaining non-zero probability outside the interval $[\sigma_w^2 - \beta\vartheta, \sigma_w^2 + \beta\vartheta]$ are neglected.

3. Due to the interval $[(2-\rho)\,\sigma_w^2, \rho\,\sigma_w^2]$ that was used in the parametrization, the model is still comparable to other models that use a single noise uncertainty factor ρ in their description. (Typically, the upper boundary of the interval is relevant for robustly setting the threshold.)

4. The error model is symmetric around the nominal value σ_w^2.

Under $\mathcal{H}_1$, we again assume that the SUs are perfectly calibrated. Below, we show the existence of an SNR wall under this Gaussian average case scenario in the asymptotic regime and thereby obtain lower bounds, since the cases examined here are not the worst case scenario (see also Section 6.1 and case d) in Figure 6.1).

MME Detector

Similarly to the analysis of the MME detector (see (3.22)) from Section 6.1.1, we relate the task of finding the asymptotic mean of the test statistic under $\mathcal{H}_0$ to studying the order statistics of standard Gaussian samples.

Let $U_{(1)} \leq \cdots \leq U_{(i)} \leq \cdots \leq U_{(K)}$ denote the order statistic of a random sample with K samples from a standard Gaussian distribution (see Sections 3.6 and 3.6.2) with PDF $f_U(u) = \phi(u)$ and CDF $F_U(u) = \Phi(u)$ as given in (2.48) and (2.49).

With the affine transformation $\vartheta\, U_{(i)} + \sigma_w^2$, the asymptotic mean of the test statistic under $\mathcal{H}_0$ can be expressed as

$$\begin{aligned} \mathrm{E}_{\mathcal{H}_0}[T_{\mathrm{MME}}] &= \mathrm{E}\left[\frac{\vartheta\, U_{(K)} + \sigma_w^2}{\vartheta\, U_{(1)} + \sigma_w^2}\right] = \mathrm{E}\left[\frac{U_{(K)} + \sigma_w^2\, \vartheta^{-1}}{U_{(1)} + \sigma_w^2\, \vartheta^{-1}}\right] \\ &= \mathrm{E}\left[\frac{U_{(K)} + \beta\,(\rho-1)^{-1}}{U_{(1)} + \beta\,(\rho-1)^{-1}}\right]. \end{aligned} \tag{6.45}$$

Finding the exact form of (6.45) would involve finding the joint density of two order statistics (see (3.58)), transforming it to find the ratio and subsequently calculating the mathematical expectation. Already the CDF of a standard Gaussian cannot be given in closed form, so that it seems hopeless to find a tractable exact form for (6.45). Since we had success in approximating $\mathrm{E}_{\mathcal{H}_0}[T_{\mathrm{MME}}]$ using a first order Taylor expansion in (6.9), we use it here again to obtain:

$$\mathrm{E}_{\mathcal{H}_0}[T_{\mathrm{MME}}] \approx \frac{\mathrm{E}_{\mathcal{H}_0}[\lambda_K]}{\mathrm{E}_{\mathcal{H}_0}[\lambda_1]} = \frac{\mathrm{E}[U_{(K)} + \beta\,(\rho-1)^{-1}]}{\mathrm{E}[U_{(1)} + \beta\,(\rho-1)^{-1}]} = \frac{\mathrm{E}[U_{(K)}] + \beta\,(\rho-1)^{-1}}{\mathrm{E}[U_{(1)}] + \beta\,(\rho-1)^{-1}}\,. \tag{6.46}$$

There exists a relation for the mean of Gaussian order statistics, cf. (3.61), with which we find that

$$\mathrm{E}[U_{(1)}] = -\mathrm{E}[U_{(K)}]\,. \tag{6.47}$$

Thus, we only need to find an expression for the mean of either the largest or the smallest Gaussian order statistic.

Since the mean of Gaussian order statistics remains unknown for a general number of samples, a lot of research has been conducted to find suitable approximations and bounds, see, e.g., [109, p. 82 ff.]. The approximation we make use of here is

of a convenient form that can be readily evaluated with the help of the inverse standard Gaussian CDF Φ^{-1}, which is either available in tabulated form or can be numerically evaluated using algorithms that are widely included in mathematical software libraries. The approximation

$$\mathrm{E}[U_{(i)}] \approx -\Phi^{-1}\left(\frac{K-i+1-\psi}{K-2\psi+1}\right), \tag{6.48}$$

was given in [131], where a compromise value for the parameter ψ — that generally depends on both K and i to achieve the best possible approximation — was suggested to be $\psi = \frac{3}{8}$. For small K, say $K \leq 20$ [109, p. 86], this value is a decent compromise. However, it was shown that this choice of ψ is too low for higher K and better values can be found in [132]. In the numerical evaluation in Section 6.1.5 we vary K between two and 24. From [132, Tables 2 & 3] we find that for the largest (or smallest) order statistic the value $\psi = \frac{3}{8}$ is close to the optimal choice for $K = 24$. Since the approximation is quite stable for small K, we do not adjust ψ in this work. If one desires to evaluate this approximation and the formulas derived from it for larger K, the value ψ should be chosen with the help of the tables or formulas from [132].

Using the relations and approximations from (3.61), (6.46) and (6.48), we derive our approximation for $\mathrm{E}_{\mathcal{H}_0}[T_{\mathrm{MME}}]$:

$$\begin{aligned}
\mathrm{E}_{\mathcal{H}_0}[T_{\mathrm{MME}}] &\approx \frac{\mathrm{E}[U_{(K)} + \beta\,(\rho-1)^{-1}]}{\mathrm{E}[U_{(1)} + \beta\,(\rho-1)^{-1}]} = \frac{2\beta\,(\rho-1)^{-1} - \mathrm{E}[U_{(1)} + \beta\,(\rho-1)^{-1}]}{\mathrm{E}[U_{(1)} + \beta\,(\rho-1)^{-1}]} \\
&= \frac{2\beta\,(\rho-1)^{-1}}{\mathrm{E}[U_{(1)} + \beta\,(\rho-1)^{-1}]} - 1 = \frac{2\beta\,(\rho-1)^{-1}}{\beta\,(\rho-1)^{-1} - \Phi^{-1}\left(\frac{K-\psi}{K-2\psi+1}\right)} - 1 \\
&= \frac{2}{1-\beta^{-1}\,(\rho-1)\,\Phi^{-1}\left(\frac{K-\psi}{K-2\psi+1}\right)} - 1\,. \qquad \textbf{(6.49)}
\end{aligned}$$

Choosing $\psi = \frac{3}{8} = 0.375$ results in the approximation that we use in the remainder of this work:

$$\mathrm{E}_{\mathcal{H}_0}[T_{\mathrm{MME}}] \approx \frac{2}{1-\beta^{-1}\,(\rho-1)\,\Phi^{-1}\left(\frac{K-0.375}{K+0.25}\right)} - 1\,, \qquad \textbf{(6.50)}$$

which is intended for $K \leq 24$.

While there are some conditions, which can be stated about the correlation between λ_1 and λ_K, a simple general form like in the rectangular case does not seem to exist, cf. [110].

Since under $\mathcal{H}_1$ the model is the same as in Section 6.1.1, the lower bound for the SNR wall is given by (6.18). By inserting (6.50) into (6.18) we gain an approximation of the lower bound on the SNR wall of the MME detector using this Gaussian

scenario:

$$\alpha_{\text{wall}}^{\text{MME}} \gtrapprox \frac{1}{K}\left(\frac{2}{1-\beta^{-1}\,(\rho-1)\,\Phi^{-1}\left(\frac{K-0.375}{K+0.25}\right)}-2\right). \tag{6.51}$$

A detailed numerical evaluation of this result is performed in Section 6.1.5.

GLRT Detector

For the investigation of the GLRT (see (3.24)), we can make use of results that were obtained in the preceding derivations and in Section 6.1.1. If $K = 2$ the GLRT and MME detectors are equal. Therefore, we presume $K \geq 3$ in the following derivations.

To obtain the mean of the test statistic under $\mathcal{H}_0$, we employ the first order Taylor approximation from (6.20). Using the affine transformation $\vartheta\, U_{(i)} + \sigma_w^2$ we may relate the mean of the i-th eigenvalue to the i-th order statistic of a standard Gaussian sample for $i = 1, \ldots, K$. Hence, we can simplify the denominator significantly as follows:

$$\begin{aligned}\sum_{i=1}^{K-1} \mathrm{E}_{\mathcal{H}_0}[\lambda_i] &= \sum_{i=1}^{K-1} \mathrm{E}[\vartheta\, U_{(i)} + \sigma_w^2] = \vartheta \sum_{i=1}^{K-1} \mathrm{E}[U_{(i)}] + (K-1)\,\sigma_w^2 \\ &= \vartheta\, \mathrm{E}[U_{(1)}] + (K-1)\,\sigma_w^2\,. \end{aligned} \tag{6.52}$$

The last step deserves some further explanation. From (3.61), we see that there is a symmetry, such that all summands cancel out except $i = 1$ if K is even. If K is odd only the summands $i = 1$ and $i = \frac{K+1}{2}$ remain. Moreover, in the latter case we find from (3.62) that $\mathrm{E}\left[U_{\left(\frac{K+1}{2}\right)}\right] = 0$, such that the same result follows for both even and odd K.

Using the result from (6.52), the relation from (3.61) and the already familiar approximation from (6.48) for the mean of standard Gaussian order statistics, we derive an approximation for $\mathrm{E}_{\mathcal{H}_0}[T_{\text{GLRT}}]$:

$$\begin{aligned}\mathrm{E}_{\mathcal{H}_0}[T_{\text{GLRT}}] &\approx \frac{\mathrm{E}_{\mathcal{H}_0}[\lambda_K]}{\sum_{i=1}^{K-1}\mathrm{E}_{\mathcal{H}_0}[\sigma_{w_i}^2]} = \frac{\mathrm{E}[\vartheta\, U_{(K)} + \sigma_w^2]}{\vartheta\,\mathrm{E}[U_{(1)}] + (K-1)\,\sigma_w^2} \\ &= \frac{2\sigma_w^2 - \mathrm{E}[\vartheta\, U_{(1)} + \sigma_w^2]}{\vartheta\,\mathrm{E}[U_{(1)}] + (K-1)\,\sigma_w^2} = \frac{\sigma_w^2 - \vartheta\,\mathrm{E}[U_{(1)}]}{\vartheta\,\mathrm{E}[U_{(1)}] + (K-1)\,\sigma_w^2} \\ &= \frac{K\,\sigma_w^2}{\vartheta\,\mathrm{E}[U_{(1)}] + (K-1)\,\sigma_w^2} - 1 \approx \frac{K\,\sigma_w^2}{(K-1)\,\sigma_w^2 - \vartheta\,\Phi^{-1}\left(\frac{K-\psi}{K-2\psi+1}\right)} - 1 \\ &= \frac{K}{(K-1) - \beta^{-1}\,(\rho-1)\,\Phi^{-1}\left(\frac{K-\psi}{K-2\psi+1}\right)} - 1\,. \end{aligned} \tag{6.53}$$

By choosing $\psi = \frac{3}{8} = 0.375$, we gain the approximation intended for $K \leq 24$ that is used in the remainder of this work:

$$\mathrm{E}_{\mathcal{H}_0}[T_{\mathrm{GLRT}}] \approx \frac{K}{(K-1) - \beta^{-1}\,(\rho-1)\,\Phi^{-1}\left(\frac{K-0.375}{K+0.25}\right)} - 1\,. \tag{6.54}$$

Analogously to the examination of the MME, due to the fact that the $\mathcal{H}_1$ models are the same for Sections 6.1.1 and 6.1.2, the lower bound on the SNR wall from (6.24) holds here as well. Thus, we can insert (6.54) into (6.24) to find an approximation of the SNR wall of the GLRT in this Gaussian model:

$$\alpha_{\mathrm{wall}}^{\mathrm{GLRT}} \gtrapprox \frac{1}{1 - \frac{\rho-1}{\beta(K-1)}\,\Phi^{-1}\left(\frac{K-0.375}{K+0.25}\right)} - 1\,, \tag{6.55}$$

which is evaluated numerically in Section 6.1.5.

In Section 6.1.1 with rectangular distributed noise powers after calibration, further approximations to the denominator of (6.52) were made. One could argue, that the same approach might be successful here. If we utilize said approximation from (6.27) as well as the affine transformation $\vartheta\,U_{(i)} + \sigma_w^2$ from and the relation (3.61) we gain the following result:

$$\begin{aligned}
\mathrm{E}_{\mathcal{H}_0}[T_{\mathrm{GLRT}}] &\approx \frac{\mathrm{E}_{\mathcal{H}_0}[\lambda_K]}{\sum_{i=1}^{K-1}\mathrm{E}_{\mathcal{H}_0}[\sigma_{w_i}^2]} \approx \frac{\mathrm{E}[\vartheta\,U_{(K)} + \sigma_w^2]}{(K-1)\,\sigma_w^2} \\
&= \frac{(\rho-1)\beta^{-1}\,\sigma_w^2\,\mathrm{E}[U_{(K)}] + \sigma_w^2}{(K-1)\,\sigma_w^2} = \frac{(\rho-1)\beta^{-1}\,\mathrm{E}[U_{(K)}] + 1}{(K-1)} \\
&= \frac{-(\rho-1)\beta^{-1}\,\mathrm{E}[U_{(1)}] + 1}{(K-1)} \approx \frac{(\rho-1)\beta^{-1}\,\Phi^{-1}\left(\frac{K-\psi}{K-2\psi+1}\right) + 1}{(K-1)}\,.
\end{aligned} \tag{6.56}$$

Inserting the result from (6.56) into the lower bound on the SNR wall from (6.24) and choosing $\psi = \frac{3}{8} = 0.375$, we gain another approximation for the lower bound on the SNR wall of the GLRT detector intended for $K \leq 24$ in this Gaussian scenario:

$$\alpha_{\mathrm{wall}}^{\mathrm{GLRT}} \gtrapprox \frac{(\rho-1)\,\Phi^{-1}\left(\frac{K-0.375}{K+0.25}\right)}{\beta\,K}\,. \tag{6.57}$$

However, in Section 6.1.5 it is shown that the accuracy of this approximation is not satisfactory.

QST Detector

In the test statistic of the QST (see (3.25)), no ordering of the eigenvalues is present. Hence, under $\mathcal{H}_0$ the joint PDF of the eigenvalues can be readily stated as

$$f_{\boldsymbol{\lambda}}(\boldsymbol{\lambda}) = \prod_{i=1}^{K} \frac{1}{\sqrt{2\pi}\,\vartheta} e^{-\frac{\left(\lambda_i - \sigma_w^2\right)^2}{2\vartheta^2}} = \frac{1}{(2\pi\vartheta^2)^{\frac{K}{2}}} \exp\left(-\frac{1}{2\vartheta^2}\sum_{i=1}^{K}\left(\lambda_i - \sigma_w^2\right)^2\right)\,, \tag{6.58}$$

which is the joint PDF of K i.i.d. random variables following a $\mathcal{N}(\sigma_w^2, \vartheta^2)$ distribution, i.e., the joint distribution is $\mathcal{N}(\sigma_w^2 \mathbf{1}_K, \vartheta^2 \mathbf{I}_K)$. As we have discussed in the beginning of Section 6.1.2, the fact that the support of the PDF from (6.58) is the K-dimensional space of real numbers ($\mathbb{R}^K$) is problematic, since the eigenvalues of the (sample) covariance matrix must be non-negative.

Thus, we use a scaled and truncated version of the PDF from (6.58) to ensure the eigenvalues are non-negative by excluding the values outside the interval $[(2-\rho)\,\sigma_w^2, \rho\,\sigma_w^2]$ and scaling the resulting function, such that it becomes a valid PDF. This results in the following scaled and truncated Gaussian PDF:

$$\check{f}_{\boldsymbol{\lambda}}(\boldsymbol{\lambda}) = \frac{1}{p^K}\, f_{\boldsymbol{\lambda}}(\boldsymbol{\lambda})\, \mathbb{I}_{[(2-\rho)\,\sigma_w^2, \rho\,\sigma_w^2]^K}(\boldsymbol{\lambda})\,. \tag{6.59}$$

This PDF is a suitable approximation for an intermediate amount of cooperating SUs. For example, if $\beta = 3$ is chosen and if $K > 40$ one has to decide whether this Gaussian model can still be applied since the probability that all the SUs' noise powers after calibration lie in the interval $[(2-\rho)\,\sigma_w^2, \rho\,\sigma_w^2]$ (which is p^K) falls below 0.9. At some point the area under the PDF outside this interval may become to large to be neglected. In our numerical evaluations, we consider values for K in the interval $[2, 24]$ for which $p^K \geq 0.9346$ for $\beta = 3$.

Using (6.59), we can find an approximation of $\mathrm{E}_{\mathcal{H}_0}[T_{\mathrm{QST}}]$ as:

$$\begin{aligned}
\mathrm{E}_{\mathcal{H}_0}[T_{\mathrm{QST}}] &= \int_{-\infty}^{\infty} \cdots \int_{-\infty}^{\infty} \frac{\|\boldsymbol{\lambda}\|_2}{\|\boldsymbol{\lambda}\|_1}\, \check{f}_{\boldsymbol{\lambda}}(\boldsymbol{\lambda})\, \mathrm{d}\lambda_1 \ldots\, \mathrm{d}\lambda_K \\
&= \frac{1}{p^K} \int_{(2-\rho)\sigma_w^2}^{\rho\sigma_w^2} \cdots \int_{(2-\rho)\sigma_w^2}^{\rho\sigma_w^2} \frac{\|\boldsymbol{\lambda}\|_2}{\|\boldsymbol{\lambda}\|_1}\, f_{\boldsymbol{\lambda}}(\boldsymbol{\lambda})\, \mathrm{d}\lambda_1 \ldots\, \mathrm{d}\lambda_K \\
&= \frac{1}{p^K\,(2\pi\vartheta^2)^{\frac{K}{2}}} \int_{(2-\rho)\sigma_w^2}^{\rho\sigma_w^2} \cdots \int_{(2-\rho)\sigma_w^2}^{\rho\sigma_w^2} \frac{\|\boldsymbol{\lambda}\|_2}{\|\boldsymbol{\lambda}\|_1} \prod_{i=1}^{K} e^{-\frac{\left(\lambda_i - \sigma_w^2\right)^2}{2\vartheta^2}}\,. \qquad \textbf{(6.60)}
\end{aligned}$$

Regrettably, a closed form solution to this integral does not exist to the best of our knowledge. Instead, we have used the "cubature" multidimensional integral evaluation library from [130] to calculate concrete values of (6.60).

Since Sections 6.1.1 and 6.1.2 share the same model under $\mathcal{H}_1$, the lower bound on the SNR wall from (6.41) holds here as well. In Section 6.1.5, we evaluate this bound by inserting numerically calculated values of (6.60).

6.1.3 Lower Bounds on the SNR Wall

In order to obtain tighter lower bounds on the SNR wall we consider a different scenario, where no concrete distribution of the SU noise powers after calibration is assumed under $\mathcal{H}_0$. Instead, a worst case analysis is performed where it

is assumed that the noise powers of the SUs after calibration are in the interval $\sigma_{w_i}^2 \in [\rho^{-1}\sigma_w^2, \rho\sigma_w^2]$ for $i = 1, \ldots, K$. In the following derivations we presume, w.l.o.g., $\sigma_w^2 = 1$. Note, that the presented derivations can be easily extended to general (finite) noise power intervals if desired.

By assuming the SUs are perfectly calibrated under $\mathcal{H}_1$, lower bounds on the SNR wall can be derived, cf. Section 6.1 and case c) in Figure 6.1. In Section 6.1.4 we additionally derive upper bounds on the SNR walls for the MME and the GLRT.

MME Detector

Obviously, for the worst case under $\mathcal{H}_0$, the test statistic of the MME detector (see (3.22)) must be as large as possible. It can be easily seen that this happens when the largest and the smallest eigenvalue attain the largest and smallest possible value in the interval $[\rho^{-1}, \rho]$, respectively. Hence, the worst case eigenvalue vector is given by

$$\boldsymbol{\lambda}_{\mathrm{MME,wc}}^{\mathcal{H}_0} = \left(\rho^{-1}, *, \ldots, *, \rho\right)^{\mathrm{T}}, \tag{6.61}$$

where $*$ stands for any admissible value. By inserting these worst case eigenvalues into the test statistic (3.22), we obtain an attainable upper bound on the mean of the test statistic under $\mathcal{H}_0$

$$\mathrm{E}_{\mathcal{H}_0}[T_{\mathrm{MME}}] \leq \frac{\rho}{\rho^{-1}} = \rho^2 \,. \tag{**6.62**}$$

The $\mathcal{H}_1$ model is the same as in Sections 6.1.1 and 6.1.2 and consequently the lower bound for the SNR wall from (6.18) is valid here as well. Inserting (6.62) into (6.18), we get

$$\alpha_{\mathrm{wall}}^{\mathrm{MME}} \geq \frac{\rho^2 - 1}{K} \,, \tag{**6.63**}$$

which is a tighter lower bound on the SNR wall than the ones studied before, since we consider the worst case under $\mathcal{H}_0$ here. The bound from (6.63) has an interesting relation to the approximation of the lower bound under the rectangular model from (6.19), where the latter is smaller by a factor of $\left(\frac{K-1}{K+\rho^2}\right) \leq 1$.

A numerical evaluation of this lower bound is performed in Section 6.1.5.

GLRT Detector

For the GLRT detector, the test statistic (see (3.24)) must be as large as possible in the worst case. Consequently, due to the ratio, we notice that the numerator must attain the largest value possible, while the denominator must take on the smallest

permissible value. Hence, it is readily seen that the worst case eigenvalue vector for the GLRT is

$$\boldsymbol{\lambda}_{\mathrm{GLRT,wc}}^{\mathcal{H}_0} = \left(\rho^{-1}, \rho^{-1}, \ldots, \rho^{-1}, \rho\right)^{\mathrm{T}}, \tag{6.64}$$

i.e., all eigenvalues except the largest take on the smallest value in the interval $[\rho^{-1}, \rho]$, while the largest eigenvalue must be the largest value in said interval. Calculating the test statistic with the worst case eigenvalues results in an attainable upper bound on the mean of the test statistic under $\mathcal{H}_0$:

$$\mathrm{E}_{\mathcal{H}_0}[T_{\mathrm{GLRT}}] \leq \frac{\rho}{(K-1)\,\rho^{-1}} = \frac{\rho^2}{(K-1)}\,. \tag{**6.65**}$$

The $\mathcal{H}_1$ model used here is the same as in Sections 6.1.1 and 6.1.2. Therefore, the lower bound from (6.24) is also valid here. Inserting (6.65) into (6.24) finally gives the tighter lower bound

$$\alpha_{\mathrm{wall}}^{\mathrm{GLRT}} \geq \frac{\rho^2 - 1}{K}\,. \tag{**6.66**}$$

Notice, that the result coincides with the one obtained for the MME detector in (6.63).

This may seem counter intuitive at first. One would expect that the GLRT is more resilient to imperfect noise power calibration compared to the MME, since it effectively computes a (non-normalized) average in the denominator instead of using only the smallest eigenvalue like the MME. The reason for the above result is that to derive the (lower bound) of the SNR wall a worst case analysis is performed. There, we saw that for the GLRT *all* $K-1$ smallest eigenvalues have the smallest value ρ^{-1} in the worst case and consequently the averaging effect disappears. If we compare the worst case eigenvalue vectors for the GLRT and MME from (6.61) and (6.64), respectively, we see that the latter case has a much higher practical relevance than the former. In practice, it is much more likely to find two out of K receivers, which are very badly calibrated (where one has a very low noise power and one has a very high noise power) than finding a situation where exactly $K-1$ receivers have a very low noise power and the last one has a very high noise power. Hence, we still expect the GLRT to be less sensitive to noise uncertainty than the MME in practice. If we are interested in a performance limit below which meaningful detection cannot be *guaranteed* under imperfect noise power calibration, however, then we find from (6.63) and (6.66) that the lower bound on this limit is the same for both detectors. Still, we have to keep in mind that this is not the actual SNR wall, since we did not study the worst case scenario under $\mathcal{H}_1$.

In Section 6.1.5, a numerical evaluation of these findings is conducted.

6.1.4 Upper Bounds on the SNR Wall

In order to find an upper bound on the SNR wall, it is necessary to lower bound $\mathrm{E}_{\mathcal{H}_1}[T]$. While we have identified the worst case (or smallest upper bound) of $\mathrm{E}_{\mathcal{H}_0}[T]$ for the MME and the GLRT, finding the worst case under $\mathcal{H}_1$ seems much more difficult. Under $\mathcal{H}_1$, due to the model of the noise calibration uncertainty, the additivity of the eigenvalues of $\mathbf{R_x}$ and $\mathbf{R_w}$ from (4.14) is lost, since $\mathbf{R_w}$ is no longer a scaled identity matrix. While there are many results on the eigenvalues of the sum of two Hermitian matrices (see [133]), finding the worst case exactly for this model still seems to be a very elaborate problem. Thus, we derive a lower bound on the test statistics for the MME and the GLRT to subsequently derive an upper bound for their respective SNR walls, see also Section 6.1 and case a) in Figure 6.1. For this, we utilize the same model as in Section 6.1.3, where the noise powers of the SUs after calibration are in the interval $\sigma_{w_i}^2 \in [\rho^{-1}, \rho]$ for $i = 1, \ldots, K$ without being assigned a concrete distribution. The SNR wall upper bounds are especially meaningful when studied in conjunction with the lower bounds from Section 6.1.3. Note, that an extension of the following results to general (finite) noise power intervals is straightforward.

MME Detector

To lower bound $\mathrm{E}_{\mathcal{H}_1}[T_{\mathrm{MME}}]$, we follow analogous reasoning as we did for finding the (attainable) upper bound of $\mathrm{E}_{\mathcal{H}_0}[T_{\mathrm{MME}}]$. The numerator of the test statistic T_{MME} (see (3.22)) must be as small as possible, while the denominator must get as large as possible simultaneously. Consequently, we individually bound the largest and smallest asymptotic eigenvalues under $\mathcal{H}_1$. In order to do so, we need two relations about the eigenvalues of the sum of two Hermitian matrices. We review them in the following.

Let $\check{\mathbf{A}}$, $\check{\mathbf{B}}$ and $\check{\mathbf{C}}$ denote $K \times K$ Hermitian matrices and let $\mathbf{a}$, $\mathbf{b}$ and $\mathbf{c}$ stand for their ordered eigenvalue vectors in the same order, respectively. Consider the sum $\check{\mathbf{C}} = \check{\mathbf{A}} + \check{\mathbf{B}}$. Then, we find from [133, Eq. (2)] that

$$c_1 \leq a_1 + b_K \tag{6.67}$$

and

$$c_{K-1} \leq a_{K-1} + b_K \,. \tag{6.68}$$

Another helpful relation can be derived from [133, Eq. (11)], which is:

$$c_K \geq a_K + b_1 \,. \tag{6.69}$$

Using (6.67) and (4.11) we can now upper bound the smallest eigenvalue λ_1 under $\mathcal{H}_1$ as

$$\lambda_1 \leq \underbrace{\min(\mathrm{eig}\,(\mathbf{R}_\mathbf{x}))}_{=0} + \max(\mathrm{eig}\,(\mathbf{R}_\mathbf{w})) \leq \rho\,, \tag{6.70}$$

since $\max(\mathrm{eig}\,(\mathbf{R}_\mathbf{w})) \leq \rho$.

Similarly, a lower bound on the largest eigenvalue can be found with the help of (4.10), (4.11) and (6.69):

$$\begin{aligned}\lambda_K &\geq \max(\mathrm{eig}\,(\mathbf{R}_\mathbf{x})) + \min(\mathrm{eig}\,(\mathbf{R}_\mathbf{w})) = \alpha K + \min(\mathrm{eig}\,(\mathbf{R}_\mathbf{w})) \\ &\geq \alpha K + \rho^{-1}\,,\end{aligned} \tag{6.71}$$

since $\min(\mathrm{eig}\,(\mathbf{R}_\mathbf{w})) \geq \rho^{-1}$.

We have obtained lower and upper bounds for the numerator and denominator of T_{MME}, respectively. Thus, by inserting these into (3.22) we obtain a lower bound on $\mathrm{E}_{\mathcal{H}_1}[T_{\mathrm{MME}}]$:

$$\mathrm{E}_{\mathcal{H}_1}[T_{\mathrm{MME}}] \geq \frac{\alpha K + \rho^{-1}}{\rho}\,. \tag{\textbf{6.72}}$$

Note, that this bound is only valid for

$$\alpha \geq \frac{\rho^2 - 1}{\rho K}\,, \tag{6.73}$$

since $\lambda_K \geq \lambda_1$ must hold.

To obtain the upper bound for the SNR wall, the value for the SNR must be found, such that $\mathrm{E}_{\mathcal{H}_0}[T_{\mathrm{MME}}]$ and $\mathrm{E}_{\mathcal{H}_1}[T_{\mathrm{MME}}]$ overlap under this model. With the help of (6.62) and (6.72) we find:

$$\alpha_{\mathrm{wall}}^{\mathrm{MME}} \leq \frac{\rho}{K}\left(\rho^2 - \frac{1}{\rho^2}\right) = \frac{\rho^2 - 1}{K}\,\frac{\rho^2 + 1}{\rho} = \alpha_{\mathrm{wall}}^{\mathrm{ED}}\,\frac{\rho^2 + 1}{K}\,. \tag{\textbf{6.74}}$$

Since $\rho^2 + 1 \geq 2$, the condition (6.73) is obviously fulfilled.

The upper bound (6.74) is evaluated in Section 6.1.5. Note, that the upper bound may be related to the lower bound by the factor $\frac{\rho^2+1}{\rho}$. Similarly, we observe that the upper bound shows a relation to the SNR wall of ED. If $K > \rho^2 + 1$, it can be seen from (6.74) that the SNR wall of the MME detector is guaranteed to be lower than the one of ED.

GLRT Detector

For the GLRT we can reuse certain results from the preceding analysis of the MME. Similarly, we can develop a lower bound on the test statistic by lower and upper bounding the numerator and denominator, respectively. From (6.71), a lower bound on the largest eigenvalue is already available.

The denominator can be upper bounded by realizing from (6.68) that the second largest eigenvalue can be upper bounded as

$$\lambda_{K-1} \leq \underbrace{[\mathrm{eig}\,(\mathbf{R}_\mathbf{x})]_{K-1}}_{=0} + \max(\mathrm{eig}\,(\mathbf{R}_\mathbf{w})) \leq \rho\,. \tag{6.75}$$

Since it holds that $\lambda_1 \leq \cdots \leq \lambda_{K-1} \leq \lambda_K$, we may readily construct an upper bound of the denominator as

$$\sum_{i=1}^{K-1} \lambda_i \leq (K-1)\,\lambda_{K-1} \leq (K-1)\,\rho\,. \tag{6.76}$$

Hence, using (6.71) and (6.76) the lower bound for the test statistic of the GLRT under $\mathcal{H}_1$ becomes

$$\mathrm{E}_{\mathcal{H}_1}[T_{\mathrm{GLRT}}] \geq \frac{\alpha K + \rho^{-1}}{(K-1)\,\rho}\,. \tag{**6.77**}$$

Finding the SNR value for which $\mathrm{E}_{\mathcal{H}_0}[T_{\mathrm{GLRT}}]$ and $\mathrm{E}_{\mathcal{H}_1}[T_{\mathrm{GLRT}}]$ coincide using (6.65) and (6.77) gives the upper bound on the SNR wall of the GLRT:

$$\alpha_{\mathrm{wall}}^{\mathrm{GLRT}} \leq \frac{\rho}{K}\left(\rho^2 - \frac{1}{\rho^2}\right) = \frac{\rho^2-1}{K}\,\frac{\rho^2+1}{\rho}\,. \tag{**6.78**}$$

Note, that again the upper bounds of the SNR wall of the MME and the GLRT are equal (cf. (6.74) and (6.78)).

In Section 6.1.5 this upper bound is evaluated.

6.1.5 Numerical Evaluation

The following part is dedicated to a numerical evaluation of the results derived in the preceding Sections 6.1.1 to 6.1.4. In particular, the accuracy of the approximations for the asymptotic mean of the test statistic ($\mathrm{E}_{\mathcal{H}_0}[T]$) are evaluated for both the rectangular and the Gaussian average case scenarios. Then, the lower bounds of the SNR walls — and their respective approximations — are investigated. It is shown which of the approximations are practical for the range of parameters considered here (0.1 dB $\leq \rho_{\mathrm{dB}} \leq$ 2.0 dB and $2 \leq K \leq 24$). Moreover, the consequences of these findings for eigenvalue-based spectrum sensing systems is discussed.

Evaluation of the Results for Rectangular Distributed Noise Powers

First, we visualize the exact value of $\mathrm{E}_{\mathcal{H}_0}[T]$ (where available) and the derived approximations for the three detectors MME, GLRT and QST for the rectangular model, from Section 6.1.1. Thereafter, we investigate the relative deviations of the approximations. Finally, we take a look at the relative deviations of $\mathrm{E}_{\mathcal{H}_0}[T]$ for the rectangular scenario case from the worst case values of (6.62) and (6.65), which gives insights into the difference of robustness against noise calibration errors between the MME and the GLRT.

To verify the derivations of exact results and to obtain a "ground truth" in case the exact result is unknown, Monte Carlo simulations using `MATLAB` [128] were conducted. There, the results from 10^7 Monte Carlo instances were averaged for each parameter combination. In every instance, K samples from a rectangular distribution with support $[\rho^{-1}, \rho]$ were drawn, which serve as the asymptotic eigenvalues. With these the test statistics of the three detectors in question (MME, GLRT and QST) were calculated. This procedure was done for each combination of integer K with $2 \leq K \leq 24$ and noise uncertainty factors 0.1 dB $\leq \rho_{\mathrm{dB}} \leq$ 2.0 dB in steps of 0.1 dB.

For the evaluation of the integral from (6.35) the "cubature" multidimensional numerical integration library [130, Version 1.0.2] was utilized. To do so, a program in the programming language `C` was developed that calls the adaptive `hcubature` integration routine of the library, which is based on [134, 135]. For convergence, it was requested that each integrand individually satisfies the error constraint (i.e., the `norm` parameter was set to `ERROR_INDIVIDUAL`). A relative error of 10^{-3} was set as the error constraint. In this way, for $K \leq 24$ the integral from (6.35) can be evaluated. For $K \geq 25$ the memory demands of the integration routine begin to exceed practical ranges with these settings. Note, that we describe the values obtained by evaluating (6.35) in this way as "results". Strictly speaking, this is of course not correct as the numerical integration routine approximates the true value of the integral. However, the conservatively estimated numerical errors are required to fulfill the relative error constraint, i.e., 10^{-3}. Hence, for our purposes these values can be considered as the exact values. If desired, one can evaluate even more precise values with the techniques described above.

In Figure 6.4, we plot $\mathrm{E}_{\mathcal{H}_0}[T]$ using exact values (where possible), the approximations derived in Section 6.1.1 and empirical results from a Monte Carlo simulation for the MME, GLRT and QST detectors, see the description of the figure for more details. We see that the empirical resuls are in very good agreement with the exact values obtained from our theoretical investigation. Moreover, at this scale there is barely any deviation visible between the approximations and exact / empirical values. In addition, we see that the MME seems to converge to the worst case value as K gets larger. For the GLRT the distance to the worst case also seems to

decrease slightly, however no definitive conclusion can be drawn from studying this plot, which is why we study this effect in more detail below.

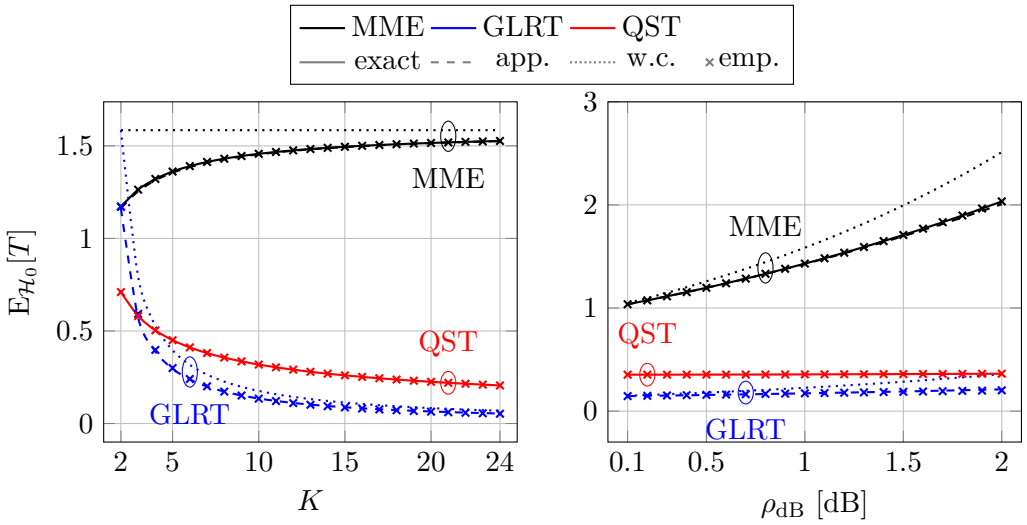

Figure 6.4: Evaluation of $\mathrm{E}_{\mathcal{H}_0}[T]$ for the MME, GLRT and the QST. For the MME and the QST the exact values are depicted using (6.7) and (6.35), respectively. For the MME and the GLRT approximations (app.) are shown from (6.13) and (6.32), while the worst case upper bounds (w.c.) are evaluated from (6.62) and (6.65), respectively. Empirical values (emp.) from a Monte Carlo simulation are drawn for all three detectors. *Left:* $\rho_{\mathrm{dB}} = 1$ dB. *Right:* $K = 8$.

We subsequently investigate the approximations in a more meaningful way by studying their relative deviation (also called relative error) from a reference v, which we define as

$$\frac{u - v}{|v|}\,. \tag{6.79}$$

There, u denotes the approximated value under investigation. For the approximations, if the exact value is known it is taken as the reference, otherwise the empirical values are used instead.

The relative deviation of the approximation of the mean of the test statistic of the MME from the exact value is depicted in Figure 6.5. As expected, the approximation gets tighter for increasing K. We see that for moderate values of the noise uncertainty factor ρ — say $\rho_{\mathrm{dB}} \leq 1$ dB — the relative error stays well below -1 % for $K = 8$. For higher values of ρ the accuracy of the approximation deteriorates. However, values of $\rho_{\mathrm{dB}} \geq 2$ dB correspond to uncertainty factors of $\rho \geq 1.5849$, which already represent very large calibration errors. The worst relative error over the parameter range studied here (0.1 dB $\leq \rho_{\mathrm{dB}} \leq 2$ dB, $2 \leq K \leq 24$) is ca. -3.3 %.

Thus, we argue from this analysis that the approximation from (6.13) is very accurate and we favor it over the exact formulation from (6.7) due to its significantly simpler form for the ranges of parameters studied here.

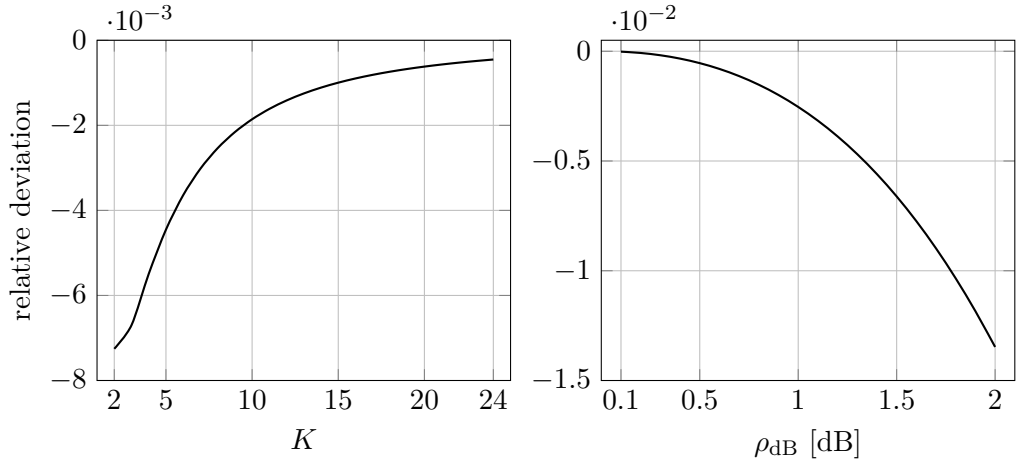

Figure 6.5: Relative deviation of the approximation of $\mathrm{E}_{\mathcal{H}_0}[T_{\mathrm{MME}}]$ of (6.13) from the exact result of (6.7). *Left:* $\rho_{\mathrm{dB}} = 1$ dB. *Right:* $K = 8$.

Three approximations of increasing simplicity for $\mathrm{E}_{\mathcal{H}_0}[T_{\mathrm{GLRT}}]$ were derived in Section 6.1.1, see (6.22), (6.30) and (6.32). Their relative deviation from the empirical values resulting from a Monte Carlo simulation are shown in Figure 6.6. The most accurate and also most complicated approximation from (6.22) stays well within -1 % of relative error and can be considered a very good substitute for the exact value, which remains unknown. We notice also, that it gets tighter as K increases. Over the whole parameter range considered here ($0.1 \text{ dB} \leq \rho_{\mathrm{dB}} \leq 2$ dB, $2 \leq K \leq 24$) the worst relative error is around -1.9 %. A significant bias can be observed for the approximation (6.30). Since it performs worst of the three alternatives, we do not consider it in the remainder of this work. The simplifying step from (6.31), which was taken to further simplify (6.30) into the most elementary approximation (6.32) seems to counteract the negative bias of its ancestor. Hence, (6.32) shows a more balanced error profile, exhibiting a negative bias for small K or ρ, while showing a positive bias for larger K or ρ. Especially for intermediate values of ρ — say $\rho_{\mathrm{dB}} \leq 1$ dB — the much simpler expression of (6.32) is a viable alternative over (6.22) if one is willing to trade off interpretability over precision. Over the whole parameter range ($0.1 \text{ dB} \leq \rho_{\mathrm{dB}} \leq 2$ dB, $2 \leq K \leq 24$) the worst relative error is around 8.6 %.

Figure 6.7 confirms that the GLRT is more resilient to noise calibration errors than the MME, despite the fact that their lower bounds on the SNR wall are equal (cf. (6.63) and (6.66)). As already argued in Section 6.1.3, since the MME only uses the extreme eigenvalues in its test statistic (see (3.22)), it is much more susceptible

to large calibration errors. Additionally, as K increases, it becomes more likely that two SUs show a very low and a very high noise power after calibration, respectively. This effect is prevented by normalizing the largest eigenvalue by the sum of the remaining $K-1$ smallest eigenvalues as done in the test statistic of the GLRT, cf. (3.24). Note, that for increasing K the relative deviation of $\mathrm{E}_{\mathcal{H}_0}[T_{\mathrm{GLRT}}]$ from its worst case seems to level off, while $\mathrm{E}_{\mathcal{H}_0}[T_{\mathrm{MME}}]$ seems to converge to towards the worst case value. As ρ increases, the relative deviation of $\mathrm{E}_{\mathcal{H}_0}[T]$ from the worst case values increases for both the MME and the GLRT. This is explained by the increase in variance of the rectangular distribution.

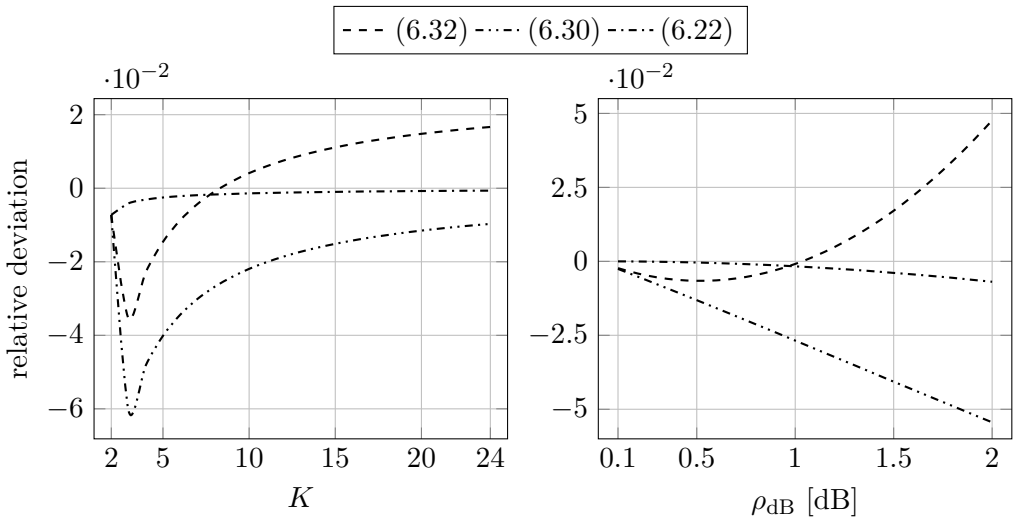

Figure 6.6: Relative deviation of the approximations of $\mathrm{E}_{\mathcal{H}_0}[T_{\mathrm{GLRT}}]$ of (6.22), (6.30) and (6.32) from empirical results obtained by Monte Carlo simulation. *Left:* $\rho_{\mathrm{dB}} = 1$ dB. *Right:* $K = 8$.

Evaluation of the Results for Gaussian Distributed Noise Powers

The analysis that was performed for the rectangular model case in the preceding section is similarly repeated here for the Gaussian model, which was investigated in Section 6.1.2. Note, however, that no exact results for $\mathrm{E}_{\mathcal{H}_0}[T]$ are available for all three detectors, such that empirical results from a Monte Carlo simulation serve as the reference.

Empirical results were generated using a Monte Carlo simulation, that is analogous to the one performed for the rectangular scenario. Here, in each of the 10^7 instances, K Gaussian samples were drawn independently from a $\mathcal{N}(1, \vartheta^2)$ distribution, where ϑ depends on both β and ρ (cf. (6.43)). The additional parameter β is fixed as $\beta = 3$ for this chapter, since for viable choices of β the results do not change fundamentally.

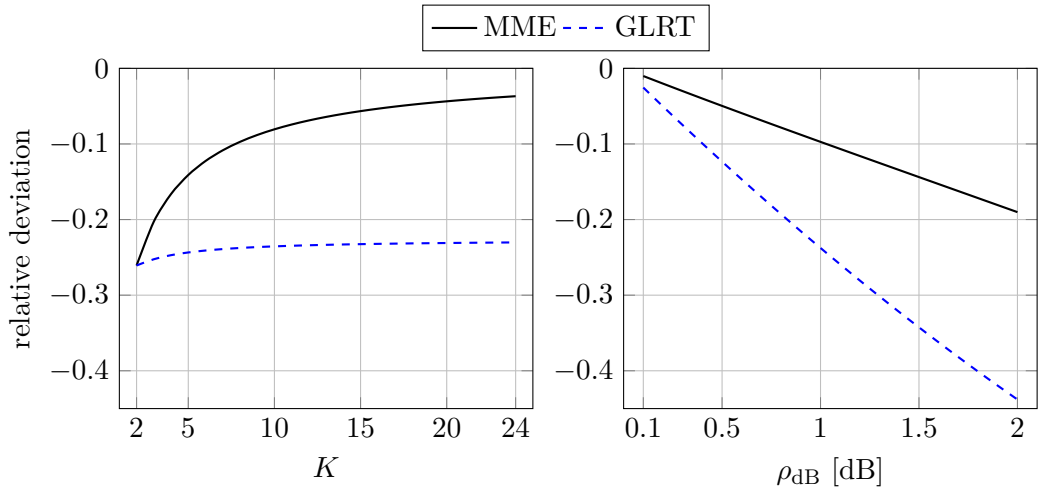

Figure 6.7: Relative deviation of $\mathrm{E}_{\mathcal{H}_0}[T]$ from the worst case upper bound (see (6.62) and (6.65), respectively). For the MME the exact value from (6.7) is used and for the GLRT empirical results from a Monte Carlo simulation are evaluated. *Left:* $\rho_{\mathrm{dB}} = 1$ dB. *Right:* $K = 8$.

For the numerical evaluation of (6.60) we again made use of the "cubature" library using the same settings already explained for the rectangular scenario. Unfortunately, (6.60) converges slower than (6.35), such that the computation time and memory demands exceed practical limits for $K \geq 12$ with the chosen method and settings. Since we have the results of the Monte Carlo simulation and we have shown that one can obtain the value of (6.60) by numerical evaluation in principle, we did not further pursue alternative methods of numerical evaluation to calculate it for larger K.

Figure 6.8 depicts $\mathrm{E}_{\mathcal{H}_0}[T]$ using the results derived in Section 6.1.2 and the empirical results from the Monte Carlo simulation for the three detectors MME, GLRT and QST. Additionally, the worst case values from (6.62) and (6.65) are shown, see the figure caption for details. At this scale, not much can be deduced about the accuracy of the approximations. We note, however, that the convergence of $\mathrm{E}_{\mathcal{H}_0}[T]$ to the worst case value for the MME seems to be less profound than under the rectangular model.

In Figure 6.9 the relative deviation of (6.50) from the empirical results is drawn. It can be observed, that the approximation error increases for larger K. For intermediate values of ρ, that is $\rho_{\mathrm{dB}} \leq 1$, the relative error is well below ± 1 % and the approximation is very precise. The worst relative error is ca. -3.2 % over the parameter range studied here (0.1 dB $\leq \rho_{\mathrm{dB}} \leq 2$ dB, $2 \leq K \leq 24$). We conclude that for the ranges of parameters studied here, this approximation is highly significant, since an exact formulation remains unknown.

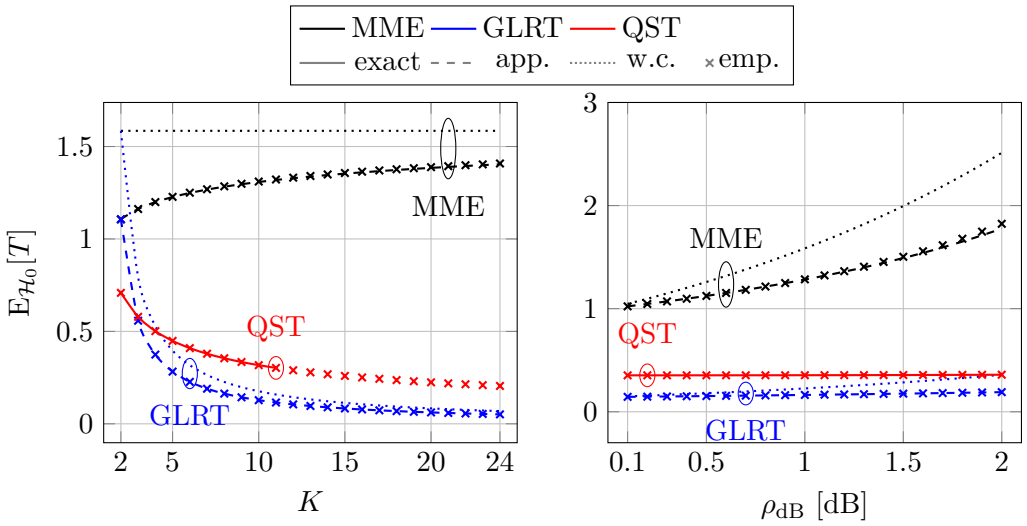

Figure 6.8: Evaluation of $\mathrm{E}_{\mathcal{H}_0}[T]$ for the MME, GLRT and the QST. For QST the exact values are depicted using (6.60) for $K \leq 11$. For the MME and the GLRT approximations (app.) are shown from (6.50) and (6.54), while the worst case upper bounds (w.c.) are evaluated from (6.62) and (6.65), respectively. Empirical values (emp.) from a Monte Carlo simulation are drawn for all three detectors. *Left:* $\rho_{\mathrm{dB}} = 1$ dB. *Right:* $K = 8$.

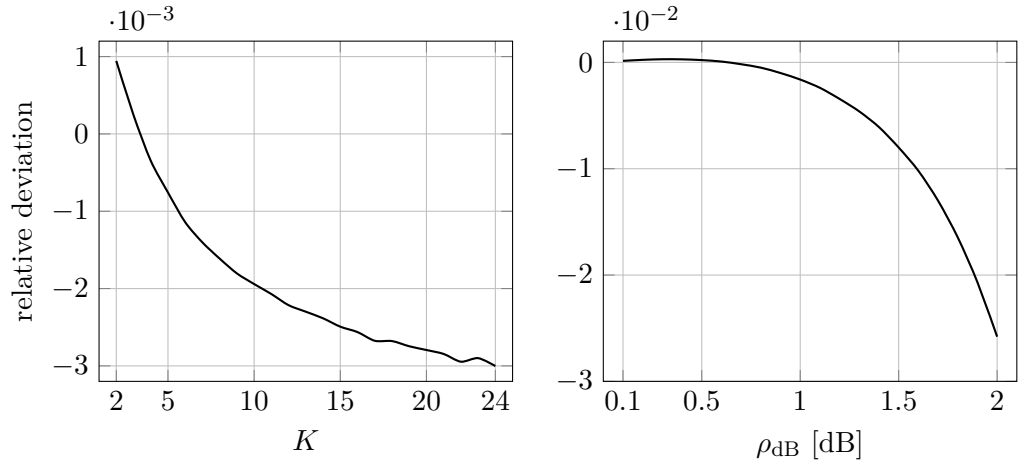

Figure 6.9: Relative deviation of the approximation of $\mathrm{E}_{\mathcal{H}_0}[T_{\mathrm{MME}}]$ of (6.50) from empirical results obtained by Monte Carlo simulation. *Left:* $\rho_{\mathrm{dB}} = 1$ dB. *Right:* $K = 8$.

A comparison between the relative errors of the approximations (6.54) and (6.56) is displayed in Figure 6.10. It is directly evident that (6.54) is superior. For 0.1 dB $\leq \rho_{\mathrm{dB}} \leq$ 2 dB, $2 \leq K \leq 24$ and $\beta = 3$ the worst relative error is around -0.44 %, while for the most parameter combinations it stays way below ± 0.1 %. Thus, we conclude that the approximation from (6.54) is an excellent substitute for the unknown exact expression of $\mathrm{E}_{\mathcal{H}_0}[T_{\mathrm{GLRT}}]$.

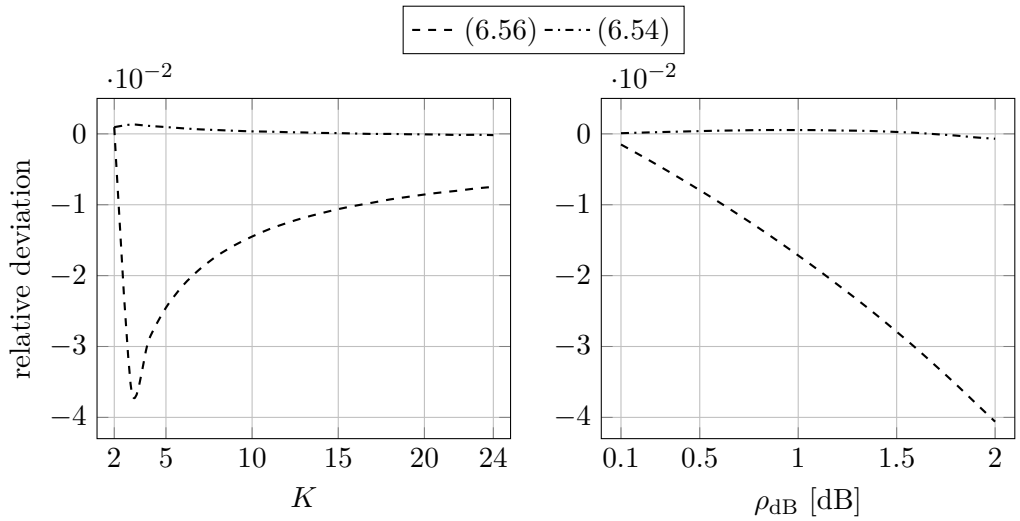

Figure 6.10: Relative deviation of the approximations of $\mathrm{E}_{\mathcal{H}_0}[T_{\mathrm{GLRT}}]$ of (6.54) and (6.56) from empirical results obtained by Monte Carlo simulation. *Left:* $\rho_{\mathrm{dB}} = 1$ dB. *Right:* $K = 8$.

From Figure 6.11 the observation that the GLRT is more robust towards noise calibration errors than the MME can be confirmed in the Gaussian scenario as well. Here one can see that the convergence to the worst case value is less profound for the MME, which is due to the shape of the PDF. That is, small deviations from the nominal value are more likely than large ones.

Evaluation of the SNR Wall Lower Bounds

Finally, we numerically evaluate the results regarding the lower bounds of the SNR walls derived in Sections 6.1.1 to 6.1.4, respectively. First, we take a look at the relative deviations of the approximations from the exact (where available) or empirical results. Then, we interpret the results and their implications for eigenvalue-based spectrum sensing systems. Note, that $\beta = 3$ for results concerning the Gaussian model.

In the preceding sections we evaluated the accuracy of the $\mathrm{E}_{\mathcal{H}_0}[T]$ approximations. Since these are used in the derivations to obtain approximations to the SNR wall

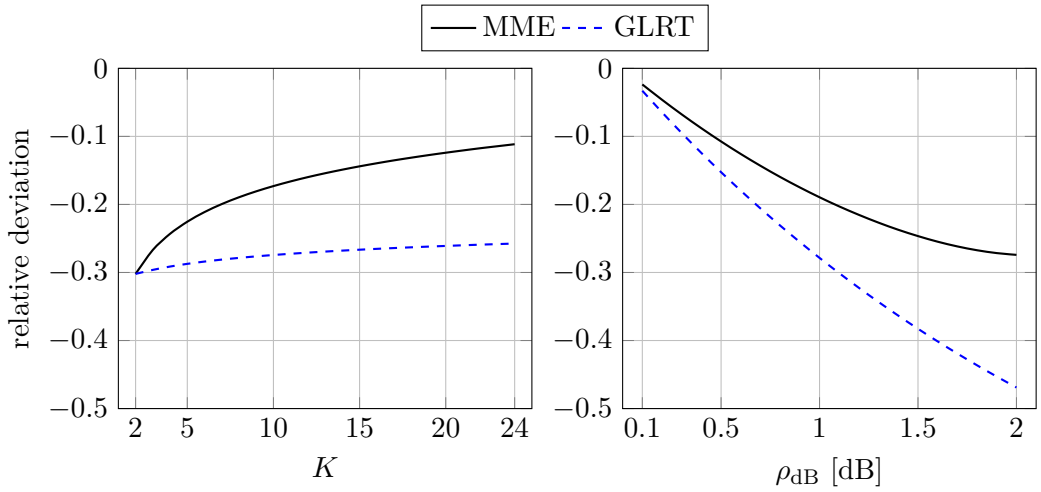

Figure 6.11: Relative deviation of $\mathrm{E}_{\mathcal{H}_0}[T]$ from the worst case upper bound (see (6.62) and (6.65), respectively). For both the MME and the GLRT empirical results from a Monte Carlo simulation are evaluated. *Left:* $\rho_{\mathrm{dB}} = 1$ dB. *Right:* $K = 8$.

lower bounds, it is of interest to evaluate their error behavior as well. For the rectangular scenario, Figure 6.12 shows the relative deviations of the approximations of the SNR wall lower bounds (i.e., (6.19), (6.25) and (6.33)) from the exact / empirical results. We notice that the relative errors are amplified compared to the ones observed for $\mathrm{E}_{\mathcal{H}_0}[T]$. However, one must keep in mind that SNR walls are typically evaluated in dB, i.e., in a logarithmic scale. Hence, errors are perceived less serious there. For example the relative deviation of ca. -0.226 attained for (6.33) at $K = 3$ and $\rho_{\mathrm{dB}} = 1$ dB translates to an error of about -1.11 dB as seen in Figure 6.14. We conclude that (6.19) and (6.25) are suitable approximations. Due to its better interpretability (6.33) might be of interest, however, one must account for larger approximation errors then. Table 6.3 summarizes the worst errors in dB-scale for the SNR wall lower bound approximations over the parameter space investigated here.

In Figure 6.13 the relative errors of the approximations to the SNR wall lower bounds (cf. (6.51) and (6.55)) are shown for the Gaussian scenario. The relative errors increase by about an order of magnitude with respect to the $\mathrm{E}_{\mathcal{H}_0}[T]$ approximations. However, one can see that the relative errors are around ± 1 % in the left part of the figure for $\rho_{\mathrm{dB}} = 1$ dB, which translates to an error of ca. ± 0.04 dB. Hence, the approximations derived for the *Gaussian* average case perform very well for the parameter space in question, see also Table 6.3.

In Figures 6.14 and 6.15 the lower bounds of the SNR walls are depicted under the rectangular and the Gaussian model, respectively. As a reference, the SNR wall of ED is shown. Both figures also depict the tighter lower bounds from (6.63)

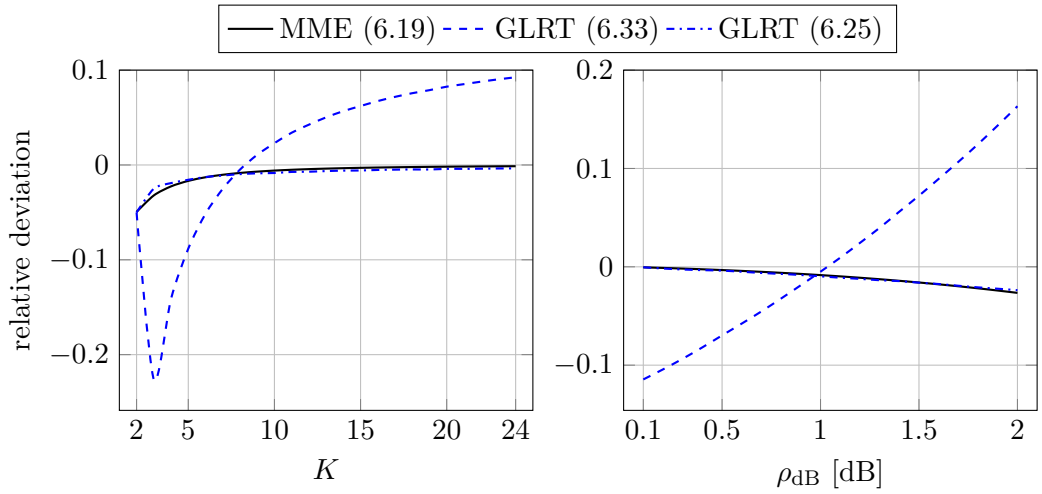

Figure 6.12: Relative deviation of the approximations of the lower bounds of the SNR wall from the exact result (MME, cf. (6.18) with inserted values from (6.7)) / empirical result (GLRT) under the *rectangular* model, respectively. For the MME the relative deviation of the approximation from (6.19) is considered, while for the GLRT the approximation (6.33) and the more accurate approximation (6.25) are evaluated. *Left:* $\rho_{\mathrm{dB}} = 1$ dB. *Right:* $K = 8$.

worst error in [dB] *rectangular* model			worst error in [dB] *Gaussian* model	
MME (6.19)	GLRT (6.25)	GLRT (6.33)	MME (6.51)	GLRT (6.55)
−0.5569 dB	−0.2975 dB	−1.6954 dB	−0.2978 dB	0.1102 dB

Table 6.3: Worst errors of the SNR wall lower bound approximations over the investigated parameter space $2 \leq K \leq 24$ and 0.1 dB $\leq \rho_{\mathrm{dB}} \leq 2.0$ dB. Note, that for the Gaussian scenario $\beta = 3$ and that $K \geq 3$ for approximations concerning the GLRT.

and (6.66) and the upper bounds from (6.74) and (6.78). The area between the upper and lower bounds is shaded to visually emphasize the region in which the true SNR wall must be located.

From the bounds one can infer that the SNR walls of the MME and the GLRT under noise calibration uncertainty are lower (for $K \geq 3$) than the SNR wall of ED under noise uncertainty, which is at -3.3292 dB for $\rho_{\mathrm{dB}} = 1$ dB. Also, in contrast to ED, a larger number of cooperating SUs leads to an improvement of the detection limit for noise calibration uncertainty for all three detectors under investigation.

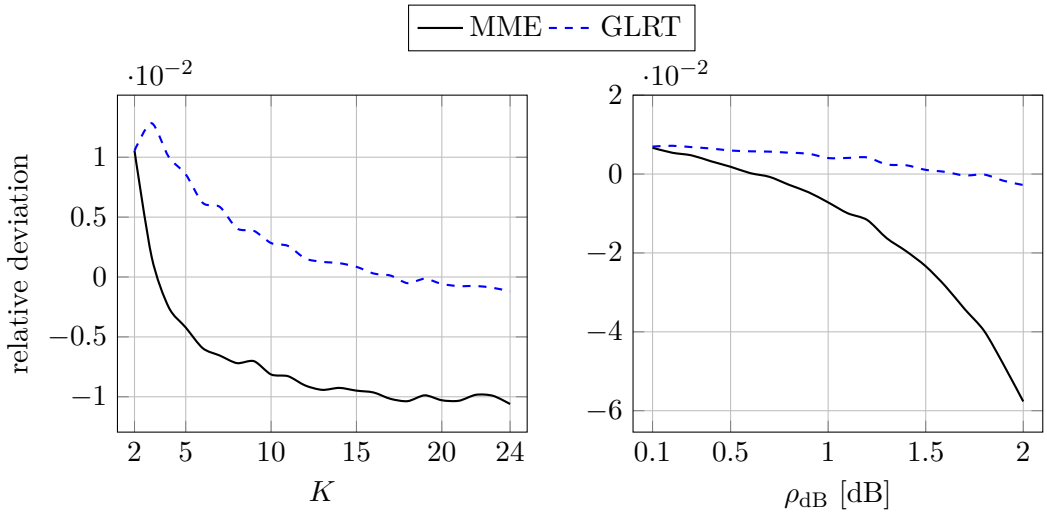

Figure 6.13: Relative deviation of the approximations of the lower bounds of the SNR wall from empirical results stemming from a Monte Carlo simulation under the *Gaussian* model. The approximations from (6.51) for the MME and (6.55) for the GLRT are evaluated here. *Left:* $\rho_{\mathrm{dB}} = 1$ dB. *Right:* $K = 8$.

To assess the fundamental performance limits of cooperative eigenvalue-based detection under noise calibration uncertainty, the SNR wall lower and upper bounds from (6.63), (6.66), (6.74) and (6.78) are the most relevant results. Since the upper and the lower bounds may be related by a factor, which is only dependent on the noise uncertainty factor ρ, the location of the exact SNR wall must lie within

$$10 \log_{10} \left(\frac{\rho^2 + 1}{\rho} \right) \mathrm{dB} \tag{6.80}$$

above the lower bound. Remarkably, the term from (6.80) is relatively stable for the parameter range considered here ($0.1\ \mathrm{dB} \leq \rho_{\mathrm{dB}} \leq 2.0\ \mathrm{dB}$), ranging from 3.0115 dB to 3.4554 dB there. In other words, these results determine the SNR wall with a remaining uncertainty of roughly 3 dB.

From these bounds, we can derive system design equations that return valuable information about the amount of required cooperating SUs and the necessary accuracy of the calibration process. The minimum required number of cooperating SUs K_{min} given a fixed average SNR α and a fixed noise calibration uncertainty factor ρ, such that the system is asymptotically guaranteed to be able to perform at an operating point of $P_{\mathrm{FA}} \leq 0.5$ and $P_{\mathrm{MD}} \leq 0.5$ is between

$$\left\lceil \frac{\rho^2 - 1}{\alpha} \right\rceil \leq K_{\mathrm{min}} \leq \left\lceil \frac{\rho^2 - 1}{\alpha} \frac{\rho^2 + 1}{\rho} \right\rceil . \tag{6.81}$$

Similarly, given a fixed average SNR α and a fixed number of cooperating SUs K, the maximum factor of tolerable noise calibration uncertainty $\rho_{\max}$ might be as small as

$$\sqrt{\alpha K + 1} \leq \rho_{\max} \,. \tag{6.82}$$

As a first example, consider the situation where the noise uncertainty factor is $\rho_{\mathrm{dB}} = 1.0$ dB and the system is expected to asymptotically detect at an SNR of $\alpha_{\mathrm{dB}} = -22$ dB, then (6.81) evaluates to $93 \leq K_{\min} \leq 191$. That means at least 93 users are needed, while without knowledge of the exact location of the SNR wall the minimum number of users might be as large as 191.

For the second example let us again assume that the desired asymptotic operating range includes $\alpha_{\mathrm{dB}} = -22$ dB and $K = 8$ cooperating SUs are available. From (6.82) we learn that without exact knowledge of the SNR wall the maximum tolerable noise uncertainty factor might be as low as $\rho_{\mathrm{dB}} = 0.1069$ dB or equivalently $\rho = 1.0249$. In other words, for this system the noise power uncertainty must not exceed ca. 2.5% after calibration.

Precise estimation of the receiver noise power is a daunting problem in spectrum sensing, see Section 6.1. Hence, typical values for the noise uncertainty factor ρ considered in the literature are comparatively large, i.e., values of $\rho_{\mathrm{dB}} = 0.5$ dB up to $\rho_{\mathrm{dB}} = 3$ dB are discussed there, cf. [17, 18, 41, 48]. As a consequence, the results obtained above indicate that cooperative eigenvalue-based spectrum sensing under noise calibration uncertainty is reliant on a high number of cooperating users to guarantee operation in the very low SNR regime. To amend the detection performance, another possibility is to extend the cooperative eigenvalue-based detectors to also exploit time correlation, see Sections 3.2 and 4.1. However, also eigenvalue-based detection using time correlation is not free of SNR walls, as shown in Section 6.2. There, uncertainty about spectral coloring of the noise process and correlation across receivers lead to fundamental detection limits.

To gain some additional insights about the robustness towards noise calibration uncertainty of the MME and the GLRT we study the gap between the tighter SNR wall lower bounds from (6.63) and (6.66) and the SNR wall lower bounds under the rectangular / Gaussian model. This evaluation also reveals the amount of "headroom" the detectors have in average cases compared to the worst case situation. While the gaps can also be seen in Figures 6.14 and 6.15, Table 6.4 gives the minimum / maximum gap over the whole parameter range studied here. As one would expect, the Gaussian prior leads to larger gaps due to the shape of its PDF. Furthermore, the greater robustness of the GLRT towards noise calibration uncertainty compared to the MME is unveiled once again in Table 6.4.

Figures 6.16 to 6.21 show the results of a Monte Carlo simulation with the aim to verify the SNR wall predictions under the average case scenarios from Sections 6.1.1

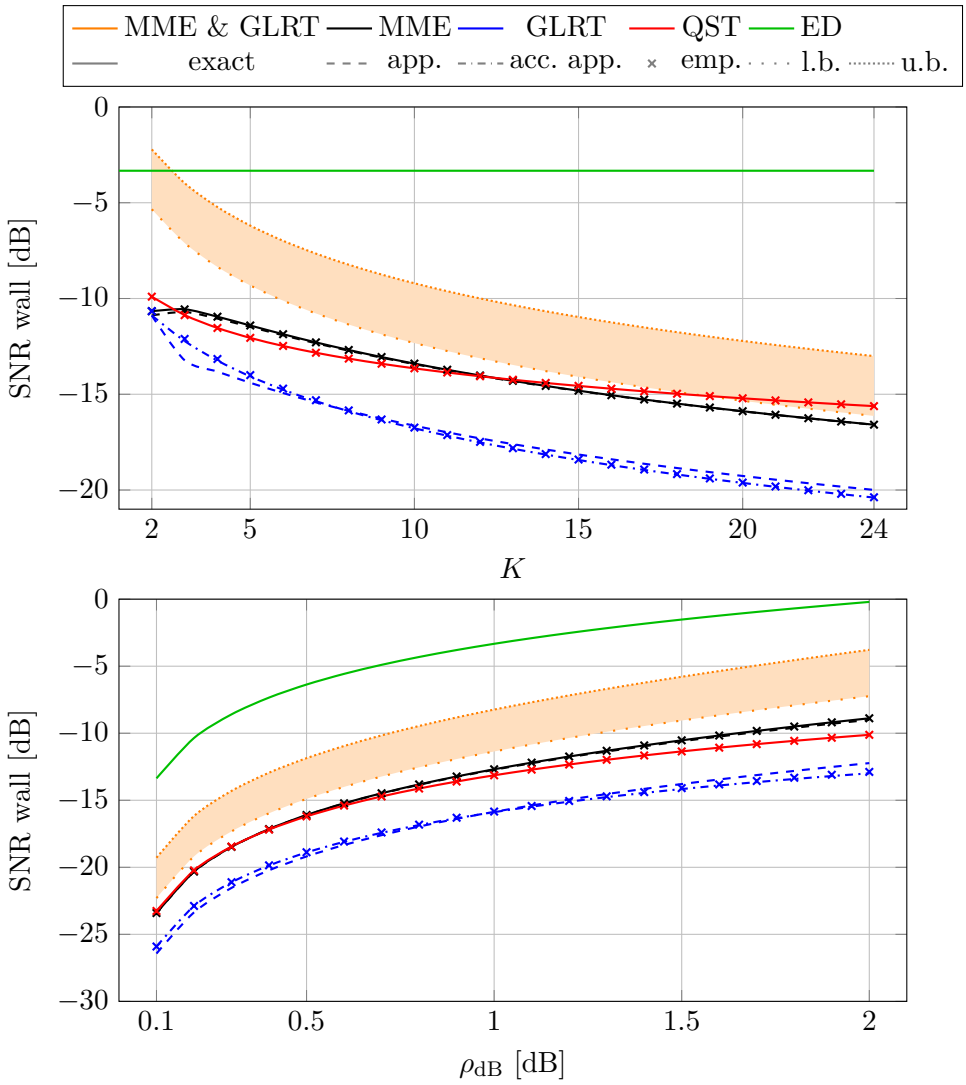

Figure 6.14: SNR walls under the *rectangular* scenario. As a point of reference, the SNR wall of ED is shown (cf. (3.53)). For the MME and the QST, the exact lower bounds are shown from (6.18) and (6.41) by inserting the exact values from (6.7) and (6.35), respectively. For the MME and the GLRT approximations (app.) to the lower bounds are evaluated from (6.19) and (6.33), where for the GLRT additionally the more precise approximation (acc. app.) from (6.25) is depicted. Empirical values (emp.) from a Monte Carlo simulation are drawn for all three detectors. Moreover, the tighter lower bounds (l.b.) from (6.63) and (6.66) and the upper bounds (u.b.) from (6.74) and (6.78), are evaluated for the MME and the GLRT, respectively. *Top:* $\rho_{\mathrm{dB}} = 1$ dB. *Bottom:* $K = 8$.

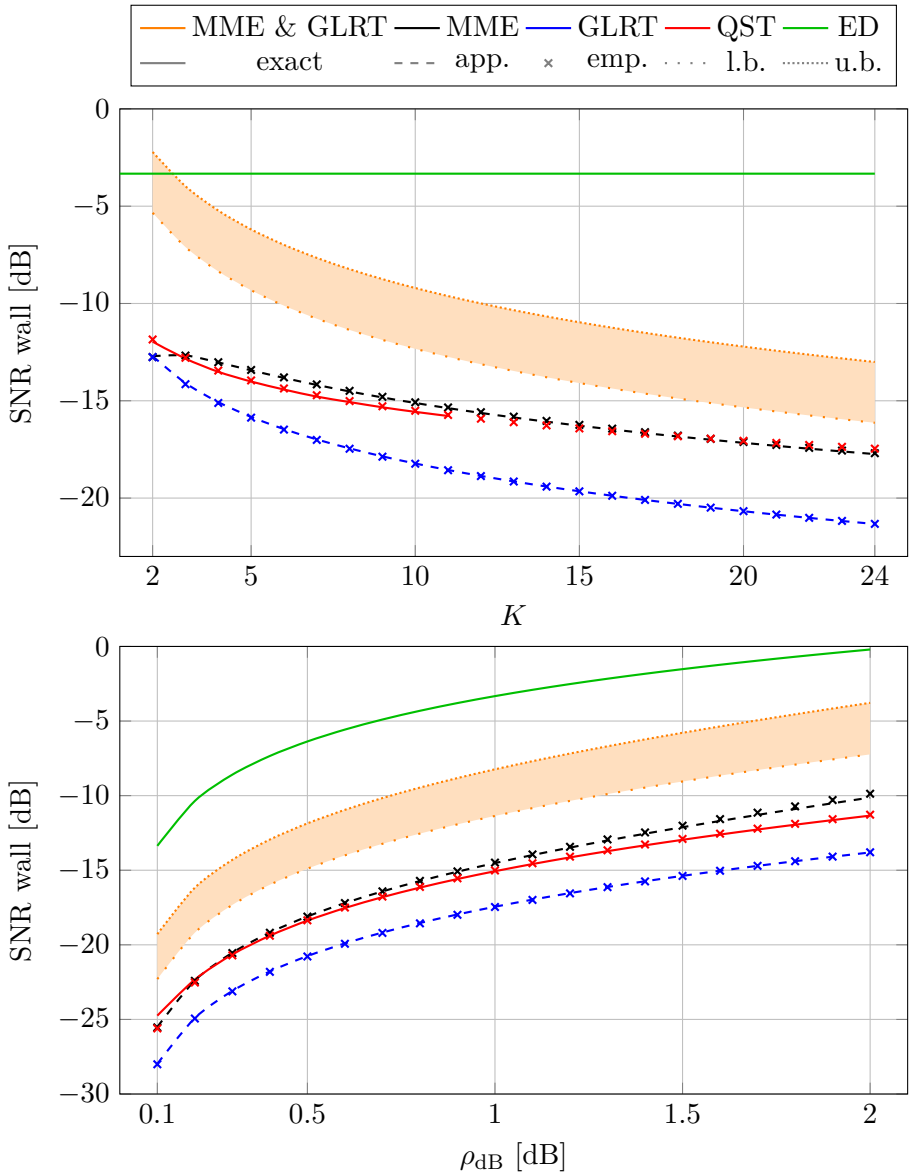

Figure 6.15: SNR walls under the *Gaussian* scenario. As a point of reference, the SNR wall of ED is shown (cf. (3.53)). For the QST, the exact lower bound is shown from (6.41) by inserting the exact values from (6.60) for $K \leq 11$. For the MME and the GLRT approximations (app.) to the lower bounds are evaluated from (6.51) and (6.55). Empirical values (emp.) from a Monte Carlo simulation are drawn for all three detectors. Moreover, the tighter lower bounds (l.b.) from (6.63) and (6.66) and the upper bounds (u.b.) from (6.74) and (6.78), are evaluated for the MME and the GLRT, respectively. *Top:* $\rho_{\mathrm{dB}} = 1$ dB. *Bottom:* $K = 8$.

	gap in [dB] *rectangular* model		gap in [dB] *Gaussian* model	
detector	min.	max.	min.	max.
MME	0.3700	5.9867	0.6690	7.4308
GLRT	3.2844	5.9127	4.7490	7.2725

Table 6.4: Minimum and maximum gap in [dB] between the tighter SNR wall lower bounds from (6.63) and (6.66) and the SNR wall lower bounds in the rectangular / Gaussian scenario over the parameter range 0.1 dB $\leq \rho_{\text{dB}} \leq$ 2 dB and $2 \leq K \leq 24$. For the MME under the rectangular average case, the exact lower bound (6.18) is used to find the gaps by inserting exact values from (6.7). For lower bounds of the GLRT under both models and the MME under the Gaussian average case empirical values from a Monte Carlo simulation are taken to calculate the gaps. Note, that for the Gaussian model $\beta = 3$ and that $K \geq 3$ for the values concerning the GLRT.

and 6.1.2, respectively. There, the results were averaged from a Monte Carlo simulation with 50000 instances, which was developed in `MATLAB` [128]. In each instance, a block detection attempt with N samples taken from the K cooperating users. Under $\mathcal{H}_0$, the complex Gaussian noise was drawn according to the model from Sections 6.1.1 and 6.1.2, respectively. Under $\mathcal{H}_1$, perfect calibration was assumed, such that the noise vector $\mathbf{w}(t)$ was drawn i.i.d. from a complex circularly symmetric standard Gaussian distribution ($\mathcal{CN}(\mathbf{0}_K, \mathbf{I}_K)$). The K channel coefficients, that remain constant during one instance, were drawn i.i.d. from a $\mathcal{CN}(0,1)$ distribution and the channel coefficient vector was subsequently normalized to accelerate convergence of the simulations. The PU signal under $\mathcal{H}_1$ used a PSK modulation with eight signaling points on the unit circle. Each symbol was drawn uniformly from this modulation alphabet and was subsequently scaled, such that the desired average SNR from (4.10) is achieved statistically. In every instance, each of the three detectors in question was executed under both Hypotheses. Finally, the P_{MD} was estimated for a target $P_{\text{FA}} = 0.5$, i.e., the detection threshold was chosen to be the median of the 50000 instances of the test statistics under $\mathcal{H}_0$. This procedure was repeated for a range of block sizes N ranging from 50000 to 500000 in steps of 50000 samples and for a range of different SNRs in 0.2 dB steps.

The Figures 6.16 to 6.21 depict the resulting estimate of P_{MD} color coded from blue (0) via white (0.5) to red (1), where each little block in the image corresponds to the parameter combination of the average SNR α and the block size N indicated by the axes. In all figures, a very rapid transition between perfect detection ($P_{\text{MD}} = 0$) to complete detection failure ($P_{\text{MD}} = 1$) is seen. This is the visualization of the SNR wall encountered by the detectors. Also, it can be seen that the predictions

stemming from the derivations in Sections 6.1.1 and 6.1.2 match the empirical results very closely.

Beyond that, two interesting effects of the finite sample size detectors are visualized, one of which is rather intuitive and the other is not. Consider Figure 6.17, where both effects are particularly apparent. Before the SNR wall, increasing the block size results in higher detection performance, which can be seen in the column showing the results with an SNR of -15.8 dB. In the column above (SNR: -16.0 dB), however, increasing the block size increases the probability of missed detection P_{MD}. There, the medians of the test statistic under both hypotheses have switched their order, which is evident by noting that $P_{\mathrm{MD}} > 0.5$ for $P_{\mathrm{FA}} = 0.5$. Since increasing the block size decreases the variance of the test statistic PDFs, also the overlap of the PDFs is reduced. Hence, when the order of the medians is swapped, P_{MD} may increase when N is increased. For practical settings of the false alarm rate (for example $P_{\mathrm{FA}} = 0.01$), however, successful detection is almost impossible then.

6.1.6 Summary

This section investigated the effects of an imperfect noise power calibration on the performance of cooperative eigenvalue-based spectrum sensing systems on the example of three well-known detectors: MME, GLRT and QST. It was shown that uncertainties in the noise power calibration lead to fundamental performance limits, which present themselves through an SNR threshold below which reliable detection becomes impossible, even if the number of samples goes to infinity. Said phenomenon is called an SNR wall. Three scenarios were examined in this context: two average case scenarios with rectangular / Gaussian distributed SU noise powers after calibration and the worst case analysis.

The worst case analysis resulted in lower- and upper bounds on the SNR wall for the MME and the GLRT detector in the asymptotic regime. Said bounds allow localizing the SNR wall within a remaining uncertainty of roughly 3 dB. Additionally, the bounds show that the SNR wall is dependent on the number of cooperating SUs, such that the detection limit can be counteracted by increasing their number. Perhaps surprisingly, MME and GLRT share the same lower- and upper bounds. It is therefore tempting to conjecture that their exact SNR wall, which is unknown and must be derived under the worst case, might coincide as well.

The average case scenarios, under which lower bounds on the SNR walls were developed for all three detectors in the asymptotic regime, show that the GLRT is more resilient to noise calibration uncertainties than the MME. The obtained results for the rectangular and Gaussian scenarios give viable indications about the

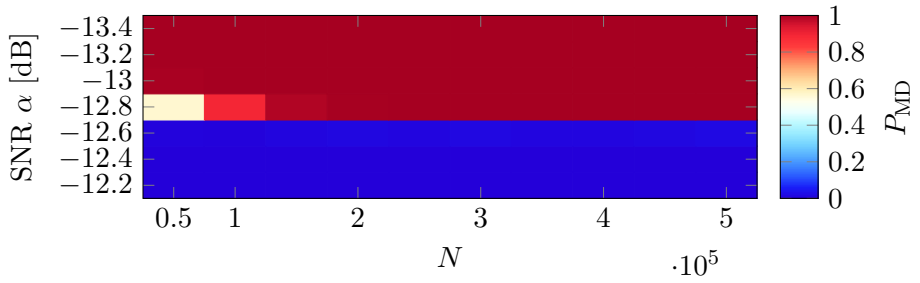

Figure 6.16: P_{MD} of the MME estimated by Monte Carlo simulations using different block sizes N for $K = 8$, $\rho_{\mathrm{dB}} = 1$ dB and target $P_{\mathrm{FA}} = 0.5$ under the *rectangular* model. The SNR wall is predicted by (6.18) (inserting exact values from (6.7)) at -12.6883 dB in this case.

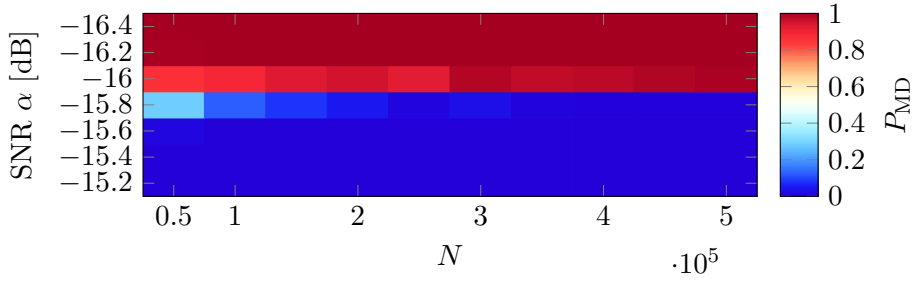

Figure 6.17: P_{MD} of the GLRT estimated by Monte Carlo simulations using different block sizes N for $K = 8$, $\rho_{\mathrm{dB}} = 1$ dB and target $P_{\mathrm{FA}} = 0.5$ under the *rectangular* model. The SNR wall is predicted by (6.25) at -15.8855 dB in this case.

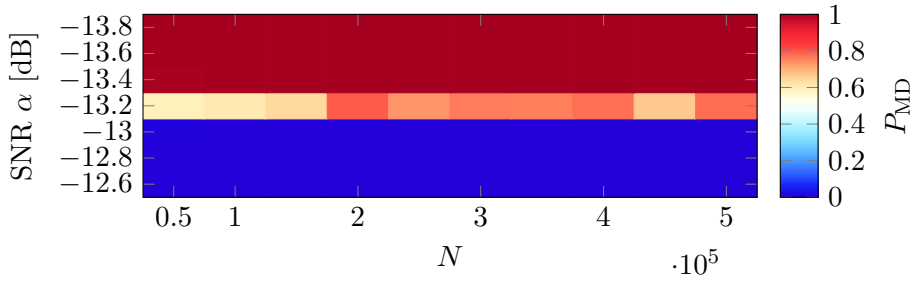

Figure 6.18: P_{MD} of the QST estimated by Monte Carlo simulations using different block sizes N for $K = 8$, $\rho_{\mathrm{dB}} = 1$ dB and target $P_{\mathrm{FA}} = 0.5$ under the *rectangular* model. The SNR wall is predicted by (6.41) (inserting exact values from (6.35)) at -13.1381 dB in this case.

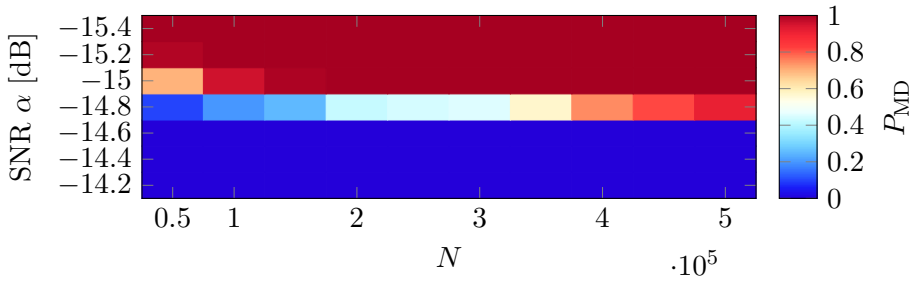

Figure 6.19: P_{MD} of the MME estimated by Monte Carlo simulations using different block sizes N for $K = 8$, $\rho_{\mathrm{dB}} = 1$ dB, $\beta = 3$ and target $P_{\mathrm{FA}} = 0.5$ under the *Gaussian* model. The SNR wall is predicted by (6.51) at -14.5201 dB in this case.

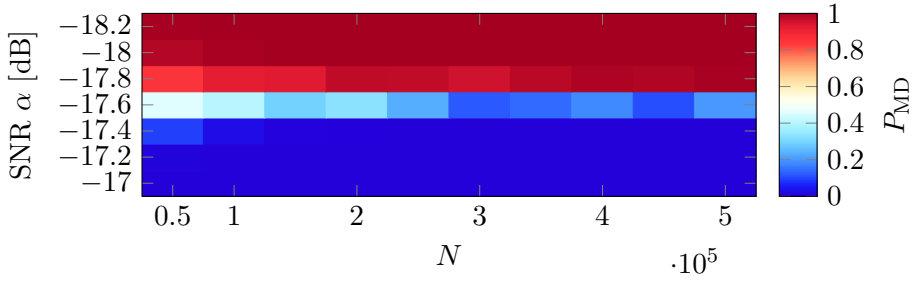

Figure 6.20: P_{MD} of the GLRT estimated by Monte Carlo simulations using different block sizes N for $K = 8$, $\rho_{\mathrm{dB}} = 1$ dB, $\beta = 3$ and target $P_{\mathrm{FA}} = 0.5$ under the *Gaussian* model. The SNR wall is predicted by (6.55) at -17.4469 dB in this case.

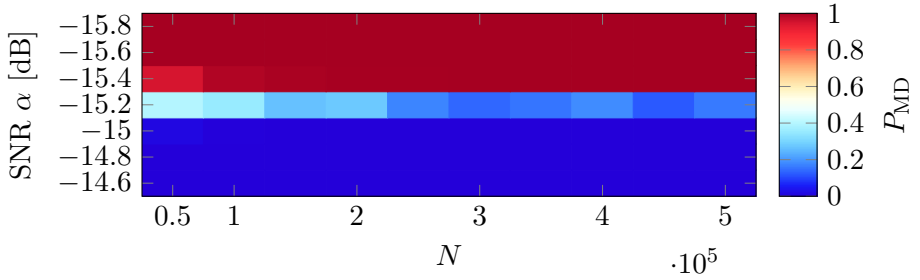

Figure 6.21: P_{MD} of the QST estimated by Monte Carlo simulations using different block sizes N for $K = 8$, $\rho_{\mathrm{dB}} = 1$ dB, $\beta = 3$ and target $P_{\mathrm{FA}} = 0.5$ under the *Gaussian* model. The SNR wall is predicted by (6.41) (inserting exact values from (6.60)) at -15.0665 dB in this case.

amount of headroom a certain detector has in average case situations in contrast to its worst case behavior.

In summary, it was concluded that a very high number of cooperating SUs or a very precise noise calibration is needed to ensure a detection limit that is below the desired SNRs in spectrum sensing, which are as low as -22 dB. It is doubtful, that operation of cooperative eigenvalue-based spectrum sensing systems can be guaranteed in practical settings without also exploiting correlation over time.

6.2 Colored and Correlated Noise

In this section, we briefly study the effect of colored and correlated noise in a cooperative eigenvalue-based spectrum sensing system. The performance limits in the presence of these model uncertainties are quantified on the example of the MME detector, which was introduced in Section 3.2.1. Parts of this section have been published in [29, 30].

Eigenvalue-based detectors rely on the assumption that a receivers' noise can be modeled as a white random process and that the noise is uncorrelated among different receivers, see Section 3.2. Since the detectors are sensitive to correlations, it is obvious that noise coloring and noise correlation have adverse effects on the detection performance.

The aggregate noise experienced by a SU can be divided into internal and external parts. Internal noise is caused by the receivers' radio frequency front end, which includes the electronic circuitry after the antenna up to and including the analog-to-digital converter. While some types of noise, such as thermal noise, are accurately modeled by AWGN, other types of noise have frequency dependent power spectral densities, cf. [136, p. 5 ff., Ch. 1].

Moreover, coloring of the noise process may be caused by the receivers' filtering. In [19] it is assumed that the receiver filter is perfectly known and that its effects may thus be reversed by applying certain pre-whitening procedures. However, ideal filter design is not exactly realizable in practice and also the processing intended to invert the coloring is unlikely to be perfect. As a result, a residual amount of coloring is easily conceivable.

External noise is the superposition of unintended disturbances that are not intrinsically generated by the receiver itself. Realistic examples of non-white noise are atmospheric noise, galactic radiation noise and man-made noise. The former two have power spectral densities which are not flat [137]. The latter may cause correlations due to two effects. Firstly, it is impulsive in nature, see [138, 139]. Thus, it affects samples in bursts and leads to correlations over time. Secondly, it may cause noise correlation among receivers, if their geographical location subjects them to

noise which is partially generated by the same sources. Since man-made noise is created by electronic devices and power transmission lines, it can hardly be avoided.

In summary, assuming perfectly white noise which is uncorrelated between different receivers is a simplification that is only accurate up to a certain degree.

For the analysis, model $\mathcal{M}_{\mathrm{DM}}$ from Section 4.2.1 is used and it is assumed that the channel coefficients are equal, i.e., $\mathbf{h} = \mathbf{1}_K$. As a result, all SUs experience the same SNR. This simplification is chosen to achieve tractable results. While the random processes describing signal and noise ($\mathbf{x}(t)$ and $\mathbf{w}(t)$) are still presumed to be wide-sense stationary, the noise process is not considered to be white and uncorrelated between different SUs anymore. As a result, $\mathbf{R}_{\tilde{\mathbf{w}}} \neq \sigma_w^2 \mathbf{I}_{\tilde{K}}$.

We describe the correlation in the noise covariance matrix $\mathbf{R}_{\tilde{\mathbf{w}}}$ by noise correlation coefficients $\epsilon_{ij} = \frac{\mathrm{Cov}[\tilde{w}_i, \tilde{w}_j]}{\sigma_w^2}$ for $1 \leq i, j \leq \tilde{K}$. Analogously, the signal covariance matrix is represented by the signal correlation coefficients $\varrho_{ij} = \frac{\mathrm{Cov}[\tilde{x}_i, \tilde{x}_j]}{\sigma_s^2}$ for $1 \leq i, j \leq \tilde{K}$. Hence, under our system model it holds that $[\mathbf{R}_{\tilde{\mathbf{w}}}]_{1 \leq i,j \leq \tilde{K}} = \sigma_w^2 \epsilon_{ij}$ and $[\mathbf{R}_{\tilde{\mathbf{x}}}]_{1 \leq i,j \leq \tilde{K}} = \sigma_s^2 \varrho_{ij}$, where $\epsilon_{ii} = \varrho_{ii} = 1$.

Based on the definitions above, a lower bound on $\mathrm{E}_{\mathcal{H}_0}[T_{\mathrm{MME}}]$ and an upper bound on $\mathrm{E}_{\mathcal{H}_1}[T_{\mathrm{MME}}]$ in the asymptotic regime ($N \to \infty$) can be derived. By characterizing the SNR region under which the bounds overlap, conservative lower bound on the SNR wall was found in [29, 30].

In the following, we summarize simplified results for the situation in which $\epsilon_{ij} = 0$ for $i \neq j$ under $\mathcal{H}_1$ is assumed. Please refer to [29, 30] for the detailed derivations. The lower bound on the SNR wall for the MME detector under the system model described above is

$$\alpha_{\mathrm{wall}}^{\mathrm{MME}} \geq \frac{c_\epsilon - 1}{1 + c_\varrho + c_\epsilon (c_\varrho - 1)} \,. \tag{6.83}$$

There, $\epsilon_{\max} = \max_{i \neq j} \epsilon_{ij}$ and the constants c_ϵ and c_ϱ are defined as

$$c_\epsilon = \frac{1 + |\epsilon_{\max}|}{1 - |\epsilon_{\max}|} \tag{6.84}$$

and

$$c_\varrho = \max_i \sum_{\substack{j=1 \\ j \neq i}}^{\tilde{K}} |\varrho_{ij}| \,, \tag{6.85}$$

respectively. Note, that this bound is only valid if the following condition is fulfilled:

$$\alpha < \frac{1}{c_\varrho - 1} \,. \tag{6.86}$$

As can be seen from (6.83) and (6.85), $\tilde{K}-1$ parameters ϱ_{ij} are needed to evaluate the lower bound. Defining $\varrho_{\max} = \max_{i \neq j} \varrho_{ij}$, it is easy to see that

$$(\tilde{K}-1)\,|\varrho_{\max}| \geq c_{\varrho}\,. \tag{6.87}$$

Thus, by replacing c_{ϱ} by its upper bound from (6.87) in (6.83) we loosen the bound and obtain a new lower bound on the SNR wall of the MME:

$$\alpha_{\text{wall}}^{\text{MME}} \geq \frac{c_{\epsilon}-1}{1+(\tilde{K}-1)\,|\varrho_{\max}|\,(1+c_{\epsilon})-c_{\epsilon}}\,. \tag{\textbf{6.88}}$$

Although the new bound from (6.88) is not as tight as (6.83), it only depends on the parameters $\tilde{K}$, $|\varrho_{\max}|$ and $|\epsilon_{\max}|$. Thus, it is more convenient to evaluate than (6.83). Note, that this bound is valid under the condition

$$\alpha < \frac{1}{(\tilde{K}-1)\,|\varrho_{\max}|-1}\,. \tag{\textbf{6.89}}$$

Evidently, $|\varrho_{\max}| \leq 1$ holds for the (largest) signal correlation coefficient. Hence, by evaluating (6.88) with $|\varrho_{\max}| = 1$, a lower bound for the best case situation in terms of signal correlation is obtained. This implies that the signal covariance matrix $\mathbf{R}_{\tilde{\mathbf{x}}}$ must be of rank one in this case.

In Figure 6.22, the lower bound from (6.88) is evaluated with $|\varrho_{\max}| = 1$ and for different values of $\tilde{K}$ and $|\epsilon_{\max}|$. Even for best case signal correlation, it can be seen that the lower bound on the SNR wall only drops below -20 dB for some combinations of $\tilde{K}$ and $|\epsilon_{\max}|$. As we mentioned above, we expect this lower bound to be rather loose in practice, i.e., we conjecture the true SNR wall to be located considerably above the bound.

In summary, even for this very idealized system model with constant channel $\mathbf{h} = \mathbf{1}_{\tilde{K}}$, equal SNR and perfect signal correlation, the lower bound on the SNR wall of the MME detector in the presence of colored / correlated noise lies in the immediate vicinity of the desired low SNR operating range. Hence, these results suggest that the detrimental effect of noise coloring and correlated receiver noise must be carefully considered in practical systems. It seems reasonable to aim at extending our findings to more realistic system models in future studies and to strive for obtaining tighter bounds. Furthermore, it would be sensible to investigate the performance limits of other eigenvalue-based detectors.

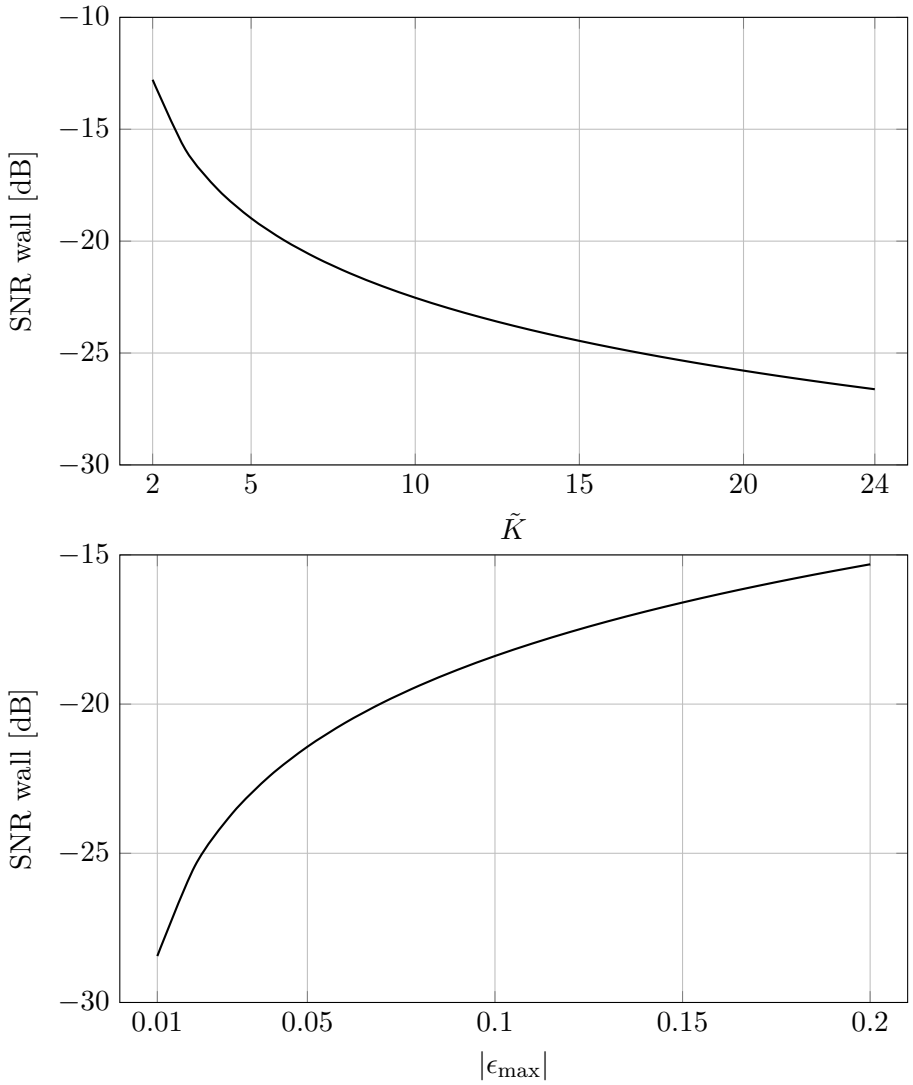

Figure 6.22: Lower bound on the SNR wall of the MME detector in the presence of colored and correlated noise from (6.88) evaluated with $|\varrho_{\max}| = 1$. *Top:* $|\epsilon_{\max}| = 0.05$. *Bottom:* $\tilde{K} = 8$.

6.3 Summary

In this chapter, the effect of model uncertainties on cooperative eigenvalue-based spectrum sensing systems was examined. Insights on the robustness of certain detectors and performance limits in the form of bounds on the SNR walls were obtained. Two practical model uncertainties were considered.

Firstly, imperfect calibration of the SUs noise powers was analyzed and the performance impact in the asymptotic regime ($N \to \infty$) on three detectors (MME, GLRT and QST, see Sections 3.2.1 to 3.2.3) was studied. For this investigation, no time correlation was incorporated. It was found that all three detectors suffer from the SNR wall phenomenon. An average case analysis, which assumes the calibrated noise powers follow a known probability distribution, yielded lower bounds on the SNR wall for rectangular and Gaussian distributions. The GLRT was found to be the most resilient detector in this case. Using a worst case analysis, upper and (tighter) lower bounds on the SNR wall were derived for the GLRT and the MME detector. The latter bounds allow location of the SNR wall with a remaining uncertainty of roughly 3 dB. However, all of these bounds are inversely proportional to the number of SUs K, such that the SNR threshold can be influenced to a certain degree.

Secondly, the effect of colored and correlated noise was briefly studied on the example of the MME detector. A conservative lower bound on the SNR wall was derived, which depends on three parameters: the dimension $\tilde{K}$ of the sample covariance matrix, the maximum signal correlation coefficient and the maximum noise correlation coefficient under $\mathcal{H}_0$.

For both model uncertainties the (lower) bounds on the SNR walls lie above or in close vicinity of the desired low SNR operating range, i.e., -20 dB to -22 dB. This suggests, that in practical scenarios proper noise calibration must be implemented and coloring / correlation in the noise must be taken into account if one desires to achieve robust detection in the low SNR regime.

7 Theoretical Analysis of the MMME Block Detector

In this chapter, the MMME detector [24] is analyzed from a theoretical perspective. Under a very simple system model, i.e., model $\mathcal{M}_{\mathrm{DM}}$ with two cooperating SUs, the PDFs of the test statistic under both hypotheses are derived in Section 7.1. Since under this model, also the test statistic PDFs of the MME detector can be derived under both hypotheses (see Sections 5.3.2 and 5.3.3), the performance of both detectors can be compared on the basis of these theoretical results. This is done in Section 7.2. Parts of this chapter have been published in [26].

7.1 Test Statistic Distributions

For the derivations, system model $\mathcal{M}_{\mathrm{DM}}$ from Section 4.2.1 without exploiting time correlation and without oversampling ($Q = M = 1$) is employed, which is a very simple AWGN model. While this model allows identifying the distributions of the sample covariance matrices under both hypotheses for a general number of cooperating SUs K (see Section 5.3.1), we confine the model to $K = 2$ to obtain analytical results.

In order to derive the PDFs of the test statistic T_{MMME}, see (3.27), the joint PDF of the ordered eigenvalues of the sample covariance matrix is needed under both hypotheses. For both derivations in Sections 7.1.1 and 7.1.2, the non-normalized sample covariance matrix $\hat{\mathbf{R}}$ is utilized and additionally the noise variance is assumed to be $\sigma_w^2 = 1$. This is done to ease the readability of the derivations. Subsequently, using a suitable transformation, the derived PDFs are generalized to allow arbitrary noise powers and to respect the normalization present in standard sample covariance matrices.

Let the joint PDF of the ordered eigenvalues of the non-normalized sample covariance matrix $\hat{\mathbf{R}}$ be denoted by $f_{\hat{\boldsymbol{\lambda}}}(\hat{\boldsymbol{\lambda}})$. Since we confine the number of SUs to $K = 2$, the eigenvalues and the test statistic of the MMME are related by the following transformation

$$\hat{\lambda}_2 = \hat{\lambda}_1 + T_{\mathrm{MMME}}\,. \tag{7.1}$$

Performing said transformation on the joint PDF of the eigenvalues gives the desired PDF of the test statistic:

$$\tilde{f}(\tilde{T}) = \int_0^\infty f_{\hat{\boldsymbol{\lambda}}}(\hat{\lambda}_1, \hat{\lambda}_1 + \tilde{T})\,\mathrm{d}\hat{\lambda}_1\,. \tag{7.2}$$

Here, the notation $\tilde{f}$ and $\tilde{T}$ stands for the PDF and test statistic belonging to the non-normalized version of the detector with the additional assumption $\sigma_w^2 = 1$, respectively. Hence, for both hypotheses the derivation of the test statistic PDF corresponds to solving the integral above. This is done in Section 7.1.1 under $\mathcal{H}_0$ and in Section 7.1.2 under $\mathcal{H}_1$, respectively.

7.1.1 Derivation of the Test Statistic PDF under Hypothesis $\mathcal{H}_0$

Under $\mathcal{H}_0$, the non-normalized sample covariance matrix $\hat{\mathbf{R}}_0$ with $\sigma_w^2 = 1$ is a complex uncorrelated central Wishart matrix of dimension K with N degrees of freedom, see Section 5.3.1. A convenient representation of the joint PDF of the eigenvalues of $\hat{\mathbf{R}}_0$ for this case can be found with Table 3.1 and (3.39).

Since we assume that $K = 2$, the PDF simplifies to

$$f_{\hat{\boldsymbol{\lambda}}}(\hat{\boldsymbol{\lambda}}) = \frac{(\hat{\lambda}_2 - \hat{\lambda}_1)^2 (\hat{\lambda}_1 \hat{\lambda}_2)^{(N-2)} e^{-(\hat{\lambda}_1 + \hat{\lambda}_2)}}{(N-1)!\,(N-2)!}\,. \tag{7.3}$$

Inserting (7.3) into the transformation (7.2) and solving the integral yields:

$$\begin{aligned}\tilde{f}_0(\tilde{T}) &= \frac{\tilde{T}^2\, e^{-\tilde{T}}}{(N-1)!\,(N-2)!} \int_0^\infty e^{-2\hat{\lambda}_1} (\hat{\lambda}_1 + \tilde{T})^{(N-2)} \hat{\lambda}_1^{(N-2)}\,\mathrm{d}\hat{\lambda}_1 \\ &= \frac{\tilde{T}^{\left(N+\frac{1}{2}\right)}\, \mathcal{K}_{\left(\frac{3}{2}-N\right)}\left(\tilde{T}\right)}{\sqrt{\pi}\,\Gamma(N)\, 2^{\left(N-\frac{3}{2}\right)}}. \end{aligned} \tag{7.4}$$

There, we used the definite integral from [32, p. 348, Eq. (3.383.8)], where $\mathcal{K}_a(v)$ is the modified Bessel function of the second kind of order a, cf. [32, p. 910 ff., Sec. 8.4] or [31, p. 374 ff., Sec. 9.6]. Furthermore, we have used the relation from (2.24). Note, that (7.4) is only valid for $\tilde{T} \geq 0$ and that $\tilde{f}_0(\tilde{T}) = 0$ for $\tilde{T} < 0$.

In contrast to the MME detector the MMME detector is dependent on the noise power σ_w^2 as well as the typically present normalization factor of the sample covariance matrix $\hat{\mathbf{R}}$. When considering the normalized sample covariance matrix, the eigenvalues $\hat{\boldsymbol{\lambda}}$ must be scaled by N^{-1} compared to the non-normalized case

derived above. Similarly, a noise power $\sigma_w^2 \neq 1$ results in a scaling factor σ_w^2 for the eigenvalues. Hence, using the simple transformation

$$T = \frac{\sigma_w^2}{N}\tilde{T} \tag{7.5}$$

that results in the transformed PDF

$$f(T) = \frac{N}{\sigma_w^2}\,\tilde{f}\left(\frac{TN}{\sigma_w^2}\right), \tag{7.6}$$

one may find the desired generalized version of the PDF.

Applying this transformation to (7.4) results in the test statistic PDF of the MMME under $\mathcal{H}_0$:

$$f_0(T) = \frac{T^{\left(N+\frac{1}{2}\right)} N^{\left(N+\frac{3}{2}\right)} \mathcal{K}_{\left(\frac{3}{2}-N\right)}\left(\frac{TN}{\sigma_w^2}\right)}{\sqrt{\pi}\,\Gamma(N)\,2^{\left(N-\frac{3}{2}\right)}\,\sigma_w^{(2N+3)}}, \tag{7.7}$$

which is only valid for $T \geq 0$, while $f_0(T) = 0$ for $T < 0$.

A plot of $f_0(T)$ is shown in Figure 7.1 for different numbers of samples N and fixed noise variance $\sigma_w^2 = 1$. As one would expect, increasing the number of samples N reduces the variance of the PDF and also reduces its mean. The latter is a bias due resulting from the estimation of the covariance matrix with a finite amount of samples. Asymptotically, i.e., for $N \to \infty$, the T_{MMME} is zero under $\mathcal{H}_0$, see also [24].

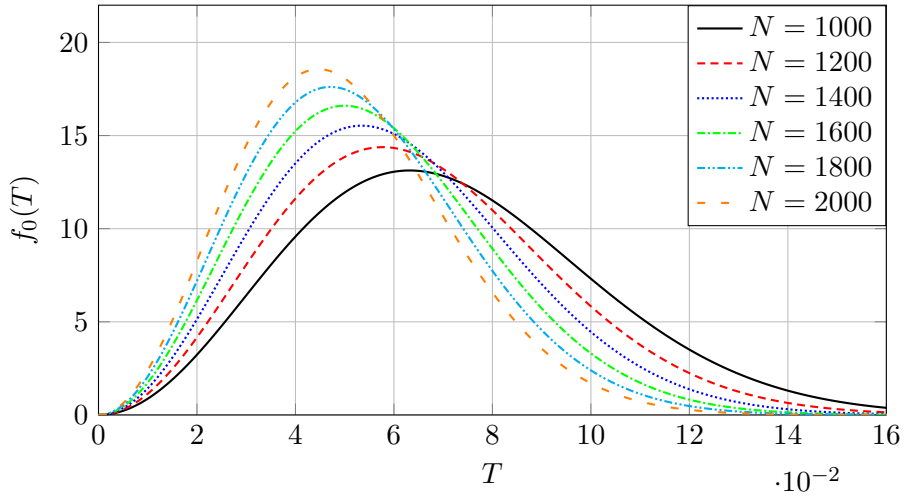

Figure 7.1: $f_0(T)$ for different number of samples N and noise power $\sigma_w^2 = 1$.

In Figure 7.2, the dependency of $f_0(T)$ on the noise variance σ_w^2 is visualized by plotting the PDF with varying σ_w^2 and fixed N. It can be clearly seen that increasing σ_w^2 increases the variance and also shifts the mean away from zero.

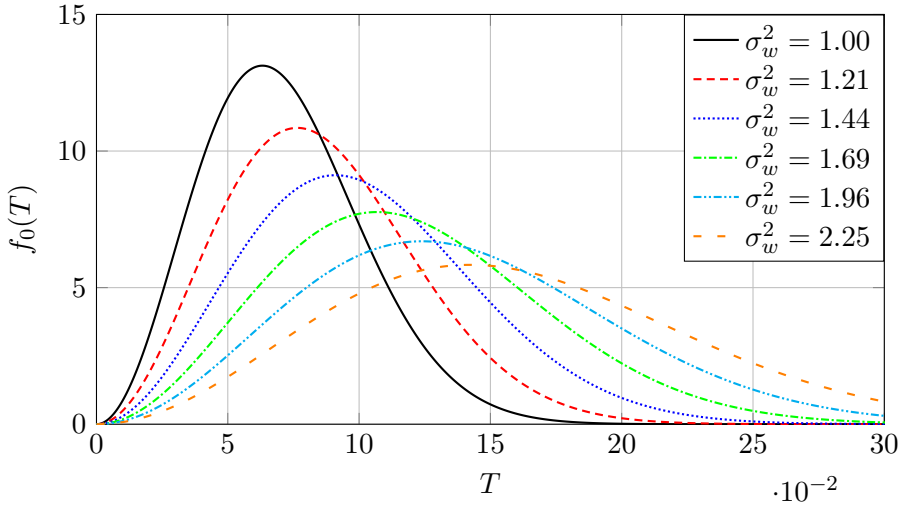

Figure 7.2: $f_0(T)$ for different values of the noise variance σ_w^2 and $N = 1000$ number of samples.

The influence of the noise variance σ_w^2 or more precisely the uncertainty about the same is further investigated in Section 7.2.2.

7.1.2 Derivation of the Test Statistic PDF under Hypothesis $\mathcal{H}_1$

Under $\mathcal{H}_1$ the non-normalized sample covariance matrix $\hat{\mathbf{R}}_1$ with $\sigma_w^2 = 1$ is a complex uncorrelated non-central Wishart matrix of dimension K with N degrees of freedom, see Section 5.3.1. This distribution depends on a parameter called the non-centrality matrix $\boldsymbol{\Omega}$. Under model $\mathcal{M}_{\mathrm{DM}}$, it is a rank one matrix and can be given explicitly as $\boldsymbol{\Omega} = \alpha N \, \mathbf{1}_{K\times K}$. Thus, also the vector of ordered eigenvalues $\boldsymbol{\omega}$ of $\boldsymbol{\Omega}$ may be given analytically, cf. (5.7). Here, where $K = 2$, these follow as $\omega_2 = 2\alpha N$ and $\omega_1 = 0$. As argued in Section 5.3.1, this model is exact for PUs using PSK modulations and a very good approximation for general digitally modulated PU signals.

The joint PDF of the eigenvalues of the non-normalized sample covariance matrix $\hat{\mathbf{R}}_1$ with $\sigma_w^2 = 1$ can be found with see also Table 3.1 and (3.39). Partially substituting the parameter vector $\boldsymbol{\omega}$ with the explicit values given above and inserting $K = 2$ leads to the following form:

$$f_{\hat{\boldsymbol{\lambda}}}(\hat{\boldsymbol{\lambda}}) = \frac{e^{-(2\alpha N)} e^{-(\hat{\lambda}_1+\hat{\lambda}_2)} (\hat{\lambda}_2 - \hat{\lambda}_1)(\hat{\lambda}_1\hat{\lambda}_2)^{(N-2)}}{2\alpha N \left[(N-2)!\right]^2} \left|\mathbf{F}(\hat{\boldsymbol{\lambda}};\boldsymbol{\omega})\right| . \tag{7.8}$$

There, $\left|\mathbf{F}(\hat{\boldsymbol{\lambda}};\boldsymbol{\omega})\right|$ is the determinant of a 2×2 matrix where the (i,j)-th entry is composed of ${}_0\mathcal{F}_1(N-1;\hat{\lambda}_{(3-j)}\omega_{(3-i)})$, which is defined using the standard generalized hypergeometric function (2.29).

Here, where $K = 2$ and $\omega_2 \neq \omega_1$, the determinant can be explicitly calculated to

$$\begin{aligned}\left|\mathbf{F}(\hat{\boldsymbol{\lambda}};\boldsymbol{\omega})\right| &= {}_0\mathcal{F}_1(N-1;2\alpha N\hat{\lambda}_2)\,{}_0\mathcal{F}_1(N-1;0) - {}_0\mathcal{F}_1(N-1;2\alpha N\hat{\lambda}_1)\,{}_0\mathcal{F}_1(N-1;0)\\ &= {}_0\mathcal{F}_1(N-1;2\alpha N\hat{\lambda}_2) - {}_0\mathcal{F}_1(N-1;2\alpha N\hat{\lambda}_1)\,, \end{aligned} \tag{7.9}$$

where it was used that ${}_0\mathcal{F}_1(N-1;0) = 1$. Inserting (7.8) into the transformation (7.2) yields:

$$\begin{aligned}\tilde{f}_1(\tilde{T}) =& \frac{\tilde{T}\,e^{-\tilde{T}}e^{-(2\alpha N)}}{2\alpha N\,[(N-2)!]^2}\int_0^\infty e^{-(2\hat{\lambda}_1)}\hat{\lambda}_1^{(N-2)}(\hat{\lambda}_1+\tilde{T})^{(N-2)}\\ &\left[{}_0\mathcal{F}_1(N-1;2\alpha N(\hat{\lambda}_1+\tilde{T})) - {}_0\mathcal{F}_1(N-1;2\alpha N\hat{\lambda}_1)\right]\mathrm{d}\hat{\lambda}_1\,. \end{aligned} \tag{7.10}$$

To the best of our knowledge, the definite integral in (7.10) does not possess a closed-form solution. Hence, we take a similar path to the work in [25,126] (compare also Section 5.3.3), and aim at obtaining a series representation of the PDF. Firstly, we rewrite the hypergeometric function in terms of the modified Bessel function of the first kind of order a, denoted by $\mathcal{I}_a(v)$, by using the identity (5.31). Secondly, we proceed to replace the Bessel function by its series expansion, see (5.33).

Inserting (5.31) and (5.33) into (7.10) and simplifying gives

$$\begin{aligned}\tilde{f}_1(\tilde{T}) =& \frac{\tilde{T}e^{-\tilde{T}}e^{-(2\alpha N)}}{2\alpha N\,\Gamma(N-1)}\sum_{i=0}^{\infty}\frac{(2\alpha N)^i}{\Gamma(i+1)\,\Gamma(i+N-1)}\\ &\left[\int_0^\infty \hat{\lambda}_1^{(N-2)}(\hat{\lambda}_1+\tilde{T})^{(i+N-2)}\,e^{-2\hat{\lambda}_1}\,\mathrm{d}\hat{\lambda}_1\right.\\ &\left.-\int_0^\infty \hat{\lambda}_1^{(i+N-2)}(\hat{\lambda}_1+\tilde{T})^{(N-2)}\,e^{-2\hat{\lambda}_1}\,\mathrm{d}\hat{\lambda}_1\right], \end{aligned} \tag{7.11}$$

where we have also used the relation from (2.24). To find a solution to the integrals in (7.11), we perform the substitution $\Lambda = \frac{\hat{\lambda}_1}{\tilde{T}}$ and obtain

$$\begin{aligned}\tilde{f}_1(\tilde{T}) =& \frac{e^{-\tilde{T}}e^{-(2\alpha N)}}{2\alpha N\,\Gamma(N-1)}\sum_{i=0}^{\infty}\frac{(2\alpha N)^i\,\tilde{T}^{(i+2N-2)}}{\Gamma(i+1)\,\Gamma(i+N-1)}\\ &\left[\int_0^\infty \Lambda^{(N-2)}(\Lambda+1)^{(i+N-2)}\,e^{-(2\tilde{T}\Lambda)}\,\mathrm{d}\Lambda\right.\\ &\left.-\int_0^\infty \Lambda^{(i+N-2)}(\Lambda+1)^{(N-2)}\,e^{-(2\tilde{T}\Lambda)}\,\mathrm{d}\Lambda\right]. \end{aligned} \tag{7.12}$$

Now, both definite integrals in (7.12) can be found in terms of Tricomi's confluent hypergeometric function, denoted by $\mathcal{U}(a,b,c)$, see (2.30). Using the definite integrals, we finally get:

$$\tilde{f}_1(\tilde{T}) = \frac{e^{-\tilde{T}} e^{-(2\alpha N)}}{\Gamma(N-1)} \sum_{i=0}^{\infty} \frac{(2\alpha N)^{(i-1)} \tilde{T}^{(i+2N-2)}}{\Gamma(i+1)\,\Gamma(i+N-1)} \left[\Gamma(N-1)\,\mathcal{U}\left(N-1, i+2N-2, 2\tilde{T}\right) - \Gamma(i+N-1)\,\mathcal{U}\left(i+N-1, i+2N-2, 2\tilde{T}\right)\right], \tag{7.13}$$

which is only valid for $\tilde{T} \geq 0$ and $\tilde{f}_1(\tilde{T}) = 0$ for $\tilde{T} < 0$.

Analogous to the approach in Section 7.1.1, we must apply the transformation from (7.6) to (7.13) such that arbitrary noise powers σ_w^2 and the typically present normalization factor of the sample covariance matrix are accounted for. Applying said transformation finally results in the test statistic of the MMME under $\mathcal{H}_1$:

$$f_1(T) = \frac{e^{-\left(\frac{TN}{\sigma_w^2}\right)} e^{-(2\alpha N)}}{\Gamma(N-1)} \sum_{i=0}^{\infty} \frac{(2\alpha N)^{(i-1)} N^{(i+2N-1)} T^{(i+2N-2)}}{\Gamma(i+1)\,\Gamma(i+N-1)\,\sigma_w^{(2i+4N-2)}} \left[\Gamma(N-1)\,\mathcal{U}\left(N-1, i+2N-2, \frac{2TN}{\sigma_w^2}\right) - \Gamma(i+N-1)\,\mathcal{U}\left(i+N-1, i+2N-2, \frac{2TN}{\sigma_w^2}\right)\right], \tag{7.14}$$

which is only valid for $T \geq 0$ and $f_1(T) = 0$ for $T < 0$.

Figure 7.3 visualizes $f_1(T)$ for different SNRs and also depicts $f_0(T)$ as a reference. Higher SNRs predominantly increase the mean of the PDF, while only slightly increasing the variance.

To verify the theoretical findings, a Monte Carlo simulation with 50000 instances was performed using `MATLAB` [128]. In each instance a sample covariance matrix was calculated using $N = 1000$ samples, where the samples were generated according to the specifications of model $\mathcal{M}_{\mathrm{DM}}$ with $K = 2$ SUs. There, the PU used PSK modulation with eight signaling points. The MMME detector was run on the estimated matrix in each instance. Finally, a histogram of the obtained values of the test statistic under the respective hypothesis was created. In Figure 7.3, the resulting empirical PDFs are drawn as crosses for $f_0(T)$ and for $f_1(T)$ with $\alpha = -13$ dB. Clearly, the empirical results confirm our theoretical derivations.

7.1.3 Techniques for Numerical Evaluation of the PDFs for Large N

Both test statistic PDFs of the MMME are expressed using functions that are difficult to evaluate for large N, which are required in very low SNR spectrum sensing

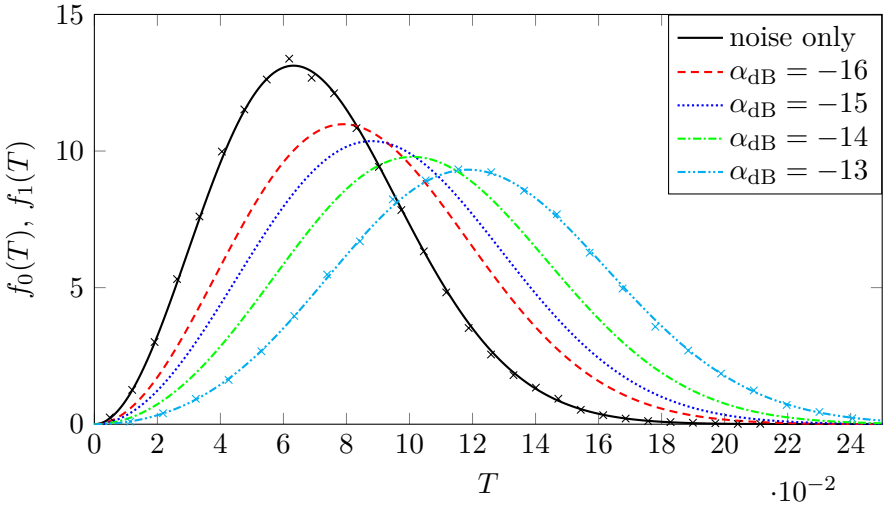

Figure 7.3: $f_0(T)$ and $f_1(T)$ for different values of the SNR α_{dB} in [dB], $N = 1000$ number of samples and noise power $\sigma_w^2 = 1$. Empirical results from a Monte Carlo simulation are indicated by crosses.

applications. Even advanced numerical computing software such as `MATLAB` [128] typically cannot handle evaluating $\mathcal{K}_a(v)$, $\mathcal{U}(a, b, v)$ and $\Gamma(v)$ for large N, which appear in (7.4) and (7.13), with built-in routines. More precisely, the numerical range needed to evaluate these functions exceeds the (64 bit) IEEE 754 double precision floating point format (also called binary64) [127]. This section presents techniques to tackle this problem and gives versions of both PDFs, which were used to evaluate the PDF in this chapter.

Evaluation of the $\mathcal{H}_0$ PDF for large N

To increase readability of the derivations, we start with the formulation from (7.4), which assumes a non-normalized sample covariance matrix and fixed noise power $\sigma_w^2 = 1$. However, the transformation from (7.6) can easily be implemented in software, such that the result can be readily generalized.

Starting from (7.4), we first use the following identity [32, p. 928, Eq. (8.485)]

$$\mathcal{K}_a(v) = \frac{\pi}{2} \frac{\mathcal{I}_{-a}(v) - \mathcal{I}_a(v)}{\sin(a\pi)}, \tag{7.15}$$

where a must not be integer. Obviously this condition is always fulfilled in (7.4).

Inserting (7.15) into (7.4) results in:

$$\begin{aligned}\tilde{f}_0(\tilde{T}) &= \frac{\sqrt{\pi}\,\tilde{T}^{\left(N+\frac{1}{2}\right)}}{\Gamma(N)\,2^{\left(N-\frac{3}{2}\right)}\,\sin\left(\left(\frac{3}{2}-N\right)\pi\right)}\,\left(\mathcal{I}_{\left(N-\frac{3}{2}\right)}(\tilde{T})-\mathcal{I}_{\left(\frac{3}{2}-N\right)}(\tilde{T})\right)\\ &= \frac{\sqrt{\pi}}{\sin\left(\left(\frac{3}{2}-N\right)\pi\right)}\left(\underbrace{\frac{\tilde{T}^{\left(N+\frac{1}{2}\right)}\,\mathcal{I}_{\left(N-\frac{3}{2}\right)}(\tilde{T})}{2^{\left(N-\frac{3}{2}\right)}\Gamma(N)}}_{:=\varsigma_1(\tilde{T})}-\underbrace{\frac{\tilde{T}^{\left(N+\frac{1}{2}\right)}\,\mathcal{I}_{\left(\frac{3}{2}-N\right)}(\tilde{T})}{2^{\left(N-\frac{3}{2}\right)}\Gamma(N)}}_{:=\varsigma_2(\tilde{T})}\right). \quad (7.16)\end{aligned}$$

Note, that we have defined two functions $\varsigma_1(\tilde{T})$ and $\varsigma_2(\tilde{T})$, which are treated separately in the following.

The goal of the following steps is to obtain a series representation of the terms $\varsigma_1(\tilde{T})$ and $\varsigma_2(\tilde{T})$, where we try to perform the numerically critical parts of the calculations in the logarithmic space to increase the scope of the parameter N that can be successfully evaluated using (64 bit) IEEE double precision floating point arithmetic. For this we make use of the logarithmic Gamma function $\log(\Gamma(v))$ for which the built-in `gammaln` routine is available in `MATLAB` [128] that allows numerically stable evaluation of said function for large arguments v.

Inserting the series representation for $\mathcal{K}_a(v)$ from (5.33) into $\varsigma_1(\tilde{T})$ as defined in (7.16) and rearranging the numerically critical calculations such that they are performed in the logarithmic domain, it follows:

$$\begin{aligned}\varsigma_1(\tilde{T}) &\approx \sum_{i=0}^{I_s}\frac{\tilde{T}^{(2N+2i-1)}}{4^{(N+i-1)}\,\Gamma(i+1)\,\Gamma(N)\,\Gamma\left(N+i-\frac{1}{2}\right)}\\ &= \sum_{i=0}^{I_s}\exp\Bigg(\,(2N+2i-1)\log(\tilde{T})-(N+i-1)\log(4)\\ &\quad -\log(\Gamma(i+1))-\log(\Gamma(N))-\log\left(\Gamma\left(N+i+\frac{1}{2}\right)\right)\Bigg). \qquad (\mathbf{7.17})\end{aligned}$$

Note, that if $I_s \to \infty$ the approximation converges to the true value of $\varsigma_1(\tilde{T})$. Naturally, for numerical evaluation this is impossible, such that after $i = I_s$ the summation is stopped. This approximation is viable, since we have observed that after a certain point the contribution of the further summands becomes negligible. One can see, that by exploiting the logarithmic identities we have transformed the numerically critical evaluations of the Gamma functions in the ratio to subtractions in the logarithmic domain.

Inserting the series expansion (5.33) of $\mathcal{K}_a(v)$ into $\varsigma_2(\tilde{T})$ as defined in (7.16) we gain the following form after simplifying:

$$\varsigma_2(\tilde{T}) \approx \frac{1}{2}\sum_{i=0}^{I_s}\frac{\tilde{T}^{(2i+2)}}{4^i\,\Gamma(i+1)\,\Gamma(N)\,\Gamma\left(\frac{1}{2}+i-(N-2)\right)}. \qquad (7.18)$$

There, the term $\Gamma\left(\frac{1}{2}+i-(N-2)\right)$ is problematic, since depending on the values of i and N, the argument of the Gamma function is negative. In contrast to positive arguments, for negative arguments the Gamma function may become negative itself. Evidently, evaluating it in the logarithmic space is not possible directly in this case. Hence, we must distinguish the two cases $i < N-2$ and $i \geq N-2$. In the latter case, the argument of the Gamma function is always positive and we may directly evaluate its values in logarithmic scale. To handle cases when $i < N-2$, the following identity is helpful, with $v \in \mathbb{N}$ [129, p. 479, Eq. (8.106f)]:

$$\Gamma\left(\frac{1}{2}-v\right) = \frac{(-1)^v\, 4^v\, \Gamma(v+1)\,\sqrt{\pi}}{\Gamma(2v+1)}\,, \tag{7.19}$$

where we have also used the relation (2.24).

Treating the two cases separately, using (7.19) and performing the critical calculation in the logarithmic domain leads to:

$$\begin{aligned}
\varsigma_2(\tilde{T}) &= \frac{1}{2}\sum_{i=0}^{N-3} \frac{(-1)^{(N-2-i)}\,\tilde{T}^{(2i+2)}\,\Gamma(2(N-2-i)+1)}{4^{(N-2)}\,\Gamma(i+1)\,\Gamma(N)\,\Gamma(N-1-i)\,\sqrt{\pi}} \\
&\quad + \frac{1}{2}\sum_{i=N-2}^{I_s} \frac{\tilde{T}^{(2i+2)}}{4^i\,\Gamma(i+1)\,\Gamma(N)\,\Gamma\left(\frac{1}{2}+i-(N-2)\right)} \\
&= \frac{1}{2}\sum_{i=0}^{N-3} \frac{(-1)^{(N-2-i)}}{\sqrt{\pi}} \exp\Big((2i+2)\log(i) + \log(\Gamma(2(N-2-i)+1)) \\
&\qquad - (N-2)\log(4) - \log(\Gamma(i+1)) - \log(\Gamma(N)) - \log(\Gamma(N-1-i))\Big) \\
&\quad + \frac{1}{2}\sum_{i=N-2}^{I_s} \exp\Bigg((2i+2)\log(\tilde{T}) - i\log(4) - \log(\Gamma(i+1)) \\
&\qquad - \log(\Gamma(N)) - \log\left(\Gamma\left(\frac{1}{2}+i-(N-2)\right)\right)\Bigg)\,.
\end{aligned} \tag{7.20}$$

Choosing a suitable limit I_s for the sum, the PDF $\tilde{f}_0(\tilde{T})$ can now be numerically approximated with the results from above as

$$\tilde{f}_0(\tilde{T}) = \frac{\sqrt{\pi}}{\sin\left(\left(\frac{3}{2}-N\right)\pi\right)}\left(\varsigma_1(\tilde{T}) - \varsigma_2(\tilde{T})\right)\,. \tag{7.21}$$

Using this representation, we were able to evaluate the PDF for $N > 100000$. The appropriate limit I_s depends on the parameters. However, for most cases $I_s \leq 1000$ are sufficient. That also means that evaluating the sum for the second case ($i \geq N-2$) in (7.20) is not needed in most cases with large N.

Evaluation of the $\mathcal{H}_1$ PDF for large N

The goal in this section is the same as in the preceding one. Namely, to reformulate the test statistic PDF in order to perform numerically critical calculations in the logarithmic domain.

Besides this, however, the function $\mathcal{U}(a,b,c)$ is typically not directly included in many mathematical software libraries. Hence, we manually evaluate the function in its integral form (2.30) numerically. It is problematic that the integral is improper since the upper limit is infinity. A common technique in numerical integration is to transform improper integrals using a suitable substitution, such that the resulting integrand can be integrated over a standard interval, e.g., $[0,1]$. Here, the substitution $v = a + \frac{u}{1-u}$ with $u = \frac{v-a}{1+v-a}$ and $\mathrm{d}v = \frac{1}{(1-u)^2}\,\mathrm{d}u$, is appropriate. For a general integrand $o(v)$ it follows:

$$\int_a^\infty o(v)\,\mathrm{d}v = \int_0^1 o\left(a + \frac{u}{1-u}\right)\frac{1}{(1-u)^2}\,\mathrm{d}u\,. \tag{7.22}$$

Performing this substitution on the integral in question leads to the following form of the function $\mathcal{U}(a,b,c)$:

$$\mathcal{U}(a,b,c) = \frac{1}{\Gamma(a)}\int_0^1 \exp\left(\frac{-cv}{1-v}\right)\frac{v^{(a-1)}}{(1-v)^b}\,\mathrm{d}v\,. \tag{7.23}$$

Starting from (7.13), which assumes a non-normalized sample covariance matrix and $\sigma_w^2 = 1$, by inserting (7.23) we arrive at:

$$\begin{aligned}\tilde{f}_1(\tilde{T}) = \frac{e^{-\tilde{T}}e^{-(2\alpha N)}}{\Gamma(N-1)}\sum_{i=0}^{\infty}\frac{(2\alpha N)^{(i-1)}\tilde{T}^{(i+2N-2)}}{\Gamma(i+1)\,\Gamma(i+N-1)} \\ \left(\int_0^1 \exp\left(\frac{-2\tilde{T}v}{1-v}\right)\frac{v^{(N-2)}}{(1-v)^{(i+2N-2)}}\,\mathrm{d}v\right. \\ \left. - \int_0^1 \exp\left(\frac{-2\tilde{T}v}{1-v}\right)\frac{v^{(i+2N-2)}}{(1-v)^{(i+2N-2)}}\,\mathrm{d}v\right)\,.\end{aligned} \tag{7.24}$$

Rewriting this result, so that the critical calculations are done in the logarithmic domain, leads to the following formulation, which also incorporates the approxima-

tion of the infinite series by a finite one stopping after $i = I_s$:

$$\begin{aligned}\tilde{f}_1(\tilde{T}) = \sum_{i=0}^{I_s} \Bigg(\int_0^1 \exp\Bigg(& -(2\alpha N) - \tilde{T} - \frac{2\tilde{T}v}{1-v} + (i-1)\log(2\alpha N) \\ & + (i+2N-2)\log(\tilde{T}) - \log(\Gamma(i+1)) - \log(\Gamma(i+N-1)) \\ & - \log(\Gamma(N-1)) + (N-2)\log(v) + (i+2N-2)\log(1-v) \Bigg) \, \mathrm{d}v \\ - \int_0^1 \exp\Bigg(& -(2\alpha N) - \tilde{T} - \frac{2\tilde{T}v}{1-v} + (i-1)\log(2\alpha N) \\ & + (i+2N-2)\log(\tilde{T}) - \log(\Gamma(i+1)) - \log(\Gamma(i+N-1)) \\ & - \log(\Gamma(N-1)) + (i+2N-2)\log(v) \\ & + (i+2N-2)\log(1-v) \Bigg) \, \mathrm{d}v \Bigg) \, . \end{aligned} \tag{7.25}$$

In every summand, a numerical integration must be performed for which we chose a trapezoidal quadrature rule (see [31, p. 885, Eq. (25.4.2)]) with a step size of $5 \cdot 10^{-5}$ to evaluate (7.25) in this work.

Using the formulation from (7.25) we were able to numerically evaluate the PDF for $N > 100000$. Appropriate choices of I_s are dependent on the parameters. In most cases, though, $I_s \leq 4000$ yields a very precise approximation. Note, that the transformation from (7.6), which can be easily applied to (7.25) in software, allows generalization to normalized sample covariance matrices and noise variances $\sigma_w^2 \neq 1$.

7.2 Performance Comparison with the MME Block Detector

This section compares the performance of the MME and the MMME detector based on theoretical results. For both detectors, the test statistic PDFs are now available for both hypotheses under model $\mathcal{M}_{\mathrm{DM}}$ (cf. Section 4.2.1) with $K = 2$ cooperating SUs. Said results can be found in Section 7.1 for the MMME (see (7.7) and (7.14)) and Sections 5.3.2 and 5.3.3 for the MME (see (5.25) and (5.38)).

7.2.1 Receiver Operating Characteristic

The most common way of assessing and comparing the performance of detectors is by examining the ROC, see also Section 3.1. If the CDFs of the test statistic were

known under both hypotheses, the ROC could be calculated directly. Although a CDF is known for the MME detector under Hypothesis $\mathcal{H}_0$ [125], the other PDFs are highly complicated and analytical forms of their respective integrals remain unknown to us. However, having exact expressions for the PDFs, the CDFs can be evaluated by numerical integration very accurately.

Let, for this comparison, the PDFs of the test statistic of the MME be denoted by g_0 under $\mathcal{H}_0$ and g_1 under $\mathcal{H}_1$. Their corresponding CDFs are identified by G_0 and G_1, respectively. The threshold of the MME is denoted by h_{MME}, so that its probability of false alarm $P_{\mathrm{fa,MME}}$ and its probability of detection $P_{\mathrm{d,MME}}$ can be related to the CDFs / PDFs using (3.3) to (3.5). Likewise, let f_0, f_1 and F_0, F_1 denote the PDFs and CDFs of the MMME detector under $\mathcal{H}_0$ and $\mathcal{H}_1$, respectively. Then, with its threshold h_{MMME}, the probability of false alarm $P_{\mathrm{fa,MMME}}$ and the probability of detection $P_{\mathrm{d,MMME}}$ of the MMME can be determined analogously.

Using numerical integration with a trapezoidal quadrature rule (cf. [31, p. 885, Eq. (25.4.2)]) the CDFs were obtained for both detectors for a range of 100 thresholds each. In Figure 7.4, the ROCs of both detectors are depicted for three different SNRs with $N = 1000$ number of samples per block and noise power $\sigma_w^2 = 1$.

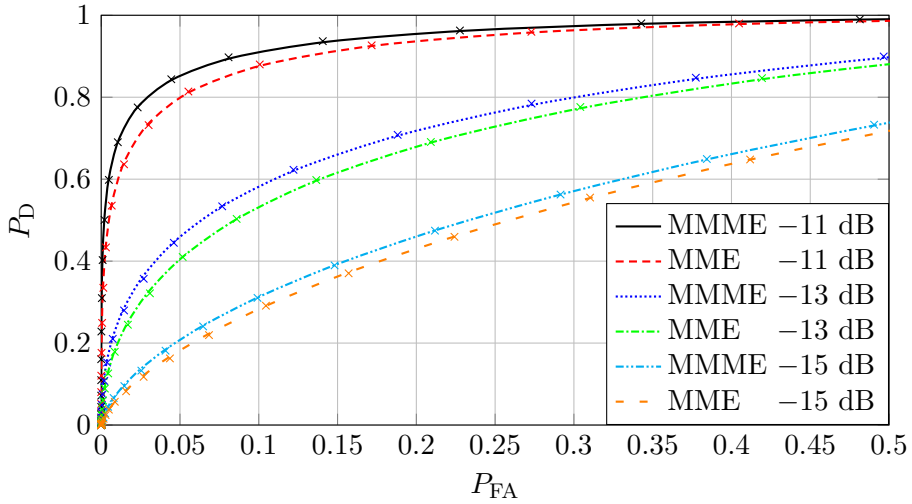

Figure 7.4: ROCs of the MMME and the MME detector for different SNRs with $N = 1000$ number of samples and noise power $\sigma_w^2 = 1$. The crosses indicate empirical values obtained from a Monte Carlo simulation.

As a verification of the theoretical results, a Monte Carlo simulation with 50000 blocks was performed. There, in each instance, both detectors were run on samples created according to model $\mathcal{M}_{\mathrm{DM}}$ under the $\mathcal{H}_0$ and $\mathcal{H}_1$ hypotheses. A vector of 100 equally spaced thresholds was used to estimate the corresponding CDFs, which were used to calculate the ROCs. These are drawn with crosses in Figure 7.4. A similar calculation of the ROC for the MME was performed for $N = 500$ in [25].

Firstly, we note that the predicted performance is in agreement with the empirical results. Secondly, as was reported in [24] under a different system model, the MMME detector clearly outperforms the MME detector.

7.2.2 Noise Uncertainty Evaluation

The test statistic PDFs of the MME is independent of the noise variance σ_w^2 under $\mathcal{H}_0$ and only dependent on the SNR α under $\mathcal{H}_1$. Hence, in order to set the detection threshold h_{MME} knowledge of σ_w^2 is not required. In contrast, both test statistic PDFs of the MMME are dependent on the noise variance. This means, that the noise variance σ_w^2 must be known in order to set the threshold precisely for this detector.

We have shown that the MMME detector performs better than the MME detector under ideal conditions in the preceding Section 7.2.1. Since the precise noise power σ_w^2 is usually unknown at the receiver, it must be estimated. For a robust detection the uncertainty of the noise power estimation must be taken into account when setting the detector threshold of the MMME, see also Section 3.5. Hence, its performance deteriorates as the noise power uncertainty increases. If the noise power of all SUs is equal, the performance of the MME remains unaffected. Naturally, the question arises how much noise uncertainty can be tolerated, so that the MMME detector still performs better or equal than the MME detector.

For this analysis, let σ_w^2 and α denote the actual noise power and SNR, respectively. The noise power estimation is assumed to return a value that is accurate within a bounded interval $[\rho^{-1}\,\sigma_w^2, \rho\,\sigma_w^2]$, compare also Section 3.5. When designing the threshold h_{MMME}, it is usually desired to attain a false alarm rate that is below or equal to a predefined value. Thus, in order to have an upper bounded $P_{\mathrm{fa,MMME}}$, the noise power must be assumed to be $\rho\,\sigma_w^2$ to set the threshold robustly.

Suppose the threshold of the MME detector h_{MME} was set, so that the false alarm rate is $P_{\mathrm{fa,MME}}$. In order to find the threshold of the MMME detector h_{MMME}, which results in the same detection performance, it must hold $P_{\mathrm{d,MME}} = P_{\mathrm{d,MMME}}$ and hence

$$h_{\mathrm{MMME}} = F_1^{-1}(G_1(h_{\mathrm{MME}}))\,. \tag{7.26}$$

Then, we have to find the largest possible ρ, such that for the chosen threshold h_{MMME} it holds $P_{\mathrm{fa,MMME}} = P_{\mathrm{fa,MME}}$, that is

$$F_0(h_{\mathrm{MMME}}; \rho\sigma_w^2) \stackrel{!}{=} P_{\mathrm{fa,MME}}\,. \tag{7.27}$$

Here, $F_0(h_{\mathrm{MMME}}; \rho\sigma_w^2)$ denotes the CDF of the MMME detector under hypothesis $\mathcal{H}_0$ evaluated for the upper bounded noise power. With this procedure, we find the

largest admissible value for the noise power uncertainty ρ, such that it is guaranteed that $P_{\mathrm{d,MMME}} \geq P_{\mathrm{d,MME}}$ while $P_{\mathrm{fa,MMME}} \leq P_{\mathrm{fa,MME}}$.

Deriving a closed-form expression for finding ρ is not feasible, since closed-form expressions for the (inverse) CDFs are unknown to us. However, analogous to the ROC calculation, ρ can be readily found by numerical evaluation of the formulas involved. Table 7.1 shows the values for ρ (also in decibel scale, see (3.54)) found by numerically evaluating the process described above for $N = 1000$ number of samples per block, actual noise power $\sigma_w^2 = 1$ and target probability of false alarm $P_{\mathrm{fa,MME}}, P_{\mathrm{fa,MMME}} \leq 0.01$ for different SNRs α.

	max. tolerable noise uncertainty	
SNR α_{dB} in [dB]	ρ_{dB} in [dB]	ρ
-10	0.3904	1.0941
-11	0.3163	1.0755
-12	0.2563	1.0608
-13	0.2062	1.0486
-14	0.1662	1.0390
-15	0.1321	1.0309

Table 7.1: Maximum noise uncertainty ρ tolerable, so that $P_{\mathrm{d,MMME}} \geq P_{\mathrm{d,MME}}$ with upper bounded $P_{\mathrm{fa,MME}}, P_{\mathrm{fa,MMME}} \leq 0.01$ for $N = 1000$ and $\sigma_w^2 = 1$.

Thus, if an estimation of the noise power is available that is at least as accurate as summarized in Table 7.1 it would be beneficial to use the MMME detector instead of the MME detector. As an example, if the SNR is -11 dB, we can deduce from the table that the noise power estimate may be approximately 7.6% larger than the actual value before the MMME starts to perform worse than the MME.

Although it might seem that these results are encouraging at first sight, one has to keep in mind that in the literature noise power uncertainties as large as $\rho_{\mathrm{dB}} = 3$ dB are mentioned. Most authors study values in the range 0.5 dB $\leq \rho_{\mathrm{dB}} \leq$ 2 dB (see Section 3.5 or [17, 18, 41, 48]). Hence, we must conclude that for this model the MMME should be favored over the MME only when the noise power of the receiver can be very accurately estimated or when the detector is to be designed for higher SNRs, for which the MMME has a larger lead in detection performance. Note, however, that the MME detector is sensitive to errors in the noise power calibration, i.e., if the noise power of the SU are not exactly equal, as shown in Section 6.1.

7.3 Summary

In this chapter the MMME detector from [24] was analyzed theoretically. Utilizing results from random matrix theory, the test statistic PDFs under both hypotheses were derived in Section 7.1 for the simple system model $\mathcal{M}_{\mathrm{DM}}$ from Section 4.2.1 with two cooperating SUs. Moreover, in Section 7.1.3 it was discussed how the presented PDFs can be evaluated numerically for large numbers of samples that are customary in low SNR spectrum sensing. There, reformulated expressions of both PDFs were given, which can be evaluated using standard double precision arithmetic.

Furthermore, in Section 7.2 a performance comparison between the MMME and the MME block detectors was carried out. This was done based on theoretical results, since also the test statistic PDFs of the MME are available under the system model considered in this chapter, cf. Sections 5.3.2 and 5.3.3. Firstly, it was shown that the MMME outperforms the MME under ideal conditions by examining their ROCs, which were calculated on the basis of the corresponding PDFs. Secondly, since the MMME detector requires knowledge of the receiver noise power, the amount of tolerable noise power uncertainty was investigated, such that the detection performance of the MMME remains superior to the MME. It was concluded that for this model the MMME should only be used when the noise power estimation is very precise or the detector is intended for higher SNR ranges, where the MMMEs lead in detection performance is larger.

Although the results presented here are obtained under a very simple system model with only two cooperating SUs, the investigation process remains valid for other system models. It is doubtful, however, that exact results for the test statistic PDFs can be derived under more complex models. There, the exact PDFs may be replaced by estimated versions stemming from Monte Carlo simulations or measurements.

8 Conclusions

8.1 Summary

In opportunistic spectrum access, reliable spectrum sensing is the essential technology to minimize harmful interference for the licensed primary system. A spectrum sensing algorithm is responsible for detecting whether a frequency band is currently used by the licensed system (hypothesis $\mathcal{H}_1$) or not (hypothesis $\mathcal{H}_0$). It is therefore required to exhibit high detection performance even in low SNR scenarios.

The class of detectors operating on the eigenvalues of the sample covariance matrix is subsumed under the term eigenvalue-based spectrum sensing. It aims at exploiting correlations in the received signal over time or among multiple cooperating users in the presence of a licensee. Since the receiver noise is typically assumed to be a white random process which is uncorrelated among different receivers, the received signal samples should be free of correlations when the frequency band in question is vacant. Eigenvalue-based spectrum sensing is a prominent detection method since it requires very little knowledge about the signal characteristics of the primary system, while still displaying good detection performance. This thesis makes contributions to this field in three areas. Firstly, it explores the potential of reducing detection delays using results from the theory of quickest detection. Secondly, performance limits of well-known detectors in the presence of practical model uncertainties are studied. Finally, this work advances the theoretical analysis of detectors with the help of random matrix theory.

The concept of centralized, collaborative quickest eigenvalue-based spectrum sensing was introduced. Moreover, the characteristics and requirements of relevant change detection problems were discussed. A time-dependent system model was established, which is convenient for the development of algorithms and the comparison to classical eigenvalue-based block detection. For digitally modulated signals, flat fading wireless channels and additive white Gaussian noise, the distributions for the sample covariance matrix and the joint distributions of its ordered eigenvalues were given under both hypotheses. Quickest detection algorithms for known and unknown SNR were introduced for the special case of two cooperating receivers and for both types of possible hypothesis changes. They utilize the well-known maximum-minimum eigenvalue (MME) test statistic, for which analytical distributions could be obtained under both hypotheses. It was found that compared to the classical MME block detector, the quickest detection approach offers reduced

detection delay at comparable or better detection performance for a wide range of SNRs for the $\mathcal{H}_0$ to $\mathcal{H}_1$ change. For the $\mathcal{H}_1$ to $\mathcal{H}_0$ change, however, the results indicate that classical block detection performs favorably.

Furthermore, the adverse effects of model uncertainties on cooperative eigenvalue-based spectrum sensing systems were studied. On the example of two practical model uncertainties, insights on the robustness of detectors and performance limits in the form of bounds on the SNR walls were obtained. The SNR wall represents a threshold below which detection becomes impossible in the presence of model uncertainties, even when the number of samples N is arbitrarily large. Two practical model uncertainties were analyzed in the asymptotic regime ($N \to \infty$). Firstly, the influence of imperfect calibration of the receiver noise powers on three well-known detectors was investigated. It was shown that all three detectors suffer from the SNR wall phenomenon. Lower bounds on the SNR wall were derived in average case scenarios for rectangular and Gaussian distributed noise powers after calibration. The worst case analysis yielded upper and lower bounds on the SNR wall for two detectors. With the help of the latter bounds, the asymptotic SNR wall may be located to within roughly 3 dB of uncertainty for practical scenarios. All of these mentioned bounds are inversely proportional to the number of cooperating receivers, such that the SNR threshold may be alleviated up to a certain degree. Secondly, we briefly examined the influence of colored and correlated noise on the MME detector. A conservative lower bound on the SNR wall was derived, which depends on three parameters: the dimension of the sample covariance matrix, the maximum signal correlation coefficient and the maximum noise correlation coefficient. In the numerical evaluation it was found that for both model uncertainties the lower bounds on the SNR walls are located above or in close vicinity of the desired low SNR operating range for practical values of the system's parameters.

Moreover, the maximum-minus-minimum eigenvalue (MMME) detector was analyzed theoretically and compared to the well-known MME detector. Under a simple system model with flat fading and two cooperating receivers, the PDFs of the MMME test statistic were derived under both hypotheses. On the one hand, this allows precise calculation of the detection threshold. On the other hand, the detection performance may be accurately predicted. Since analogous theoretical results were obtained for the MME detector, an analytical comparison was conducted. It was found that the MMME outperforms the MME under ideal conditions. However, if the noise power is not known precisely, the results showed that the MME performs favorably.

8.2 Outlook

For practical application of the quickest eigenvalue-based detection algorithms, a more realistic model with an arbitrary number of cooperating receivers and a more

general wireless channel model is needed. Since it is probably intractable to derive the required PDFs of the test statistic exactly in this case, an approximation that is applicable in a variety of different channel scenarios is desired. Furthermore, a hybrid detection strategy in which the strengths of both quickest detection and block detection are combined may be worth investigating in future research.

The performance limits of cooperative eigenvalue-based spectrum sensing systems may be generalized in a number of ways. Firstly, it may be possible to derive similar bounds on the SNR wall in the non-asymptotic regime. Secondly, a combined treatment of multiple model uncertainties at the same time may yield even more valuable insights for practical applications. From a theoretical point of view, an interesting question is whether it is possible to prove that all eigenvalue-based detectors suffer form an SNR wall under certain model uncertainties. Particularly the results on colored and correlated noise would benefit from a generalization to a more realistic system model and the examination of additional detectors.

List of Symbols

$\mathbf{0}_N, \mathbf{0}_{K\times N}$	vector and matrix containing only zeros of dimensions N and $K \times N$, respectively
$\mathbf{1}_N, \mathbf{1}_{K\times N}$	vector and matrix containing only ones of dimensions N and $K \times N$, respectively
α	signal-to-noise ratio (SNR)
β	factor of standard deviations considered for modeling the SU noise power after calibration with a Gaussian distribution
ϵ_{ij}	noise correlation coefficient related to the covariance matrix $\mathbf{R}_{\tilde{\mathbf{w}}}$
$\epsilon_{\max}$	maximum noise correlation coefficient $\epsilon_{\max} = \max_{i\neq j} \epsilon_{ij}$
${}_p\mathcal{F}_q(\cdot;\cdot;v)$	generalized hypergeometric function
$\Gamma(v)$	Gamma function
$\mathcal{H}_0$	noise only hypothesis
$\mathcal{H}_1$	signal and noise hypothesis
$\mathcal{I}_a(v)$	a-th order modified Bessel function of the first kind
$\mathbb{I}_{\mathcal{B}}(v)$	indicator function with respect to the set $\mathcal{B}$
$\mathbf{I}_N$	identity matrix of dimension N
$\mathcal{K}_a(v)$	a-th order modified Bessel function of the second kind
λ_i	i-th increasingly ordered eigenvalue of the statistical covariance matrix $\mathbf{R}$
$\hat{\lambda}_i$	i-th increasingly ordered eigenvalue of the sample covariance matrix $\hat{\mathbf{R}}$
$\boldsymbol{\lambda}$	increasingly ordered eigenvalue vector of the statistical covariance matrix $\mathbf{R}$

$\hat{\boldsymbol{\lambda}}$	increasingly ordered eigenvalue vector of the sample covariance matrix $\hat{\mathbf{R}}$
$\mathcal{M}_{\mathrm{DM}}$	system model for digitally modulated PU signals with flat fading and a memoryless channel
$\mathcal{M}_{\mathrm{FF}}$	system model with flat fading and a memoryless channel
$\mathcal{M}_{\mathrm{MP}}$	system model with a multipath propagation channel
$\boldsymbol{\Omega}$	non-centrality matrix of the non-central Wishart distribution
ϕ, Φ	PDF and CDF of the univariate standard Gaussian distribution, respectively
ψ	parameter in the approximation of the mean of Gaussian order statistics
ρ	noise (power) uncertainty factor
ϱ_{ij}	signal correlation coefficient related to the covariance matrix $\mathbf{R}_{\tilde{\mathbf{x}}}$
$\varrho_{\max}$	maximum signal correlation coefficient $\varrho_{\max} = \max_{i \neq j} \varrho_{ij}$
σ_s	standard deviation of the PU signal
σ_w	standard deviation of the SU noise
σ_{w_i}	standard deviation of the i-th SU's receiver noise
$\bar{\tau}_{\mathrm{d}}$	mean time to detection (conditional mean delay)
$\bar{\tau}_{\mathrm{d}}^{\star}$	worst mean delay
$\bar{\tau}_{\mathrm{fa}}$	mean time to false alarm
ϑ	standard deviation of the Gaussian distribution used to model the SU noise power after calibration
$\mathcal{U}(a, b, c)$	Tricomi's confluent hypergeometric function
ζ_{C}	output of the cumulative sum (CUSUM) algorithm
ζ_{G}	output of the generalized likelihood ratio (GLR) algorithm
F	cumulative distribution function (CDF)
f	probability density function (PDF)

h	detection threshold
$h_i(t)$	channel impulse response of the wireless channel from the PU to SU i in the $\mathcal{M}_{\mathrm{MP}}$ model
$\mathbf{h}$	channel coefficient vector in the $\mathcal{M}_{\mathrm{FF}}$ and $\mathcal{M}_{\mathrm{DM}}$ models
K	number of cooperating SUs
$\tilde{K}$	number of eigenvalues of the (sample) covariance matrix, i.e., $\tilde{K} = KQ$
k	block index
l	log-likelihood ratio (LLR)
M	oversampling factor
m	estimated change time in the GLR algorithm
N	number of samples
p	area under the density of the Gaussian distribution within a $\beta\vartheta$ environment around the mean, which is used to model the SU noise power after calibration
P_{D}	probability of detection
P_{FA}	probability of false alarm
P_{MD}	probability of missed detection
Q	smoothing factor, i.e., number of consecutive time points considered for exploiting time correlation
$\mathbf{R}$	statistical covariance matrix of the processing vector $\mathbf{z}$
$\hat{\mathbf{R}}$	sample covariance matrix of the processing vector $\mathbf{z}$
$\hat{\mathbf{R}}(k)$	sample covariance matrix estimated from the k-th consecutive processing matrix $\mathbf{Z}(k)$
$\mathbf{R}_0$	statistical covariance matrix of the processing vector $\mathbf{z}$ under $\mathcal{H}_0$
$\hat{\mathbf{R}}_0$	sample covariance matrix of the processing vector $\mathbf{z}$ under $\mathcal{H}_0$
$\mathbf{R}_1$	statistical covariance matrix of the processing vector $\mathbf{z}$ under $\mathcal{H}_1$

$\hat{\mathbf{R}}_1$	sample covariance matrix of the processing vector $\mathbf{z}$ under $\mathcal{H}_1$
$\mathbf{R}_{\mathbf{x}}$	statistical covariance matrix of the filtered and distorted signal vector $\mathbf{x}$
$\mathbf{R}_{\tilde{\mathbf{x}}}$	statistical covariance matrix of the reordered filtered and distorted signal vector $\tilde{\mathbf{x}}$
$\mathbf{R}_{\mathbf{w}}$	statistical covariance matrix of the noise vector $\mathbf{w}$
$\mathbf{R}_{\tilde{\mathbf{w}}}$	statistical covariance matrix of the reordered noise vector $\tilde{\mathbf{w}}$
$s(t)$	PU signal at time index t
T	test statistic
T_{GLRT}	test statistic of the GLRT detector
T_{MME}	test statistic of the MME detector
T_{MMME}	test statistic of the MMME detector
T_{QST}	test statistic of the QST detector
$T(k)$	test statistic calculated from the k-th consecutive sample covariance matrix $\hat{\mathbf{R}}(k)$
t	discrete time index
t_{a}	alarm time
t_{c}	change time
$\mathbf{w}(t)$	N dimensional vector of the SU receiver noise at time index t
$\mathbf{W}$	$N \times N$ matrix containing a block of N SU receiver noise vectors
$\tilde{\mathbf{w}}(t), \tilde{\mathbf{W}}$	reordered versions of $\mathbf{w}(t)$ and $\mathbf{W}$ for exploiting time correlation, respectively
$\mathbf{x}(t)$	N dimensional vector of the filtered and distorted signal at time index t
$\mathbf{X}$	$N \times N$ matrix containing a block of N distorted and filtered signal vectors

$\tilde{\mathbf{x}}(t), \tilde{\mathbf{X}}$	reordered versions of $\mathbf{x}(t)$ and $\mathbf{X}$ for exploiting time correlation, respectively
$\mathbf{y}(t)$	N dimensional vector of the SU's received samples at time index t
$\mathbf{Y}$	$N \times N$ matrix containing a block of N SU received sample vectors
$\mathbf{z}(t), \mathbf{Z}$	processing vector and matrix, which are reordered versions of $\mathbf{y}(t)$ and $\mathbf{Y}$ for exploiting time correlation, respectively
$\mathbf{Z}(k)$	processing matrix of the k-th consecutive block of N samples of the processing vector $\mathbf{z}$

Acronyms

AWGN	additive white Gaussian noise
BCED	blindly combined energy detection
CDF	cumulative distribution function
CUSUM	cumulative sum
ED	energy detection
GLR	generalized likelihood ratio
GLRT	generalized likelihood ratio test
i.i.d.	independently and identically distributed
LLR	log-likelihood ratio
MIMO	multiple-input and multiple-output
MLE	maximum likelihood estimation
MME	maximum-minimum eigenvalue
MMME	maximum-minus-minimum eigenvalue
OFDM	orthogonal frequency-division multiplexing
PDF	probability density function
PMF	probability mass function
PSK	phase-shift keying
PU	primary user
QAM	quadrature amplitude modulation
QD	quickest detection
QST	quadratic sphericity test
RLRT	Roy's largest root test
RMT	random matrix theory
ROC	receiver operator characteristic

SCN	standard condition number
SNR	signal-to-noise ratio
SU	secondary user
w.l.o.g.	without loss of generality

Bibliography

[1] "Frequenzplan," Bundesnetzagentur, Germany, Apr. 2016. [Online]. Available: http://www.bundesnetzagentur.de/SharedDocs/Downloads/DE/Sachgebiete/Telekommunikation/Unternehmen_Institutionen/Frequenzen/Frequenzplan.pdf

[2] "FCC Online Table of Frequency Allocations," FCC Office of Engineering and Technology Policy and Rules Division, Aug. 2016. [Online]. Available: https://transition.fcc.gov/oet/spectrum/table/fcctable.pdf

[3] "Tätigkeitsbericht 2000 / 2001," Regulierungsbehörde für Telekommunikation und Post, Bonn, Germany, Dec. 2000. [Online]. Available: http://www.bundesnetzagentur.de/SharedDocs/Downloads/DE/Allgemeines/Bundesnetzagentur/Publikationen/Berichte/2001/Taetigkeitsbericht2000_2001Id206pdf.pdf?___blob=publicationFile&v=2

[4] "Mobiles Breitband - Projekt 2016," Bundesnetzagentur, Germany, Jun. 2015. [Online]. Available: http://www.bundesnetzagentur.de/cln_1412/DE/Sachgebiete/Telekommunikation/Unternehmen_Institutionen/Frequenzen/Projekt2016_Frequenzauktion/projekt2016-node.html

[5] "Report of the Spectrum Efficiency Working Group," FCC Spectrum Policy Task Force, Federal Communications Commission, USA, Nov. 2002. [Online]. Available: https://transition.fcc.gov/sptf/files/SEWGFinalReport_1.pdf

[6] "Spectrum Reports," Shared Spectrum Company (SSC), Vienna, VA, USA, 2004-2009. [Online]. Available: http://www.sharedspectrum.com/papers/spectrum-reports/

[7] Q. Zhao and B. M. Sadler, "A Survey of Dynamic Spectrum Access," *IEEE Signal Processing Magazine*, vol. 24, no. 3, pp. 79–89, May 2007.

[8] J. Mitola, "Cognitive Radio for Flexible Mobile Multimedia Communications," in *IEEE International Workshop on Mobile Multimedia Communications (MoMuC)*, 1999, pp. 3–10.

[9] S. Haykin, "Cognitive Radio: Brain-Empowered Wireless Communications," *IEEE Journal on Selected Areas in Communications*, vol. 23, no. 2, pp. 201–220, Feb. 2005.

[10] A. M. Wyglinski, M. Nekovee, and T. Hou, *Cognitive Radio Communications and Networks: Principles and Practice*. Academic Press, 2009.

[11] T. Yücek and H. Arslan, "A Survey of Spectrum Sensing Algorithms for Cognitive Radio Applications," *IEEE Communications Surveys & Tutorials*, vol. 11, no. 1, pp. 116–130, 2009.

[12] E. Axell, G. Leus, E. G. Larsson, and H. V. Poor, "Spectrum Sensing for Cognitive Radio: State-of-the-Art and Recent Advances," *IEEE Signal Processing Magazine*, vol. 29, no. 3, pp. 101–116, 2012.

[13] D. Cabric, S. M. Mishra, and R. W. Brodersen, "Implementation Issues in Spectrum Sensing for Cognitive Radios," in *Asilomar Conference on Signals, Systems and Computers*, vol. 1, 2004, pp. 772–776.

[14] A. Ghasemi and E. S. Sousa, "Collaborative Spectrum Sensing for Opportunistic Access in Fading Environments," in *IEEE International Symposium on New Frontiers in Dynamic Spectrum Access Networks (DySPAN)*, Nov. 2005, pp. 131–136.

[15] G. Ganesan and Y. Li, "Cooperative Spectrum Sensing in Cognitive Radio Networks," in *IEEE International Symposium on New Frontiers in Dynamic Spectrum Access Networks (DySPAN)*, Nov. 2005, pp. 137–143.

[16] S. M. Mishra, A. Sahai, and R. W. Brodersen, "Cooperative Sensing among Cognitive Radios," in *IEEE International Conference on Communications (ICC)*, Jun. 2006, pp. 1658–1663.

[17] Y. Zeng and Y.-C. Liang, "Maximum-Minimum Eigenvalue Detection for Cognitive Radio," in *IEEE International Symposium on Personal, Indoor and Mobile Radio Communication (PIMRC)*, Athens, Greece, 2007.

[18] Y. Zeng, Y.-C. Liang, and R. Zhang, "Blindly Combined Energy Detection for Spectrum Sensing in Cognitive Radio," *IEEE Signal Processing Letters*, vol. 15, pp. 649–652, 2008.

[19] Y. Zeng and Y.-C. Liang, "Eigenvalue-Based Spectrum Sensing Algorithms for Cognitive Radio," *IEEE Transactions on Communications*, vol. 57, no. 6, pp. 1784–1793, Jun. 2009.

[20] P. Bianchi, J. Najim, G. Alfano, and M. Debbah, "Asymptotics of Eigenbased Collaborative Sensing," in *IEEE Information Theory Workshop (ITW)*, 2009.

[21] A. Taherpour, M. Nasiri-kenari, and S. Gazor, "Multiple Antenna Spectrum Sensing in Cognitive Radios," *IEEE Transactions on Wireless Communications*, vol. 9, no. 2, pp. 814–823, Feb. 2010.

[22] P. Wang, J. Fang, N. Han, and H. Li, "Multiantenna-Assisted Spectrum Sensing for Cognitive Radio," *IEEE Transactions on Vehicular Technology*, vol. 59, no. 4, pp. 1791–1800, 2010.

[23] J. Font-Segura, J. Riba, J. Villares, and G. Vazquez, "Quadratic Sphericity Test for Blind Detection over Time-Varying Frequency-Selective Fading Channels," in *IEEE International Conference on Acoustics, Speech and Signal Processing (ICASSP)*, May 2013, pp. 4708–4712.

[24] A. Bollig and R. Mathar, "MMME and DME: Two New Eigenvalue-Based Detectors for Spectrum Sensing in Cognitive Radio," in *IEEE Global Conference on Signal and Information Processing (GlobalSIP)*, Austin, USA, 2013, pp. 1210–1213.

[25] M. Arts, A. Bollig, and R. Mathar, "Quickest Eigenvalue-Based Spectrum Sensing Using Random Matrix Theory," *arXiv:1504.01628 [cs.IT]*, Apr. 2015. [Online]. Available: http://arxiv.org/abs/1504.01628

[26] ——, "Analytical Test Statistic Distributions of the MMME Eigenvalue-Based Detector for Spectrum Sensing," in *International Symposium on Wireless Communication Systems (ISWCS)*, Brussels, Belgium, Aug. 2015.

[27] ——, "Exact Quickest Spectrum Sensing Algorithms for Eigenvalue-Based Change Detection," in *International Conference on Ubiquitous and Future Networks (ICUFN)*, Vienna, Austria, Jul. 2016.

[28] M. Arts and R. Mathar, "Performance Limits of Cooperative Eigenvalue-Based Spectrum Sensing Under Noise Calibration Uncertainty," in *International Conference on Ubiquitous and Future Networks (ICUFN)*, Vienna, Austria, Jul. 2016.

[29] A. Bollig, C. Disch, M. Arts, and R. Mathar, "SNR-Walls in Eigenvalue-Based Spectrum Sensing," *arXiv:1610.03892 [cs.IT]*, Oct. 2016. [Online]. Available: http://arxiv.org/abs/1610.03892

[30] ——, "SNR walls in eigenvalue-based spectrum sensing," *EURASIP Journal on Wireless Communications and Networking*, vol. 2017, no. 1, p. 109, Jun 2017.

[31] M. Abramowitz, I. A. Stegun, and others, *Handbook of Mathematical Functions*, 10th ed. Dover New York, 1972.

[32] A. Jeffrey and D. Zwillinger, *Table of Integrals, Series, and Products*, 7th ed. Academic Press, 2007.

[33] G. Casella and R. L. Berger, *Statistical Inference*, 2nd ed. Duxbury Pacific Grove, CA, USA, 2002.

[34] S. Kay, *Intuitive Probability and Random Processes Using MATLAB®*. Springer Science & Business Media, 2006.

[35] B. Picinbono, "Second-Order Complex Random Vectors and Normal Distributions," *IEEE Transactions on Signal Processing*, vol. 44, no. 10, pp. 2637–2640, Oct. 1996.

[36] S. M. Kay, *Fundamentals of Statistical Signal Processing: Detection Theory.* Prentice Hall, 1998, vol. II.

[37] ——, *Fundamentals of Statistical Signal Processing: Estimation Theory.* Upper Saddle River: Prentice Hall, 1993, vol. I.

[38] M. Basseville and I. V. Nikiforov, *Detection of Abrupt Changes: Theory and Application.* Prentice Hall, 1993.

[39] J. Neyman and E. S. Pearson, "On the Problem of the Most Efficient Tests of Statistical Hypotheses," *Philosophical Transactions of the Royal Society of London. Series A, Containing Papers of a Mathematical or Physical Character*, vol. 231, pp. 289–337, 1933.

[40] A. Sahai, R. Tandra, S. M. Mishra, and N. Hoven, "Fundamental Design Tradeoffs in Cognitive Radio Systems," in *International Workshop on Technology and Policy for Accessing Spectrum (TAPAS)*, New York, NY, USA, 2006.

[41] R. Tandra and A. Sahai, "SNR Walls for Feature Detectors," in *International Symposium on New Frontiers in Dynamic Spectrum Access Networks (DySPAN)*, Apr. 2007, pp. 559–570.

[42] D. Cabric, I. D. O'Donnell, M. S. W. Chen, and R. W. Brodersen, "Spectrum Sharing Radios," *IEEE Circuits and Systems Magazine*, vol. 6, no. 2, pp. 30–45, 2006.

[43] C. R. Stevenson, G. Chouinard, Z. Lei, W. Hu, S. J. Shellhammer, and W. Caldwell, "IEEE 802.22: The First Cognitive Radio Wireless Regional Area Network Standard," *IEEE Communications Magazine*, vol. 47, no. 1, pp. 130–138, Jan. 2009.

[44] "IEEE Standard for Information Technology - Local and Metropolitan Area Networks - Specific Requirements - Part 22: Cognitive Wireless RAN Medium Access Control (MAC) and Physical Layer (PHY) Specifications: Policies and Procedures for Operation in the TV Bands," IEEE Standard 802.22-2011, Jul. 2011.

[45] H. Urkowitz, "Energy Detection of Unknown Deterministic Signals," *Proceedings of the IEEE*, vol. 55, no. 4, pp. 523–531, Apr. 1967.

[46] A. Sahai, N. Hoven, and R. Tandra, "Some Fundamental Limits on Cognitive Radio," in *Allerton Conference on Communication, Control, and Computing*, Allerton, USA, 2004.

[47] E. Axell and E. G. Larsson, "Optimal and Sub-Optimal Spectrum Sensing of OFDM Signals in Known and Unknown Noise Variance," *IEEE Journal on Selected Areas in Communications*, vol. 29, no. 2, pp. 290–304, Feb. 2011.

[48] R. Tandra and A. Sahai, "SNR Walls for Signal Detection," *IEEE Journal of Selected Topics in Signal Processing*, vol. 2, no. 1, pp. 4–17, Feb. 2008.

[49] W. A. Gardner, A. Napolitano, and L. Paura, "Cyclostationarity: Half a Century of Research," *Signal Processing*, vol. 86, no. 4, pp. 639–697, Apr. 2006.

[50] A. V. Dandawate and G. B. Giannakis, "Statistical Tests for Presence of Cyclostationarity," *IEEE Transactions on Signal Processing*, vol. 42, no. 9, pp. 2355–2369, 1994.

[51] W. A. Gardner, "Signal Interception: A Unifying Theoretical Framework for Feature Detection," *IEEE Transactions on Communications*, vol. 36, no. 8, pp. 897–906, Aug. 1988.

[52] J. Lundén, V. Koivunen, A. Huttunen, and H. V. Poor, "Spectrum Sensing in Cognitive Radios Based on Multiple Cyclic Frequencies," in *International Conference on Cognitive Radio Oriented Wireless Networks and Communications (CrownCom)*, Aug. 2007, pp. 37–43.

[53] ——, "Collaborative Cyclostationary Spectrum Sensing for Cognitive Radio Systems," *IEEE Transactions on Signal Processing*, vol. 57, no. 11, pp. 4182–4195, 2009.

[54] H. Li, "Cyclostationary Feature Based Quickest Spectrum Sensing in Cognitive Radio Systems," in *IEEE Vehicular Technology Conference Fall (VTC)*, Ottawa, Canada, 2010, pp. 1–5.

[55] A. Bollig, M. Arts, A. Lavrenko, and R. Mathar, "Compressive Cyclostationary Spectrum Sensing with a Constant False Alarm Rate," *arXiv:1610.04027 [cs.IT]*, Oct. 2016. [Online]. Available: http://arxiv.org/abs/1610.04027

[56] H. Tang, "Some Physical Layer Issues of Wide-Band Cognitive Radio Systems," in *IEEE International Symposium on New Frontiers in Dynamic Spectrum Access Networks (DySPAN)*, Baltimore, MD, USA, Nov. 2005, pp. 151–159.

[57] D. Cabric, A. Tkachenko, and R. W. Brodersen, "Spectrum Sensing Measurements of Pilot, Energy, and Collaborative Detection," in *IEEE Military Communications Conference (MILCOM)*, Washington, DC, USA, Oct. 2006.

[58] X. Yang, K. Lei, S. Peng, and X. Cao, "Blind Detection for Primary User Based on the Sample Covariance Matrix in Cognitive Radio," *IEEE Communications Letters*, vol. 15, no. 1, pp. 40–42, Jan. 2011.

[59] R. A. Horn and C. R. Johnson, *Matrix Analysis*, 2nd ed. Cambridge University Press, 2012.

[60] F. Penna, R. Garello, and M. A. Spirito, "Cooperative Spectrum Sensing Based on the Limiting Eigenvalue Ratio Distribution in Wishart Matrices," *IEEE Communications Letters*, vol. 13, no. 7, pp. 507–509, 2009.

[61] F. Penna, R. Garello, D. Figlioli, and M. A. Spirito, "Exact Non-Asymptotic Threshold for Eigenvalue-Based Spectrum Sensing," in *International Conference on Cognitive Radio Oriented Wireless Networks and Communications (CROWNCOM)*, Hannover, Germany, Jun. 2009.

[62] A. Kortun, T. Ratnarajah, M. Sellathurai, C. Zhong, and C. Papadias, "On the Performance of Eigenvalue-Based Cooperative Spectrum Sensing for Cognitive Radio," *IEEE Journal of Selected Topics in Signal Processing*, vol. 5, no. 1, pp. 49–55, Feb. 2011.

[63] L. Wei and O. Tirkkonen, "Spectrum Sensing with Gaussian Approximated Eigenvalue Ratio Based Detection," in *International Symposium on Wireless Communication Systems (ISWCS)*, York, GB, Sep. 2010, pp. 961–965.

[64] M. Z. Shakir, A. Rao, and M.-S. Alouini, "On the Decision Threshold of Eigenvalue Ratio Detector Based on Moments of Joint and Marginal Distributions of Extreme Eigenvalues," *IEEE Transactions on Wireless Communications*, vol. 12, no. 3, pp. 974–983, Mar. 2013.

[65] F. Penna, R. Garello, and M. A. Spirito, "Probability of Missed Detection in Eigenvalue Ratio Spectrum Sensing," in *IEEE International Conference on Wireless and Mobile Computing, Networking and Communications (WIMOB)*, Marrakech, Morocco, Oct. 2009, pp. 117–122.

[66] P. Bianchi, M. Debbah, M. Maida, and J. Najim, "Performance of Statistical Tests for Single-Source Detection Using Random Matrix Theory," *IEEE Transactions on Information Theory*, vol. 57, no. 4, pp. 2400–2419, Apr. 2011.

[67] B. Nadler, F. Penna, and R. Garello, "Performance of Eigenvalue-Based Signal Detectors with Known and Unknown Noise Level," in *IEEE International Conference on Communications (ICC)*, Jun. 2011.

[68] S. N. Roy, "On a Heuristic Method of Test Construction and Its Use in Multivariate Analysis," *The Annals of Mathematical Statistics*, vol. 24, no. 2, pp. 220–238, 1953.

[69] H. V. Poor and O. Hadjiliadis, *Quickest Detection*. Cambridge University Press, 2009.

[70] G. Lorden, "Procedures for Reacting to a Change in Distribution," *The Annals of Mathematical Statistics*, vol. 42, no. 6, pp. 1897–1908, 1971.

[71] E. S. Page, "Continuous Inspection Schemes," *Biometrika*, vol. 41, no. 1/2, pp. 100–115, 1954.

[72] L. Lai, Y. Fan, and H. V. Poor, "Quickest Detection in Cognitive Radio: A Sequential Change Detection Framework," in *IEEE Global Telecommunications Conference (GLOBECOM)*, New Orleans, USA, 2008.

[73] G. V. Moustakides, "Optimal Stopping Times for Detecting Changes in Distributions," *The Annals of Statistics*, vol. 14, no. 4, pp. 1379–1387, 1986.

[74] Y. Ritov, "Decision Theoretic Optimality of the CUSUM Procedure," *The Annals of Statistics*, vol. 18, no. 3, pp. 1464–1469, 1990.

[75] G. Lorden, "On Excess over the Boundary," *The Annals of Mathematical Statistics*, vol. 41, no. 2, pp. 520–527, 1970.

[76] ——, "Open-Ended Tests for Koopman-Darmois Families," *The Annals of Statistics*, vol. 1, no. 4, pp. 633–643, Jul. 1973.

[77] A. Wald, *Sequential Analysis*. Wiley, 1947.

[78] ——, "Sequential Tests of Statistical Hypotheses," *The Annals of Mathematical Statistics*, vol. 16, no. 2, pp. 117–186, Jun. 1945.

[79] R. J. Muirhead, *Aspects of Multivariate Statistical Theory*, 2nd ed. John Wiley & Sons, 2005.

[80] E. P. Wigner, "Random Matrices in Physics," *SIAM Review*, vol. 9, no. 1, pp. 1–23, Jan. 1967.

[81] A. M. Tulino and S. Verdú, *Random Matrix Theory and Wireless Communications*. now Publishers Inc., 2004.

[82] J. Wishart, "The Generalised Product Moment Distribution in Samples from a Normal Multivariate Population," *Biometrika*, vol. 20A, no. 1/2, pp. 32–52, 1928.

[83] A. T. James, "Distributions of Matrix Variates and Latent Roots Derived from Normal Samples," *The Annals of Mathematical Statistics*, vol. 35, no. 2, pp. 475–501, 1964.

[84] T. W. Anderson and M. A. Girshick, "Some Extensions of the Wishart Distribution," *The Annals of Mathematical Statistics*, vol. 15, no. 4, pp. 345–357, 1944.

[85] T. W. Anderson, "The Non-Central Wishart Distribution and Certain Problems of Multivariate Statistics," *The Annals of Mathematical Statistics*, vol. 17, no. 4, pp. 409–431, Dec. 1946.

[86] M. Weibull, "The Distribution of T- and F-Statistics and of Correlation and Regression Coefficients in Stratified Samples from Normal Populations with Different Means," *Scandinavian Actuarial Journal*, vol. 1953, no. sup2, pp. 1–106, Jul. 1953.

[87] A. T. James, "The Non-Central Wishart Distribution," *Proceedings of the Royal Society of London. Series A, Mathematical and Physical Sciences*, vol. 229, no. 1178, pp. 364–366, 1955.

[88] ——, "A Generating Function for Averages Over the Orthogonal Group," *Proceedings of the Royal Society of London A: Mathematical, Physical and Engineering Sciences*, vol. 229, no. 1178, pp. 367–375, May 1955.

[89] ——, "Zonal Polynomials of the Real Positive Definite Symmetric Matrices," *Annals of Mathematics*, vol. 74, no. 3, pp. 456–469, 1961.

[90] A. G. Constantine, "Some Non-Central Distribution Problems in Multivariate Analysis," *The Annals of Mathematical Statistics*, vol. 34, no. 4, pp. 1270–1285, 1963.

[91] N. R. Goodman, "Statistical Analysis Based on a Certain Multivariate Complex Gaussian Distribution (An Introduction)," *The Annals of Mathematical Statistics*, vol. 34, no. 1, pp. 152–177, 1963.

[92] G. Letac and H. Massam, "The Noncentral Wishart as an Exponential Family, and Its Moments," *Journal of Multivariate Analysis*, vol. 99, no. 7, pp. 1393–1417, Aug. 2008.

[93] F. Nielsen and V. Garcia, "Statistical Exponential Families: A Digest with Flash Cards," *arXiv:0911.4863 [cs.LG]*, 2009. [Online]. Available: http://arxiv.org/abs/0911.4863

[94] R. A. Fisher, "The Sampling Distribution of Some Statistics Obtained from Non-Linear Equations," *Annals of Eugenics*, vol. 9, no. 3, pp. 238–249, Aug. 1939.

[95] M. A. Girshick, "On the Sampling Theory of Roots of Determinantal Equations," *The Annals of Mathematical Statistics*, vol. 10, no. 3, pp. 203–224, 1939.

[96] P. L. Hsu, "On the Distribution of Roots of Certain Determinantal Equations," *Annals of Eugenics*, vol. 9, no. 3, pp. 250–258, Aug. 1939.

[97] S. N. Roy, "P-Statistics or Some Generalisations in Analysis of Variance Appropriate to Multivariate Problems," *Sankhyā: The Indian Journal of Statistics (1933-1960)*, vol. 4, no. 3, pp. 381–396, 1939.

[98] A. T. James, "The Distribution of the Latent Roots of the Covariance Matrix," *The Annals of Mathematical Statistics*, vol. 31, no. 1, pp. 151–158, 1960.

[99] A. Takemura, *Zonal Polynomials*, ser. Lecture Notes - Monograph Series. Institute of Mathematical Statistics, 1984, no. 4.

[100] C. G. Khatri, "On the Moments of Traces of Two Matrices in Three Situations for Complex Multivariate Normal Populations," *Sankhyā: The Indian Journal of Statistics, Series A (1961-2002)*, vol. 32, no. 1, pp. 65–80, 1970.

[101] M. Chiani, M. Z. Win, and A. Zanella, "On the Capacity of Spatially Correlated MIMO Rayleigh-Fading Channels," *IEEE Transactions on Information Theory*, vol. 49, no. 10, pp. 2363–2371, Oct. 2003.

[102] A. Zanella, M. Chiani, and M. Z. Win, "On the Marginal Distribution of the Eigenvalues of Wishart Matrices," *IEEE Transactions on Communications*, vol. 57, no. 4, pp. 1050–1060, 2009.

[103] W. Zhang, G. Abreu, M. Inamori, and Y. Sanada, "Spectrum Sensing Algorithms via Finite Random Matrices," *IEEE Transactions on Communications*, vol. 60, no. 1, pp. 164–175, Jan. 2012.

[104] A. Sonnenschein and P. Fishman, "Radiometric Detection of Spread-Spectrum Signals in Noise of Uncertain Power," *IEEE Transactions on Aerospace and Electronic Systems*, vol. 28, no. 3, pp. 654–660, Jul. 1992.

[105] D. Cabric, A. Tkachenko, and R. W. Brodersen, "Experimental Study of Spectrum Sensing Based on Energy Detection and Network Cooperation," in *International Workshop on Technology and Policy for Accessing Spectrum (TAPAS)*, Boston, MA, USA, 2006.

[106] R. Tandra and A. Sahai, "Fundamental Limits on Detection in Low SNR under Noise Uncertainty," in *International Conference on Wireless Networks, Communications and Mobile Computing*, vol. 1, Maui, HI, USA, Jun. 2005, pp. 464–469.

[107] P. Dhakal, D. Rivello, F. Penna, and R. Garello, "Impact of Noise Estimation on Energy Detection and Eigenvalue Based Spectrum Sensing Algorithms," in *IEEE International Conference on Communications (ICC)*, Jun. 2014, pp. 1367–1372.

[108] S. Kritchman and B. Nadler, "Non-Parametric Detection of the Number of Signals: Hypothesis Testing and Random Matrix Theory," *IEEE Transactions on Signal Processing*, vol. 57, no. 10, pp. 3930–3941, Oct. 2009.

[109] H. A. David and H. Nagaraja, *Order Statistics*. John Wiley & Sons, 2004.

[110] M. Ahsanullah, V. B. Nevzorov, and M. Shakil, *An Introduction to Order Statistics*, ser. Atlantis Studies in Probability and Statistics. Atlantis Press, 2013, no. 3.

[111] S. Zarrin and T. J. Lim, "Cooperative Quickest Spectrum Sensing in Cognitive Radios with Unknown Parameters," in *IEEE Global Telecommunications Conference (GLOBECOM)*, Honululu, HI, USA, 2009.

[112] M. Shakir, A. Rao, and M.-S. Alouini, "Collaborative Spectrum Sensing Based on the Ratio between Largest Eigenvalue and Geometric Mean of Eigenvalues," in *IEEE GLOBECOM Workshops (GC Wkshps)*, Houston, TX, USA, Dec. 2011, pp. 913–917.

[113] A. Goldsmith, *Wireless Communications*. Cambridge University Press, 2005.

[114] J. Ohm and H. D. Lüke, *Signalübertragung: Grundlagen der Digitalen und Analogen Nachrichtenübertragungssysteme*, 10th ed. Springer, 2007.

[115] H. Li, C. Li, and H. Dai, "Quickest Spectrum Sensing in Cognitive Radio," in *IEEE Conference on Information Sciences and Systems (CISS)*, Princeton, USA, 2008, pp. 203–208.

[116] H. Li, H. Dai, and C. Li, "Collaborative Quickest Spectrum Sensing via Random Broadcast in Cognitive Radio Systems," *IEEE Transactions on Wireless Communications*, vol. 9, no. 7, pp. 2338–2348, 2010.

[117] E. Hanafi, P. A. Martin, P. J. Smith, and A. J. Coulson, "Extension of Quickest Spectrum Sensing to Multiple Antennas and Rayleigh Channels," *IEEE Communications Letters*, vol. 17, no. 4, pp. 625–628, 2013.

[118] C. Tsinos and K. Berberidis, "Decentralized Adaptive Eigenvalue-Based Spectrum Sensing for Multiantenna Cognitive Radio Systems," *IEEE Transactions on Wireless Communications*, vol. 14, no. 3, pp. 1703–1715, Mar. 2015.

[119] L. Wei and O. Tirkkonen, "Cooperative Spectrum Sensing of OFDM Signals Using Largest Eigenvalue Distributions," in *IEEE International Symposium on Personal, Indoor and Mobile Radio Communications (PIMRC)*, Tokyo, Japan, Sep. 2009, pp. 2295–2299.

[120] P. Lancaster and M. Tismenetsky, *The Theory of Matrices*. Academic Press, May 1985.

[121] M. Chiani, M. Win, and H. Shin, "Capacity of MIMO Systems in the Presence of Interference," in *IEEE Global Telecommunications Conference (GLOBECOM)*, San Francisco, CA, USA, Nov. 2006.

[122] M. Chiani, M. Z. Win, and H. Shin, "A General Result on Hypergeometric Functions of Matrix Arguments and Application to Wireless MIMO Communication," in *First International Conference on Next-Generation Wireless Systems (ICNEWS)*, Dhaka, Bangladesh, 2006, pp. 196–200.

[123] S. Jin, M. R. McKay, X. Gao, and I. B. Collings, "MIMO Multichannel Beamforming: SER and Outage Using New Eigenvalue Distributions of Complex Noncentral Wishart Matrices," *IEEE Transactions on Communications*, vol. 56, no. 3, pp. 424–434, 2008.

[124] A. M. Mood, F. Graybill, and D. Boes, *Introduction to the Theory of Statistics*, 3rd ed. McGraw Hill, 1974.

[125] M. Matthaiou, M. R. Mckay, P. J. Smith, and J. A. Nossek, "On the Condition Number Distribution of Complex Wishart Matrices," *IEEE Transactions on Communications*, vol. 58, no. 6, pp. 1705–1717, Jun. 2010.

[126] M. Matthaiou, D. I. Laurenson, and C.-X. Wang, "On Analytical Derivations of the Condition Number Distributions of Dual Non-Central Wishart Matrices," *IEEE Transactions on Wireless Communications*, vol. 8, no. 3, pp. 1212–1217, 2009.

[127] "IEEE Standard for Floating-Point Arithmetic," IEEE Standard 754-2008, Aug. 2008.

[128] "MATLAB Release 2015a," The Mathworks, Inc., Natick, Massachusetts, United States, 2015.

[129] I. N. Bronstein, K. A. Semendjajew, G. Musiol, and H. Mühlig, *Taschenbuch der Mathematik*, 6th ed. Verlag Harri Deutsch, 2005.

[130] S. G. Johnson, "Cubature 1.0.2. - Adaptive Multidimensional Integration Routines for Vector-Valued Integrands over Hypercubes," 2014. [Online]. Available: http://ab-initio.mit.edu/wiki/index.php/Cubature

[131] G. Blom, *Statistical Estimates and Transformed Beta-Variables*. Stockholm: Almquist and Wiksell, 1958.

[132] H. L. Harter, "Expected Values of Normal Order Statistics," *Biometrika*, vol. 48, no. 1/2, pp. 151–165, 1961.

[133] W. Fulton, "Eigenvalues, Invariant Factors, Highest Weights, and Schubert Calculus," *arXiv:math/9908012 [math.AG]*, Aug. 1999. [Online]. Available: http://arxiv.org/abs/math/9908012

[134] P. Van Dooren and L. de Ridder, "An Adaptive Algorithm for Numerical Integration over an N-Dimensional Cube," *Journal of Computational and Applied Mathematics*, vol. 2, no. 3, pp. 207–217, 1976.

[135] J. Berntsen, T. O. Espelid, and A. Genz, "An Adaptive Algorithm for the Approximate Calculation of Multiple Integrals," *ACM Transactions on Mathematical Software (TOMS)*, vol. 17, no. 4, pp. 437–451, 1991.

[136] C. D. Motchenbacher and J. A. Connelly, *Low-Noise Electronic System Design*. Wiley New York, 1993.

[137] "Recommendation ITU-R P.372-12: Radio Noise," International Telecommunication Union, Jul. 2015. [Online]. Available: https://www.itu.int/rec/R-REC-P.372-12-201507-I/en

[138] A. J. Wagstaff and N. Merricks, "Man-Made Noise Measurement Programme (AY4119) Final Report," Mass Consultants Limited, Tech. Rep., 2003.

[139] A. Wagstaff and N. Merricks, "Man-Made Noise Measurement Programme," *IEE Proceedings - Communications*, vol. 152, no. 3, pp. 371–377, Jun. 2005.

Curriculum Vitæ

Martijn Franciscus Arts	Born on 31st of March 1986 in Venray, Netherlands
1992 - 1995	Elementary school in Altrich, Germany
1995 - 1996	Elementary school in Wittlich, Germany
1996 - 2005	Academic high school in Wittlich, Germany
3rd of March 2005	General qualification for university entrance (Abitur)
2005 - 2011	RWTH Aachen University, Faculty of Electrical Engineering and Information Technology, Aachen, Germany
November 2009 - April 2010	Internship in the Biomedical Sensor Systems Department, Philips Research, Philips Electronics Nederland B.V., Eindhoven, Netherlands
28th of April 2011	Diploma degree in Computer Engineering from RWTH Aachen University, Aachen, Germany
June 2011 - November 2011	Graduate assistant at the Philips Chair for Medical Information Technology of RWTH Aachen University, Aachen Germany
December 2011 - March 2017	Scientific Staff Member (Research Assistant) at the Institute for Theoretical Information Technology of RWTH Aachen University, Aachen, Germany
From April 2017	Data Scientist, Qlaym GmbH, Düsseldorf, Germany